Investigation on the multiscale multiphysics based approach to modelling and simulation in abrasive flow machining of aerofoil structures and its application perspectives

A thesis submitted for the degree of

Doctor of Philosophy

By

Yizhi Shao

College of Engineering, Design and Physical Sciences

Brunel University London

September 2020

Abstract

Abrasive Flow Machining technology is attracting more and more attentions and expanding into more areas by the industry and research community, particularly in the context of increasing demands for post-processing of complex aerofoil structures and additively manufactured components. This thesis presents an analytical scientific approach for investigating the material removal and surface generation in Abrasive Flow Machining in relation to the affecting factors from the material properties of fluid media, abrasive grains, operation conditions and workpiece material with the aid of multiscale multiphysics modelling and simulation.

The multiscale multiphysics approach combined with micro-cutting mechanics is further presented to modelling and analysis of the surface roughness and topography profile generation in the AFM process. The analysis is developed and implemented by using the COMSOL multiphysics computational environment integrated with MATLAB programming as needed. The work described is fundamental but essential as a part of the efforts for developing the simulation-based virtual AFM system.

The improved Preston equation is developed in this PhD research, which aims to enhance the scientific understanding of the AFM process and its industrial application. The improved Preston equation can be used to aid the engineers to optimise the process for desired surface roughness and edge tolerance characteristics on complex geometries in an intuitive and scientific manner. The methodology of deriving the equation underpins the fundamental cutting mechanics of abrasive flow machining assuming all abrasive particles within the media are spherical as manufacturers defined. Further to the derivation, four factorial experimental trials and computational fluid dynamics (CFD) simulations are implemented to generate the flow features of media on a coupon to evaluate and validate the equation for its competency and accuracy on prediction of material removals. The modified Preston equation can significantly contribute to the optimisation of the AFM process, which will advantage the integrated machine-process design to predict the virtual surface roughness and material removal rates.

In this doctoral research, micro cutting mechanics analysis and Monte Carlo (MC) algorithms are integrated to support the virtual AFM system on the generation of surface texture and topography in the AFM process, through abrasive micro machining with thousands of grains with the complex machining trajectories and advanced analysis in a multiscale multiphysics manner.

The method and basic design to determine the viscosity functions are studied and explored using a capillary rheometer and the geometric properties of the solid abrasive particles in the fluidic media. Those particles properties and media viscosity are the bare minimum required for developing multiscale multiphysics simulations on the AFM process. The method is used to evaluate the relative importance of the elastic effects of the polymer filled with particles.

AFM trials and industrial case studies on aerofoil structures are conducted to validate the modelling and simulations developed against industrial requirements. There are good agreements between the results of simulations and the trials, further supported by industrial manufacturing data. The effects of process variables and tooling characteristics on material removal and surface roughness generation are investigated by analysing the results of AFM trials and simulations. AFM trials on IBR (Integrally Bladed Rotor) segments are carried out to validate the modelling and simulation mainly focusing on the profile accuracy control of leading/trailing edges of the IBR blades.

Acknowledgement

First and foremost, I would like to express my gratitude to my supervisor, Professor Kai Cheng, for his enthusiastic scientific support, insightful guidance, and patience throughout this research. Without his precious advices and encouragement, the completion of the PhD project would not have been possible.

I would like to thank Brunel University London and the National Aerospace Technology Programme (NATEP) for their financial support which made this research possible. I am also grateful to my colleagues, Dr Mayo Adetoro, Mr Rodrigo Merlo Bodenhorst, Mr Mitul Jadva, and Mr Jorge Rodriguez, for their assistance in the abrasive flow machining trials, simulations development and valuable discussions.

Project partners, including ITP Engines UK Ltd and Extrude Hone Ltd, have also to be acknowledged for their support, assistance and constructive suggestions in this research project. I am also grateful to industrial colleagues, Dr Raybin Yu, Mr David Peerless, Mr Neil Drurey and Mr Kevin Ngoe, from those partner companies for their kind help on the technical trials and experiments.

I am deeply indebted to my parents, Dongxiang Shao and Jiwen Mao, for their continuous encouragement and support.

Table of Contents

List of Figures

List of Tables

Nomenclature

A= the contact area (mm^2)

B_p= Back Pressure (bar)

C= the ratio of mean contact stress over uniaxial flow stress of the material

C_i= Viscosity co-efficient in Improved Preston Equation

D= deformation rate tensor or rate of strain tensor

d_g= diameter of a spherical grain (mm)

D_p= Piston Diameter (mm)

d_s= the depth of indentation (mm)

E_m= the Young's modulus of elasticity

E_p= the extrusion pressure (bar)

F= volume force matrix

f= Force (N)

F_d = damping force of the media (N)

F_n= the indenting force (N)

F'_{ng}= represents the normal force acting on the cutting tool (N)

$\mathbf{F}_T$= a sum of pressure and viscous forces (N)

H_w= Brinell hardness coefficient of the material

I= the unit diagonal matrix

K, a_1, a_2, a_3, a_4= fluid properties of abrasive media

k = stiffness

K_m = media constant in Improved Preston Equation

K_p = Empirically determined constant known as Preston co-efficient

K_t = time constant in Improved Preston Equation

K_{va1}= Coefficient used in Abrasion Model

K_{va2}= Coefficient used in Abrasion Model

L_d= the length of die (mm)

L_i= Contact length of ith abrasive grain with the work piece

l_s= stroke length (mm)

MRR_v= The material removal rate by volume

n= the normal vector to the boundary

n= Power law index

p= Pressure

p_0= the maximum pressure at the point of contact

Q= Flow rate

$\dot{r}$= local calculated shear rate

R_1= the radius of curvature for each individual peak along the surface

R_2= the radius of the abrasive particles

R_c= Remove rate at P = 0 and v = 0

R_d= the die radius

R_e= Reynolds number

R_{mc}= radius of media cylinder

R_p= The radius of grains

R_w= radius of cylindrical workpiece (mm)

SF_{avg}= Average of Shape Factor

SF_{max}= Maximum of Shape Factor

SF_{min}= Minimum of Shape Factor

T= the stress tensor;

t= Depth of indentation;

$\overset{\triangledown}{\mathrm{T}}$= the upper convected time derivative of stress tensor;

T_1= Stress of Viscoelastic component

T_2= Stress of Purely viscous component

T_l= Local calculated temperature

V= Total Processing Volume

v= fluid velocity

V_1= The volume of the initial cycle

x = extension of distance (mm)

ΔP= the pressure drop along the well-developed region

α = The angle between the grain and the surface and

β= The angle of the corner which is pressing the surface now from the grain

$\dot{\gamma}$= magnitude of the strain rate

$\dot{\gamma}_a$= the corrected apparent shear rate

$\dot{\gamma}_{simulated}$= The shear rate at the wall obtained in simulation

σ= the uniaxial flow stress

η_0= the total viscosity composed of solvent and polymer components

λ_1= the relaxation time;

λ_2= the retardation time $= \frac{\eta_s}{\eta_0}\lambda_1$;

μ= viscosity of abrasive media

μ_0= zero shear rate viscosity

ρ= Density

τ_{rc}= the corresponding corrected shear stress

Abbreviations

AFF	Abrasive Flow Finishing
AFM	Abrasive Flow Machining
ALE	Arbitrary Lagrangian-Eulerian
CAD	Computer-Aided Design
CFD	Computational Fluid Dynamics
CMP	Chemical- Mechanical Polishing
CNC	Computer Numerical Control
DOE	U.S. Department of Energy
EDS	Energy-Dispersive X-ray Spectroscopy
EH	Extrude Hone Ltd
FEM	Finite Element Method
FSI	Fluid- Structure Interaction
IBR	Integrally Bladed Rotor
ID	Inside Diameter
ITP	ITP Engines UK Ltd
M&M	Multiscale and Multiphysics
MC	Monto Carlo Method
MD	Molecular Dynamics
MR	Material Removal
MRR	Material Removal Rate
NS	Navier-Stokes Equation
OD	Outside Diameter

QC	Quasi-Continuum Method
R&D	Research and Development
SD	Standard Deviation
SEM	Scanning Electron Microscope
SF	Shape Factor
SR	Surface Roughness
UMT	Universal Testing Machine

Chapter 1 Introduction

1.1 Background and significance of the research

The development of precision manufacturing techniques has changed our lives significantly in terms of increased living standards. High precision manufacturing offers not only quality and reliability for conventional products but also makes possible entirely new products, especially where mechatronics, miniaturisation and high performance are essential [1]. Precision manufacturing is taking more and more status because of the rapidly increasing need for high precision products and components in advanced science and technology for energy, computer technology, electronics, data processing and defence applications. Examples are seen in the manufacturing of optics for inertial confinement fusion reactors, aluminium scanner mirrors, aluminium substrate drums in photocopy machines and aluminium substrates for computer hard disks [2]. All of these products or components require an excellent surface finish of a few tens nanometres (p-v) roughness and micrometre to sub-micrometre form accuracy [2].

Since its inception in the 1960s, the abrasive flow machining (AFM) process has been applied successfully to high-value manufacturing industries for polishing, edge-rounding and removal of recast layer [3]. Especially suited to the processing of features inaccessible by hand, production methodology is well-established, typically consisting of a single design stage to control the introduction of the abrasive media. With an increasing trend toward harder and tougher workpiece materials and more complex geometry, the limitations of the AFM process are becoming apparent, none more so than in material removal ability and in the flexibility of machine hardware.

In industry, the AFM process is a widely-accepted form of edge and surface-conditioning with primary application in parts with internal cavities inaccessible by traditional hand tools [4-6]. A principal concern in the production environment is the accuracy and repeatability with which an engineer can claim to control a process – AFM is subject to multi-order interactions between its (approximately) 25 variables which dictate the final part condition [7-8]. Most of these variables are passively altered,

(i.e. friction accumulating thermal energy within the media) although there are three key groups of factors which allow full control, that can be split into the machine, media and geometry categories for ease of description [9].

On the other hand, the adverse effects of surface roughness caused by natural degradation processes influence hardly on the gas turbines. The effects of surface roughness on gas turbine performance are reviewed based on publications in the open literature over the past 60 years [10]. The degradation of gas turbines with service is a severe problem that must be appropriately addressed for the efficient and safe operation of both land-based (power) and aero propulsion gas turbines. Both compressors and turbines are affected by surface roughness. The profile losses and surface heat transfer of bladed rotors are primarily due to the rich parameter space required to characterise roughness adequately.

Currently, the manufacturing of integrally bladed rotors is limited to the performance of roughness. In a previous method of manufacturing, integrally bladed rotors can be manufactured by milling from the entire unit or by welding the individual vanes to the carrier. It is a method of repairing and manufacturing such a rotor in which initially a collar is welded to the stubs projecting over the peripheral surface of the carrier around its entire periphery and subsequently a replacement vane is welded to this enlarged bonding surface, made up of stub and collar, which has a considerably widened bonding collar on the vane base. One disadvantage is that the vane cannot be welded in its final finished form, and a substantial amount of subsequent machining is required due to the two collars [11].

The performance of the Centrifugal Compressor Impeller is related to the mark characteristics that are by-products of machining, namely cusp height, cutter path roughness, and orientation of the cutter path relative to the local flow velocity [12]. Surface roughness is known to influence compressor performance and 'generally rougher impellers result in poorer compressor efficiency. The improvement of roughness will decrease the cost and increase the use of time service. The AFM can improve the surface roughness, and it will save expense on the integrally bladed rotors.

In the hypothetical process, the manufacturing of integrally bladed rotors (IBR) can be divided into two parts. First is the CNC milling, which will create a basic shape of integrally bladed rotors. From the CNC milling, the semi-finished product will be

produced and it is necessary to do more different machining processes to improve the design and performance of IBRs. After that, the AFM will be used to improve the performance of integrally bladed rotors. By the use of AFM, the surface roughness and the shape of the trailing-edge and leading-edge will be improved significantly. In this project, the simulation experiment and profile setting method of the final part are mainly researched and tested.

Currently, the challenge is mainly focused on how to build the virtual AFM manufacturing system by developing the modelling method and simulation. The modelling on material removal, profile accuracy of the leading-edge and trailing edge, surface roughness and even surface texture is essential for industrial purpose. What is more, the link between fluid property is also linked to micro-cutting mechanics. So a significant approach is necessary for building up a fundamental theoretical basis to the bridge between microscale to macroscale in the modelling and simulation.

1.2 Aim and objectives of the research

This PhD research is closely linked to a program which focuses on the manufacturing process of integrally bladed rotors. Currently, the process of the manufacturing still needs to be optimized to improve the performance of bladed rotors. The performance can be improved by decreasing the roughness of the surface, improve the trading edge and leading-edge and improve the texture of the surface. It is necessary to bring out a method to improve the manufacturing process. By way of Abrasive Flow Machining (AFM), the surface can be improved and desired surface texture likely obtained for better aerodynamic performance.

The distinct objectives of this research are to:

- Develop an innovative approach to multiscale multiphysics modelling and simulation of abrasive flow machining for engineering manufacture of aerofoil structures.
- Modify the Preston equation which is used in multiscale Multiphysics modelling and simulation and to predict the material removal in abrasive flow machining by COMSOL Multiphysics.

- Develop the user-defined MATLAB codes model integrated to COMSOL multiphysics modules to simulate the high precision surfaces generation in abrasive flow machining (AFM).
- Optimise the machining parameters of abrasive flow machining in the manufacturing of IBR, T50 and other aerofoil structures.
- Carry out a series of machining experiments and industrial cases studies to evaluate and validate the approach and implementation perspectives.

In the first part of this research, the simulation method of Abrasive Flow Machining will be built and tested. A Multiphysics/multiscale 3D numerical simulation will be approached to simulate the manufacturing process of Abrasive Flow Machining. The simulation is focused on building a relationship between the roughness, shape of the trading edge and the setting parameters of Abrasive Flow Machining. Such as the viscosity of the flow, the pressure of the working environment and the velocity of flow media will influence a lot on the roughness and material removal rate.

After the first part of the project, the first version of simulations is developed, and some experiment result is also required to elevate the performance of the simulations. Many influences in the fluid model are based on the regression model and the statistical model. These models need to gather the result from the experiment and find out a better way to forecast the result. In this process, a series of methods should be brought out to test the influence of different aspects. On the other hand, the result of the experiment will also influence the method used in the multiphasic/multiscale simulation. With these two methods combined, the simulation will be approached to reality.

In the third part, this research is aimed to build a more reliable and more accessible model to describe the relationship between the workpiece and working environment which aims to enhance the function of this simulation. With the help of a combination of experiment and simulation, a simple model which shows the relationship between performance and set-up of the machine will be brought up. It is essential to find out which character is more important during the manufacturing process. On the other hand, it is also easier to find out the best combination of set-ups with the simulation model by computer. The model will indicate the most efficient way and the best performance way of manufacturing.

This project is aiming to develop a multiscale multiphysics simulation method for Abrasive Flow Machining (AFM). It will help substantially in manufacturing and research purpose with a more acceptable model for people to predict the result of the whole process.

This work was linked with a National Aerospace Technology Programme (NATEP) funded project where Brunel University is a partner to ITP Engines UK Ltd and Extrude Hone Ltd (EH). The initial trials for this project were undertaken in EH to evaluate the influence of input parameters on the process response and as validation data for the simulation model proposed here.

1.3 Scope of the thesis

As illustrated in Figure 1.1, the thesis is presented in eight chapters. Chapter 1 explains the motivation and objectives of the work. Chapter 2 reviews the modelling technique for metal cutting, including the traditional metal cutting theory, continuous mechanics method - Finite Element Method (FEM), empirical method and Molecular Dynamics (MD) simulation. The literature survey shows that the investigation of a new

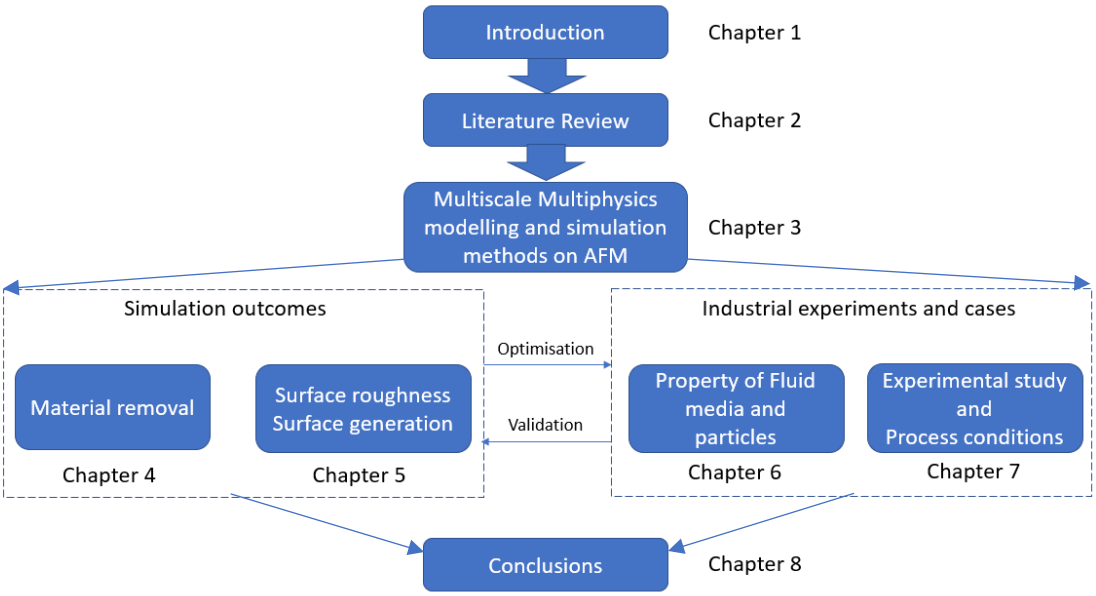

Figure 1.1 Research scope and chapter plan of this thesis

approach is essential in order to provide an effective method and to further obtain a scientific understanding of the generation of high precision surfaces about the complex machining system and processes.

Chapter 3 critically summarise the development of modelling and simulation approach used in this research, and critically introduced how these simulations linked with each other and collaborated as the whole multiscale Multiphysics modelling and simulation. The simulation contains from material removal, profile accuracy of leading-edge and trailing-edge as macro-scale to surface roughness and surface generation as micro-scale. The interaction of solid deformation and the flow of high viscosity fluid media contributes to Multiphysics modelling and simulation.

Chapter 4 specifically introducing how the modelling and simulation predict the material removal of Abrasive Flow Machining process. With the help of CFD simulation and FSI modelling method, an improved Preston equation is introduced in the chapter which aims to predict the material removal based on the process parameter of real Abrasive Flow Machining process, and relevant experimental result and further discussion are also introduced.

Chapter 5 describes the methods and simulation tools used in predicting the surface roughness and surface generation of Abrasive Flow Machining process. Hertz Contact theory and Monto Carlo method are used with the collaboration of COMSOL and MATLAB simulation to predict the generation of the surface.

Chapter 6 describes the method of gathering and measuring grains in fluid media which aims to guide the generation of particles used in the simulation and the methodology to test the viscosity and other rheologic properties of AFM media by Capillary Rheometry.

Chapter 7 presents the simulation setup, experimental setup and results of four different cases based on Abrasive Flow Machining (AFM) machining process. A discussion on the simulations of four cases and the evaluation and validation process with the experiments are also included.

Chapter 8 concludes the results of this investigation. Recommendations are made for future work.

Chapter 2 Literature review

2.1 Introduction

Nowadays, the optimisation of the structural configuration and surface performance of a general composite aerofoil structure is a big problem in many aerofoil manufacturing industries. Since the surface finishing has become an essential requirement that influences the engine performance, how to increase both the service life and the performance of machined components is becoming more and more important. As a result, the method to achieve a better surface finish of aerofoil structures has been an issue in the manufacturing industry. Currently, in many production lines, finishing operations usually cost roughly 15% of the total machining cost in one production cycle [5]. Traditional methods like lapping or honing are labour involving, time-consuming, and less controllable. However, the most significant disadvantage of these traditional methods is that they cannot be used for complex geometries and the geometries inside the workpiece [3]. On the other hand, the grinding has been widely and extensively used for finishing of external surfaces, but it may cause thermal degradation, which is important in the manufacturing of aerofoil structures. In order to finish the complex geometries and inaccessible areas, the abrasive flow machining (AFM) was developed by Extrude Hone Co. in the 1960s.

The competition to predict the manufacturing result of abrasive flow machining (AFM) process has attracted widespread research interest in the aerofoil structure manufacturing industrial areas. Over the past century, investigators and researchers have made great efforts to try to understand and simulate the abrasive flow machining (AFM) process and its relevant phenomenon. This research has been carried out from the following aspects:

- The application of abrasive flow machining on aerofoil structures
- Multiscale and Multi-physics based modelling methodology and simulation
- Computational Fluid Dynamics based simulation
- Fluid-Structure interaction-based modelling and simulation
- Abrasion Modelling applied on Abrasive Flow Machining process

2.2 Abrasive Flow Machining of aerofoil structures

Abrasive Flow Machining (AFM) is a process where material removal (MR) and surface roughness (SR) improvement are attained by extruding a viscoelastic fluid which carries abrasive grit through a workpiece. It is normally used when interior features need to be polished, rounded or de-burred and are unreachable by conventional processes.

While commonly used for holes and cavities, the process is also being used as a final stage polish for turbine parts including Integrally Bladed Rotors (IBR) via tooling that contains the media to flow around the bladed section of the disk.

IBR manufacture, in particular, requires polishing the blades to a target SR (R_a 0.63μm) while maintaining a tight control of the entire profile of the blades, with particular attention being paid to the geometry of the leading and trailing edges, the CFD based simulation of the process shown here could be particularly useful this application, where predicting MR and SR along an entire profile and in multiple sections of the blade could significantly diminish the amount of testing and iterations required for obtaining the process parameters and be an invaluable aid when designing the rather complex tooling that is required for this particular application of AFM.

2.2.1 Brief introduction on Abrasive Flow Machining

Abrasive Flow Machining (AFM) is widely used as deburring, polish or radius surfaces and edges by flowing some semisolid abrasive media over these machining areas. Abrasive Flow Machining always experienced a wide range of available applications. Such as critical aerospace, medical components to high production volumes of parts. AFM can also reach even the most inaccessible areas, such as processing the holes, slots or edges of the workpiece in one operation. Advances in fluid media formulation and the tool design coupled with significant capabilities in processing and the automation have established the abrasive flow process as a way of satisfying tough

manufacturing requirements economically and productively [3]. As shown in Figure 2.1 and Figure 2.2, the surfaces of blades are more bright and delicate after AFM process.

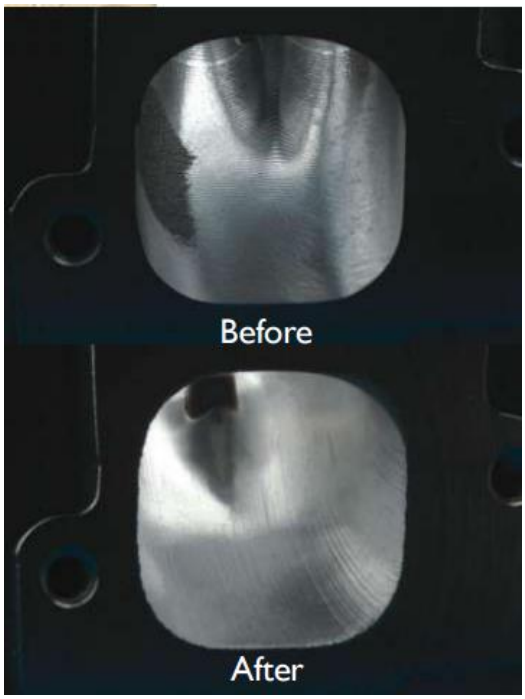

Figure 2.1 Application example by using AFM

There are several other techniques for surface finishing like magnetorheological finishing, magnetic abrasive finishing, elastic emission machining and magnetic float polishing. These methods have also been developed during the last decades [16]. Comparing with these manufacturing methods, the main advantage of AFM is with the help of the self-deformable tool and the abrasive media, AFM changes shape according to the geometry of the workpiece by itself. In AFM process, the abrasive media is a mixture of abrasives and a semi-viscous carrier. The abrasive fluid media flows through a restrictive passage formed by the fixture and workpiece [3]. On the other hand, the abrasive particles in the abrasive fluid media have random cutting edges with indefinite orientation and geometry for effective removal of material to form micro-chips [18].

Figure 2.2 AFM used on the machining of integrally bladed rotors

The abrasive flow machine consists of two vertically opposed media cylinders which hydraulically close to holding a part or fixture between them as shown in Figure 2.3 [70]. By repeatedly extruding media from one cylinder to the other, the abrasive actions are produced wherever the media enters and passes through a restrictive passage as it travels through or across the workpiece. By controlling the cycle time and number of cycles, the machine can perform differently. The control systems of Abrasive Flow Machine may be added to monitor and control additional process parameters such as media temperature, working pressure. On the other hand, the viscosity and size of grains in fluid media are also necessary to be controlled during the machining process. AFM systems designed for production applications often include part cleaning and unload/reload stations, media maintenance devices and cooling units [71]. These automated systems can process thousands of parts per day with processing times typically ranging between one and three minutes for each pallet loaded with workpieces.

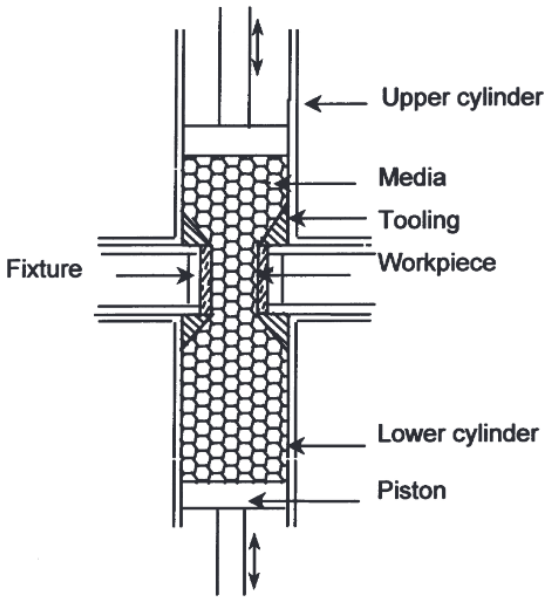

Figure 2.3 Schematic diagram of the abrasive flow machining process

Nowadays, Abrasive Flow Machining is widely used in the aerospace industry, automotive industry and dies and mould industry. It has many advantages in this type of manufacturing. Such as it has an excellent process control system that does not require the operator operating during the whole process, it can also finish both the ID and OD of the component at the same time. Compared with other kinds of abrasive machining, AFM is good at the control of radius generation, and it performs better with the manufacturing of complex surface. These advantages can benefit the performance of integrally bladed rotors after the complete machining. It is helpful on improving surface quality, enhancing high cycle fatigue strength and increasing airflow feature. By producing optimised combustion and hydraulics, the integrally bladed rotors will gain more extended component life.

2.2.2 Material removal mechanisms of Abrasive flow machining (AFM)

Previous researchers' main contributions to the methodology and simulation work of AFM will be summarised here, with a more specific discussion of their contribution arranged into different topics in the following sections.

A fairly extensive literature review on the subject is given by Santhosh in 2016. In this paper, the author review lots of existing literature which contributes to this research's central themes, i.e. process prediction, simulation and material characterisation as they can be applied for processing aerofoil structures manufacturing [70].

The earliest works attempting to understand the influential process parameters and how these different parameters influence the machining results are related to a series of technical articles authored by Lawrence J. Rhoades and his colleagues. Lawrence J. Rhoades is the former president of Extrude Hone Corporation which is the first and largest supporter and manufacturer of Abrasive Flow Machining (AFM) process. These technical documents date from 1972 to 1998 and mostly serve to highlight the process characteristics, capabilities and control variables [15,17,19].

Among these works, there is another report written by Williams in 1989 in the series worth discussing. The experiments in his work were conducted to determine the effect of pressure, viscosity, flow rate and the properties of the particle in the fluid media on material removal. In these experiments, a strong effect was found with regards to the pressure and flow rate. The method of varying flow rate by variation of temperature can be criticised that the process will produce an undesired variation of viscosity. From the experiments, we can derive that one cannot isolate extrusion pressure or flow rate for the same material viscosities and geometries, because all these parameters will influence others, and they cannot be considered separately [25].

The doctoral dissertation of Williams published in 1993 contains the information about 4 AFM experiments [26]. These experiments in his thesis provide valuable insight into the process behaviour, specifically since the response was obtained for each consecutive cycle. These experiments give valuable information about the shape and evolution of the responses as described below:

On the initial cycles, the roughness improvement and material removal are markedly bigger than on subsequent passes; this can be explained primarily by the relatively easy removal of "peaks" found within the initial surface condition, further improvement of roughness requires significantly higher work as the plateaus that remain are tougher. This has the logical consequence that, for a low number of cycles, the initial roughness does have an effect on the final roughness that can be achieved, obviously further improvement can be made if the valleys are removed, the result is then driven to a

limiting condition that depends on the grit size, hardness of the workpiece, and pressure. Figure 2.4 illustrates a schematic representation of the phenomena and Figure 2.5 for a plot of the author's data for Experiment 1 in William's research displaying this behaviour.

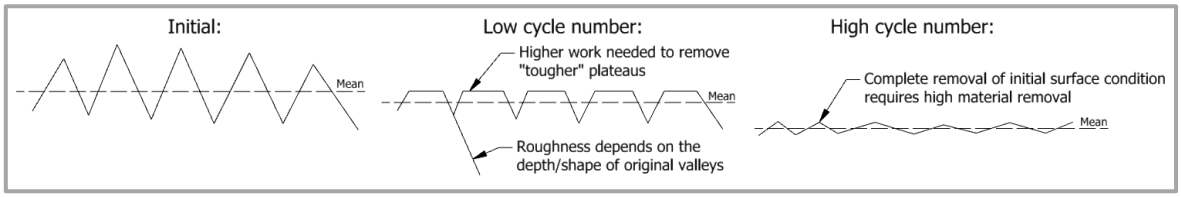

Figure 2.4 Schematic representation of surface modification

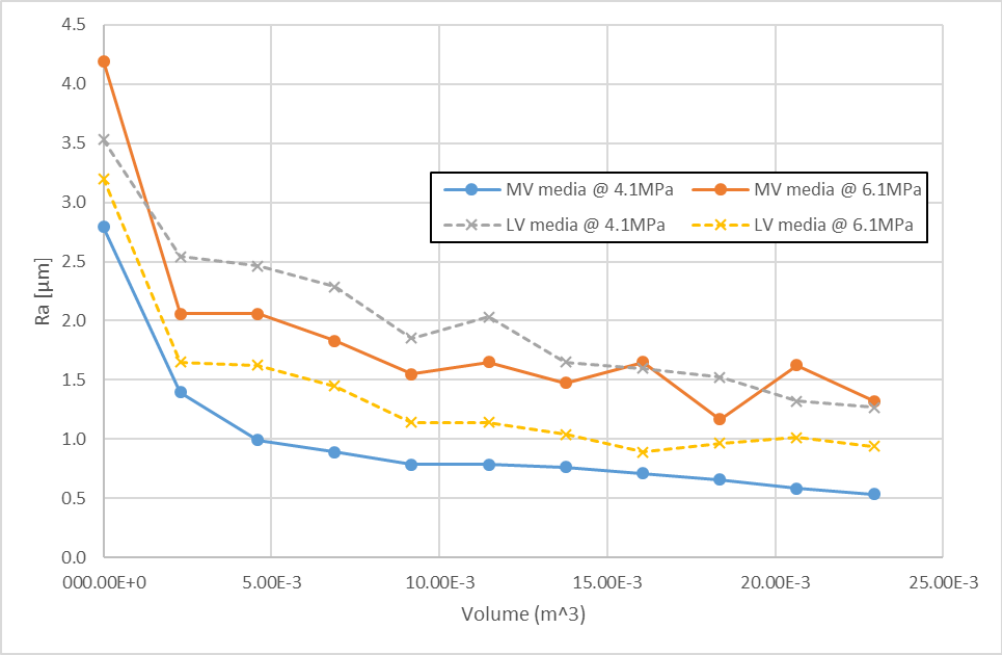

Figure 2.5 Surface roughness improvement per cycle [26]

In some literature published later, the material removal results from the same experiment also shine some light in this research. As shown in Figure 2.6, the high linearity of the response may allow for a model to complement CFD simulation. In this simulation, it appears that the material removal of the workpiece is linear with processing volume, and the removal of material is also heavily depended on the pressure of process. The bulk of the non-linear response present corresponds to the first cycle (line not graphed), and afterwards a simple model which fits 2 different straight lines to the plot (higher gradient for the first cycle) is more likely to be used to model the material removal, and as a result different curves should be used for different media and workpiece material combinations.

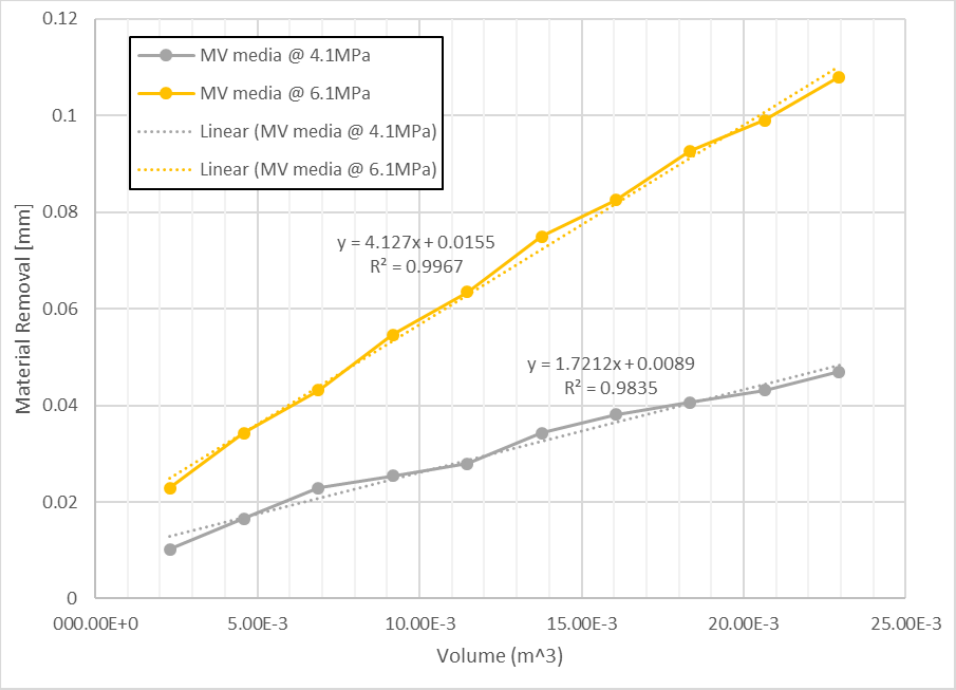

Figure 2.6 Material removal per cycle

After Williams work, the doctoral dissertation of Davies in 1993 contains data from trials performed on mild steel die with 15 mm diameter by 15 mm depth hole. The data from the trials were specifically documented, and in particular, the information on pressure drop, flow rate and material removal can be used as main parameters and factors for this simulation attempt. The trials of his research included three different media viscosities with three different abrasive grit concentrations [24].

The dissertation of Davies also provides collaborated information about the shear history characteristics of the media, and the material exhibits different properties which are depended on the time that has passed since it was last processed. This result probably constitutes the origin of the procedure now commonly used to pre-shear the material by flowing it through a restriction before processing actual components. This process before machining is done in order to eliminate this time-dependent behaviour from affecting the repeatability of the produced items. The step should be taken into consideration when designing experiments, a strong dependence of the viscosity with temperature is also evidenced, although the effect is hard to separate from the shear history behaviour because of the way the experiments were conducted [24].

Afterwards in the research of Jain in 1999, some experiments on abrasive flow machining were carried out to test the influence of 4 process parameters on the result

of material removal and surface roughness of the processed parts. These parameters studied are reduction ratio (which determines the speed of the fluid at the point of work), media pressure, the concentration of abrasives and the number of cycles in each process. In these experiments, the extrusion pressure seems to have a direct effect on material removal and the model obtained by response surface analysis shows good fit. However, the accuracy of the model to represent other parameter changes cannot be evaluated as the experimental values are not involved in the paper [28].

In the following paper of Jain in the same year, micro-cutting and micro ploughing are identified as the primary cutting mechanism. At the same time, a simplified model of material removal was developed. In this paper, an impressive correlation was found for the effect of changing mesh size and concentration of abrasives with regards to material removal. As shown in Figure 2.7, the model in Jain's research assumed that spherical grains which aim to remove material based on the geometrical intersection that occurs when an indenting grain translates across the surface. The predictions for the effect of injecting velocity or any other parameter on material removal or surface roughness were not as accurate as required. Reasons of these results could be that the CFD simulation was overly simplified for the former case by assuming the fluid media of AFM process as a Newtonian fluid and the model for surface roughness only considered a simplified surface topography that was not detailed enough to capture the process. As described in the paper, any model that attempts to represent the issue from basic mechanism analysis can be used to gain insight as to what are the driving parameters for the process. However, in this particular case, the strong influence of the workpiece initial surface condition is a major challenge that can be identified [29].

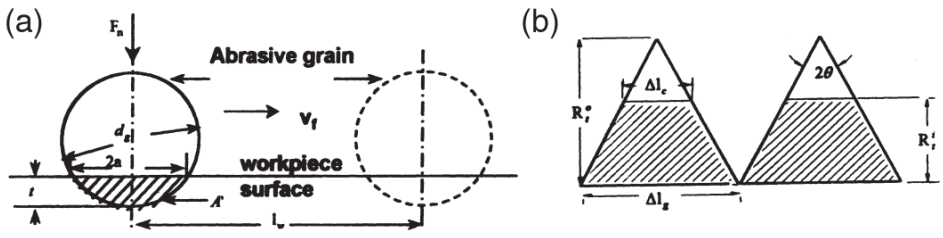

Figure 2.7 Grain indentation and material removal schematic. [29]

With a rather different approach by Jain and Adsul in 2000, the method in this paper can arguably yield a more readily useful model, and it is used to develop an empirical

equation through curve fitting. In this literature, an equation of the form $y = a_0 {x_1}^{a_1} {x_2}^{a_2} {x_3}^{a_3} {x_4}^{a_4}$ was fitted on the experimental values. The process parameters in this research used are (in the order of most important to less important): Abrasive Mesh Size, Concentration of abrasive, Media Flow Speed, Number of cycles. In this paper, a good agreement was found with previous researchers' data. For example, the material removal was found to be linear with respect to the processed volume (i.e. number of the cycles). However, the results in this research are not readily translatable to experiments shown here experiments due to the choice of aluminium and brass as workpiece materials [72].

In a later paper by Jain in 2009, a model with polynomial form was devised, but the results differed considerably from the experimental values [4].

After Jain's work, Schmitt and Diebels built a Taylor-Couette flow rheometer with the concentric cylinder geometry in 2013. Similar to the Jain's previous work described above, the AFM media flow that is driven by a moving boundary applies to shear rates which are lower than the ones seen in the AFM extrusion process. This result is mainly due to the fact that inertia and end effects cannot be neglected at the circumstance with higher shear rates [44].

In two closely related papers by Uhlmann in 2013, Uhlmann measured the abrasive media using oscillatory rheometry and a multimode relaxation Maxwell model was described, the details about the material characterization will be discussed in a separate section below, a simulation of the flow around 2 test parts was performed in an article by Uhlmann in 2015 and qualitative correlations were found between the flow variables and the surface response, also important is that wall slip as an important effect for this flow was again recognized in research [57,58].

2.2.3 Material properties of Abrasive Flow Machining media

Abrasive flow media is categorized as non-Newtonian fluids, as which the material shear rate is non-linear to the shear stress, this makes prediction of flow behaviour around complex geometry very difficult. Polymer - the base material for the carrier fluid in AFM process, is known for following properties:

- Undergoing fast deformation under fast stress, due to the slow untangling of long chain molecules. Therefore, the material will exhibit high elasticity and low dissipation of energy.
- During slow deformation, dissipation of energy is low as the polymer has no problem adapting to stress.
- Under slow stress, dissipation of energy reaches its peak and elasticity raises.

2.2.3.1 Introduction on the flow properties of Abrasive Flow Machining media

Viscosity is one of the flow properties that dominates the abrasive effect in AFM process, however the property itself is temperature dependent. Numerical model was established to describe the correlation between temperature and the viscosity.

As shown in Figure 2.8, power Law is used to describe the effect of the temperature on the viscosity along with shear rate, it is presented as:

$$\mu = K\mu_0 e^{(a_1 T - a_2 T^2)} \dot{r}^c$$

Where: $$c = n - 1 + a_3 \ln(\dot{r}) + a_4 T$$

μ_0= zero shear rate viscosity

μ= viscosity of abrasive media

$\dot{r}$= local calculated shear rate

n= Power law index

T= Local calculated temperature

K, a_1, a_2, a_3, a_4= fluid properties of abrasive media

The equation above describes the general behaviour of non-Newtonian fluid based on Ostwald-de Waele formulation, with shear thinning fluid having power law index between 0 and 1. In order to derive the coefficients of power law, the correlations between the rheological properties needs to be measured. The graph below shows the relation between viscosity and shear rate. As the graph shows, the viscosity decreases as shear rate increases, A-silicone shows higher viscosity values therefore higher surface finishing is expected from the material.

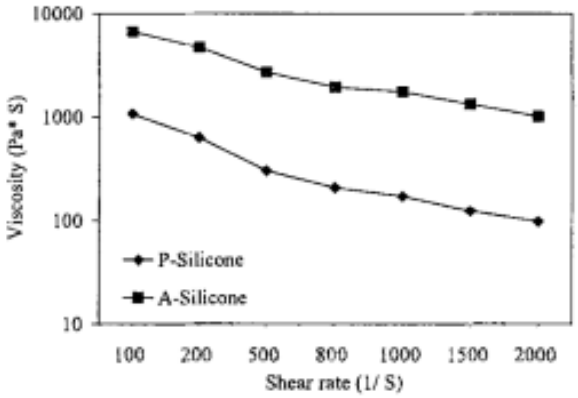

Figure 2.8 Viscosity vs Shear rate for abrasive gel samples

Previous attempts to understand the flow behaviour of the abrasive media were carried out involving rheological devices to study the flow parameters in detail. One method is the use of oscillatory rheometer, where the visco-elastic abrasive media is characterized by complex shear modulus. The shear modulus *G** is consisting of the two terms *G'* and *G''*, which represents storage modulus and loss modulus respectively. Both moduli can be derived as a function of oscillatory frequency and shear viscosity *η** is given as the ratio between the shear modulus and the oscillation frequency.

Maxwell model was developed to represent the visco-elastic fluid in terms of simple oscillatory system. The fluid is modelled by Maxwell element, which consists of a purely elastic spring with stiffness coefficient of G and damping element with damping factor of *η*. The combination represents material with certain polymer fraction and its characteristic relaxation time. The oscillatory rheometric measurement is modelled by three Maxwell elements which implies seven coefficients (*G0, G1, G2, G3, η1, η2, η3*), *G0* represents steady state shear modulus for quasi-static fluid. These coefficients are then used to calculate the continuous function of loss and storage moduli through a frequency dependent function. Uhlmann et al implemented a program to determine the optimum number of Maxwell elements for abrasive media modelling, where the number was incrementally increased with calculated initial conditions to generate non-linear curves which approximate the experimental data. Reliable model was detected when the number of elements is equal to five, as further increase in element number do not yield substantial decrease in deviation from the experimental results. Steady state viscosity information can be obtained from oscillatory measurement by invoking

Cox-Merz Rule, which suggests that for equal oscillatory frequency and shear strain rate, the magnitude of the complex shear modulus is equal to the shear viscosity under steady state. This rule is valid for most polymer including Maxwell fluid.

Slip behaviour near the wall is studied over the years. It is found that energy loss of media will get transferred into abrasive force in the polishing process. Many researchers have discovered that the pressure drop is greatest near the wall region, which corresponds to high surface shear rate. It is also found that higher deformation of the media will lead to higher abrasive force due to the narrow flow area. Past CFD simulations have approximated wall slip velocity based on Navier's linear slip law where the local slip velocity is determined by local shear stress and will only take place when critical shear stress value is reached.

2.2.3.2 Review on capillary rheometer

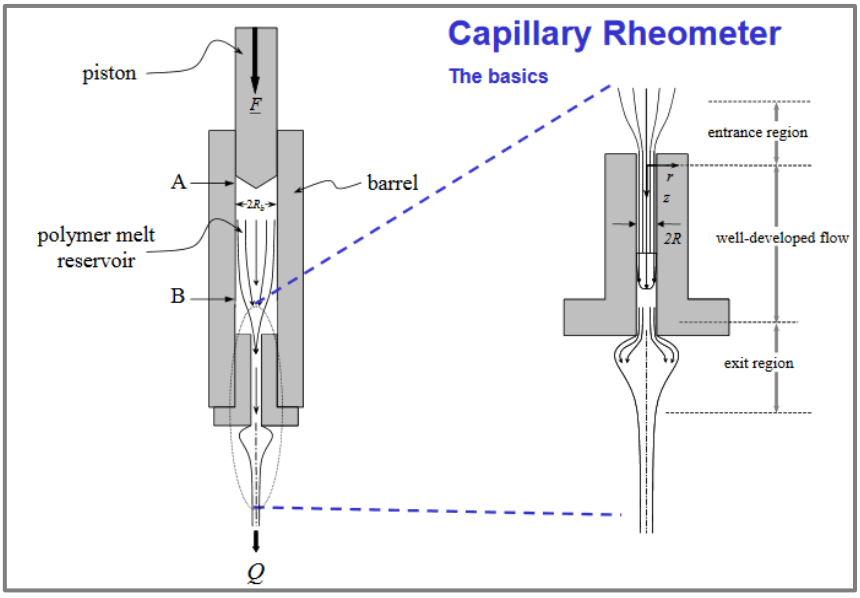

Figure 2.9 Illustration of the working principle of a Capillary Rheometer [24]

In a capillary rheometer as depicted in Figure 2.9, the flow in the well-developed region of the capillary has an analytic solution for Power-law fluids given by the following equations:

Shear Stress at the wall:

$$\tau_R = \frac{\Delta P \cdot R_d}{2 \cdot L_d} \tag{2.1}$$

In Equation (2.2), ∆P is the pressure drop along the well-developed region, R_d is the die radius and L_d is the length.

The shear rate at the wall (Power Law Fluids):

$$\dot{\gamma}_{apparent} = \dot{\gamma}_a = \frac{4Q_2}{\pi {R_d}^3} = \frac{4V_p R_p^2}{{R_d}^3} \tag{2.2}$$

$$\dot{\gamma} = \frac{4Q}{\pi {R_d}^3}\left[\frac{(3+b)}{4}\right] \; where \; b = \frac{d\, ln(\dot{\gamma}_a)}{d\, ln(\tau_r)} = \frac{1}{n} \tag{2.3}$$

Where Q is the mass flow rate through the die.

The piston speed on the experiment should be accurately controlled while measuring the force response of the material being extruded, readers familiar with material testing will notice that this is the same conditions encountered in a machine undergoing traditional tensile testing, i.e. the specimen is deformed at a constant rate and the force required to do so is measured, the data is then transformed into stress vs elongation curves by simple mathematical operations.

In the case of conducting capillary rheometry with this equipment, many factors influence the relationship between the measured parameters (Piston Force and Piston Speed) and the rheological response, and as such, at least three corrections have to be made to account for the strongest of these effects.

2.2.3.3 Pressure correction (Bagley correction)

The equation for shear stress at the wall is valid only for the section of the capillary with well-developed flow, but the proposed measurement system obtains the pressure

drop by sensing the force on the piston which means that the obtained pressure value includes the end and entrance effects, a method for removing the pressure drop that occurs due to these effects is needed, to accomplish this, capillaries of different lengths have to be tested, a plot of the total pressure drop (P_d) against L/R is prepared for different apparent shear rates and a correction factor for each apparent shear rate is obtained according to Figure 2.10. The corrected shear stress at the wall is then:

$$\tau_{Rc} = \frac{P_d}{2 \cdot (L/R + e)} \tag{2.4}$$

Where e*R is the length of a fully developed capillary flow that will produce a pressure drop equal to the pressure drop resulting from the end effects [133].

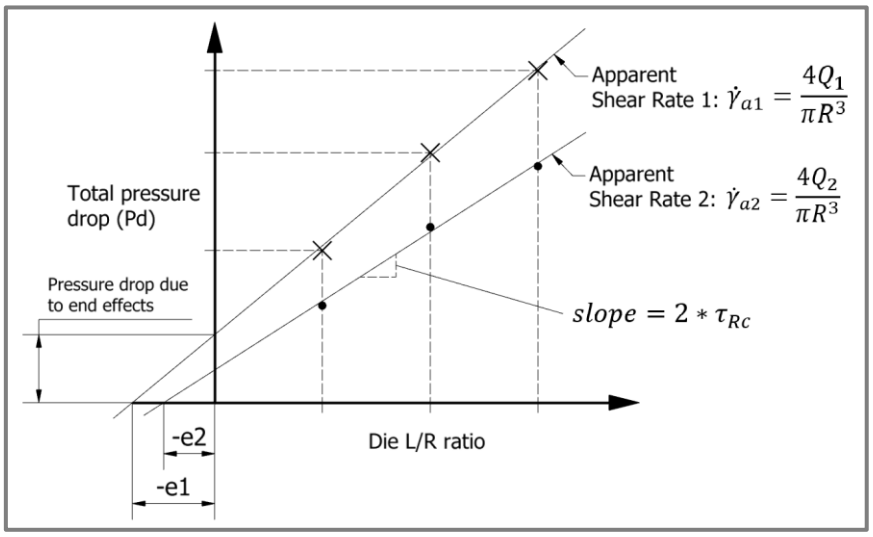

Figure 2.10 Bagley pressure correction composited [131,133]

2.2.3.4 Wall slip correction (Mooney correction)

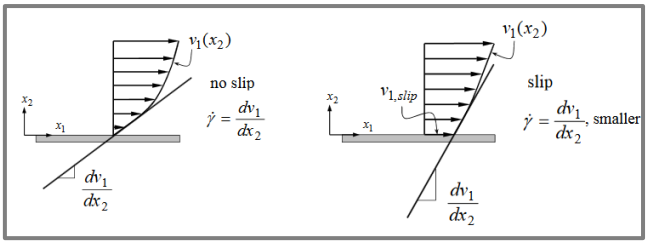

Figure 2.11 Flow profile with wall slip with permission from [8]

The influence of wall slip on the flow profile in a capillary is shown in Figure 2.11, the obtained apparent shear rate needs to be corrected to account for the existence of slip, this requires testing the material at constant wall shear stresses (piston force) and logging the flow rate, the equation and procedure shown here is described in literature from Morrison in 2001 [133].

$$\frac{4Q}{\pi R^3} = 4v_{slip}\frac{1}{R} + \frac{4v_{true}}{R} \tag{2.5}$$

$$\frac{4Q}{\pi R^3} = (slope)\frac{1}{R} + (intercept) \tag{2.6}$$

Figure 2.12 shows a schematic graph for the above equation, it can be seen that the slip velocity and corrected apparent shear rate can be found by testing multiple capillaries of different diameter at the same shear stress.

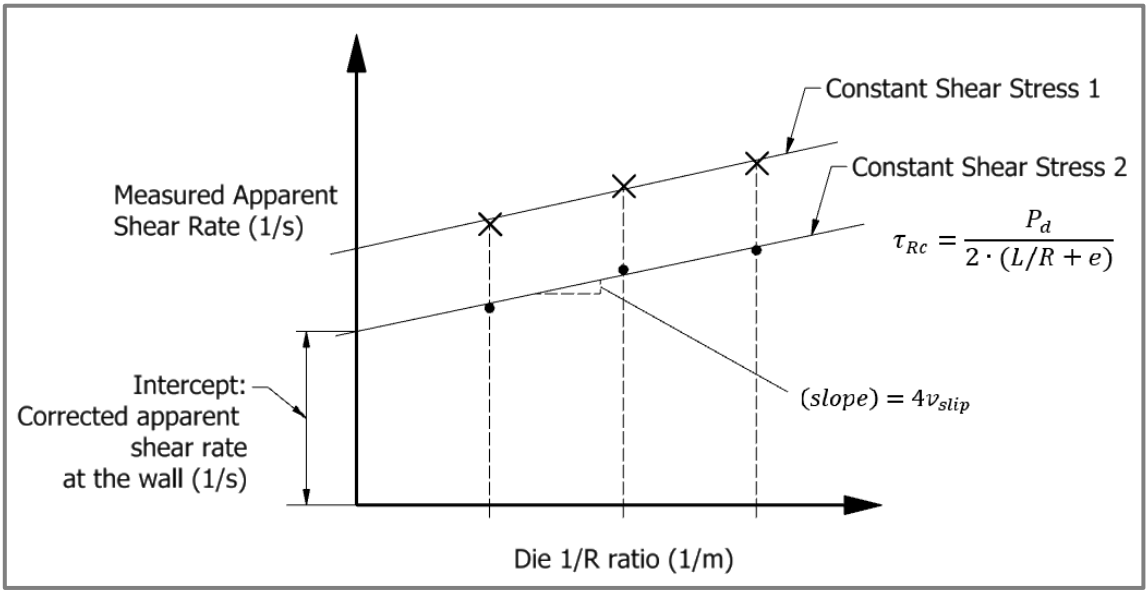

Figure 2.12 Mooney wall slip correction adapted with permission [26]

2.2.3.5 Non-parabolic velocity profile correction (Weissenberg Rabinowitsch correction)

It is known that the velocity distribution of developed flow is non-parabolic for a non-Newtonian fluid, the expected shape of the flow profile is shown in Figure 2.13, a correction can be made to the apparent shear rate at the wall to account for this if one assumes a constitutive equation for the viscosity, in the case of a power-law fluid, the shear rate at the wall reduces to the equation presented at the beginning of this section, the factor that corrects the apparent shear rate depends on $ln(\dot{\gamma}_a)$ and $ln(\tau_{rc})$:

$$slope = b = \frac{d\ ln(\dot{\gamma}_a)}{d\ ln(\tau_{rc})} \tag{2.7}$$

$$ln(\tau_{rc}) = \ln\left(\frac{P_d}{2 \cdot \left(\frac{L}{R} + e\right)}\right) \tag{2.8}$$

By plotting a graph of $ln(\dot{\gamma}_a)$ vs $ln(\tau_r)$ the correction factor may be found as the slope of the curve at any point, where $\dot{\gamma}_a$ is the corrected apparent shear rate from the previous chapter and τ_{rc} is the corresponding corrected shear stress obtained from the Bagley corrections as shown in Figure 2.14, after using the factor to correct the shear rate one last time, the viscosity may be found from:

$$\mu = \frac{\tau_{rc}}{\dot{\gamma}_a} \tag{2.9}$$

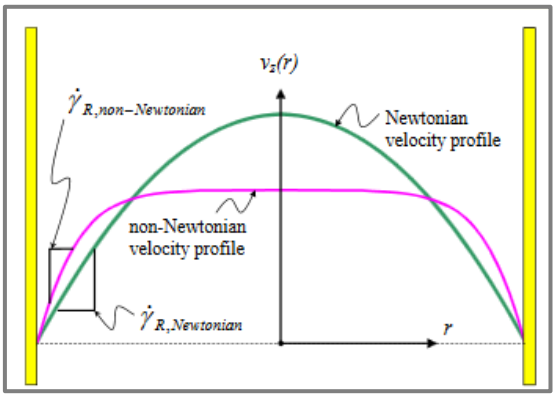

Figure 2.13 Non-parabolic velocity profile at the wall with permission [26]

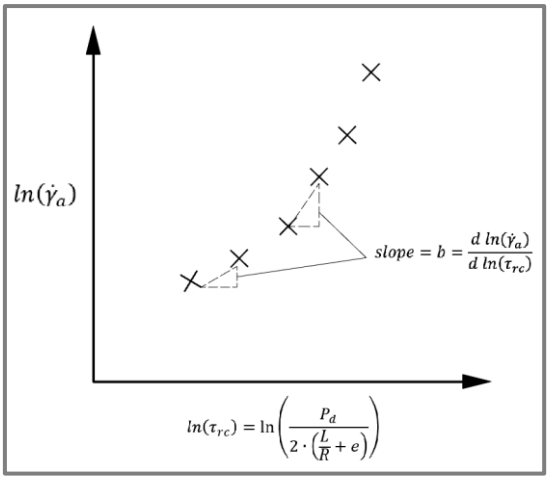

Figure 2.14 Weissenberg-Rabinowitsch correction, adapted with permission [26]

The experimental methods summarised here could also provide a starting point to evaluate the importance of the media's elastic response by measuring the die swell produced at the capillary exit. There is a reason to believe that the introduction of the media particles in the elastic putty may limit the elastic response [134]. Finding if the flow can be accurately represented by the more widely available, purely viscous model should be one of the main objectives along with the determination of the viscosity dependence on shear rate and possibly temperature.

2.2.4 Previous research on simulations for Abrasive Flow Machining

There is plenty of work on the simulation for AFM before. In this section, these researches will be introduced and discussed how to improve them and use new Multiscale Multiphysics modelling methods and simulation to solve and simulate the AFM process better.

In the journal article by Wan in 2014, CFD simulation of the flow is presented. What is most important is the fact that an equation is built to calculate the expected slip velocity at the wall is shown for the first time in the area of CFD simulation. In this simulation, it considers the wall slip to be a function of the shear stress at the wall. It became an empirical model to estimate the material removal and surface roughness in AFM process while the main inputs to the model are the wall slip velocity which is calculated from the simulated shear stress and the simulated pressure. The equations in this

model seem to have reasonable accuracy when predicting the surface roughness. However, the procedure that was used to obtain the constants required for the models is presented in another document that is not available on the public. However, a power-law model used to describe the viscosity dependence on the shear rate of Extrude-Hone media described qualitatively as “soft” was presented in his literature [54].

Jain utilised a 2D CFD model in 1999 in which assumed constant media viscosity of 543.48 $Pa \cdot s$ from an unidentified source. In his project, the simulation was used to determine the stresses on the workpiece in order to use them as inputs for the abrasion model described in the previous section. And in his simulation no more procedure was used to validate the flow simulation against the real measured values from processes [28].

The simulation model presented by Jain in another article in the same year considered an ideal geometrical assumption that material removal occurred whenever and wherever an assumed spherical simulated grain contacted the workpiece. The shape of the scratch left by the grains was determined by a formula used to calculate the depth of indentation and length. On the other hand, the positions and size of the grains were randomly generated, which allowing the surface to be continuously modified throughout the simulation. Through this way, the model brought out by Jain was able to predict the trend of the material removal and the possible change in surface roughness with the variations of extrusion pressure, grit concentration, size of the grains and the hardness of the workpiece [29].

In the doctoral thesis of Howard published in 2014, Howard simulated the flow with a CFD model which considers both the shear rate and temperature with the dependence of viscosity. The simulation results of Howard are compared with machining results in a point of interest which aimed to determine the model which could relate the flow fields. At the same time, a resulting model was used to predict the radius at points of interest in industrially relevant parts in Howard’s research field (oil and gas component manufacturing). This result suggests that a similar approach can be used to predict material removal along with the entire profile rather than focus on a single value to describe the whole complex shape. However, the report does not present the thermal and viscous properties so that it can be reused in other simulation packages [55].

At the same time, Schmitt used data obtained from a purpose-built with Taylor-Couette rheometer in order to fit a power-law model and trying to simulate the flow with the CFD model in 2013 [44]. The simulated pressure in the CFD model was then used to compare with an extrusion experiment which shows discrepancy attributed to the need to develop a slip model which can describe the flow. The researchers with Schmitt provide the idea that abrasion can be modelled by coupling the CFD simulation with the ALE moving mesh formulation. Even though they did not compare the results with the experimental data but recommend the method as an avenue for further research which is something addressed in the following sections of this research.

In two papers published in 2013 and 2015, Uhlmann developed a Maxwell material model which should be capable of describing the viscoelastic characteristics of the media. However, in the paper published later, Uhlmann implemented a viscous-only simulation to compare machining results with the flow field qualitatively. The paper by Uhlmann recommends further work to focus on developing quantitative relations between material removal and flow fields, development of a slip model and the simulation of the full viscoelastic problem [57,58].

In one journal article submitted by Fu in 2016, the flow around a simplified model of the integrated bladed rotor (IBR) was tested and simulated by using the CFD model. In this simulation, the model uses a purely viscous Newtonian (μ=2500 $Pa \cdot s$) fluid formulation with turbulence. However, the reason of using constant viscosity and a non-laminar flow is not discussed in the paper and cannot be justified by the theory proposed. As it will be shown in the main part of this thesis, the Reynolds number for typical IBR geometries is too low to indicate turbulence and many other researches and literatures shows that the fluid media has a non-constant viscosity. The research of Fu provide valuable qualitative insight into how the pressure distribution in the blade influences the surface roughness distribution [59].

2.3 Multiscale Multiphysics modelling and analysis

With the development of technology, many physical problems we are trying to solve are too complex to model and simulate within one scale and one physic field. Many of the problems consist of several separate physical processes that each contribute to

the other processes and the overall problem. In these simulations, different processes each take place on a specific space or time scale. For example, on some occasions, the interactions between molecules usually happen on a spatial scale of several nanometers and at a time scale of several nanoseconds. However, the interactions on the cellular level of these models and simulations require considerably larger space and time scales.

Historically from the outcome of that exercise, many problems have been investigated by both modelling and simulating a physical process in isolation. This modelling and simulation determine its contribution to the whole complex physical problem. However, in the last two decades, a new approach has become widespread that many researchers from different fields used to construct models and simulations which aims to capture multiple physical processes with individual sub-models. This approach is now known as Multiscale Multiphysics modelling and simulation.

2.3.1 Introduction

Multiphysics modelling and simulation refers to a model that captures different multiple physical processes that each process capture different types of physics. Such as the model of a star cluster is considered to be a Multiphysics model that uses one submodel to simulate Newtonian gravitational interactions while another sub-model used to solve the ageing of stars, even if these sub-models were hypothetically used to operate on the same space and time scale. However, the star cluster model that uses two different sub-models for the Newtonian gravitational interaction of stars generally is not considered to be Multiphysics, even if the models are applied on a different space or time scale.

Even though Multiscale modelling and Multiphysics modelling are two different concepts, they do have one commonality: they both consist of different sub-models that have been combined or coupled together to solve one physical problem. A major challenge both in multiscale modelling and Multiphysics modelling lies in coupling these sub-models so that the overall model is not only accurate enough to be scientifically relevant and reproducible but also efficient enough to be executed conveniently by modern computing resources. Multiscale and Multiphysics modelling

and simulation exist in a wide range of scientific and engineering communities and process. By its nature, multiscale modelling is highly interdisciplinary, and the developments of multiscale modelling occur independently across research domains.

2.3.2 Multiscale modelling methods

With the development of modelling and simulation on sciences, multiscale simulations are most frequently applied in many different research fields: engineering, energy, astrophysics, biology, material science, environmental science, and so on. On these related fields, several coherent multiscale communities and some initiatives emerged and grew over the last decades. There are also several multiscale projects outside these domains which were related to theoretical mathematical modelling of multiscale problems and somehow indirectly related to some other scientific fields.

Currently, multiscale modelling and simulations have been applied to a wide range of engineering problems. The microscopic properties can be of vital importance for the quality of the overall design of engineering. In related works, engineering is presented in these areas: the former focuses on simulating specific structures, devices, and chemical processes, whereas the material sciences focus more on the properties of individual materials.

Jacob Fish edited a comprehensive review of the most commonly used multiscale techniques of engineering field in 2010.[68] Additionally, the International Journal of Multiscale Computational Engineering specifically focused on multiscale modelling and simulations in engineering in recent years. The engineering projects in multiscale are common within the domain of not only the chemical engineering fields but also include efforts in aerospace engineering, stochastic simulations of kinetic theory models, chemical engineering, nonequilibrium physics and hydrology's coupling of atomistic and continuum methods [69].

2.3.3 Multiphysics modelling and analysis

With the development of technology of computer science and mathematics methodologies, simulations that couple multiple different physical phenomena are as old as simulations themselves. However, Multiphysics simulation deserve fresh assessment as a result of steadily increasing computational capability and the greater aspirations for simulation in domains of engineering design, scientific prediction, and even policy making. A well spread motivation for extreme computing is to relax the assumptions of decoupling. However, it is no longer obvious that the promises claimed for coupled Multiphysics models and simulation will be realized in extreme-scale computational environments in the principal way that individual codes will be coupled through divide-and-conquer operator splitting nowadays. Coupling individual simulations may cause some limitations on accuracy, robustness or even stability that are much more severe than the limitations imposed by these individual components. What's more, the data structure conversions and motions required to iterate between different independent simulations that each component may cost more in latency and electrical power than those of the individually tuned components. Through these ways, ''one plus one'' may cost significantly more resources in computing than ''two'' and may be less amenable to scalable execution than expected.

In the report of Brown published in 2008, Brown emphasizes many challenges on the applied mathematics at the U.S. Department of Energy (DOE). 'Today's problems, unlike traditional science and engineering, do not involve physical processes covered by a single traditional discipline of physics or the associated mathematics. Complex systems encountered in virtually all applications of interest to DOE involve many distinct physical processes. The issue of coupling models of different events at different scales and governed by different physical laws is largely wide open and represents an enormously challenging area for future research.' [60].

In the review of Keyes published in 2013, he specifically detailed different methods of Multiphysics methodology and simulation. The Multiphysics applications can be divided from algorithmic to architectural perspectives. The 'algorithmic' methods include both mathematical analysis and computational complexity while the 'architectural' methods include both software and hardware environments. Principally, most of the Multiphysics applications can be summarised as an algebraic paradigm of which the linearization brings to bear powerful tools of analysis. The individual components (denoted here as 'uni physics' in the literature) in these tools and analysis

are represented by diagonal blocks and off-diagonal blocks which contains the Multiphysics coupling between them. Even though these analyses are not always practical for realistic applications, the model problems representative of applications discussed in the literature provides insight. The different software frameworks for Multiphysics applications currently used around the research areas have been constructed and refined within disciplinary communities and executed on leading-edge computer systems [61].

2.3.4 Multiscale modelling and simulation on the precision machining process and surface generation

Luo's research shows a natural approach to the simulation of multiscale processes, which is to combine an MD simulation for the critical regions within the system with an FE method for a continuum description [140]. The QC model can be used to solve this problem on the manufacturing of solid structure. This approach provides an atomistic description near the interface and a continuum description deep into the substrate, increasing the accessible length scales and significantly reducing the computational cost. It has referential value being applicable to different kinds of machining processes. The multiscale model shows great impact on simulating the Continuum Mechanics and Molecular Dynamics, which contributes to both the prediction of material removal and surface texture. It is necessary to find out how to provide the prediction and control of surface texture on specific areas as needed, while not influence the simulation of other areas or parts during the processing duration.

For abrasive flow machining, it is also essential to simulate the surface generation. The multiscale modelling consists of two parts, one is the CFD module and the other one is the micro cutting mechanics modelling. The CFD module can simulate the media flow and provide the required specifications for the micro cutting mechanics modelling. The micro cutting mechanics modelling is built on the mechanics for one grain and with the help of Monte Carlo Algorithm the simulation can be accumulated to mass of grains in the flow. With this combination the surface generation can be predicted and controlled by the simulations [89-93].

To develop computational approaches which are necessary to understand and model the behaviour of complex multiscale multiphysics phenomena [60]. In this doctoral research, it is important to include the multiphysics modelling and simulation in the right way and cope with the challenges coming with the methodology.

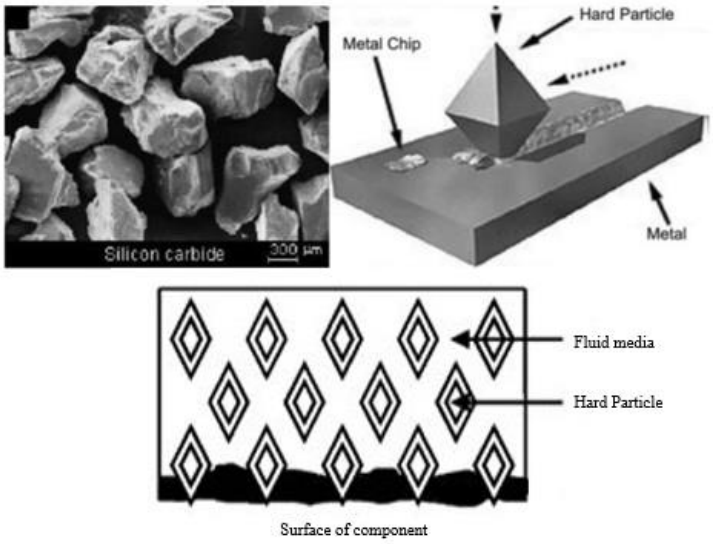

Figure 2.15 Grains in fluid media used in the AFM process

2.4 Computational Fluid Dynamics (CFD)

This section will begin with a short description of the equations behind fluid flow simulation and end with a discussion of the models used by previous researchers in this area.

Comparing among different Computational Fluid Dynamics (CFD) simulation packages, they all model fluid flow numerically by solving the Navier Stokes equations with the variation on the simplifying assumptions and constitutive models which is used for the internal stress-related components. The equations involve Conservation of momentum and Conservation of mass as follows:

$$\underbrace{\rho \frac{D\vec{v}}{Dt}}_{Acceleration} = \underbrace{-\nabla p}_{Pressure} + \underbrace{\nabla \cdot T}_{Internal\ Stress} + \underbrace{\vec{f}}_{Ext.\ forces} \tag{2.10}$$

$$\frac{d\rho}{dt} + \nabla \cdot (\rho \vec{v}) = 0 \tag{2.11}$$

Some of the constitutive equation that relates the internal stress in the fluid with the rate of deformation and deformation (in case of a viscoelastic fluid) of a fluid element is also used in the simulation packages.

A complete derivation of the previous equations used in CFD simulation packages can be found in the researches of Garg, Versteeg, Malalasekera and many other fluid dynamics books [8-10]. A simple to understand form that replaces the partial derivatives with the nabla operator (∇) and the material derivative (D/Dt) is used in these equations to illustrate the influence of different constitutive models and to simplify assumptions.

In basic terms, the conservation of momentum equation is a consequence of Newton's second law of motion applied to an element inside the fluid, and the conservation of mass equation stems from the requirement that mass cannot be created or destroyed within the control volume.

In the following paragraphs, the different types of constitutive equations will be described. These equations are a set of increasingly more detailed representations of how the material fluid and performance under different flow conditions.

First one to introduce here is the Stokes Flow. In the case where the inertial (acceleration) term of the equation can be disregarded the flow is called Stokes Flow, and it represents a correct approximation of the problem for sufficiently low Reynolds values.

Equation (2.12) represents the definition for the Reynolds number:

$$Re = \frac{inertial\ forces}{viscous\ forces} = \frac{\rho v L}{\mu} \tag{2.12}$$

The higher Reynolds number will be produced with the lower viscosity media. For a conservative estimate (in terms of finding if inertial terms should be disregarded), one can use the lowest media viscosity found by previous research work, Davis found a

value of $\mu = 340.92\ Pa.s$ for a fairly hot, low-viscosity media and abrasive mixture in 1993 [24].

It can be derived that the inertial forces produced in the process are sufficiently low compared to the viscous forces to neglect their effect, and in any case, the turbulence is definitely out of the question, and the conservation of momentum equation can be simplified as:

$$0 = \underbrace{-\nabla p}_{Pressure} + \underbrace{\nabla \cdot T}_{Internal\ Stress} + \underbrace{\vec{f}}_{External\ forces} \tag{2.13}$$

Second equation is about the incompressibility. Another significant simplification that can be made when dealing with fluid is the assumption of incompressibility, i.e. (the density is a constant throughout the domain), the conservation of mass equation thus simplifies to [20]:

$$\nabla \cdot \vec{v} = 0 \tag{2.14}$$

Next equation is pure viscous constitutive equations. Viscous models are the simplest models that can be used for the term labelled “internal stress” in the equations presented above. Fluids that fall into this category are labelled Generalized Newtonian fluids, where the stress tensor is a function of the rate of deformation, the proportionality constant is the viscosity, and the form of the equation for incompressible fluids is [8]:

$$\nabla \cdot T = \underbrace{\mu}_{Viscosity} \underbrace{\nabla^2 \vec{v}}_{Strain\ rate} \tag{2.15}$$

The most commonly used equations to model the viscosity are shown below, where $(\dot{\gamma})$ is the magnitude of the strain rate shown in vector form as $(\nabla^2 \vec{v})$ above:

Newtonian fluid

$$\mu = \mu_0 = constant \tag{2.16}$$

Power Law

$$\mu = m(\dot{\gamma})^{n-1} \tag{2.17}$$

Bird-Carreau

$$\mu = \mu_{inf} + (\mu_0 - \mu_{inf})[1 + (\lambda\dot{\gamma})]^{\frac{n-1}{2}} \tag{2.18}$$

The last equation introduced here is Viscoelastic constitutive equations. Viscoelastic fluids can be modelled by more complex constitutive equations which take into account the elastic time-dependent response of the media, perhaps the most convenient collection of viscoelastic constitutive equations can be found in the ANSYS Polyflow user guide, what follows is a summary of a large amount of information available.

The models available can be of the Oldroyd type which follows a differential equation that debates the stress term shown in the Navier-Stokes equations. The model follows the equation:

$$T = \underbrace{T_1}_{Viscoelastic\ component} + \underbrace{T_2}_{Purely\ viscous\ component} \tag{2.19}$$

The viscoelastic component formulation varies for each model; this model family includes Maxwell, Oldroyd-B, White-Metzner, Phan-Thien-Tanner and Giesekus models. The elastic behaviour for these models is normally input as one or multiple relaxation times defined as “the time required for the shear stress to be reduced to one-third of its equilibrium value once the strain rate vanishes”.

The other family of models are described by the user guide as being “written in terms of quantities that more or less refer to the topology of macromolecular chains”, models in this family are FENE-P, POM-POM and Leonov.

Each of the models from both families has their unique strengths and weaknesses and are used in industrial applications involving the flow of molten polymers which behave similarly to AFM media.

Accurately modelling a complex viscoelastic media behaviour is a key challenge while performing any CFD. Uhlmann carried out an experimental investigation on turbine blades to validate the CFD simulation performed in ANSYS CFX in 2015. The simulation was run by integrating non-Newtonian shear thinning equations of Maxwell fluid and also inelastic Navier Stokes equation. Material model of viscous media is introduced by Uhlmann himself by modifying the Maxwell fluid equation. They reckon the fluid characteristics matched by 99% as they measured the media with rotational plate/plate rheometer [58]. Figure 2.16 shows the fixture and part: on the left is a reference work piece and on the right is a turbine blade.

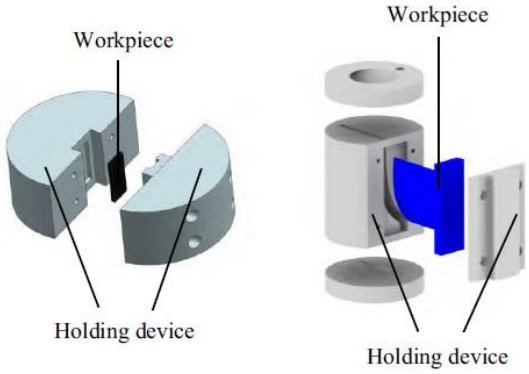

Figure 2.16 Fixture holding the workpiece on the left and a flat-bladed aero-blade on the right

Material removal is not simulated due to the complexity of the equations to be solved, but as media is shear rate dependent, the workpiece is compared for material removal with corresponding shear rates. The results suggest that material removal during the flow simulation is not completely even throughout the workpiece, it is slightly higher at the inflow and outflow and centre. Once again, a very good investigation is carried out but has not reached to the simulation which can predict the wear or material removal from the workpiece using already existing equations or modified, derived user equations.

Three main difficulties arise when trying to model AFM with these models:

- The additional need to input the material properties in the form of relaxation times or coefficients in addition to the viscosity required for the purely viscous models described in the previous section. These properties are not available from the manufacturer and almost non-existing in literature.
- Difficulty with convergence at high Weissenberg numbers which make the set-up of simulations require the addition of evolution strategies to “ramp up” different variables in other to gain convergence, from experience obtained by using ANSYS Polyflow available in Brunel University during the evaluation of these models this process is time-consuming and not guaranteed to provide convergence.
- The need for additional computational requirements will likely mean that the problem cannot be run with the available hardware in fine enough meshes.

Because of these issues, it was decided to model the flow with a purely viscous model implemented in COMSOL Multiphysics and the interaction with Matlab in this research.

2.5 Fluid-Structure Interaction (FSI)

Fluid-structure interaction (FSI) is a methodology used to solve the interaction problem of some deformable or movable structure or solid particles with the fluid flow around or surrounded.[30] FSI can be used to model the circumstance with either stable or oscillatory interactions. While in oscillatory interactions, the strain remained in the solid structure will cause the solid deforming to make the source of strain reduced, after the deformation the structure returns to its former state only for the process to repeat.

Gene gives a relevant literature review on the subject in 2012. In this paper, the author review lots of existing literature about FSI methodology and simulation, which contributes a lot to this research's modelling methodology and simulation.

In recent years, FSI modelling and simulation methodology may play more and more important roles in many scientific and engineering fields. A comprehensive study of such problems brought out by Chakrabarti in 2005 remains a challenge caused by their strong multidisciplinary and nonlinearity nature. For most FSI problems, analytical and computational solutions to the model equations are almost impossible to obtain because of the laboratory experiments are limited in scope. As a result, it is important to investigate the fundamental physics model involved in the complex interaction between fluids and solids, and with this way, the numerical simulations can be employed [31-33].

With the help of the development in computer technology, modelling and simulations of scientific and engineering systems have become more and more sophisticated and complicated. There are many examples in FSI model and simulation such as the speed requirement of the boat hull which has advanced to such a degree and with the specific speed that has outpaced the availability of testing data and existing design equations brought out by Weymouth in 2006 and 2008. In these two kinds of literature, in order to fill the technological gap, a useful numerical algorithm has been used to investigate specifically the motion of the boat and the interaction between water waves.

This investigation brought by Weymouth is typically multidisciplinary. In his research, the performance of the boat is shown as a result of the interaction between structural dynamics and water hydrodynamics [34,35]. There are also some other FSI applications brought by researches recently, but are not limited to, sedimentation by Mucha, Tornberg and Shelley in 2004, particle assembly by Liu in 2006, aerodynamics by Haase in 2001, turbulence by Kaligzin and Iaccarino in 2003, complex flows in irregular domains by Fadlun and Udaykumar in 2000, electro-hydrodynamics by Hoburg and Melcher in 1976, magneto-hydrodynamic flows by Grigoriadis in 2009, biofluid and biomechanics (such as cell aggregation and deformation, blood-heart interaction, inner ear fluid dynamics, jellyfish swimming, sperm motility, ciliary beating, etc.) [36-43].

Currently, there are two approaches in the numerical procedures to solve these FSI problems may be specifically classified into the partitioned approach and the monolithic approach. It is mostly like that the distinction between these two approaches may be viewed differently by different researchers from different fields. In this section, these two approaches will be introduced roughly from the engineering application point of view. As shown in the following, Figure 2.17 illustrates the solution procedures of the monolithic and partitioned approaches [44,45].

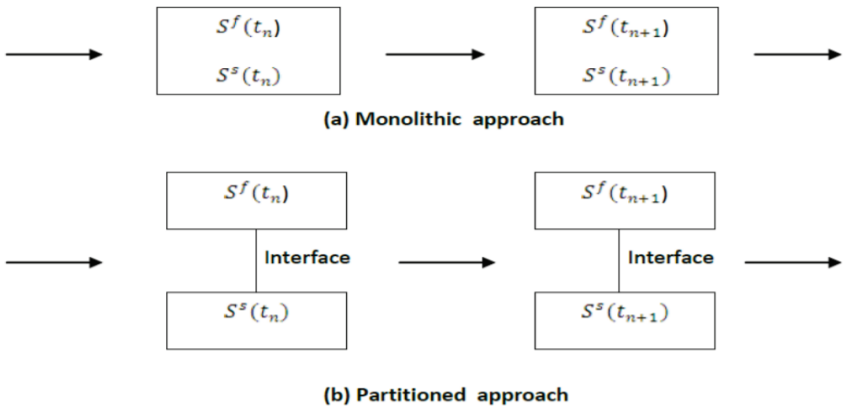

Figure 2.17 Schematic of the monolithic approach: (a) the partitioned approach; (b) for fluid-structure interactions, S^f and S^s for fluid and structure solutions, respectively

At the same time, there is another general classification of the FSI solution procedures: the conforming mesh methods and non-conforming mesh methods. These two methods are based upon the treatment of meshes. The conforming mesh methods

treat the interface conditions as physical boundary conditions. In this type of methods, the interface location is seen as part of the solution and requires meshes that is necessary to be conformed to the interface. Oppositely, the non-conforming mesh methods consider the related interface conditions and the boundary location as constraints caused by the model equations. As a result, non-conforming meshes can be employed in this type of methods. In this method, the fluid equations and solid equations can be solved independently from each other with their respective grids, and the process of re-meshing is not necessary for this method. The distinction between these two types of meshes can be observed in Figure 2.18 as following, where a solid body (in this example it is a sphere) is moving in the fluid domain. However, most of the partitioned approach-based numerical works are the conforming mesh methods while the immersed methods that perhaps represent most of the recent developments in FSI methods are the non-conforming mesh methods [46,47].

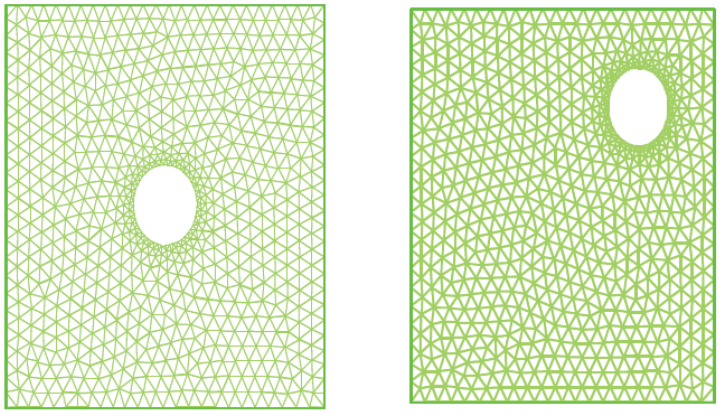

(a) Conforming mesh. Left: t = t_1; Right: t = t_2

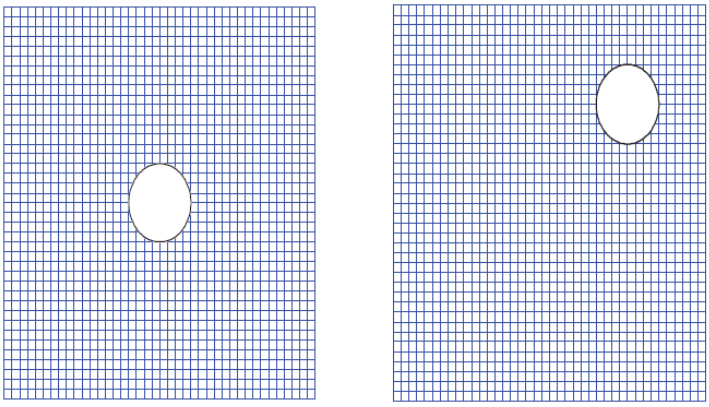

(b) Non-conforming mesh. Left: t = t_1; Right: t = t_2

Figure 2.18 Examples of meshes (a) conforming mesh; (b) non-conforming mesh

In this research, the model methodology and simulation adopt the FSI module in COMSOL Multiphysics. The FSI multiphysics interface in COMSOL Multiphysics combines fluid flow with solid mechanics in order to capture the interactions between fluid and structure. In this model, a solid mechanics interface and a Single-phase Flow Interface are used to model the solid and the fluid. In this module, the FSI couplings appear on the boundaries between the fluid and the solid. The FSI interface uses an arbitrary Lagrangian-Eulerian (ALE) method to combine the fluid flow formulated using a Eulerian description and a spatial frame with solid mechanics formulated using a Lagrangian description and a material (reference) frame. This module illustrates how fluid flow deform the structures and how to solve the flow in a continuously deforming geometry using ALE technique.

The ALE method is used in FSI module in COMSOL Multiphysics which aims to handle the dynamics of the deforming geometry and the moving boundaries with moving grids. The COMSOL Multiphysics computes with new mesh coordinates on the channel area based on the mesh smoothing and the movement of the structure's boundaries. Navier-Stokes equations are used to solve the flow which is formulated for these moving coordinates.

On the other hand, the structural mechanic's portion of the model in COMSOL does not require the ALE method. The module in COMSOL Multiphysics solves the problem in a fixed coordinate system as usual. The example of ALE method is shown as Figure 2.19. However, the strains in this model compute in this way that is the only source for computing the deformed coordinates with ALE.

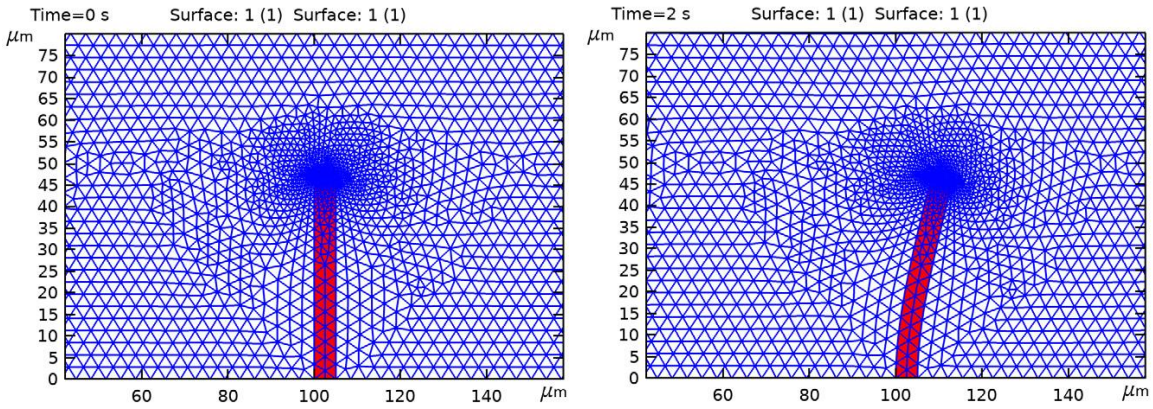

Figure 2.19 Examples of FSI module calculating result in COMSOL Multiphysics

The equations in the FSI module that COMSOL Multiphysics is using is described as follows:

First equation introduced here is the fluid flow. The fluid flow in the channel is described by the incompressible Navier-Stokes equations for the pressure, *p*, and the velocity field, **u** = (*u*, *v*) in the spatial moving coordinate system:

$$\rho\frac{\partial \boldsymbol{u}}{\partial t} - \nabla\cdot[-p\mathbf{I} + \eta(\nabla\boldsymbol{u} + (\nabla\boldsymbol{u})^T)] + \rho\big((\boldsymbol{u}-\boldsymbol{u}_m)\cdot\nabla\big)\boldsymbol{u} = \boldsymbol{F} \tag{2.20}$$

$$-\nabla\cdot\boldsymbol{u} = \mathbf{0} \tag{2.21}$$

In these equations list above, **I** denote the unit diagonal matrix while **F** represents the volume force affecting the fluid. In this model, we assumed that no gravitation or other volume forces would affect the fluid, so that **F** = 0. The coordinate system velocity in this equation is: $\boldsymbol{u}_m = (u_m, v_m)$

Next equations are related to the structural mechanics. The structural deformations are solved by using an elastic formulation and a nonlinear geometry formulation in order to simulate large deformations. The equation in this module is given as follows:

$$\mathbf{F}_T = -\boldsymbol{n}\cdot(-p\mathbf{I} + \eta(\nabla\boldsymbol{u} + (\nabla\boldsymbol{u})^T)) \tag{2.22}$$

In this equation, **n** represents the normal vector to the boundary. This load $\mathbf{F}_T$ represents a sum of pressure and viscous forces.

In the end, the Navier-Stokes equations are solved on a freely moving deformed mesh with the help of COMSOL Multiphysics, in which mesh constitutes the fluid domain. The deformation of this mesh relative to the initial shape of the domain is computed using Hyperelastic smoothing.

Fluid–structure interaction (FSI) is the interaction between the deformable or movable structure and fluid flow [84-88]. It is widely used in many different industrial fields which include fluid and the fluid influences the manufacturing process. There are two main approaches exist for the simulation of fluid–structure interaction problems. One is Monolithic approach while the other one is the Partitioned approach. The equations in Monolithic approach governing the flow and the displacement of the structure are

solved simultaneously, with a single solver. The other one solves the displacement of the structure separately, with two distinct solvers. Each of them owns its advantages and disadvantages.

A mathematical model called Newton–Raphson method can be used to solve FSI problems. The methods based on Newton–Raphson iteration can be used in both of the two approaches listed below. These methods use the structural equations and the nonlinear flow equations on the structure and fluid domain. The system of linear equations within the Newton–Raphson iteration can be solved with this method and provide the result of FSI problems.

The FSI model equation can be described by two parts as follows:

$$\rho \frac{\partial u}{\partial t} - \nabla \cdot [-pI + \eta(\nabla u + (\nabla u)^T)] + \rho\big((u - u_m) \cdot \nabla\big)u = F \tag{2.23}$$

$$-\nabla \cdot \mathrm{u} = 0 \tag{2.24}$$

In equation 2.23, I denote the unit diagonal matrix and F is the volume force affecting the fluid. Assume that no gravitation or other volume forces affect the fluid so that F = 0. The coordinate system velocity is um = (um, vm).

Structural mechanics:

$$F_T = -n \cdot (-pI + \eta(\nabla u + (\nabla u)^T)) \tag{2.25}$$

where n is the normal vector to the boundary

This method contributes a lot on building the multiphysics simulation of AFM process. It increases the accuracy of pressure and velocity of fluid media and the distribution of particles in the fluid which contributes a lot on the prediction of surface generation and profile accuracy of leading edge and trailing edge.

2.6 Development and the applications of the Abrasion model

In a paper published in 1988, Jacobson et al. established a model for simulation of abrasive wear. Abrasive grains were assumed to be in conical geometry with specified cone angle ϕ and tip radius r. Workpiece profile generation is based on a normal distribution with average surface level and surface deviation both considered to be variables since the grooving depth will be stochastically influenced by both variables. The new profile and average level are calculated after every individual grain have passed through the cross-sectional area.

Jain developed the model to simulate the mechanics of AFM process. It is strictly applied to micro-cutting without material displacement [72]. The process is considered to be a scratching action performed by the abrasive grains in the media and the force applied to the media causes the active grain to indent in the workpiece surface. Following assumptions were made:

- The trajectory of an individual grain is a straight line;
- The material is removed in the form of chips through plastic deformations without the ploughing effect, whenever grains interact with the surface;
- The abrasive grain is approximated by a sphere. This is conforming to the experimental observations, which shows that abrasive grains are generally round in shape, and are not composed of acute cutting edges;
- The abrasive particle size has been observed to lie within a narrow distribution. Hence, the distribution of abrasive radii is assumed to be normal, and symmetric about the mean grain radius.

The distribution of grains in the media is represented by Cartesian coordinates, which represent the position of grain relative to the surface. Grains are randomly positioned in the AFM media such that they are uniformly distributed within the carrier volume. The centres of the abrasive grains (x_i, y_i) are fixed to the workpiece, any active abrasive grain interacting with the surface will be recorded. The initial surface profile is expected to follow Gaussian distribution no matter how much of the individual indentations have affected the surface. The indenting grain would have some of its z coordinates below the corresponding z coordinates of the working surface. For a given

grain with radius r_i, possible modification to the work profile would be (x_i-r_i) to (x_i+r_i). The diagram of this theory is shown as Figure 2.20.

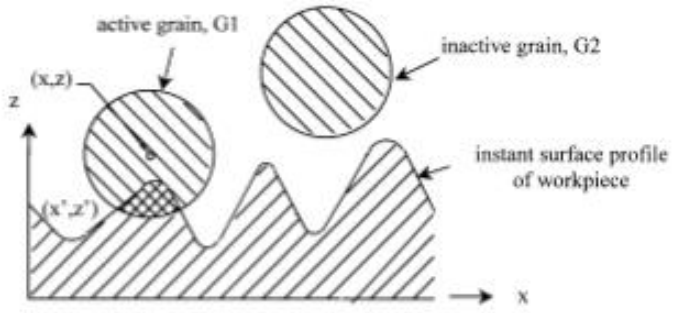

Figure 2.20 Schematic spherical grain cutting mechanism

The material removal in AFM process is modelled by transforming the coordinates of the interfering profile of individual grains to the surface, based on geometrical coordinates. The computer then computes the change in the height of the work piece profile from the grain cutting tip. This simulation demonstrated good results and allows accurate prediction of surface roughness and material removal.

Dixit modelled AFM process through the application of finite element technique to solve the governing equations in terms of three-dimensional fluid velocity and extrusion pressure assuming axisymmetric media flow under steady-state. [29] Important assumptions were made:

The media used in AFM is composed of semisolid carrier mixed with abrasives which exhibit linear viscous flow property. The media is isotropic and homogeneous. The media properties are independent of fluid temperature and constant with time and space. The media flow is axisymmetric since the cylindrical workpiece is considered and the media flow is steady.

Langrangian biquadratic shape function for velocity components and bilinear shape function for pressure over a nine noded quadrilateral element are used. The final equation is obtained by assembling the elemental coefficient matrices and right side vectors into the global coefficient matrix and right side vector, respectively. The elemental coefficient matrices are solved through Gauss quadrature integration technique.

Material removal mechanism was solved through idealized classical abrasive wear model. Where the depth of indentation *t* is given by the formula:

$$t = \frac{d_g}{2} - \sqrt{\frac{{d_g}^2}{4} - \frac{F_n}{H_w \pi}} \tag{2.26}$$

With F_n being the indenting force which is correlated to the extrusion pressure, and H_w being the Brinell hardness coefficient of the material; the volumetric material removal is given by the formula:

$$V_a = \left[\frac{{d_g}^2}{4} sin^{-1} \frac{2\sqrt{t(d_g - t)}}{d_g} - \sqrt{t(d_g - t)} \left(\frac{d_g}{2} - t \right) \right] L_i \tag{2.27}$$

d_g – Grain diameter;

t – Depth of indentation;

L_i – Contact length of *i*th abrasive grain with the work piece

Surface roughness was modelled without initial assigning of distribution to the workpiece surface. The ratio between peak to trough roughness R_t and arithmetic average roughness R_a is assumed to be constant, for AFM process, it is approximated to be 7. The actual contact length is derived based on the intersection of spherical grains with the idealized pyramidal workpiece roughness peaks. The expression is given by:

$$L_i = \left(\frac{\Delta l_c}{\Delta l_g} \right) l_w = \left[1 - \frac{{R^i}_a}{{R^0}_a} \right] l_w \tag{2.28}$$

Another method of approaching grain-work piece interaction would be the application of L'vov model, which estimates the undeformed chip thickness at the onset of chip formation [73]. The model proposed the critical depth of cut, which shows the transition from ploughing to cutting concerning the metal rolling theory. The model suggests that the force of cutting should be perpendicular to the direction of rolling. Therefore, the undeformed chip thickness is given as a function of edge radius assuming the critical depth of cut:

$$d = 0.293r \tag{2.29}$$

Hertz theory is applied in grinding process for prediction of indentation depth. As AFM process is in many ways similar to grinding process, Hertz theory can be applied in AFM process for similar estimation [74]. According to Hertz, the contact area for elastic contact between sphere of radius and a flat surface can be evaluated from:

$$\bar{\sigma} = 0.41 \times \sqrt[3]{\frac{F'_{ng}{E_m}^2}{4R^2}} \tag{2.30}$$

E_m denotes the Young's modulus of elasticity of the work piece surface and R denotes the spherical radius. F'_{ng} represents the normal force acting on the cutting tool, it is given as the expression:

$$F'_{ng} = CA\sigma \tag{2.31}$$

Where C denotes the ratio of mean contact stress over uniaxial flow stress of the material; A denotes the contact area given by $\frac{\pi b^2}{4}$ (b represents the diameter of the projected area of grain at contact) and σ denotes the uniaxial flow stress.

The depth of indentation for elastic loading is given by,

$$d' = 1.55 \times \sqrt[3]{\frac{{F'_{ng}}^2}{2R{E_m}^2}} \tag{2.32}$$

The maximum value of stress at contact area will be equal during plastic deformation will be equal to the Brinell Hardness of the material, thus following expression is derived:

$$\frac{d'}{2R} = 9.22\left[\frac{H_W}{E_m}\right]^2 \tag{2.33}$$

This expression is known as the criteria for determining different interaction regime between the work piece and the abrasive grains, three regimes were identified:

Chip forming regime: $\frac{d'}{2R} > 0.029$

Plastic regime: $9.22\left[\frac{H_W}{E_m}\right]^2 < \frac{d'}{2R} < 0.029$

Elastic regime: $\frac{d'}{2R} < 9.22\left[\frac{H_W}{E_m}\right]^2$

The criteria shows that when the penetration depth is below 6% of the grain radius, the chip will not form and the depth is below 0.058R then the displaced material will form ridges by undergoing plastic deformation and no metal will be removed. If the depth is less $18.44\left[\frac{H_W}{E_m}\right]^2$R then the grains will slide across the surface and no plastic deformation will occur.

Another method of determining the depth of indentation is proposed by Brecker et aI. A critical undeformed depth exists below which no ploughing or cutting effect will take place. [75] For a spherical grain with half cone angle greater than a critical angle, no upward flow causing chip formation will occur. This critical angle is approximated to be 80º. For 80º half cone angle, the minimum value of d_s would be: d_s = 0.0076d_g=0.0152R. d_s is the depth of indentation, in comparison with the minimum depth value as predicted by L'vov model, d_s is much lower, due to the higher half-cone angle selected. The critical load on a grain can be estimated by:

$$P' = H_w A = H_w \frac{\pi}{4}\left(\frac{d_s}{sin\frac{90-\theta'}{2}}\right)^2 \quad (2.34)$$

This equation describes the load below which only elastic deformation will occur with particles rubbing the surface only. Bowden et al proposed way to analyse the radial and axial components of force on a single grain. The axial force is consisting of two forces- ploughing and shearing forces, as suggested by the sliding action between non-metal and metal body. It is assumed that the indentation will take place until the area of contact between the surfaces is sufficient to support the applied load (F_{ng}). Rotation will not occur will not occur unless the resistance by the work piece is more than the axial force acting on the grain. The interaction between abrasive grain and work piece is assumed to be rubbing or ploughing as suggested by experimental observations.

The radial force on a single grain is estimated as:

$$F_{ng} = A\sigma = \pi \times \sigma \times \left(\frac{b}{2}\right)^2 \tag{2.35}$$

The ploughing force required for metal to displace from the front of the abrasive grain is defined as:

$$P'' = \frac{1}{16}\frac{b^3}{R}\sigma \tag{2.36}$$

and the friction force component is defined as:

$$F_R = F_{ng} \times \mu \tag{2.37}$$

So, the axial force *F* is defined as:

$$F = \frac{1}{16}\frac{b^3}{R}\sigma + \pi \times \sigma \times \left(\frac{b}{2}\right)^2 \times \mu \tag{2.38}$$

With diameter of projected area to be $2\sqrt{2Rd' - d'^2}$ and friction coefficient taken to be 0.4, the axial force formulation can be simplified into:

$$F = \left[\frac{1.414 \times (R \times d')^{1.5}}{R} + 2.5132Rd'\right] \tag{2.39}$$

An analytical model was developed by Singh and his colleagues to determine the medium properties for a cylindrical workpiece [76]. The cutting action in AFF process was simulated by passing abrasive particles over the surface roughness peaks. With Z co-ordinates of the active particles lying below the Z' co-ordinate of the surface roughness peaks. The surface roughness peak profile was then recorded based on the interaction of the abrasive particle and that specific peak. After one stroke, change in peaks was updated and used as initial surface roughness for the next AFF stroke.

First of all, abrasive particles were generated in cylindrical volume at random with a uniform distribution curve. The interfered particles will incur the regeneration process until no particles are overlapping with each other. Cross-sectional areas were divided into numbers of the diametrical plane with the surface roughness of the workpiece represented into two-dimensional plane that is perpendicular to the direction of medium flow. It is assumed that the riddance of roughness peaks is carried out by a corresponding projected radial cross-section of the active particles. Therefore it is

necessary to determine the intersection of the active particles with the diametrical plane.

Three possible scenarios can occur during the abrasion. First scenario involves having distance between the co-ordinate of the abrasive particles and the co-ordinate of the roughness peaks more than the maximum effective depth of indentation:

$$Z' - (Z(j) - R_{projected}) \geq t_e \tag{2.40}$$

The abrasive particles cannot cut through peaks greater than the maximum effective depth of indentation. Therefore the z co-ordinate after the abrasion is given by:

$$Z'' = Z' - t_e \tag{2.41}$$

The second scenario involves having distance between the co-ordinate of the abrasive particles and the co-ordinate of the roughness peaks less than the maximum effective depth of indentation:

$$Z' - (Z(j) - R_{projected}) < t_e \tag{2.42}$$

In that case, the z co-ordinate after the abrasion is given by:

$$Z'' = Z' - (Z(j) - R_{projected}) \tag{2.43}$$

The above mathematical description of active grain density is strictly applied to the cylindrical workpiece. With rectangular workpiece or more complex geometry such as rotor blade, the above analysis cannot be easily applied since the shear thinning of fluid medium greatly impacts the abrasive process. With the analysis of complex rotor geometry, the rheological properties of the media need to be considered.

2.7 Summary

This chapter has presented a critical review on the state of the art in the objective areas of this research. The review also aims to identify the knowledge gaps and research issues for this doctoral research, which can be summarized as follows:

(1) Currently, Abrasive Flow Machining (AFM) is used on manufacturing of some aerofoil structures to improve the surface roughness. However, the industry is using

the try-and-error methods to control machining process parameters and difficult to identify and apply the optimal parameters in processing aerofoil structures.

(2) There are plenty of modelling and simulation methodologies working at different scales and different physics phenomena for different industrial applications. However, they are often separately applied to many different industrial cases. Some multiscale multiphysics modelling and simulation methodologies are proposed, but it is still necessary to develop the methodologies for different industrial cases and applications.

(3) Computational Fluid Dynamics (CFD) and Fluid-Structure Interaction (FSI) modelling methods are reviewed in this chapter. They are suitable methods to simulate the conditions of fluid media in the AFM process at the macro-scale. However, more work and development need to be undertaken on simulations addressing micro-scale needs by using the multiscale multiphysics modelling methodology.

(4) The abrasion model currently used to model the process of abrasive machining provides a reliable prediction of abrasive machining in many different industrial cases. But it but did not step into the field of abrasive flow machining (AFM). The abrasion model of grains carried with fluidic media should be different from that which is previously applied in the conventional abrasive machining and grinding processes.

With above points in mind, there is a need to develop a multiscale multiphysics modelling and simulation approach to enabling the prediction and control of material removal at the macro scale and surface roughness and surface texture at the micro scale in Abrasive Flow Machining. The approach will cover the simulation of fluid and particles in different physics phenomena and optimize the AFM process parameters for manufacturing of aerofoil structures the better performance.

At present, the finished surfaces of most components, along with other attributes such as mass, accuracy, cost, and delivery time, have proven to be important for manufacturing. Industrial companies spend substantial efforts (time, manpower and money) to obtain the required final surfaces with the desired texture after machining the components. Some of the finishing processes which can help reach the required final surfaces are non-conventional finishing processes. One of those non-conventional finishing processes is Abrasive flow machining (AFM). AFM makes use of a pressurized abrasive media slurry passing through the surfaces to reach the desired surface quality. The abrasive media is classified as a kind of high viscosity

liquid; some very viscous media performed better described as putty. This media is a semi-solid medium consisting of a viscous-elastic polymer and abrasive particles mixed in a definite proportion to form a slurry. The abrasives particles contained in media are often metal oxide or carbide ceramics, such as silicon carbide and aluminium oxide. On the other hand, the diamond is also used for some special applications. To some extent, harder abrasive particles, such as diamond or Boron carbide particles, are often used for abrasive flow machining of hard or difficult-to-machine materials including tool steels, superalloys and titanium alloys.

Chapter 3 Development of the multiscale multiphysics based modelling and simulation approach for abrasive flow machining

3.1 Introduction

Engineering modelling and simulation are increasingly applied in various engineering fields at different scales, such as those focusing on the structures by macroscopic models while some by using microscopic models to improve the component accuracy in terms of its form, dimension and surface profiles, etc. Some modelling and simulations based on different physical principles are applied to analyse the manufacturing process by taking account of various factors. However, in precision engineering cases, the underlying process and system are commonly complex, i.e. involving mechanical, electrical, optical elements operating in multiple scales simultaneously. For instance, the heat transfer, air lubrication and electric-magnetic fields within a direct drive aerostatic bearing supported slideway, the above-mentioned various factors affect each other, which is critically essential in working towards high precision. Therefore, it is necessary and important to develop multiscale multiphysics based modelling and simulations in supporting precision engineering analysis, particularly for rendering simulation accuracy and the corresponding precision machining efficiency. Furthermore, it is of great significance to establishing an industrial feasible approach that is able to bridge the gaps in undertaking precision and micro/nano-manufacturing at a truly predictable, producible and highly productive manner [77].

In recent years, it can be found that many breakthroughs in multiscale modelling and the associated computational methods developed in different R&D areas and application fields. Those developments have applied to material science, chemistry, biology, fluid mechanics and precision engineering [78], one example is the nonlocal quasi-continuum method (QC) for simulating isolated defects including dislocations and cracks in single crystals. The method is conceived and developed by Tadmor in 1996 [79]. The DSMC-gas dynamics modelling method is also a multiscale modelling

method used in solving fluid mechanics problem, which is an elegant extension of the adaptive mesh refinement procedure developed through the years by Bell and his colleague [80]. However, those research and development are related to multiscale modelling and simulations limited in one phase simulation.

On the other hand, Multiphysics analysis software tools and Multiphysics modelling applications have been gaining substantial advances, although numerous software engineering challenges remain particularly in effective coupling, integration and complex problem-solving. Those Multiphysics tools provide opportunities for long-term research focusing on accurate, robust, stable, efficient and scalable Multiphysics modelling and analysis algorithms, with extensibility for application-specific customization and so on. If the application and simulation involve objectives in various dynamic states and physical fields as it often is, it should be likely to simulate it through the integration of Multiphysics modelling and analysis and thus lead to the optimal solutions.

In this chapter, the development and application of multiscale multiphysics modelling and analysis are introduced at first, particularly focusing on the core principles of some comparatively advanced ones. The modelling methods are presented separately by different scales and physical fields. Then some application exemplars are presented to show how different scales and physical fields are combined and integrated into the simulations. The interaction between different scales and physical fields is essentially important for industrial research and development because of the complexity and interdisciplinary nature involved. A real industrial case study is further introduced based on multiscale multiphysics modelling and simulation. Through the Abrasive Flow Machining (AFM) application, the rationality and feasibility of using the multiscale and multiphysics modelling and simulation are discussed and explored. Finally, the potential and future development of the approach are reviewed and further discussed.

3.2 Multiscale and multiphysics modelling, simulation, and precision machining

As a multiscale modelling and simulation, it is essential to discuss the model in different scales. The equations and theories have been divided into four different scales against the computational time which have been illustrated in Figure 3.1 [78].

Those fundamental theories and the associated implementation approaches are used to solve industrial problems on various orders of magnitude. The following description attempts to discuss some examples of each scale in a highly summative manner.

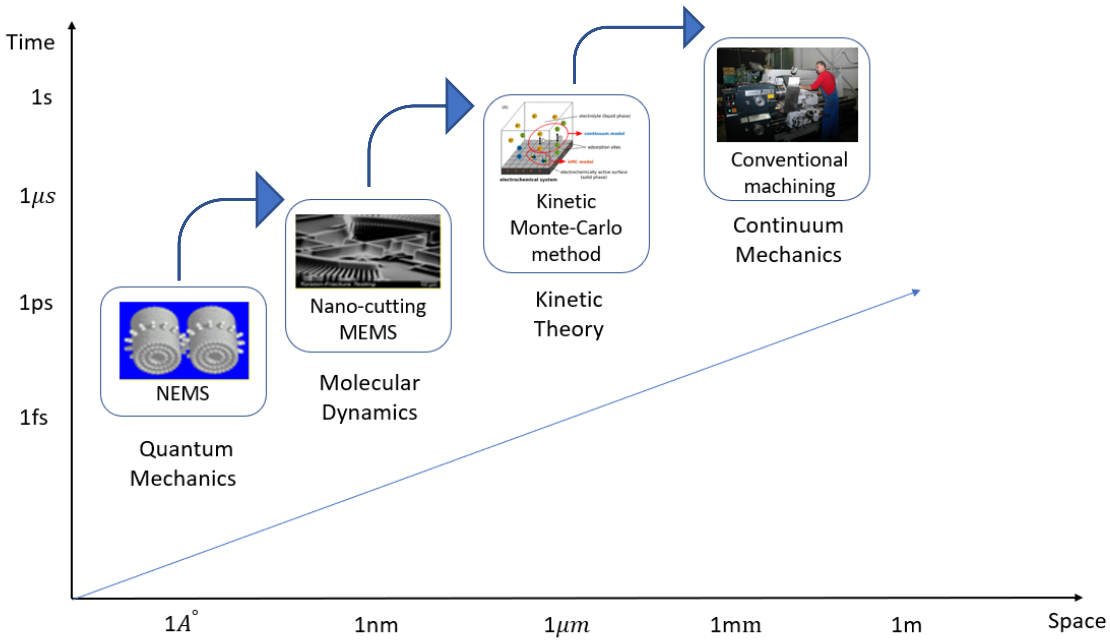

Figure 3.1 Illustration of models on four different scales and their integration

Continuum mechanics models, such as the Euler's equation and the Navier-Stokes equation, are the crudest in this hierarchy, which only concentrates on the macroscopic density, velocity and temperature fields of the fluid. Nevertheless, they are already quite sufficient in many engineering applications. Quantum mechanics models are the most detailed ones. They are required if we are interested in the details of the collision process between gas particles. Molecular dynamics models are of the intermediate complexity, which respectively captures the phase space probability distribution and the phase space dynamics of the fluid particles in the non-Newtonian fluid. Kinetic theory serves as a connection between continuum and atomistic models. It can either be viewed as an approximation to the hierarchy of equations for the many-particle probability densities obtained from molecular dynamics or as a microscopic model for the phase-space probability distribution of a particle, from which continuum models can be derived [78].

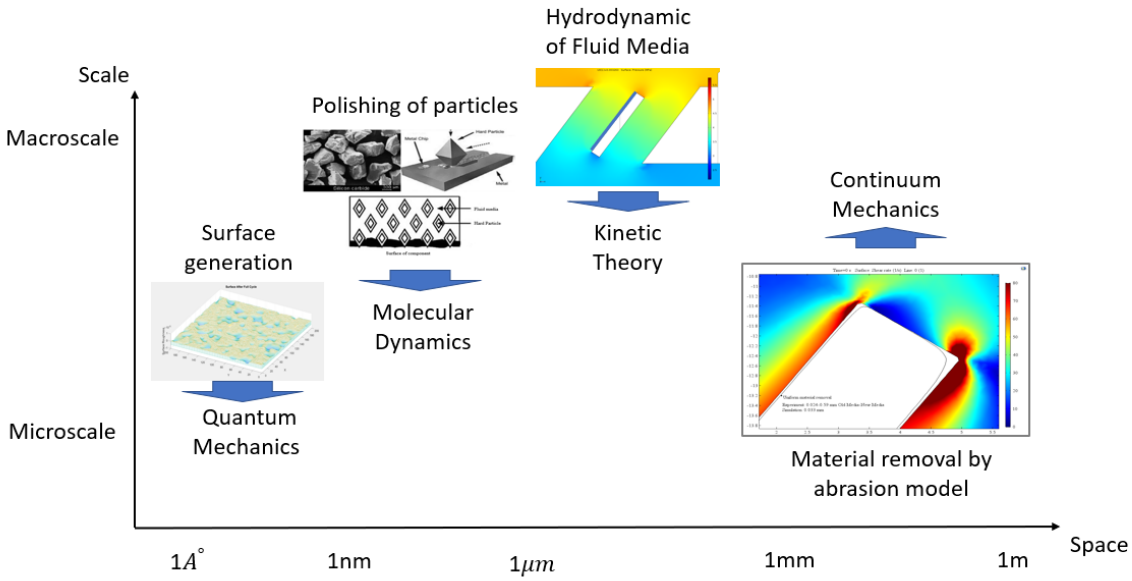

Figure 3.2 Illustration of models used in this research on different scales

3.2.1 The Oldroyd-B model based on Continuum Mechanics and Molecular Dynamics

Some fluids called complex or non-Newtonian fluids are widely used for industrial purpose. They include muds, fresh concrete, paints, and medias used in many non-traditional machining. In many cases, this particular behaviour originates from the presence of some microstructures within the fluid that is strongly coupled to the solvent dynamics, especially some of the fluid dynamics owns high viscosity itself. Deriving solutions of flexible polymer chains is necessary. A dilute solution of polymer chains consists of a solvent and polymer chains floating therein. These chains are in such a small quantity that direct interactions between the chains can be neglected[5-6]. As described in the example of Oldroyd-B model in Le Bris literature, a polymer chain is meant to be a long linear molecule built as the repetition of an elementary pattern, called the monomer (think typically of an alcane molecule CH3 (CH2)n CH3). It is observed that the rheology of the fluid (that is the way it flows) is very much affected by the polymer chains, even at a minimal concentration.

Oldroyd-B model is a microscopic-macroscopic (in short micro-macro) model to describe such high viscosity fluids. The modelling principle of Oldroyd-B model is to couple conservation laws on macroscopic quantities (such as the velocity or the

stress) while using some other models for the evolutions of microstructures. With the combination of these model, the simulation will stay a high accuracy of calculation and not have a huge cost as most of the part is stay on macroscopic modelling and simulation. The modelling part can be described by two mainly equation as follows:

Modelling of non-Newtonian fluids starts with the mass and momentum conservation equations for incompressible fluids:

$$\mathrm{T} + \lambda_1 \overset{\triangledown}{\mathrm{T}} = 2\eta_0(\mathrm{D} + \lambda_2 \overset{\triangledown}{\mathrm{D}}) \tag{3.1}$$

Where:

T - the stress tensor;

λ_1- the relaxation time;

λ_2 - the retardation time $= \frac{\eta_s}{\eta_0}\lambda_1$;

$\overset{\triangledown}{\mathrm{T}}$ is the upper convected time derivative of stress tensor which can be represented as:

$$\overset{\triangledown}{\mathrm{T}} = \frac{\partial}{\partial t}\mathrm{T} + \mathrm{v}\cdot\nabla\mathrm{T} - ((\nabla\mathrm{v})^T\cdot\mathrm{T} + \mathrm{T}\cdot(\nabla\mathrm{v})) \tag{3.2}$$

Where:

v is the fluid velocity;

η_0 is the total viscosity composed of solvent and polymer components,$\eta_0 = \eta_s + \eta_p$;

D is the deformation rate tensor or rate of strain tensor,$\mathrm{D} = \frac{1}{2}[\nabla\mathrm{v} + (\nabla\mathrm{v})^T]$.

The models for polymer chains can be written separately as:

$$\mathrm{T} = 2\eta_s D + \tau \tag{3.3}$$

This modelling method is used in the prediction of velocity and pressure of the fluid media in Abrasive Flow Machining process in the simulation part of this project.

3.2.2 Multiphysics modelling and simulation

The models on different physical fields also can be interactive to each other and contribute to multiphysics modelling and simulation. Additionally, the physical models also based on multiscale, multi physics considerations are at least as important, if not more[78]. After all, the ultimate goal of modelling is to get a better understanding of the physical problem and obtaining better models is a significant way of getting the better understanding. Also, there is a very close relation between multi scale algorithms and multiscale models. The example modelling methods in different states are listed in Table 3.1.

Table 3.1 Modelling methods in different states

Gases, plasmas	Liquids	Solids
Gas dynamics MHD	Hydrodynamics (Navier-Stokes)	Elasticity models Plasticity models
		Dislocation dynamics
Kinetic theory	Kinetic theory	
	Brownian dynamics	Kinetic Monte Carlo
Particle models	Molecular dynamics	Molecular dynamics
Quantum mechanics	Quantum mechanics	Quantum mechanics

Not only on the different states should be considered in the multi-physics simulation, but also different physical fields such as heat transfer, electricity fields and chemical reactions. Many different physical phenomena have been involved in this doctoral project and the multiphysics simulation has covered different models as shown in Figure 3.3

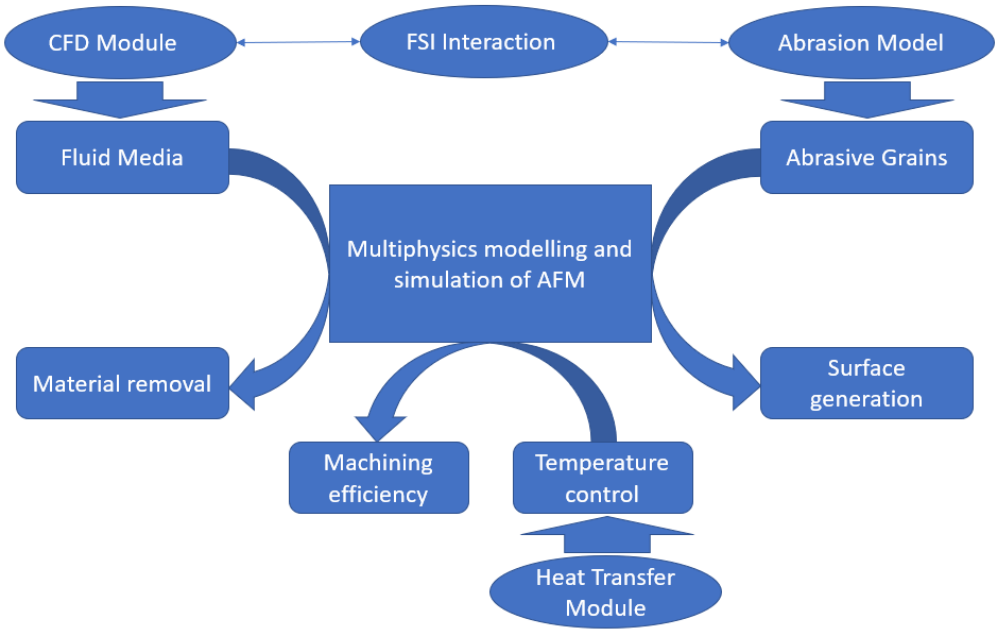

Figure 3.3 Different physics phenomena handled with multiphysics modelling and simulation in this doctoral research

3.2.3 Simulation based virtual machining system and the process optimization

With the development of computer simulation software, a concept about virtual manufacturing system has been brought out. Virtual manufacturing is the use of computers to model, simulate and optimise the critical operation parameters on the manufacturing machine and entities in factory or plant. Nowadays the virtual manufacturing system turns to be a way to design and test machine tools and expands to involve production processes and the products themselves. It can dramatically decrease the manufacturing process time and funding on the test. Now with the help of multi-physics modelling and simulation, many environmental factors can be considered in to optimise the production process. As discussed in the next section below, a Virtual AFM System has been brought out with the help of multiscale multi-physics modelling and simulation. The methodology is highlighted in Figure 3.4 and the GUI of Virtual AFM system is shown in Figure 3.5.

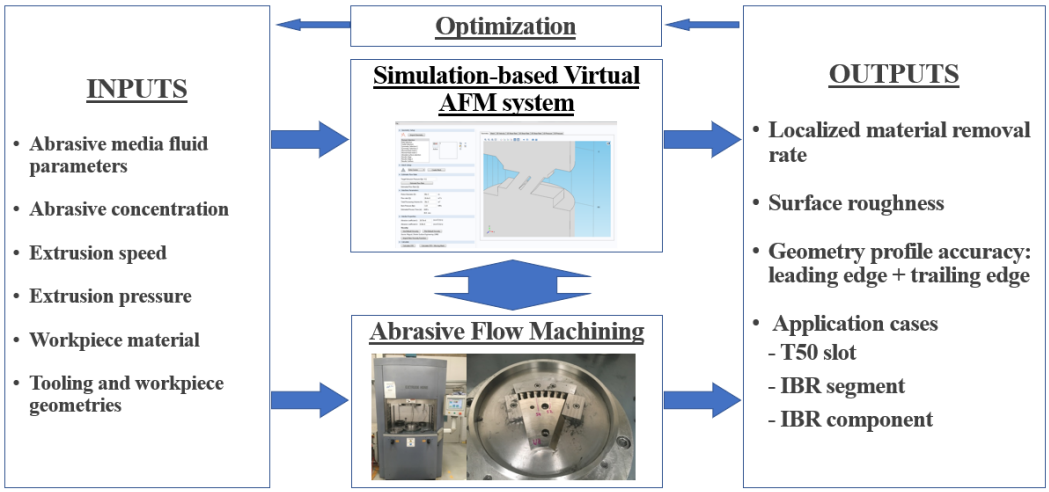

Figure 3.4 Methodology illustration of the virtual AFM system

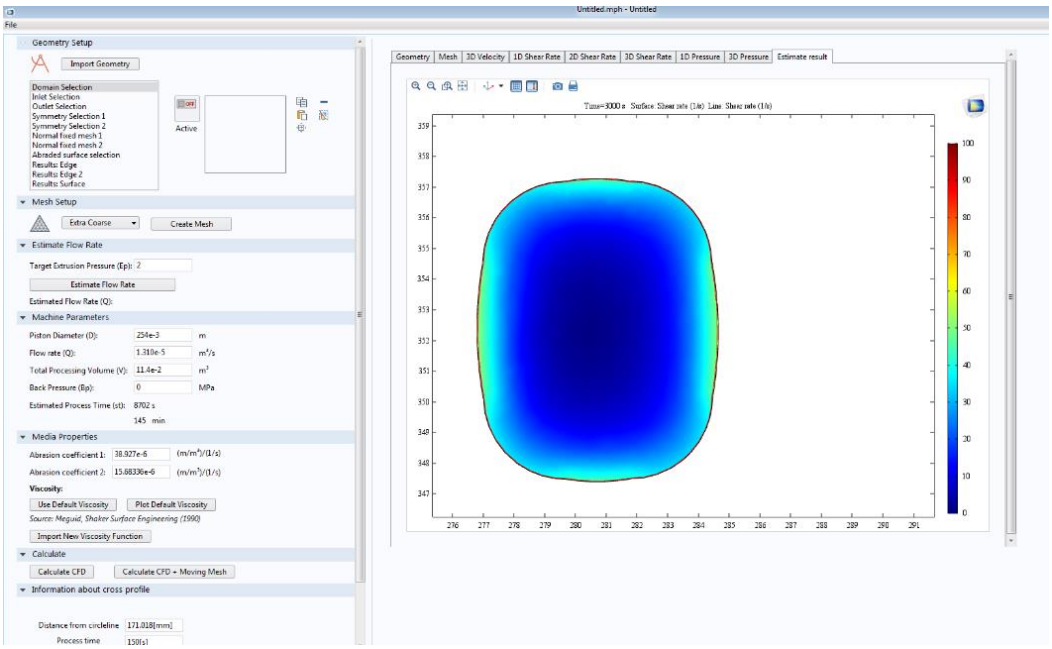

Figure 3.5 Illustration of the virtual AFM system user interface and an application exemplar

The GUI developed allows quick set-up of new AFM problems, it was built with COMSOL's integrated application builder, the left panel contains the inputs required, the graphics window on the right serves to select boundaries during set-up and displays the mesh and results of interest, the inputs required try to mimic the setup parameters on an AFM machine. The basic layout is illustrated in Figure 3.6.

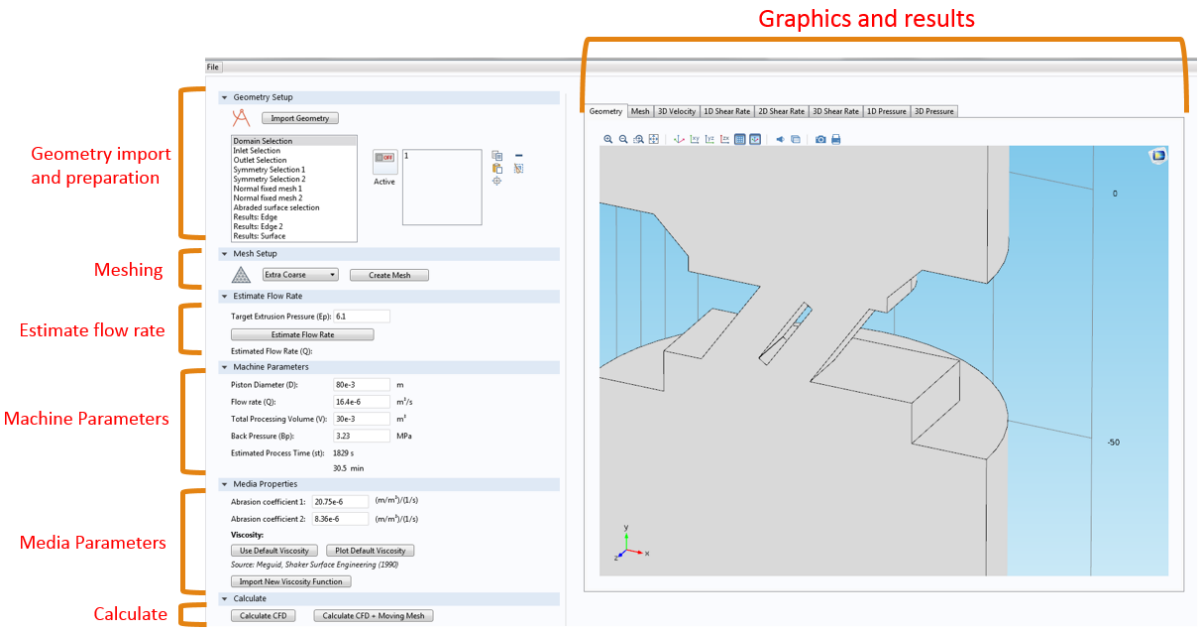

Figure 3.6 Graphical user interface and its description

In order to set up a problem the left panel needs to be worked on top to bottom, first the geometry needs to be imported with the button “Import Geometry”, the selection list contains the selections that can be made in order to specify the boundary conditions, they are labelled:

Domain: Select the fluid domain in which the simulation will run.

Inlet and outlet: Select the faces that correspond to the pushing and retracting pistons.

Symmetry 1 and 2: in order to make the problem as resource efficient (both memory and solution time-wise) to simulate as possible, the 3d file should be sectioned along any symmetry planes that can be exploited and the corresponding faces selected.

Abraded surface selection: The surfaces of interest need to be selected to enable the moving mesh interphase.

Normal fixed mesh 1 and 2: The surfaces next to the abraded walls must only be restricted in the normal direction to allow the nodes shared with them to move freely.

Results: the surface and lines of interest may be selected for the results plots.

Meshing is handled by COMSOL’s automated algorithm and the interface only asks for the overall mesh density, more complex meshing needs to be done through the standard interface.

The machine parameters that need to be set-up are the same as the ones used when setting up the AFM machine, they are: Flow Rate (Q), Piston Diameter (D), Total Processing Volume (V) and Back Pressure (Bp).

The media properties used in the simulations described below comes preloaded in the application and there is an option to import a custom-made viscosity function.

In this case, multiscale multiphysics modelling and simulation are developed in the collaboration with COMSOL and MATLAB based on CFD module, Fluid-Structure Interaction module, micro-cutting mechanics model and Monte-Carlo method. With the simulation, the material removal, profile accuracy and surface roughness of the workpiece can be predicted. With a well-designed experiment, the results of the simulation are tested. On the test of experiment, a further simulation is discussed through its application to the manufacturing process of an integrated bladed rotor. The results of the simulation are further presented on the chapter 7.

3.3 Application case studies on Multiscale Multiphysics simulations- Abrasive flow machining of integrally bladed rotors (IBRs)

3.3.1 Abrasive flow machining and specifications of integrally bladed rotors.

IBR manufacture, in particular, requires polishing the blades to a target SR while maintaining a tight control of the entire profile of the blades. With particular attention being paid to the geometry of the leading and trailing edges, the CFD based simulation of the process shown here could be especially helpful this application. Predicting MR along an entire profile and in multiple sections of the blade could significantly diminish the amount of testing and iterations required for obtaining the process parameters and be an invaluable aid when designing the rather complex tooling that is needed for this particular application of AFM [93-95].

3.3.2 Multiscale multiphysics modelling and simulation on the IBR blade

As a scientific and reliable production technique, readily available multi-physics simulation software, COMSOL can be used to analyse the flow of media in an arbitrary geometry. The CFD module in COMSOL makes it possible to simulate the Pressure Distribution and shear rate on the surface of a workpiece. With the appropriate setup of simulation, the result of Abrasive Flow Machining is predictable in controllable deviation.

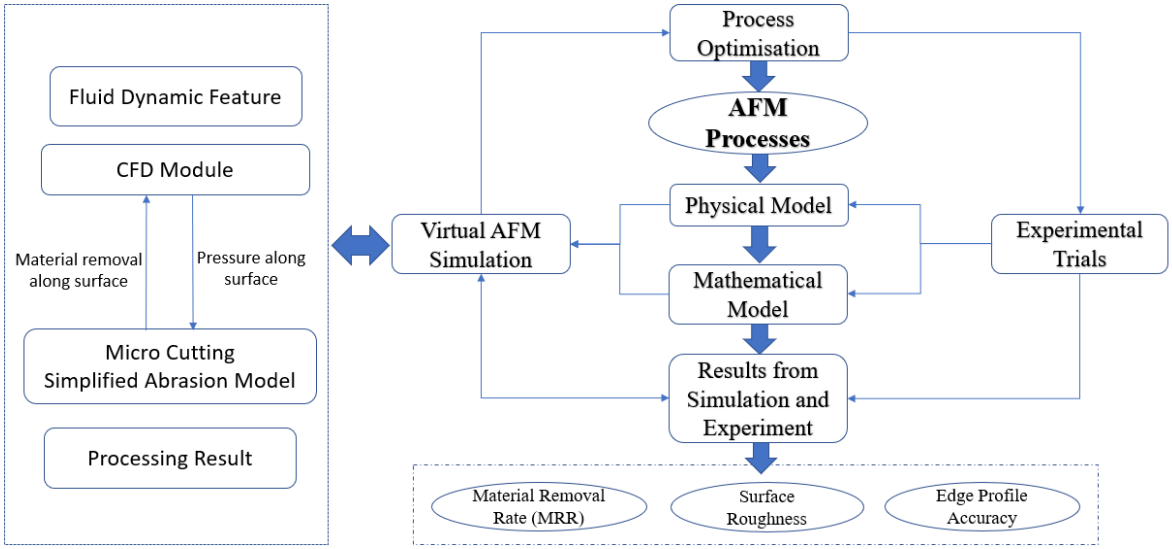

Figure 3.7 Illustration of a multiscale multiphysics modelling and simulation approach

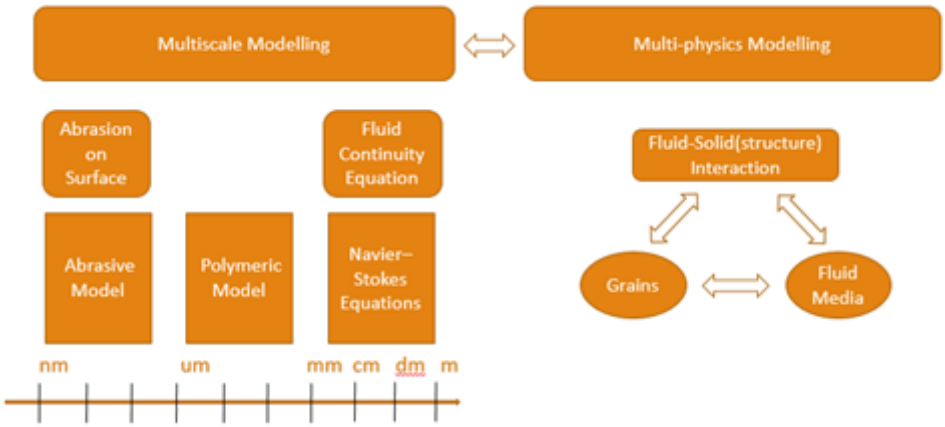

Figure 3.8 Multiscale multiphysics modelling and its integration within the AFM virtual machining system

3.3.3 CFD and multiscale modelling

The CFD Module in COMSOL uses Navier-Stokes equations to model flows in all kinds of velocity regimes. All the simulation packages used to model fluid flow numerically solve the Navier Stokes equations, with the variation on the simplifying assumptions and constitutive models utilised for the internal stress-related component. The equations are:

Conservation of momentum

$$\underbrace{\rho \frac{D\vec{v}}{Dt}}_{Acceleration} = \underbrace{-\nabla p}_{Pressure} + \underbrace{\nabla \cdot T}_{Internal\ Stress} + \underbrace{\vec{f}}_{Ext.\ forces} \tag{3.4}$$

Conservation of mass

$$\frac{d\rho}{dt} + \nabla \cdot (\rho \vec{v}) = 0 \tag{3.5}$$

The constitutive equation

It relates the internal stress in the fluid with the rate of deformation and deformation (in the case of a viscoelastic fluid) of a fluid element. The different types of constitutive equations will be described below, and they are, at their core, a set of increasingly more detailed representations of how the material experiences stress when subject to different flow conditions.

Viscoelastic fluids can be modelled by more complex constitutive equations which consider the flexible time dependent response of the media. The Oldroyd-B model is a multiscale constitutive model used to describe the flow of non-Newtonian fluids. It consists of two part with different scales. The models available can be of the Oldroyd-B type which follows a differential equation that augments the stress term shown in the Navier-Stokes equations described above so that:

$$T = \underbrace{T_1}_{Viscoelastic\ component} + \underbrace{T_2}_{Purely\ viscous\ component} \tag{3.6}$$

3.3.4 Interaction between the CFD model and simplified abrasion model

In this simulation, two different modules are running parallel and dynamically, one is the CFD module while the other is FSI module. This part is mainly contributing the Fluid-Structure Interaction modelling and simulation which predicts material removal rate possible. The CFD Module in this simulation provides the pressure distribution along the surface and the velocity of fluid media along the workpiece which is required in the calculation and prediction of material removal by Simplified Abrasion Model. On the other hand, the Simplified Abrasion Model also need to provide the material removal along the workpiece surface for CFD Module to update the profile of blade surface. With this type of communication between two models, it can predict the material removal and surface profile with process time on manufacturing.

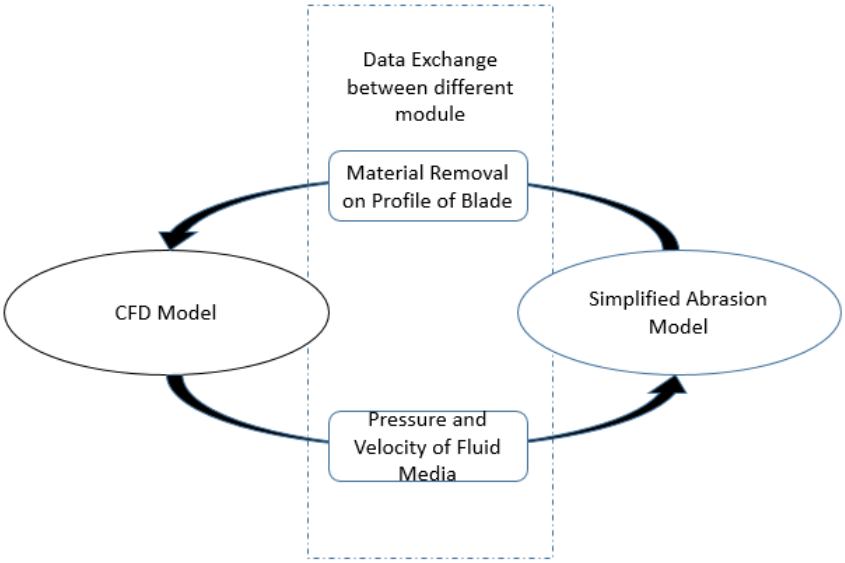

Figure 3.9 The interaction between the CFD Model and Abrasion Model

3.3.5 Micro-cutting mechanics model based on Hertz contact theory and Monte Carlo method

With the help of CFD based simulation and Abrasion Model it is possible to simulate the surface roughness and even the surface texture of Abrasive Flow Machining. Since the pressure and velocity distribution of fluid can be predicted by the CFD module, it

is necessary to find out a model to predict the micro-cutting mechanics on the surface with the grain properties. There are two part in this model which contains the generation of the grains and the cutting model of each grain.

In this model the grains need to be generated randomly but follows the statistic distribution of the grains in real fluid media. There are two factors from the shape of grains influence the cutting model for grains: diameter and shape factor. Shape factor is an index brought out by Desale, which aims to describe how sharp the grain is. Desale showed the effect of shape of particles on erosive wear in their experimental work [95]. They selected three erodent particles with different materials but the same size and determined their shape factor (SF). The definition of shape factor is shown in equation (5.15) in Chapter 5.

The grain in this model is generated with following method which aims to have the similar shape factor with the real grains. At first it will generate a sphere with the same diameter of the grain. Then this program will add some points on the edge of the sphere and link all these points to generate a grain with random shape. After the generation the program will calculate the shape factor of this grain to see if it is higher or lower than the required shape factor. If it is lower, the program will add more points on the surface of the sphere. On the other hand, if the shape factor is too high, the program will remove small amount of points from the surface to make the shape factor of generated grain lower. With several cycles the grains will be generated and follows the distribution we want to simulate the polishing process. The flow chart of this method is shown in Figure 3.10, while the simple result of one grain shown in Figure 5.5.

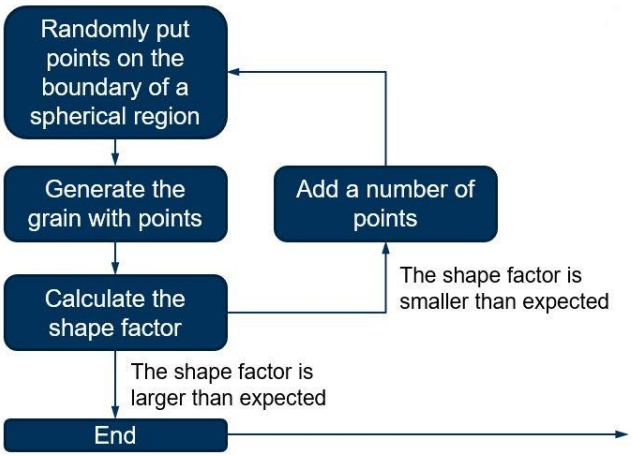

Figure 3.10 Flow chart for the generation of grains

After the generation of grains, it is important to find out a method to describe how the grains are cutting on the surface with their unique shape. In Abrasive Flow Machining process, each grain is more like rolling on the surface and the depth of cutting is changing while different corner of the grain is pressing on the surface. From the help of Hertz contact equation, it is possible to derive the depth of cutting in the situation shown in Figure 3.11. From Figure 3.11 it is possible to find out the relation between cutting depth and radius of grain with equation (3.7). On the other hand, in Abrasive Flow Machining the Force in Hertz contact theory is influenced by the pressure in the fluid and contact area between grains and the surface of workpiece. The Hertz contact equation (3.5) can be derived to equation (3.8) for Abrasive Flow Machining process. With the help of equation (3.7) and equation (3.8), the link between depth and angle of corner can be derived into equation (3.19).

$$\frac{\boldsymbol{d} \times \boldsymbol{cot\alpha} + \boldsymbol{d} \times \mathbf{cot}(\boldsymbol{\pi} - \boldsymbol{\alpha} - \boldsymbol{\beta})}{\mathbf{2}} = \boldsymbol{r} \tag{3.7}$$

$$d = 1.55 \times \sqrt[3]{\frac{P^2 \cdot A^2}{2RpE_m^2}} \tag{3.8}$$

$$d = \frac{32RpE_m^2}{3.724P^2\pi^2[cot\alpha - \cot(\alpha + \beta)]^4} \quad (3.9)$$

In these equations, Rp represents the radius of grains, E_m represents the Young's Modulus of workpiece, P represents the pressure from Fluid, α represents the angle between the grain and the surface and β represents the angle of the corner which is pressing the surface now from the grain.

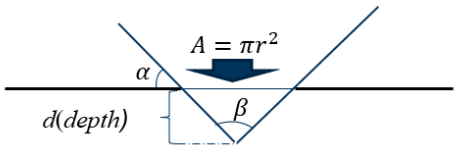

Figure 3.11 Schematic diagram of the calculation of cutting depth with one corner from the grains

After the generation of random grains, the angle of corners from each grain can be transferred into the cutting depth curve of each grain. The example of cutting depth with one grain is shown in Figure 3.11. With the angle of the corner and the distance between each corner from the grain, it is possible to simulate the generation of surface texture with the accumulate of cutting depth of each random generated grain. CFD module can provide the position of these grains during the whole cutting process as illustrated in Figure 3.12. In Figure 3.12, the y-axis means the cutting depth of grains.

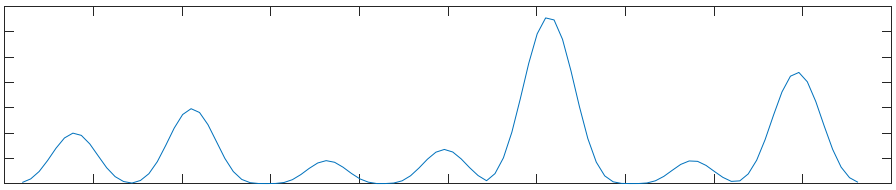

Figure 3.12 The cutting depth of one grain generated randomly

3.3.6 Simulation setup and results from validation trials

The manufacturing process parameters are listed in Table 3.2 which uses equations to calculate different values when requested by the software.

Table 3.2 Additional parameters and variables for simulation

Name	Expression	Name	Expression
Total Processing Volume (V)	60e-3 [m^3]	Processing time	V/Q
First Cycle Volume (V1)	2e-3 [m^3]	Inlet speed	Q/(pi/4*D^2)
Back Pressure	3.23 [MPa]	Abrasion coefficient 1	20.75e-6 [(m/m^3)/(1/s)]
Target Extrusion Pressure	6.1 [MPa]	Abrasion coefficient 2	8.36e-6 [(m/m^3)/(1/s)]
Flowrate (Q)	16.4e-6 [m^3/s]		

Additionally, the simulation requires validation from the manufacturing data of further AFM trials. The AFM trials were conducted on a specially designed fixture which attempts to replicate the flow condition present in a segment part from an IBR; the installation is shown in 3D CAD model in Figure 3.13. The geometry was converted through the addition of the cylinder geometry and Boolean operations into the fluid domain in Figure 3.14. The details of this simulation and experiment result will be presented in Chapter 7. More details of this experiment related to IBR segment will be presented in Chapter 7.

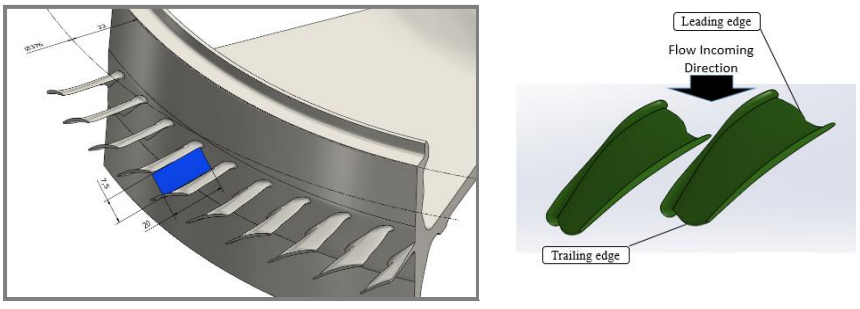

Figure 3.13 Representative flow restriction in AFM processing of IBRs

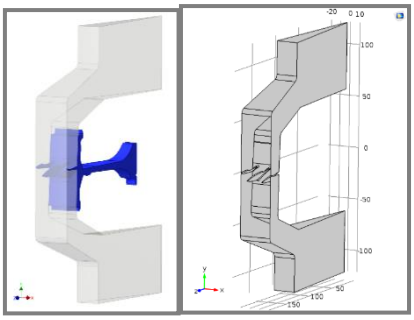

Figure 3.14 Fluid domain used in IBR geometry simulation (fluid domain in grey, while IBR section in blue)

3.4 Simulation results, analysis and discussion

3.4.1 Simulation on material removal rate of the blade surface.

The experimental trials provide more data to test the simulation model against, the conditions for the coupon with the highest material removal were simulated first. To check if the abrasion coefficients obtained independently from these tests could be used to predict the process response, they were left unmodified for this simulation, the simulated shear rate field and the material removal results in thickness shown in Figure 3.15.

The simulation could predict the resulting profile with reasonable accuracy; it is good enough that if such a prediction can be made before processing a single part, engineers could reduce the number of tests required when developing new components with the process.

3.4.2 Simulation on the accuracy control of the blade edge profile.

The rotors processed by AFM are commonly made of Inconel 718 or Ti-6Al-4V alloys. Currently, it is necessary to do some more investigation on calculating the abrasion constants for that material/media combination. The abrasion constants are derived from the real manufacturing data of IBR in ITP. Furthermore, the post AFM geometry

is measured on a point-by-point basis with no actual digital profiles available to enable a comparison, even if the profiles were routinely captured by the manufacturer, obtaining the information for academic research could prove very difficult due to the confidentiality policy.

In Figure 3.15, the predicted shear rate around the IBR profile suggests that material removal will not be uniform across along the profile. The location of the points with higher abrasion corresponds to the most repeated AFM principle: abrasion occurs at the point where media enters the point of higher restriction, with almost no abrasion present on the leading side of the low-pressure face (top) and the trailing side of the high-pressure face (bottom).

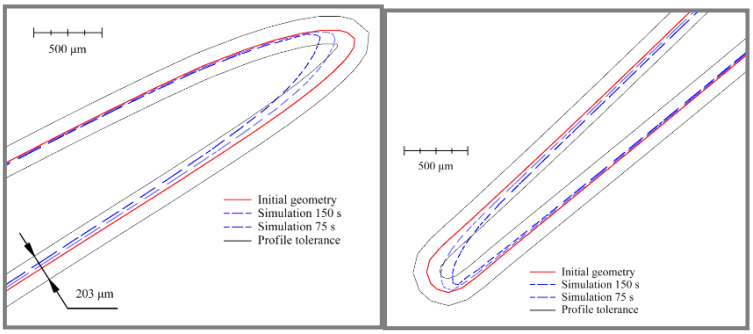

Figure 3.15 Simulated leading edge and trailing edge profiles

The results of simulation shine some light on the relative importance of the different input parameters involved in AFM. From the analysis of experimental trials, Volume (V) and Media (M) consistently created the largest difference in system response, with the volume being straightforward to modify, it should be the go-to parameter for tuning a process. Media is much harder to adjust as companies that use AFM for IBR processes will likely require prohibitively large batches for testing before switching media.

The development of the multiscale multi-physics modelling and simulation provides a convenient method for predicting the material removal of Abrasive Flow Machining and the optimise the production process of Abrasive Flow Machining.

3.4.3 Simulation of the blade surface generation.

The multiphysics simulation based on COMSOL provides a lot of information for the mechanical modelling, which ultimately aims to predict and control the generation of the surface roughness and surface texture in this doctoral project. Since the function of COMSOL is limited, it is necessary to develop MATLAB codes to enhance the function in COMSOL and provide the prediction of surface roughness efficiently and effectively. The MATLAB enhanced module in this simulation is further described below.

The user defined MATLAB coding is mainly developed on the contribution of mechanism model and Monto Carlo method and the source data from the CFD simulation based on COMSOL. The pressure along the surface and velocity of fluid media is simulated by COMSOL and import into the mechanism model. After the generation of grains in the specific range of sharp factor, the grains are imported into the mechanism model and distributed into random position with initial velocity and pressure from CFD simulation to start the calculation of material removal by each grain. With the help of Monto Carlo simulation in MATLAB, these grains applied on the mechanism model simulation and contributes to the machining process by each of them.

In this MATLAB codes the data about pressure and velocity distribution of fluid media along the workpiece surface is imported from the simulation based on COMSOL as described before. The example of pressure distribution of fluid media is shown in Figure 5.10. With the help of pressure and velocity, the mechanism model can be applied to the random generated grains built from MATLAB to simulate the generation process of AFM along a small piece of workpiece surface as an example. With one single calculation, one line of wave will be generated with the result of mechanism model which represents the cutting depth through this whole line with one grain. With the help of Monto Carlo method, the calculation is done times after times randomly and the result will be accumulated on the selected part of the surface.

After the calculation process of MATLAB code, it is necessary to bring the result back to the simulation in COMSOL for further calculation. As the result shown in Figure 20, the surface texture is somehow shown in MATLAB format. With the LiveLink for

MATLAB and COMSOL these data can be communicated and updated at the same time. With this kind of help the simulation can stay at a better stage on the prediction accuracy on both surface roughness and material removal.

After the communication, the result of material removal will be sent back to COMSOL and the workpiece will change as the exact result from MATLAB to continue the simulation in the next cycle. It is also possible for COMSOL to read the surface roughness and profile accuracy through the connection between COMSOL and MATLAB which make this simulation more like a complete virtual AFM simulation.

3.5 Summary

From the case study discussed in chapter 7, there is still some promotion can be approved on improving the performance of this virtual AFM manufacturing system. First is the part of the micro scale. At this stage, the simulation can only predict the material removal and edge profile on a macro level. It is necessary and significant for the simulation to work on the surface generation part on a micro level. In this way, the surface roughness and edge profile accuracy can be predicted, and it will be significant for further research and manufacturing. On the other hand, it is also useful to involve the heat transfer model in the simulation to provide the possible variation in temperature. The temperature will influence the material removal rate and surface quality. It will be meaningful to involve the heat by the process of simulation to increase the accuracy of prediction.

In the future, the multiscale multi-physics modelling and simulation can also provide the prediction and optimization for different types of industrial cases. It can be used in the simulation of many new non-traditional machining to provide the optimisation purpose. Many non-traditional machining cannot be simulated in the old methods because of the complicated machining process with more than three physical fields which influence each other during the whole process. With the help of multiscale multi-physics simulation, it can be more predictable and convenient for the manufacturer to adopt a new type of non-traditional machining. This point is significant in the manufacturing of aerofoil structures and components

The multiscale multi-physics modelling and simulation is a critical methodology in the future. It can dramatically improve the feasibility and accuracy comparing to the model based on one single scale and physical field [97,98]. In this chapter, some models on different scales and physical areas are brought out for further discussion. In the following chapters, some models with the coupling of different levels and physical fields are introduced and discussed. With some examples of combination among various scales and physical areas, the advantages of multiscale multi-physics modelling and simulation emerge. The possibility of virtual manufacturing system based on multiscale multi-physics simulation is shown in this methodology of research. The virtual manufacturing system should include many different scales and physical fields to improve the accuracy. With the study cases introduced and discussed in Chapter 7, multiscale multiphysics modelling and simulation are used to optimise the industrial manufacturing process. The possibility and advantages of this method have been proved. It was indicated that a multiscale multi-physics modelling and simulation are very useful, and it is significant to improve more different coupling with different physical fields on various scales.

Chapter 4 Modelling and simulation of material removal rates in Abrasive Flow Machining

4.1 Introduction

In Chapter 3, the methodology about abrasion model and how to predict the material removal in Abrasive Flow Machining is briefly described. With the help of CFD module and FSI function in COMSOL, the foundation of abrasion model is provided. In this chapter, the understanding of fundamental cutting mechanics and the application of the governing equation on AFM will be introduced. The improved Preston equation is introduced here to play the essential role as the governing equation in AFM process simulation and provides the ability to predict the material removal rate in AFM process. As discussed in Chapter 2, CFD simulations and other various complex numerical approach has been widely applied to AFM previously. This chapter discusses the development of simple industrially feasible equation applicable to the prediction of material removal rate in AFM processes. Furthermore, this section also discusses the methodology to validate the derived modified Preston equation experimentally with the details of the experiment described in Chapter 7.

4.2 Improved Preston Equation for modelling material removal rates in Abrasive Flow Machining

Chemical – mechanical polishing (CMP) also known as chemical – mechanical planarization is a process used in semiconductor manufacturing industry to give the desired surface finish. The process is complicated and remains un-optimised because the fundamental understanding of science behind the process is little known. As the research pushes the boundary of understanding, CMP is becoming helpful in production of silicon wafers.

Material removal from the surface of the wafers occurs due to microscale and nanoscale interaction between the pad and wafer going through the kinetics of

abrasion with abrasives to cool the surface. This kinetics and dynamics control the output parameters such as material removal, surface planarity and surface directivity [111].

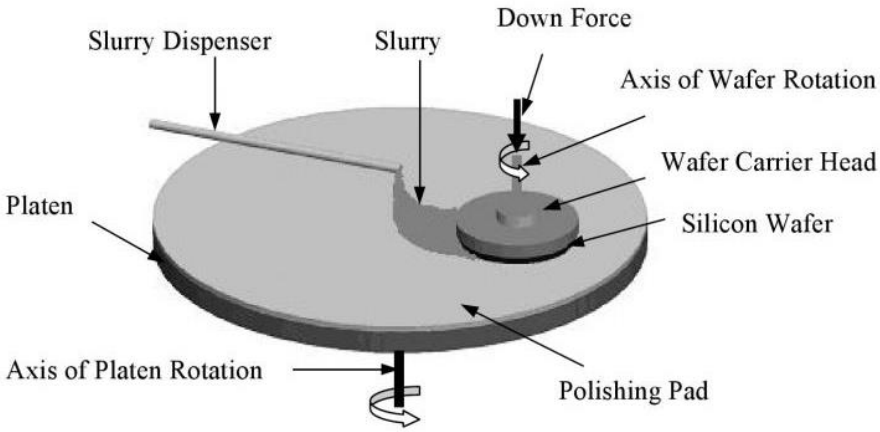

Figure 4.1 Schematic of CMP process [111]

The process is extremely difficult to grasp because of too many input variables. In addition, the time dependant process like this gives rise to wear of the tool causing challenges in the research. One such well known model is Preston Equation derived in 1927, which states that the material removal rate from surface, per unit time, is proportional to the product of the polishing velocity and pressure. The equation is expressed mathematically [111]:

$$MRR = K_p \times P \times v \tag{4.1}$$

where,

MRR - material removal rate

P - normal pressure applied on the polishing pad

v - relative velocity between the pad and wafer

K_p - empirically determined constant known as Preston co-efficient.

Preston equation successfully predicts the material removal for silicon dioxide polishing and moderately predicts for metal polishing. Figure 4.2 shows the example application of copper polishing for which Preston co-efficient being determined.

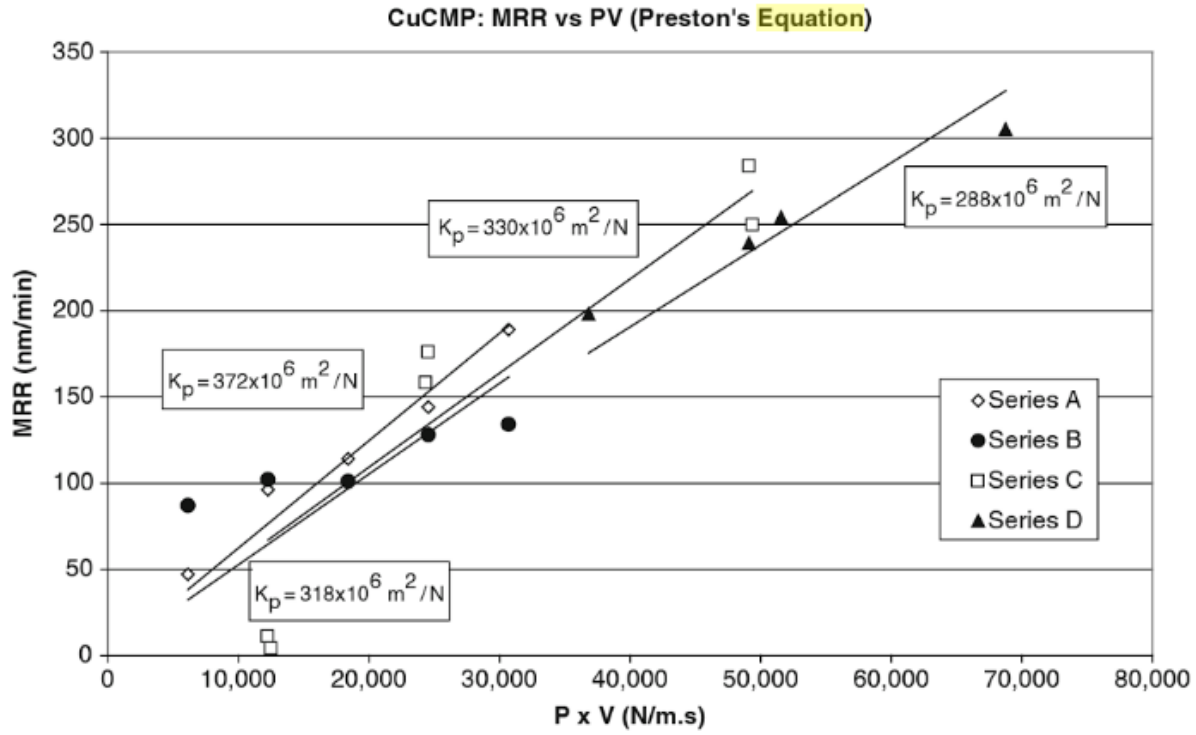

Figure 4.2 Graph showing the application of Preston equation on polishing rate of copper against the product of pressure and velocity [112]

As the equation suggests linear relationship, when $P \times v = 0$, MRR should be zero, which is not true observing from the data on the graph above. Operators performing the machining suggests that this could be due to chemical reaction between slurry and polished surface. To include this unexplained behaviour mathematically Preston equation is modified as follows:

$$MRR = (KaP + B)v + R_c \tag{4.2}$$

where, Ka and B are experimental constants and R_c represents the initial removal rate when $P = 0$ and $v = 0$.

Preston Equation has been modified previously for various applications in machining. In this chapter, an attempt to derive the modified Preston Equation for Abrasive Flow Machining is carried out.

4.2.1 Key factors and process variables

While considering the cutting mechanics, various process variables must be considered to carefully derive the effecting equation or mathematical model from estimating the material removal. The following factors and variables are considered in the equation derivation as constant or variables:

- Viscosity
- Flow rate
- Pressure
- New/ old media
- Material properties such as hardness
- Grit size
- Proportion of grit to polymer
- Temperature
- Volume

As shown in Figure 4.3, the process variables, such as the abrasive size, abrasive hardness, extrusion pressure and properties of carrier (which is a polymer-bound with the abrasive grits), need to be considered significantly. The studies so far show that only viscosity improves the surface finish as a significant parameter. The relationship between the initial surface finish and percentage improvement in the surface finish is non-linear. The findings also indicate that improved surface finish is achieved at higher extrusion pressure and the concentration of abrasive grit mainly contributes to material removal [113].

4.2.2 Derivation and assumptions made to reach the final equation

The media for abrasive flow machining is made of 32 grit which translates to 530-microns average diameter, for abrasion with viscous material and lubrication. To model this fluid as mechanical behaviour, an assumption is made that each grit is connected to a spring and a damper, as shown in the diagram of Figure 4.3.

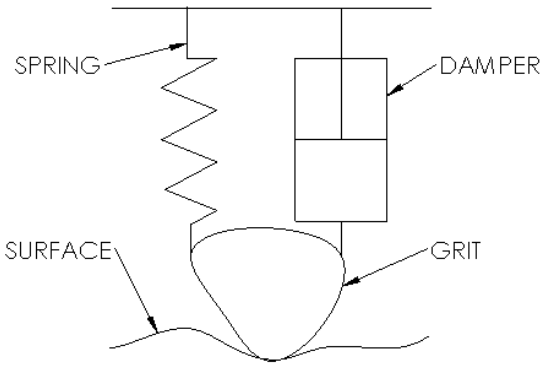

Figure 4.3 Viscosity modelled with spring and damper attached to an abrasive grit

The spring is to model the stiffness of the fluid and damper to model the viscosity.

$$F_s = k \times x \tag{4.3}$$

where, k = stiffness; x = extension of distance between the tip of the grit which is performing the cutting action and viscous media on top of it; and F_s is the force applied by the piston on the media as felt by grit.

$$F_d = C \frac{dx}{dt} \tag{4.4}$$

where, C = viscosity co-efficient; $\frac{dx}{dt}$ = velocity of the grit; and F_d = damping force of the media.

“Research on wear of metals”, paper written in 1960 by Khrushchov and Bavichov identified two processes which plays a role of abrasion when abrasive media comes in contact with the work piece. First, all abrasive grains or particles do not contribute in material removal but plastically deforms the work piece by creating micro grooves. Second, repetitive abrasive action by the grains causes the material to form micro-chips.

The rubbing action and chip formation depends on the shape of abrasive particles. Comparing a lot of studies through literature, spherical particles are observed to contribute more chip formation when indentation strain (defined as the depth of indentation divided by the diameter of the indenter) exceeds a certain value [114]. Hence, in AFM the interaction between the abrasive particles and the workpiece can be separated in two categories, micro ploughing and micro-cutting.

In this dissertation, it is assumed that all particles flowing in AFM are spherical. The force on this particle in order to create the indentation can be found by using $Force = Pressure \times Area$. Area is worked out using the model of the particle, as illustrated in Figure 4.4. In Figure 4.4 and Equation (4.5), R represents the radius of grains, d represents the cutting depth while L represents the radius of contact area.

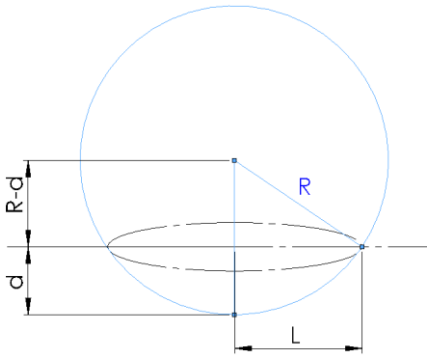

Figure 4.4 Area occupied by the grit due to indentation

$$R^2 = (R - d)^2 + L^2 \tag{4.5}$$

$$A = \pi \times L^2 \tag{4.6}$$

4.3 Evaluation and validation of the Equation by simulations and experimental trials

The set-up of simulations and experimental trials for the evaluation and validation are shown in Figure 4.5, Figure4.6 and Figure 4.7. It is impossible to find the area of indentation created by the particle on the work piece in real time. Therefore, an assumption was made that all particles are uniformly distributed throughout the viscous fluid and a simulation is created in COMSOL by Rodrigo Merlo to simulate the AFM process for two different constant flow rates. The simulation was set up according to the experimental trial carried out in Extrude Hone Ltd. Through this simulation an

average pressure is calculated for each flow rate: 16.4 ml/s with 4.12 MPa and 32.8 ml/s with 4.50 MPa.

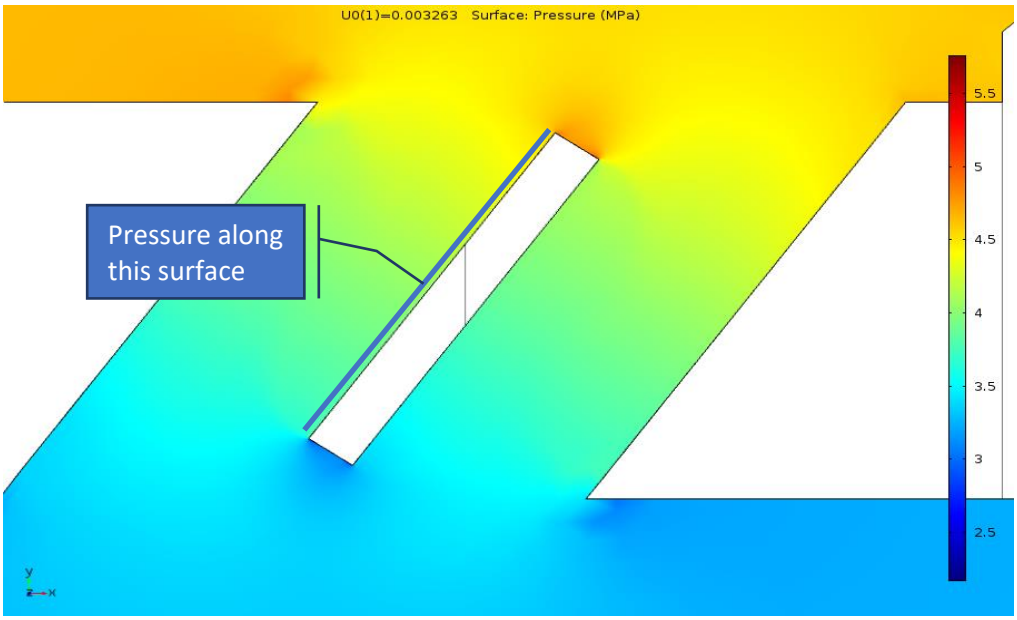

Figure 4.5 Simulation to find the pressure on coupon along the surface.

Ideally, it is necessary to find all the forces on the grit and how much ploughing is occurring during the abrasion but in real time this is impossible to achieve. Hence, force can be worked out by using the pressure from the simulation and area is worked out from the dimension of coupon which is $16mm \times (25 - 5.08)\, mm$. The area covered by the fixture is excluded. So, using $F = P \times A$ average force on the surface of the coupon can be calculated.

Through the experimental trials in AFM, it is confirmed that material removal is dependent on time as the viscous fluid passes through the work piece. The trials were only done between the processing volume of 10 litres and 30 litres and hence assuming that material removal and time relationship is linear between those volumes. Also, through the cutting mechanics it is found that force is proportional to the amount of material removed and Preston equation suggests that velocity of the media flow is proportional to material removal too.

Thus, the modified Preston equation for AFM looks as follows:

$$\int \frac{d\,MR}{dt} dt = \int (K_m \times K_t \times P \times A \times v\,) dt \tag{4.7}$$

Therefore,

$$MR = K_m \times K_t \times P \times A \times v \times t \tag{4.8}$$

MR - material removal

K_m - media constant

K_t - time constant

P - pressure

A - area

v - flow rate

t - time

This equation was put to test by the data collected during the experimental trials carried at Extrude Hone Ltd (further explanation of the experiment is explained in Chapter 7). Trials were carried by flow two different viscosity materials on a mild steel coupon to observe the material removal by measuring mass before and after. Using the density of mild steel and mass of the coupon, difference in volume was calculated initially to get an idea of material removal. For each run of the experimental trials a process time was noted from the machine to work out the material removal rate. The process time shown by the machine includes an idle time when machine is calculating pressures to maintain flow rate, so the time is very close estimate. This data is shown in Table 4.1 and Table 4.2 below. For the test of equation constant K_t is kept at 1 and constant K_m is calculated for each run by dividing the material removal by all the other variables.

$$K_m = \frac{MR}{K_t \times P \times A \times v \times t} \tag{4.9}$$

Average K_m value for each 4 runs classified by their media viscosity and age are calculated. This average is divided by K_m value for each run to observe how far the average is from the experimental value under different machining parameters. The experimental setup and results are further discussed in Chapter 7.

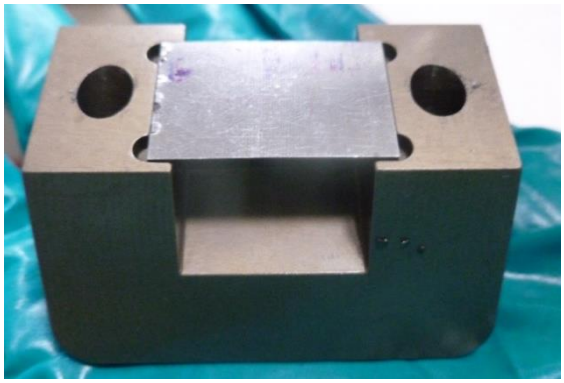

Figure 4.6 Coupon placed within the block of fixture

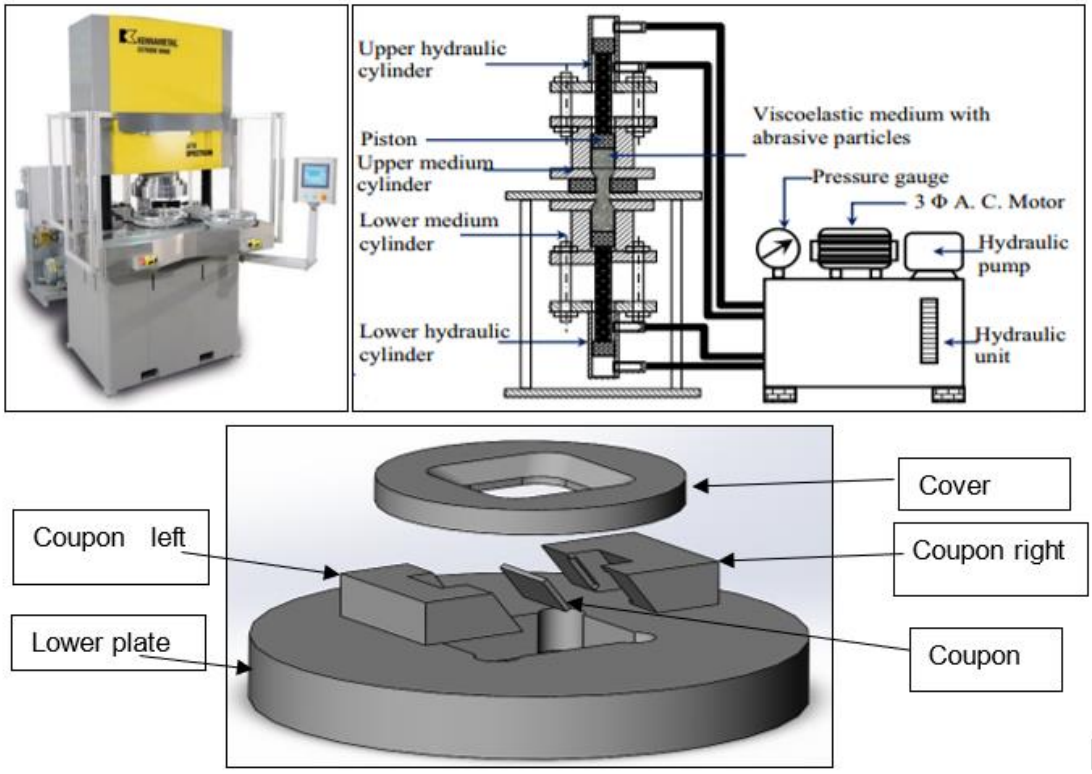

Figure 4.7 AFM machine (top left); working schematics (top right); undergoing coupon with fixture for experimental trials (bottom)

4.4 Analysis of the results from experimental trials

All the process variables are still required to link to media constant Kp, which should have the unit of 1/N. Otherwise, the equation has to be modified as units has to be consistent with quantities.

$$K_p = \frac{MR}{P \times A \times v \times t} \tag{4.10}$$

Figure 4.8 shows all the Kp value corresponding to each run. This shows that the value of constant decreases as media becomes older. For example, new media (blue) D100 yielded Kp = 8.86×10^{-11} and drops to 4.86×10^{-11} because of the media becomes old (grey), suggesting that media constant is dependent on the age of the material. During machining of AFM, every 200 hours of media being used 25% to 40% are replenished with the new media. This media constant could be further calibrated to help the company understand how the age of the media contributes to material removal to control the form accuracy on the integrally bladed rotor (IBR).

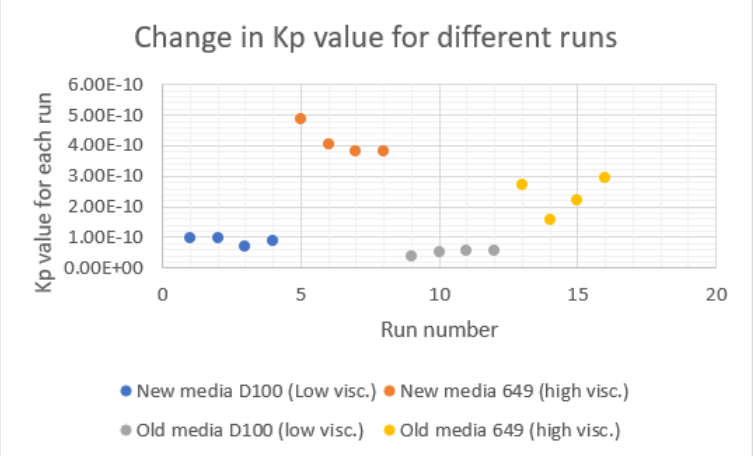

Figure 4.8 Graph showing the change in Kp values for two different kinds of media with their respective age

Also, higher viscosity has a higher value of Kp and reduces by about half as the media becomes older. For example, new media (orange) 649 has an average Kp value of 4.15×10^{-10} and drops to 2.36×10^{-10} as the media becomes older (yellow).

Hence, two significant conclusions could be made regarding the media constant Kp.

Higher viscosity values have higher value of Kp and the Kp value drops as media wears out.

These could be calibrated further with more experimental trials to further validation. Table 4.1 illustrates the calculation of material removal for the improved Preston Equation in a spreadsheet tool. Table 4.2 highlights the determination of media constant Kp through both theoretical analysis and experiments.

4.5 Summary

With the analysis of the results from experiments, the improved Preston equation throws some light on the prediction of material removal of the AFM process. The improved Preston equation is used as a model in the AFM simulation, which aims to predict the material removal on the manufacturing of the integrally bladed rotor (IBR) and other relative aerofoil structures. In this project, the simulation provides the prediction of the material removal rate and profile control under different operating conditions, which successfully decreases the cost by optimising the AFM process.

In this chapter, an improved Preston equation is developed and introduced to solve the prediction of material removal of the AFM process. The development of the improved Preston equation provides a convenient means of predicting the material removal of Abrasive Flow Machining with different operating conditions. With theoretical and experimental considerations, flow rate and pressure of the abrasive fluid have been adopted as main factors in this equation.

The experimental trials show the material removal and surface roughness results of Abrasive Flow Machining with different working conditions. It provides a general consideration that the working pressure and grit size of the abrasive fluid media influences more on the result of machining.

The experimental trials and theoretical analysis shows that the tendency and result of the improved Preston Equation are acceptable and significant in the present study. In chapter 7, details of simulation with the prediction of material removal with more

experimental data supported with different abrasive fluid media and working experiments are given and analysed theoretically.

Table 4.1: Calculation of material removal for the improved Preston Equation

Run	Coupon number	Flow rate (ml/s)	Viscosity	Media	Volume (L)	Mass before AFM(g)	Mass after AFM (g)	Density (kg/m^3)	Volume before (m^3)	Volume after (m^3)
0	1					6.504	6.116	7860	8.275E-07	7.781E-07
1	2	16.4	Low	New	10	6.357	6.336	7860	8.088E-07	8.061E-07
2	3	32.8	Low	New	30	6.284	6.217	7860	7.995E-07	7.910E-07
3	4	32.8	Low	New	10	6.495	6.476	7860	8.263E-07	8.239E-07
4	5	16.4	Low	New	30	6.353	6.297	7860	8.083E-07	8.011E-07
5	6	16.4	High	New	30	6.497	6.180	7860	8.266E-07	7.863E-07
6	7	16.4	High	New	10	6.334	6.244	7860	8.059E-07	7.944E-07
7	8	32.8	High	New	10	6.483	6.383	7860	8.248E-07	8.121E-07
8	9	32.8	High	New	30	6.506	6.227	7860	8.277E-07	7.922E-07
9	10	32.8	Low	Old	10	6.495	6.486	7860	8.263E-07	8.252E-07
10	11	16.4	Low	Old	30	6.301	6.270	7860	8.017E-07	7.977E-07
11	12	16.4	Low	Old	10	6.479	6.479	7860	8.243E-07	8.243E-07
12	13	32.8	Low	Old	30	6.332	6.295	7860	8.056E-07	8.009E-07
13	14	32.8	High	Old	10	6.471	6.404	7860	8.233E-07	8.148E-07
14	15	16.4	High	Old	10	6.269	6.235	7860	7.976E-07	7.933E-07
15	16	16.4	High	Old	30	6.505	6.362	7860	8.276E-07	8.094E-07
16	17	32.8	High	Old	30	6.452	6.241	7860	8.209E-07	7.940E-07

Table 4.2: Determination of the media constant Kp through analytical analysis and experiment

Run	Coupon number	Material removed (m^3)	Process time (sec)	Material Removal Rate (m^3/s)	Pressure (Pa)	Area (m^2)	Flow rate (m^3/s)	Kp	Average Kp for section	Kp/ average Kp
1	2	2.672E-09	1283	2.082E-12	4.12E+06	3.19E-04	1.64E-05	9.66E-11	8.86E-11	1.1
2	3	8.524E-09	1872	4.554E-12	4.50E+06	3.19E-04	3.28E-05	9.67E-11		1.1
3	4	2.417E-09	714	3.386E-12	4.50E+06	3.19E-04	3.28E-05	7.19E-11		0.8
4	5	7.125E-09	3702	1.925E-12	4.12E+06	3.19E-04	1.64E-05	8.93E-11		1.0
5	6	4.033E-08	3826	1.054E-11	4.12E+06	3.19E-04	1.64E-05	4.89E-10	4.15E-10	1.2
6	7	1.145E-08	1314	8.714E-12	4.12E+06	3.19E-04	1.64E-05	4.04E-10		1.0
7	8	1.272E-08	705	1.805E-11	4.50E+06	3.19E-04	3.28E-05	3.83E-10		0.9
8	9	3.550E-08	1966	1.806E-11	4.50E+06	3.19E-04	3.28E-05	3.83E-10		0.9
9	10	1.145E-09	629	1.820E-12	4.50E+06	3.19E-04	3.28E-05	3.87E-11	5.01E-11	0.8
10	11	3.944E-09	3660	1.078E-12	4.12E+06	3.19E-04	1.64E-05	5.00E-11		1.0
11	12	1.587E-09	1348	1.177E-12	4.12E+06	3.19E-04	1.64E-05	5.46E-11		1.1
12	13	4.707E-09	1750	2.690E-12	4.50E+06	3.19E-04	3.28E-05	5.71E-11		1.2
13	14	8.524E-09	671	1.270E-11	4.50E+06	3.19E-04	3.28E-05	2.70E-10	2.36E-10	1.1
14	15	4.326E-09	1271	3.403E-12	4.12E+06	3.19E-04	1.64E-05	1.58E-10		0.7
15	16	1.819E-08	3794	4.795E-12	4.12E+06	3.19E-04	1.64E-05	2.22E-10		0.9
16	17	2.684E-08	1931	1.390E-11	4.50E+06	3.19E-04	3.28E-05	2.95E-10		1.2

Chapter 5 Micro-cutting mechanics and surface generation in Abrasive Flow Machining

5.1 Introduction

There is substantial research work on the AFM simulation development, but most of them are focused on the CFD simulation of the process and the abrasive behaviour of the media [115-122]. However, the modelling and simulation of AFM processes as developed have some limitations, and many challenges need to be addressed further particularly on the prediction and control of the surface generation and topographical profile accuracy of the component. One of the challenges is the characterisation of the abrasive media and their complex dynamic behavior, known as viscoelastic, in the process. The other one is how to monitor the surface texture generation process in microscale. The tribology modelling method for the abrasive fluid media and the process are required for developing the scientific understanding of the AFM process both qualitatively and quantitatively, which is essentially important in developing the simulation of AFM processes

In this chapter, micro-cutting mechanics modelling intergraded with Monte Carlo (MC) algorithms/simulation is presented attempting to obtain scientific understanding of the intrinsic AFM process. The integrated modelling and simulation are developed in COMSOL-MATLAB integrated computational environment including its CFD and MATLAB user-defined modules. With the simulation, the surface roughness, topographical profile accuracy and the material removal of the blade component can be predicted, which are further evaluated and validated by using real production data provided by industrial partners.

5.2 Micro-cutting mechanics: modelling and analysis

5.2.1 Methodology for the modelling and simulation

In Abrasive flow machining, it is also essential to simulate the machined surface generation. In the multiscale model it can be divided in two parts, one is the CFD module and the other one is the micro-cutting mechanics modelling. The CFD module can simulate the media flow and provide the required specification for the micro-cutting mechanics model. The Micro cutting mechanics model is built on the mechanics for one grain and with the help of Monte Carlo Algorithm the simulation can simulate the accumulation of mass of grains in the flow. With this combination, the surface generation can be predicted by the simulation program.

In the first part, Multiphysics simulation based on Fluid-Structure Interaction (FSI) can be used to simulate the working environment configuration of viscoelastic fluid. As a readily available Multiphysics simulation tool integrated with CFD capability, COMSOL is used in this research to analyse the AFM media flow in an arbitrary geometry. The CFD modules in COMSOL make it possible to simulate the pressure distribution and shear rate on the surface of the IBR blade. With the appropriate setup of the simulation, the results of AFM process are produced and analysed in the controllable deviation. With previous work the prediction of Material removal and profile accuracy can be predicted with this simulation, it is possible to involve the mechanical model and predict the generation process of surface texture and predict the surface roughness based on the enhancement of MATLAB function codes.

In the next part, mechanical modelling will be introduced and involved in this simulation to predict the surface roughness and profile accuracy of AFM. It is necessary to build a user defined function in COMSOL to provide the simulation in micro scale which make the prediction of surface roughness possible. The MATLAB function in COMSOL is helpful to involve this micro mechanical physic model in. In this project the Micro cutting mechanics model is built on the mechanics for one grain and with the help of Monte Carlo Algorithm the simulation can be accumulated to mass of grains in the flow. With this combination the surface generation can be predicted by the simulation program.

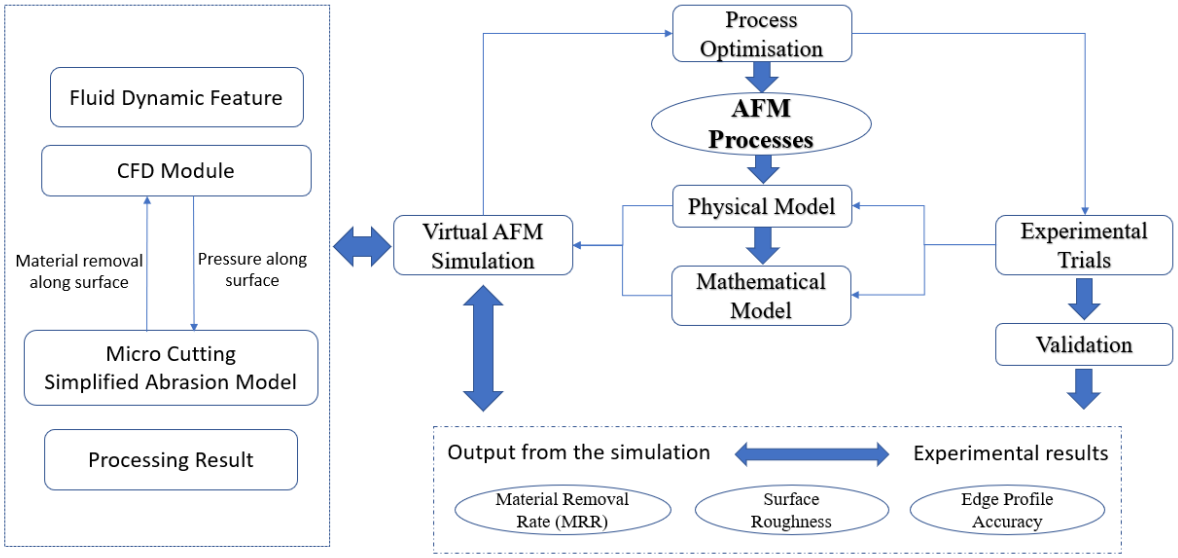

Figure 5.1 The architecture of the virtual AFM system and the associated development.

As illustrated in Figure 5.1, the simulation-based system is developed and evolved into an industrial feasible virtual AFM system for the process optimisation, and prediction and control of the blade profile accuracy and surface finishing. Currently, this project is still on-going with the prediction of surface roughness and surface texture as one of the ultimate goals of the simulation-based virtual machining system development.

5.2.2 CFD based modelling

From the introduction in the first part, it is necessary to build a CFD modelling environment to simulate the essential inputs for the mechanical modelling, such as distribution of abrasive grains, initial forces and so on. The modelling and simulation is based on multiscale modelling technique combining with multiphysics analysis by taking account of the AFM process nature and industrial production requirements of IBRs from the industrial partner. As a readily available multiphysics simulation tool integrated with CFD capability, COMSOL is used in this research to analyse the AFM media flow in an arbitrary geometry. The CFD modules in COMSOL make it possible to simulate the pressure distribution and shear rate on the surface of the IBR blade.

With the appropriate setup of the simulation, the results of AFM process are produced and analysed in the controllable deviation. As illustrated in Figure 5.1, the simulation based system is developed and evolved into an industrial feasible virtual AFM system for the process optimization, and prediction and control of the blade profile accuracy and surface finishing.

The CFD module computes multiple variations of the Navier-Stokes equations to model flows in all velocity regimes. This module in the simulation is used to model fluid flow numerically and solve the Navier-Stokes equations, with variations on the simplifying assumptions and constitutive models used for the internal stress related component.

Viscoelastic fluids can be modelled by more complex constitutive equations which consider the elastic time dependent response of the media. The Oldroyd-B model is a constitutive model used to describe the flow of viscoelastic fluids. The models available can be of the Oldroyd-B type which follow a differential equation that augments the stress term shown in the Navier-Stokes equations described above so that:

$$T = \underbrace{T_1}_{Viscoelastic\ component} + \underbrace{T_2}_{Purely\ viscous\ component} \tag{5.1}$$

5.2.3 Modelling enhancement by Monte Carlo method

Hertzian contact theory gives good estimation of contact between two bodies. The theory requires at least one of the body having circular shape, in this case the geometry of the abrasive particles is assumed to be perfectly spherical. Following assumptions need to be reinstated:

- The theory assumes very small strain occurring between two surfaces.
- The surfaces are continuous, smooth and nonconforming.
- Each solid can be considered as an elastic half-space in the proximity of the contact region.
- The contact is assumed to be frictionless.

Composite radius is defined as the radius of contact between the two surfaces, it is given by the formula:

$$\frac{1}{R} = \frac{1}{R1} + \frac{1}{R2} \tag{5.2}$$

R2 denotes the radius of the abrasive particles and in this research, the particle radii is assumed to be uniform across the carrier media. R1 denotes the radius of curvature for each individual peak along the surface, it is determined by the neighbouring height values along the X direction. For a relatively flat surface, the radius of curvature are given by numbers of large magnitude, as the surface becomes perfectly flat, the radius of curvature will theoretically approach infinity. Assuming the pressure acting on the second body is same as the first, composite of effective modulus can be defined as:

$$\frac{1}{E^*} = \frac{1 - {\nu_1}^2}{E1} + \frac{1 - {\nu_2}^2}{E2} \tag{5.3}$$

Based on these two parameters, the contact area and depth of indentation can be calculated according to following equations:

$$a = \frac{\pi p_0 R}{2E^*} \tag{5.4}$$

$$\delta = \frac{\pi p_0 a}{2E^*} \tag{5.5}$$

The term p_0 denotes the maximum pressure at the point of contact.

As AFM process is in many ways similar to the grinding process, Hertz theory can be applied in AFM process for similar estimation. According to Hertz, the contact area for elastic contact between the sphere profile and a flat surface can be evaluated from:

$$\bar{\sigma} = 0.41 \times \sqrt[3]{\frac{{F'}_{ng} {E_m}^2}{4R^2}} \tag{5.6}$$

E_m denotes the Young's modulus of elasticity of the work piece surface and R denotes the spherical radius. ${F'}_{ng}$ represents the normal force acting on the cutting tool. With this theory, the depth of indentation for elastic loading is given by:

$$d' = 1.55 \times \sqrt[3]{\frac{{F'_{ng}}^2}{2R{E_m}^2}} \tag{5.7}$$

In this equation the depth of cut by each grain can be solved numerically. With the help of Hertz contact theory described in Chapter 2, the machining process can be simulated with this modelling method.

5.3 Material removal and surface generation in Abrasive Flow Machining

5.3.1 Modelling of material removal

Abrasive Flow Machining is applied by scratching action with abrasive grains in the high viscosity fluid media. As discussed in part two, the normal force produced by the pressure of media will applied to a spherical grain which cause the grain to penetrate in the surface. After this penetration, a groove on the workpiece surface will be produced by grains and the profile of the grain will be produced on the surface [3]. With the grain translated horizontally or even deeper, it will remove material from the workpiece. An idealized classical model of abrasive wear brought out by Jain [4] provides a theoretical basis for the prediction of material removal by AFM process. Jain also evaluated it by accumulate number of active grains, the shape and depth of the groove produced can contributed to the volume of stock removal. It makes the material removal of AFM calculated and simulated roughly.

The assumptions adopted to this modelling of material removal by AFM process in Jain research [4] considered all the grains as the same shape and the load on each particle is constant and equal to the average load. It means in Jain's model the difference in grains and influence from the sharpness of each grain is not considered to cut the cost of calculation of simulation and provide a rough prediction of material removal by AFM process. The volumetric material removal in AFM is given as follows [4]:

$$V_i = 2\pi N l_s \frac{R_{mc}^2}{R_w}\left[\frac{d_g^2}{4} sin^{-1}\frac{2\sqrt{t(d_g - t)}}{d_g} - \sqrt{t(d_g - t)}\left(\frac{d_g}{2} - t\right)\right]L_i \quad (5.8)$$

In equation (5.9), N represents the number of abrasive grains simultaneously acting per unit area of contact. l_s is stroke length, R_{mc} is radius of media cylinder, R_w is radius of cylindrical workpiece, d_g is diameter of a spherical grain in this model, t represents the depth of indentation and L_i is the length of contact of grain with workpiece surface.

This equation has not considered the difference in grains and the Irregular roundness of grains which can only predict the material removal in macro scale. In the micro scale each grain should be considered in statistical methodology so that not only the accuracy of material removal but also the surface texture and profile accuracy can be predicted in better way. In this new type of model, the difference of grain will be involved, and the statistical model will be applied to make the surface closer to the real texture generated by the AFM process.

The abrasion model presented here is an example of how the flow simulation may be leveraged to produce data that can help an engineer predict the process response before first trials, reducing the amount of testing needed to develop a new part.

The idea has been explored in other works. One example that is cited as inspiration for this model development is the article published by Schmitt in 2006 [56], where the mesh was constantly deformed with a velocity proportional to the simulated shear rate value at the wall and produced the edge rounding effect as evidenced in the process. While another similar approach can be found in the doctoral dissertation by Howard in 2014 [55], in which the viscosity field resulting from CFD simulation was compared against the material removed in a point of interest. The biggest divergence from this approach is the use of the ALE model to continuously modify the geometry according to the changing flow field. Additionally:

- This model makes two main assumptions about the material removal in any given condition;
- The material removal is higher where the polymer slips faster against the wall and this occurs where the simulated velocity gradient (shear rate) is higher.

There are following assumptions after the simplification:

- Polymer slip velocity ∝ Simulated shear rate ∝ Material removal rate;
- The material removal rate is constant with respect to the processed volume, and may be estimated from two straight lines, one for the initial cycle where material removal is more aggressive, and another for subsequent cycles.

With the help of these two literatures, in this research two equations were brought out as one, which may lead an expression for the material removal as a function of both the processed volume and the shear rate:

$$MRR_v(V, \dot{\gamma}_{simulated}) \left[\frac{m}{m^3}\right] = K_{va}(V) \left[\frac{m}{m^3 \cdot s^{-1}}\right] \cdot \dot{\gamma}_{simulated}[s^{-1}] \tag{5.9}$$

$$K_{va}(V) = \begin{cases} K_{va1} & if\ V \leq V_1 \\ K_{va2} & if\ V > V_1 \end{cases} \tag{5.10}$$

Where MRR_v is the material removal rate by volume (i.e. for each cubic meter of processed media), $\dot{\gamma}_{simulated}$ is the shear rate at the wall obtained in simulation, K_{va1} and K_{va2} are proportionality constants which may be found by testing, which will depend on the media, abrasives and workpiece material used, V_1 is the volume of the initial cycle where material removal is more aggressive.

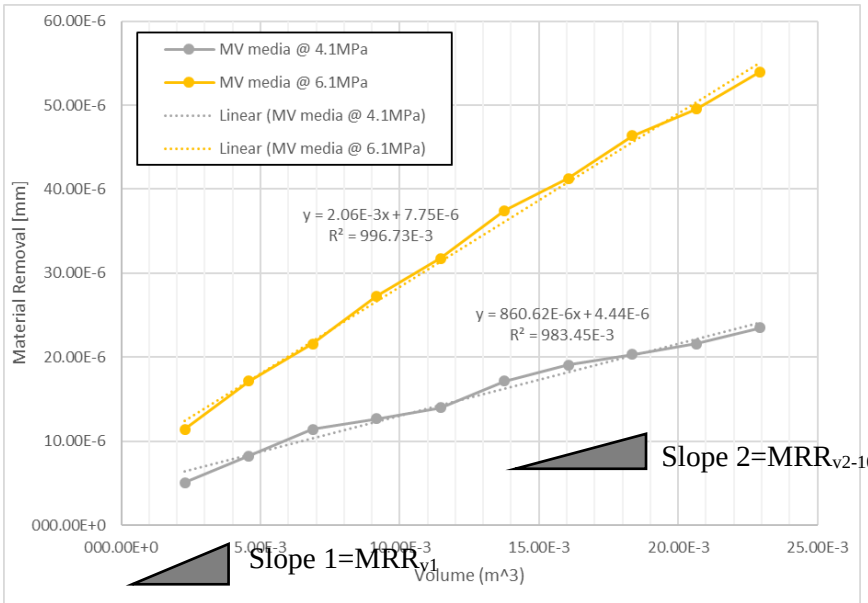

Figure 5.2 Abrasion coefficient determination data from Walliam's dissertation [26]

Another way to describe the equation is that the slope of the plot in Figure 5.2 using the experiment data in Walliam's dissertation (i.e. the material removal rate by volume MRR_v) is proportional to the shear rate at the wall, higher extrusion pressures produce a higher shear rate and consequently a steeper slope.

The procedure to determine the values for K_{va} consists of finding the removal rate on each cycle from the data and dividing it by the shear rate found by the steady state simulation of the initial geometry shown in Figure 5.3.

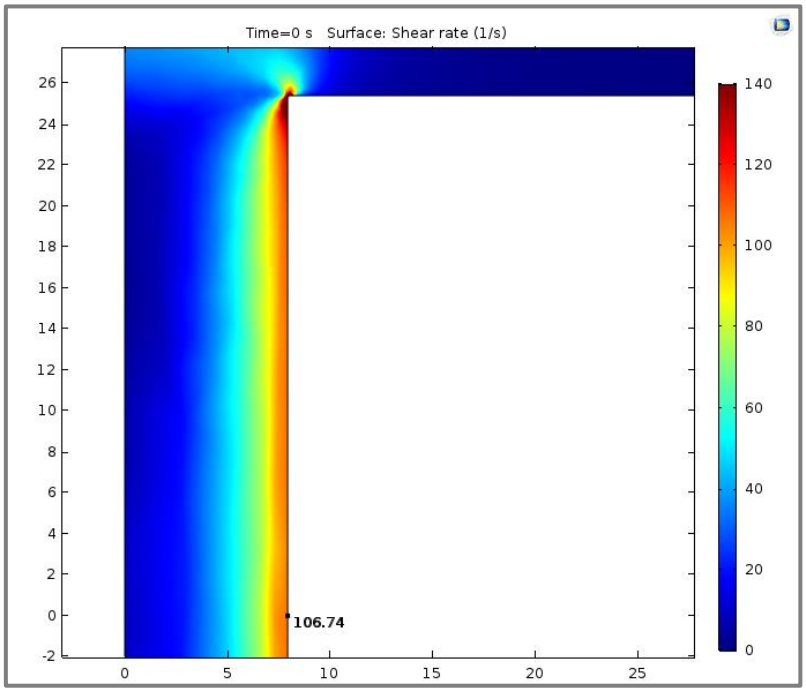

Figure 5.3 Shear rate at the wall simulated for Experiment 1 in COMSOL

The simulation was run with machine parameters $Q = 36\ \left[\frac{ml}{s}\right],\ D = 101.6\ [mm],\ V = 22.94\ [l], V1 = 2.294\ [l]$ which produce the pressure drop of 4.1 MPa measured during the experiment.

The shear rate at the point where the material removal was measured is $106.74\ [s^{-1}]$ extrusion pressure. Table 5.1 contains the MRR_v calculated for the first and subsequent cycles, the calculated abrasion coefficients are then:

$$K_{va1} = \frac{MRR_{v1}}{\dot{\gamma}_{simulated}} = \frac{2.214 \times 10^{-3}\left[\frac{m}{m^3}\right]}{106.74\ [s^{-1}]} = 20.75 \times 10^{-6}\left[\frac{m}{m^3 \cdot s^{-1}}\right] \tag{5.11}$$

$$K_{va2} = \frac{MRR_{v2-10}}{\dot{\gamma}_{simulated}} = \frac{891.94 \times 10^{-6} \left[\frac{m}{m^3}\right]}{106.74\ [s^{-1}]} = 8.36 \times 10^{-6} \left[\frac{m}{m^3 \cdot s^{-1}}\right] \quad (5.12)$$

These coefficients apply to media described by the author as “Medium Viscosity” with 70 grit SiC abrasive in a 66% concentration by weight and a Mild Steel part.

Table 5.1 Calculation of MRRv with data from Williams’s Experiment 1 [23]

Cycle	Extruded V $[m^3]$	Die Diameter $[mm]$	Die Radius $[mm]$	Total MR $[\mu m]$	DeltaV $[m^3 \times 10^{-3}]$	DeltaMR $[\mu m]$	MRRv [mm/m^3]
0	0	15.86	7.931	0	0	0	
1	2.29x10^{-3}	15.87	7.934	5.08	2.29	5.08	2.214
2	4.59x10^{-3}	15.87	7.935	8.26	2.29	3.18	1.384
3	6.88x10^{-3}	15.87	7.937	11.43	2.29	3.18	1.384
4	9.18x10^{-3}	15.88	7.938	12.70	2.29	1.27	0.554
5	11.47x10^{-3}	15.88	7.938	13.97	2.29	1.27	0.554
6	13.76x10^{-3}	15.88	7.940	17.15	2.29	3.18	1.384
7	16.06x10^{-3}	15.88	7.941	19.05	2.29	1.91	0.830
8	18.35x10^{-3}	15.88	7.941	20.32	2.29	1.27	0.554
9	20.65x10^{-3}	15.88	7.942	21.59	2.29	1.27	0.554
10	22.94x10^{-3}	15.89	7.943	23.50	2.29	1.91	0.830

To input this model into the moving mesh simulation, the displacement of the boundary needs to be programmed as a function of time not volume, the flow rate (Q) being pushed through the part is assumed constant so:

$$MRR_t \left[\frac{m}{s}\right] = Q \left[\frac{m^3}{s}\right] \cdot MRR_v \left[\frac{m}{m^3}\right] \quad (5.13)$$

The main strength of this model is that it may be used to predict the localized material removal within a part, in the case of the test geometry in Chapter 7, the edge radius

on each corner will be compared with the experimental findings, it the case of IBRs, it could be developed to predict the removal in the leading and trailing edges.

5.3.2 The evolution and regeneration of grains in the AFM process

Theoretically COMSOL@ Multiphysics software is capable of simulating surface roughness evolution during the AFM cycles, as surface roughness can be generated on the boundary surfaces as a function of randomly generated Gaussian pulses and moving mesh is capable of resolving displacement of the elements at scale of micrometres. However, the computation requires refined mesh not only at the edges but also, in the middle of the surface where elements are set to be coarse during current simulation. With regards to element size, the surface elements might require minimum element size smaller than 10 micrometres rendering problem too large to solve for current computational capacity. The use of MATLAB generated code for analysis of surface roughness evolution based on surface contact theory is attempted in this part of the research and the results generated will be compared with the experimental data as demonstrated in the next chapter.

In the first step it is necessary to identify the difference between each type of grains. The properties of solid particles such as size, shape, density, and hardness have significant influence on slurry erosive. To have better understanding of the influence of these individual parameters, the effect of each particle property on erosion needs to be studied separately. Several works have been carried out to measure the effect of individual properties on wear rate. The shape of the erosive particles is one of the parameters that affect erosive wear, but its effects are difficult to quantify. The shape of the erosive particles is one of the parameters that affect erosive wear, but its effect is difficult to quantify.

The system to measure the shape of the particles is to study the Shape Factor of them. Desale showed the effect of shape of particles on erosive wear in their experimental work [16]. They selected three different materials with the same size as erodent particles and determined their shape factor (SF) using the following relationship:

$$SF = \frac{4\pi A}{P^2} \tag{5.14}$$

In this definition, A is the projected area (μm^2) and P is the overall perimeter (μm) of the projection of a solid particle. The shape factor decreased with increase in angularity of the particles. The example of this factor is shown in Figure 5.4.

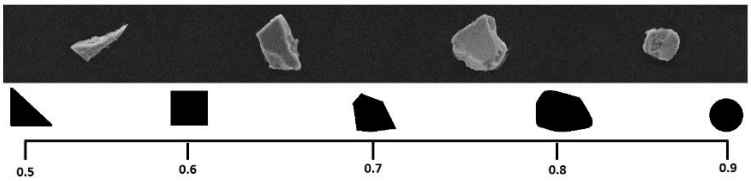

Figure 5.4 Visual representation of shape factor.

With the knowledge of shape factor, it is possible to generate random grain in different shape to make the prediction more particular and meticulous. In this model, ODEC method brought out by Sallam was adapted and be applied to 3D [126]. In this method, the grains will be generated randomly in sphere with specific radius in following steps. At first a number of points will be generated at the surface of the sphere. After the generation of these points a well-shaped graph will be created and tested to get the shape factor of this grain. If the grain does not meet the required shape factor, some more points at the surface will be added into this graph. After a few times of this step, the grain will have the same shape factor with the data from real grains.

In Sallam's paper they only adapt this method to 2D situation, it is necessary to involve it into the 3D environment. In 3D situation, the shape factor will be get from three-view drawings: front view, top view and side view. In this model, the grain generated randomly will be test in these three views and calculated by following formula:

$$Shape\ Factor = \frac{A_{front} + A_{side} + A_{top}}{C_{front}A_{front} + C_{side}A_{side} + C_{top}A_{top}} \tag{5.15}$$

In Equation (5.15), C represents the shape factor of projection from grain in each view while A represents the area of the projection from grain in each view.

This resulted in the modified values being 3–8% lower than the measured average values, the result of this for the SiC is 0.44 and the calculated for the mean of the sample of grains is 0.37, which is not far from the value.

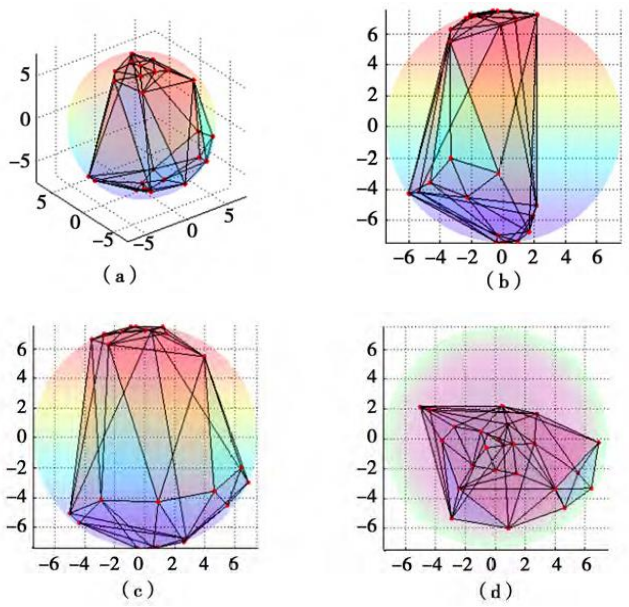

Figure 5.5 Randomly generated grains

The generation code in MATLAB helps COMSOL to build exact shape for the particles in simulation process and helps to predict the surface generation process during the AFM process. The generation of grains also provides the possible for mechanism model mentioned below to be calculated during the AFM process to predict the surface generation in micro scale.

5.3.3 The locus equation representing the machining process by one single grain

After the generation of grains, it is possible to predict the material removal in micro scale [84]. With the help of Equation (5.7), it is possible to get the cutting depth of each grain. Different from Sallam's research [126], the building of random grain will make the depth of cutting changing all the time while the grain is rolling on the workpiece surface. As described before, the grains are carried by fluid with high pressure and flowing and polishing along the surface. It means the grains will roll along the surface and leave the cutting pattern according to the shape of each grain. The depth of cut will increase while the grain is rolling and contact with the surface with its sharper side. The depth of cut will decrease while it is rolling to the other side. In Figure 5.6 a simple triangle grain is shown as an example of this model.

Figure 5.6 The cutting path of one grain (red line is the state before machining)

In Equation (5.7), the depth is mainly decided by the normal load on the grain and the average radius of grain. In Sallam's model [126] the load on the grain will not change at all time, which makes the depth keeps the same during the entire process. In physical model, the load is determined by the pressure along the surface and the contact area of the grain and workpiece surface as following equation:

$$F = P \cdot A \tag{5.16}$$

In Equation (5.16), P represents the pressure along the surface while A represents the contact area of the grain and workpiece. If we assume that the radius of grain is constant while rolling along the surface, we can get the equation with depth and contact area with Equation (5.7) and Equation (5.16) as follows:

$$d = 1.550 \sqrt[3]{\frac{P^2 \cdot A^2}{2RE_m^2}} \tag{5.17}$$

Equation (5.17) provides a method to calculate the depth of cutting while the grain is rolling along the surface in the entire process and generate a curve to simulate the locus equation of machining process by single grain. With this model the material removal and surface texture can be calculated and predicted in micro scale.

5.3.4 The Monte Carlo method applied to AFM modelling

Abrasive Flow Machining process is a type of stochastic process. Not only the shape of grains and the size distribution of the grains in fluid media, the collision positions and angles by grains are also in different scales of variation. It has been realized by many researchers that Monte Carlo simulation is a practical tool to predict the wear rate of materials. In abrasive flow machining, Monte Carlo simulation shows some light in providing a method to generate several random generated grains and make the

grains cutting at any place along the workpiece surface with a random speed and direction that is possible. With enough machining process of grains and correct distribution of machining position and direction of each grain, the Monte Carlo simulation will provide clear and accurate result on the generation of surface texture. By the mean time the prediction of material removal and surface roughness can also be provided in higher accuracy.

Table 5.2 Collection of data from the grains measured in this project

	Variance	Mean	Standard deviation
Perimeter (μm)	1337,17143	42,3424356	36,5673547
Shape factor	0,01612654	0,71243735	0,12699033
W/L aspect ratio	0,0260009	0,65829813	0,16124796

First, it is necessary to gather the information about the grains. The grains in AFM are almost all in the different shapes and the distribution of sharp factor is relatively wide. In this doctoral research, all the experiment is based on the fluid media provided by Extrude Hone, the collection of data in Table 5.2 also come from the fluid media produced by Extrude Hone.

With these data, a set of grains are generated with the normal distribution on Monte Carlo method in MATLAB to provide the calculation of mechanism modelling code. The mechanism modelling simulation will be based on these randomly generated grains and will be more accurate with the result.

On the other hand, it is also important to find out a way to put these grains into the fluid and let them start the machining along the workpiece surface. In this model the distribution of machining position is uniform distribution in the fluid media while the distribution type of the direction and speed is Gaussian distribution with the direction and speed of fluid media. With the help of Monte Carlo method, the grains are put into the fluid media with uniform distribution as the possibility of grains appearing at any position is equal. The direction of each grain will be mostly the same with the direction of fluid media as the viscosity of the media is very high. The grains will stay almost the

same method of moving with the fluid. Considering with the little deviation of each grain, the direction and speed of each grain is added with a small noise with the Gaussian distribution. After these set up, a number of grains will be calculated in mechanism model the result of material removal by each grain will be added up and contributes to a final result of material removal and surface texture of the workpiece surface. In this MATLAB code the simple surface generation will be simulated based on the results from CFD module simulation in COMSOL and the result will also be stored and import back to COMSOL simulation which make the simulation as an entirety.

Gaussian surface is generated by autocorrelation of randomly generated Gaussian noise in Z direction as a function of X and Y coordinates as shown in Figure 5.7. A factor term is multiplied by the correlation function to control the height of the Gaussian

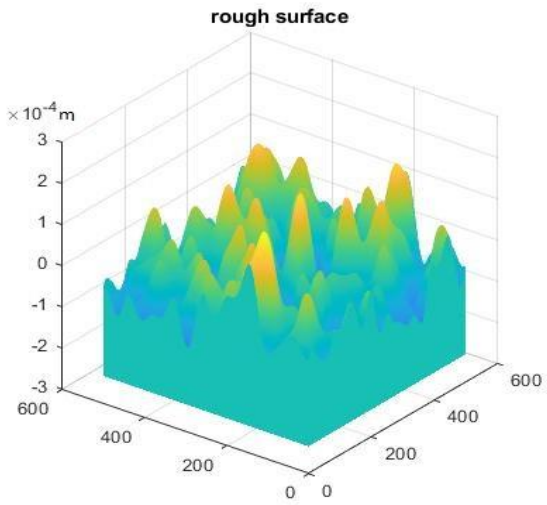

Figure 5.7 Gaussian surface using MATLAB function

noises. According to the AFM trial data, the surface roughness of a ground test piece is averaged at 0.36 with lowest value being 0.21 microns along the direction of flow, for a milled test piece the surface roughness is around 0.75 microns. The surface roughness values Ra and Rq are calculated based on numerical definition: Ra represents the arithmetic mean of surface height deviation about the mean plane, Rq represents the RMS deviation. Z represents the height while N represents the number of points selected for the measurement of surface deviation, as the surface generated is set to be a square, the number of points in both X and Y direction are set to be equal:

$$Ra = \frac{1}{N \times N} \sum_{n=1}^{N} |Z| \tag{5.18}$$

$$Rq = \sqrt{\frac{1}{N \times N} \sum_{n=1}^{N} Z^2} \tag{5.19}$$

The factor is adjusted such that surface roughness value Ra is approximately around the values observed for both ground surfaces and the surfaces after machining.

5.4 Simulation and experimental verification

5.4.1 MATLAB codes integrated with COMSOL for advanced analysis

The simulation-based CFD module within COMSOL aims to provide the prediction of material removal in this research [114]. However, it is also useful to provide the initial force and pressure for mechanical grinding model along the surface.

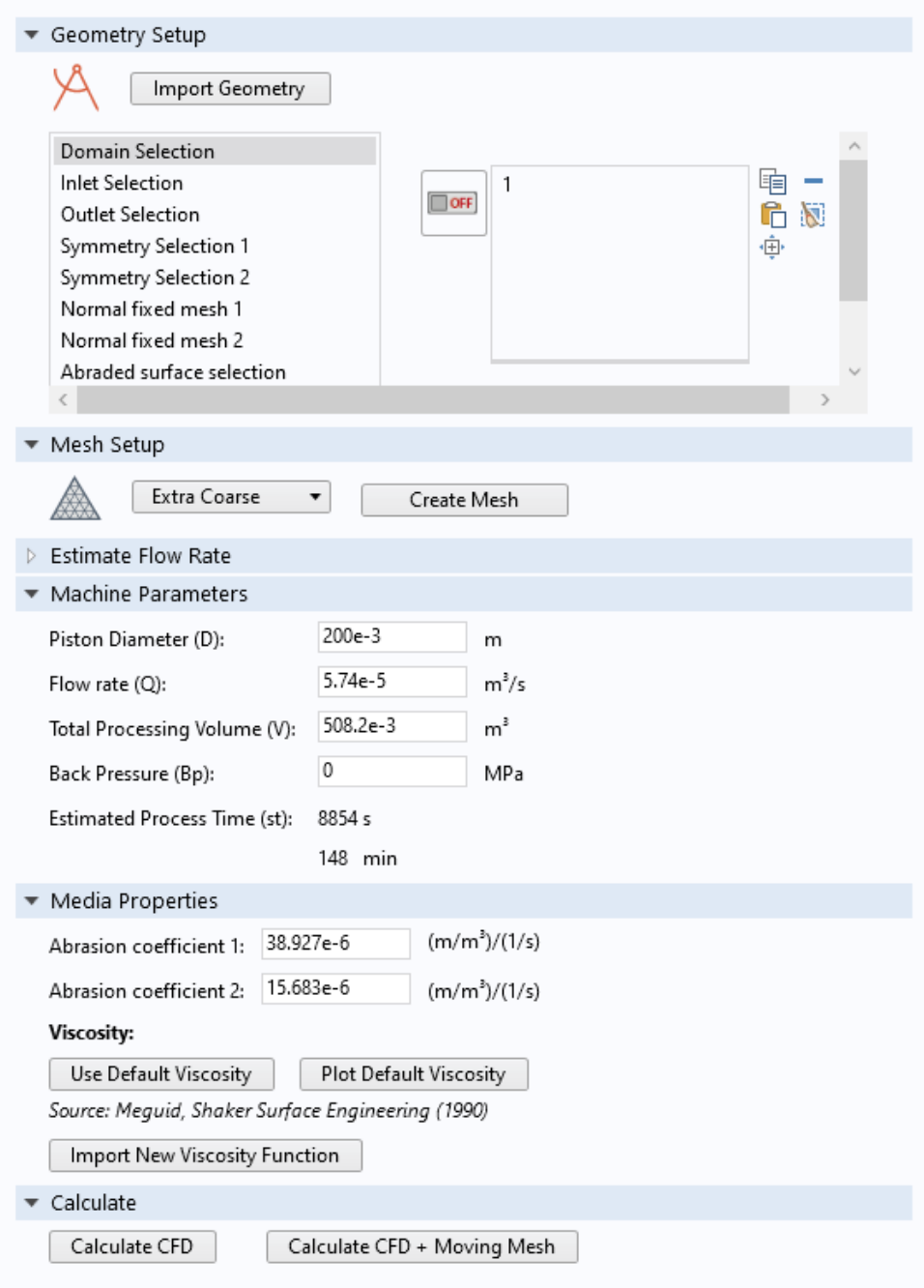

Figure 5.8 Interface of the simulation setup

The Multiphysics simulation based on COMSOL provides a lot of information for the mechanical modelling, which aims to predict the surface roughness and the generation of surface texture. The simulation setup interface is shown in Figure 5.8. It is possible to write a MATLAB code to enhance the function in COMSOL to provide the prediction of surface roughness.

The user defined MATLAB code is mainly built on the contribution of mechanism model and Monto Carlo method and the source data from the CFD simulation based

on COMSOL. The pressure along the surface and velocity of fluid media is simulated by COMSOL and import into the mechanism model. After the generation of grains in the specific range of sharp factor, the grains are imported into the mechanism model and distributed into random position with initial velocity and pressure from CFD simulation to start the calculation of material removal by each grain. With the help of Monto Carlo simulation in MATLAB, these grains applied on the mechanism model simulation and contributes to the machining process by each of them. A brief flow chart for the code programming is shown in Figure 5.9.

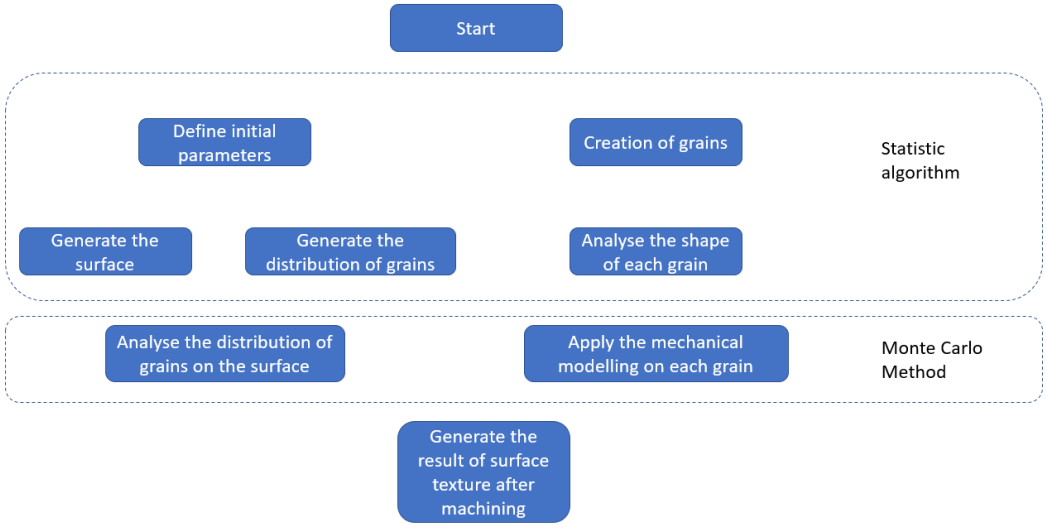

Figure 5.9 Flow chart of micro cutting mechanics modelling and anaysis.

In this MATLAB code the data about pressure and velocity distribution of fluid media along the workpiece surface is imported from the simulation based on COMSOL as described before. The example of pressure distribution of fluid media is shown in Figure 5.10. With the help of pressure and velocity, the mechanism model can be applied to the random generated grains built from MATLAB to simulate the generation process of AFM along a small piece of workpiece surface as an example. With one single calculation, one line of wave will be generated with the result of mechanism model which represents the cutting depth through this whole line with one grain. With the help of Monto Carlo method, the calculation is done times after times randomly and the result will be accumulated in this plane.

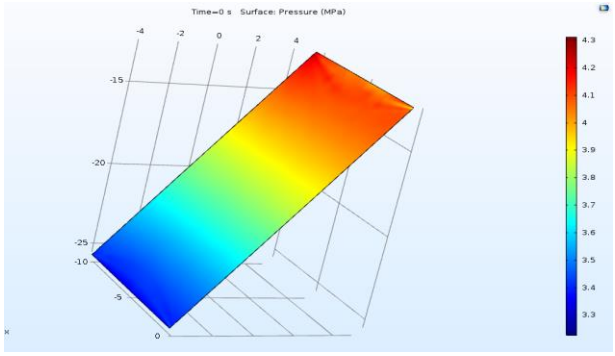

Figure 5.10 Pressure distribution of the fluid media on workpiece surface

5.4.2 Simulation for predicting the surface generation

After the calculation process of MATLAB code, it is necessary to bring the result back to the simulation in COMSOL for further calculation. As the result shown in Figure 5.11, the surface texture is somehow shown in MATLAB format. With the LiveLink for MATLAB and COMSOL these data can be communicated and updated at the same time. With this kind of help the simulation can stay at a better stage on the prediction accuracy on both surface roughness and material removal.

This part demonstrates the numerical analysis without the change in surface pressure included, the surfaces were numerically simulated based on averaged value of the pressure data extracted from the simulation. The surface roughness of the whole plane was computed rather than along vertical and radial direction. This section acts as the initial run for the numerical analysis.

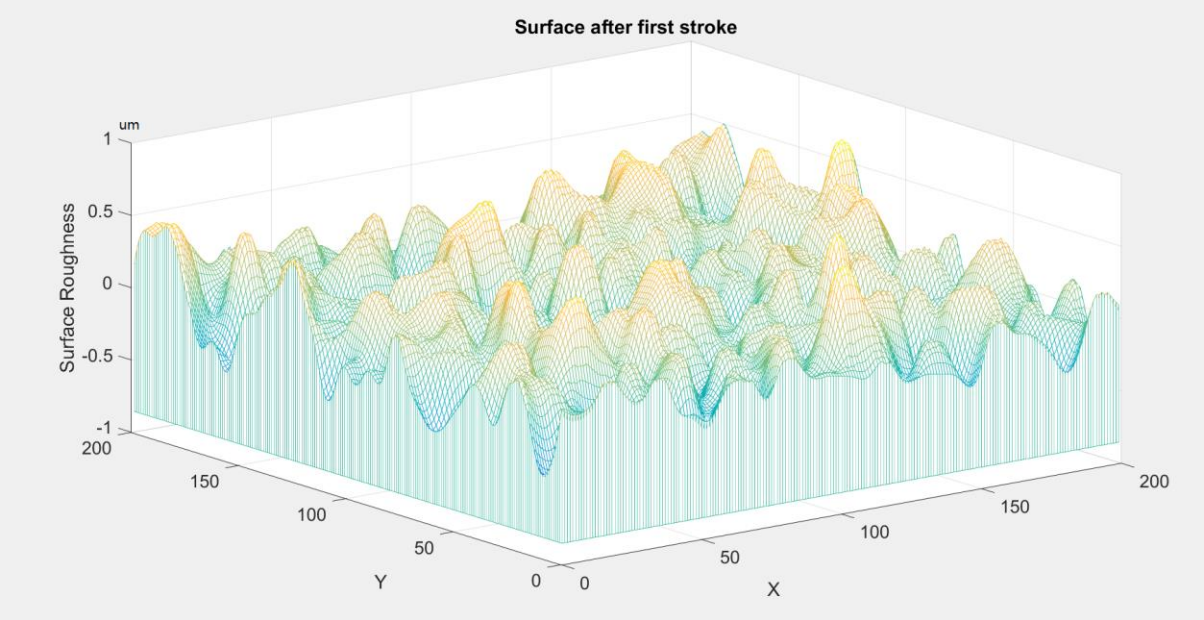

Figure 5.11 Surface topography generated by the simulation

The surface generated above shows the change in surface roughness at leading edge of the IBR after a full cycle of AFM process, the figures show gradual decrease in peak values as time progresses. Grain indentation is clearly shown in the figure. The full cycle is simulated to have less peaks in comparison with the finishing after half cycle. A clear way of indicating the gradual change in surface roughness is the change in R_a and R_q values computed according to surface deviation. Table 5.3 and 5.4 shows the R_a and R_q value of every quarter step of finishing during the first cycle.

Table 5.3 R_a value change during first cycle at leading edge

Initial R_a value:	0.56864
R_a value after quarter cycle:	0.45564
R_a value after half cycle:	0.40497
R_a value after third quarter cycle:	0.38978
R_a value after full cycle:	0.37414

Table 5.4 R_q value change during first cycle at leading edge

Initial R_q value:	6.7943
R_q value after quarter cycle:	5.7029
R_q value after half cycle:	5.2874
R_q value after third quarter cycle:	5.1824
R_q value after full cycle:	5.0825

In order to proper determine the surface roughness evolution after a full cycle, the percentage change is calculated for both coefficients in Table 5.5:

Table 5.5 Percentage change of R_a and R_q in surface roughness

Change in R_a value:	34%
Change in R_q value	25%

The values show aggressive finishing during the initial cycle, the percentage change during down-stroke shows 29% decrease, while the up-stroke shows 5% finishing improvement. This can be explained by high surface pressure at the leading edge during down-stroke and low surface pressure during up-stroke due to pressure drop.

To further prove the simulated results, the process is carried out by extracting data from trailing edge during the full cycle and import into MATLAB for numerical analysis of surface evolution.

Table 5.6 and 5.7 show the R_a and R_q values during the full cycle at the trailing edge.

Table 5.6 R_a value change during first cycle at trailing edge

Initial R_a value:	0.76644
R_a value after quarter cycle:	0.75395
R_a value after half cycle:	0.73821
R_a value after third quarter cycle:	0.67206
R_a value after full cycle:	0.58962

Table 5.7 R_q value change during first cycle at trailing edge

Initial R_q value:	9.8275
R_q value after quarter cycle:	9.6978
R_q value after half cycle:	9.5433
R_q value after third quarter cycle:	8.9523
R_q value after full cycle:	8.3344

Table 5.8 Percentage change in surface roughness

Percentage change in R_a value:	23%
Percentage change in R_q value	15%

The results shown in Table 5.8 relatively aggressive finishing during the first cycle, the percentage change in R_a value during down-stroke is calculated to be 3.6% finishing, and 19.4% finishing during up-stroke, this again can be explained by much lower depth of indentation during down-stroke at trailing edge due to the significant pressure drop.

The surface roughness value at the centre region is required for investigation of surface uniformity across the IBR after finishing process. Centre region is where pressure is relatively consistent during both strokes, therefore the percentage change during first half and second half of the cycle should demonstrate little deviation. Table 5.9 and 5.10 show the R_a and R_q values during the full cycle at centre.

Table 5.9 R_a value change during first cycle at centre

Initial R_a value:	0.68906
R_a value after quarter cycle:	0.60978
R_a value after half cycle:	0.62572
R_a value after third quarter cycle:	0.61073
R_a value after full cycle:	0.60467

Table 5.10 R_q value change during first cycle at centre and the percentage change in surface roughness

Initial R_q value:	8.3264
R_q value after quarter cycle:	8.1719
R_q value after half cycle:	8.0136
R_q value after third quarter cycle:	7.9001
R_q value after full cycle:	7.8128
% Change in R_a value:	12%
% Change in R_q value	6%

The results show much less aggressive finishing in comparison with trailing edge and leading edge during the first cycle, the percentage change in Ra value during down-stroke is calculated to be 9% finishing, and 3% finishing during up-stroke.

In Tables 5.5 and 5.8, the uniformity of finishing during the first cycle by comparing the average of trailing edge and leading edge finishing with centre finishing can be calculated as follows:

$$Rc = \frac{|4.8188 - 6.0467|}{6.0467} = 20\%$$

The result is demonstrated to be relatively uniform across the blade, the non-uniformity ratio is shown to be 20%, which is relatively small in difference of surface roughness.

The similar process was conducted for the AFM trial run during first cycle. Tables 5.11 and 5.12 show the finishing of upper surface along with percentage change in finishing, surface roughness is defined along a reference line in both radial and axial direction.

Table 5.11 R_a value change during first cycle at top region

Initial radial R_a value:	0.859
Final radial R_a value:	0.853
Initial axial R_a value:	0.485
Final axial R_a value:	0.590

Table 5.12 R_q value change during first cycle at top region

Initial radial R_q value:	0.985
Final radial R_q value:	0.984
Initial axial R_q value:	0.584
Final axial R_q value:	0.684

At the same time, the simulation which will be introduced in Chapter 7 is carried out under flow rate of 32.8 ml per second with total volume of 30 litres. According to test data, the finishing improvement is shown to be between 65 to 70%. With total flow time of 915 s, which corresponds to total of 11 cycles. The average finishing improvement for upper surface can be derived from taking the ratio of percentage improvement by the total number of cycles. This gives average improvement per cycle of 6%. The simulated results demonstrated no significant change in surface roughness, which showed mismatch to the experimental results. The similar results for lower surface are demonstrated below in Tables 5.13 and 5.14.

Table 5.13 R_a value change during first cycle at lower region

Initial radial R_a value:	0.703
Final radial R_a value:	0.714
Initial axial R_a value:	0.859
Final axial R_a value:	0.885

The simulated results showed higher than normal finishing improvement during the first cycle. According to experimental data, the range of finishing improvement is between 44 to 49%. This gives average finishing improvement per cycle of 4 %. Again, the simulated results showed no significant change in surface roughness improvement as predicted in experimental data. In contrary, the generated surface showed worsening in surface roughness after the cycle also according to R_q values shown below in Table 5.14.

Table 5.14 R_q value change during first cycle at lower surface

Initial radial R_q value:	0.985
Final radial R_q value:	0.984
Initial axial R_q value:	0.584
Final axial R_q value:	0.684

The change of R_q value for centre surface is shown in Table 5.15:

Table 5.15 R_q value change during first cycle at centre

Initial radial R_q value:	0.540
Final radial R_q value:	0.529
Initial axial R_q value:	0.92
Final axial R_q value:	0.916

The experimental data showed surface improvement ranging from 34% to 65%, this gives average finishing improvement per cycle of 5%. The percentage change in surface roughness in the radial direction is 1.1% and that in axial direction is 0.4%.

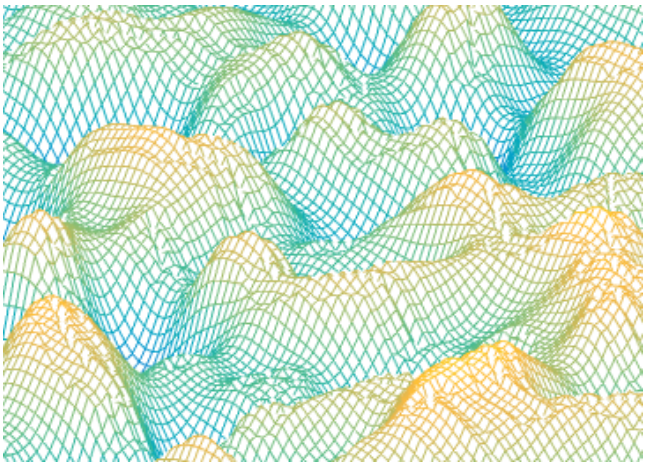

Figure 5.12 Surface indentation

Despite that surface peak values were significantly reduced during the simulated cycle, the surface roughness didn't show significant improvement as presented in experiment, on the contrary, the surface roughness has increased during two of the three regions

on simulated surface. The example of surface indentation is shown in Figure 5.12. This observation is discussed in Chapter 7.

The above simulations were carried out by taking the average pressure value along axial direction. In order to generate more accurate results, the change in pressure along the surface has to be considered. In previous chapter, the pressure change along coupon surface was plotted into a best fit function according to the Multiphysics data. This function is incorporated into MATLAB function and this allows generation of vector along axial direction with varying pressure. The results were shown below for the surface roughness at the upper surface changes along vertical and radial direction similar to that presented in the experimental results.

Table 5.16 R_a value change during first cycle at upper surface

Initial radial R_a value:	2.2
Final radial R_a value:	2.15
Initial axial R_a value:	1.44
Final axial R_a value:	1.42
Radial percentage change:	2 %
Axial percentage change:	1.5 %

The simulated results highlighted in Table 5.16 showed decrease in surface roughness as time progresses after the first cycle along radial direction. In order to verify the experimental results, analysis for second cycle is carried out as well for newly generated surface with different initial surface roughness values. The results of R_a and R_q value change during first cycle at upper surface are shown in Tables 5.17 and 5.18.

Table 5.17 R_a value change during first cycle at upper surface

Initial radial R_a value:	0.46
Final radial R_a value:	0.45
Initial axial R_a value:	0.74
Final axial R_a value:	0.72
Radial percentage change:	2 %
Axial percentage change:	3 %

Table 5.18 R_q value change during first cycle at upper surface

Initial radial R_q value:	0.62
Final radial R_q value:	0.58
Initial axial R_q value:	0.89
Final axial R_q value:	0.87
Radial percentage change:	0.7 %
Axial percentage change:	1.1 %

The surface roughness along vertical direction was shown to decrease by 3%. The R_q value gives better indication of the surface roughness, the R_q values generated for second cycle showed higher finishing along axial direction. The results can be compared to the experimental data with average improvement of 6% per cycle, which showed much higher improvement along both axial and radial directions. A decrease in finishing is shown according to R_a value along axial direction due to uneven distribution of peaks and valleys, this is related to the high level of aggressiveness during the initial cycles causing higher numbers of small deviations about of the mean plane, this might be the reason why the percentage improvement computed is lower than experimental data. The plot in Figure 5.13 shows the result of finishing after two cycles.

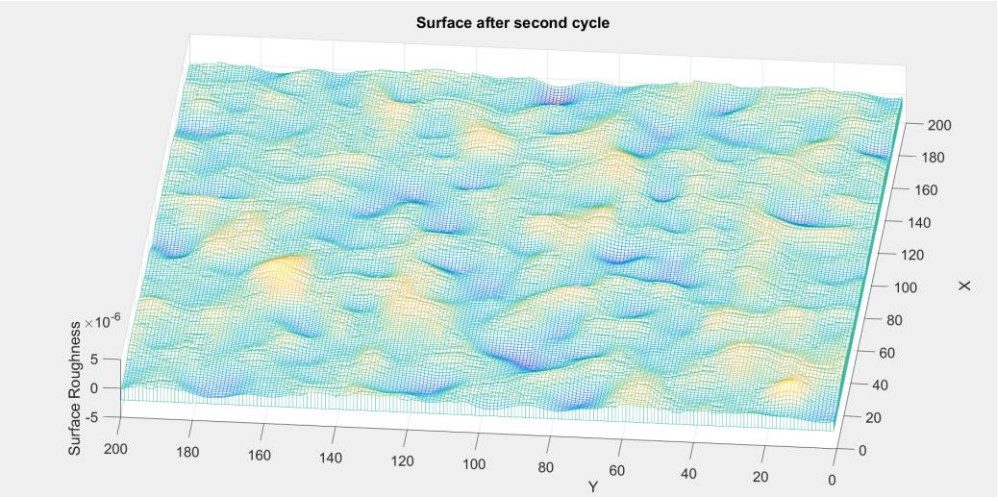

Figure 5.13 Finishing of generated surface

Clear indenting marks are shown in the graphic, which shows the high depth of indentation during the cycle. According to the plot, the surface is still relatively roughness even after material removal.

For finishing of lower surface, the simulated results of R_a and R_q value were shown in Tables 5.19 and 5.20.

Table 5.19 R_a value change during first cycle at lower surface

Initial horizontal R_a value:	0.624
Final horizontal R_a value:	0.621
Initial vertical R_a value:	0.479
Final vertical R_a value:	0.464
Radial percentage change:	0.5 %
Axial percentage change:	1.5 %

Table 5.20 R_q value change during first cycle at lower surface

Initial horizontal R_q value: (m)	0.766
Final horizontal R_q value: (m)	0.733
Initial vertical R_q value: (m)	0.564
Final vertical R_q value: (m)	0.535
Radial percentage change:	4 %
Axial percentage change:	5 %

Again, roughness improvement is shown to be higher than at axial direction than radial direction. High percentage improvement is shown at lower surface according to percentage decrease in Rq values computed, the simulated results were lower than the experimental data which showed average improvement of 12% during two cycles of abrasive finishing in axial direction and 8% of roughness improvement in radial direction. The simulated finishing results of centre surface were shown in Tables 5.21 and 5.22.

Table 5.21 R_a value change during first cycle at centre surface

Initial horizontal R_a value: (m)	0.798
Final horizontal R_a value: (m)	0.815
Initial vertical R_a value: (m)	0.609
Final vertical R_a value: (m)	0.587
Radial percentage change:	2 %
Axial percentage change:	2.2 %

Table 5.22 R_a value change during second cycle at centre surface

Initial horizontal R_a value: (m)	0.923
Final horizontal R_a value: (m)	0.907
Initial vertical R_a value: (m)	0.726
Final vertical R_a value: (m)	0.682
Radial percentage change:	2 %
Axial percentage change:	6 %

The improvement in surface roughness along axial direction is shown to be 4% higher than that in radial direction according to R_q value while R_a value showed 0.2% of percentage improvement in axial direction than radial direction. The experimental data showed 60% improvement along axial direction and radial direction. The simulated result for axial finishing agrees with the experimental data in radial for R_q value however the simulated result is significantly lower than experimental results in radial direction.

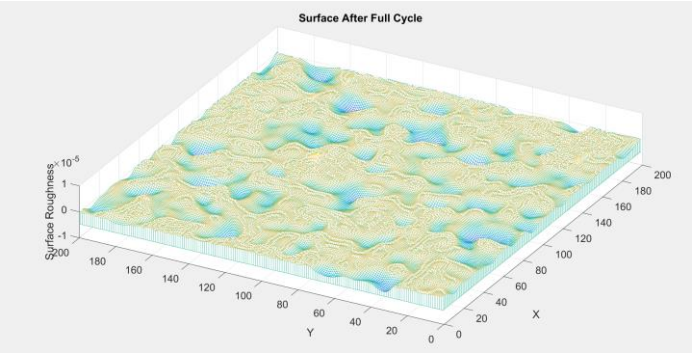

Figure 5.14 The prediction of surface roughness after first cycle.

After the communication, the result of material removal will be sent back to COMSOL and the workpiece will change as the exact result from MATLAB to continue the simulation in the next cycle. The prediction of surface roughness sent back from MATLAB to COMSOL after first cycle is shown in Figure 5.14. It is also possible for COMSOL to read the surface roughness and profile accuracy through the connection between COMSOL and MATLAB which make this simulation more like a complete virtual AFM simulation.

5.5 Summary

The modelling method and results of simulations have provided the insight on the relative importance of the different AFM process parameters involved. From the analysis of experimental trials, it is found the abrasive media (M) and its volume (V) consistently lead to the largest effect signature in the machining system. Furthermore, the volume (V) as the go-to parameter for tuning a process is exceptionally easy to be modified, while the media (M) is harder to be modified, as the industrial companies using AFM processes for IBR manufacturing will likely require prohibitively large batches for industrial testing before switching media.

The development of the abrasion model provides an effective approach for predicting the surface roughness and profile accuracy of the component in the AFM process particularly by integrating with results from CFD simulation. With theoretical and experimental considerations, flow rate and pressure distribution along the workpiece surface have been adopted as main factors in the model. With the further development of micro cutting mechanics modelling and analysis, it leads to better scientific understanding of the process, development of the prediction models and the process optimization.

The AFM modelling and simulation presented are planned under further development with more production data input from industrial partners and shop floor trials, as the part of the efforts in developing the industrial feasible virtual AFM system.

Chapter 6 Measurement and influence of fluid media properties on Abrasive Flow Machining

6.1 Introduction

In this chapter, the main emphasis has been put on how the characteristics of media are measured since the media is a mix of fluid, lubrication oil and grains inside and influences with the processed parts. Also, some effort has been placed on understanding how the geometry of the solid abrasive particles in the slurry influence the process outcome with the help of the simulation described in chapter 4 and chapter 5. In the first part of this chapter, there is a description of the measurement of the abrasive particles in new media on its shop floor which was provided by Extrude hone and similar to the one used by ITP IBR production. This is a mainly experimental work where the methodology is explained as well as a description on the nature of the data observed. The second part of this chapter is a description of the viscosity measurement of fluid media used in AFM with the aid of capillary rheometry. Furthermore, these test results are applied to mathematical models against specific challenges and industrial requirement at ITP.

6.2 Characteristics of particles in AFM fluid media

During the AFM process, the media is changing by the influence of temperature, wear, the ratio of abrasive particles to removed material debris. This has been traditionally accepted in the industry to have a marginal influence in the process, therefore most companies change only 25% of media once it is considered having lost some of its abrasion/erosion power. Given that, the media can be generally used in the process for many cycles and long periods. To measure how this industry “rule of thumb” corresponds to reality it will be advisable to measure how the geometry parameters that define grit size and sharpness (this will be defined later) changing over long periods or a high number of cycles. Acknowledging that there is not enough time to perform such a complex analysis within the deadline set for this project, what follows

is a proposal on how to practically perform such analysis. As part of the proposal, the analysis was implemented to a single set of brand-new media. To perform a complete analysis, this very same procedure should be applied to different sets of media before and after each process cycle in order to control its evolution. The Microscope used in this research is shown in Figure 6.1.

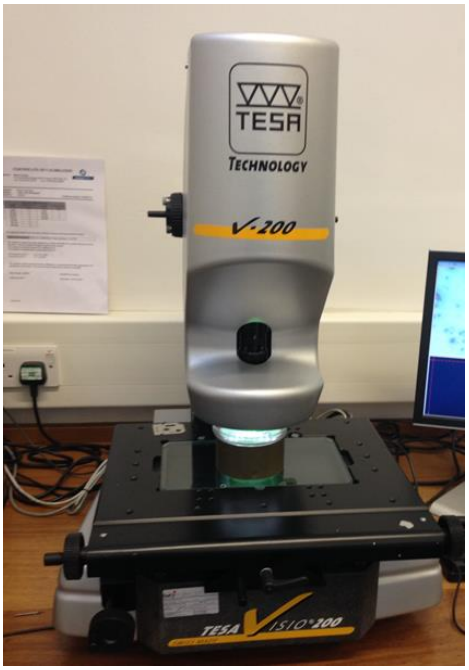

Figure 6.1 Tesa Visio 200 Microscope used in this research

In this research, a method is used to separate the media with the help of two different kinds of dissolvents: Acetone and white spirit. The procedure is described below:

Procedure Step 1 with Acetone:

The acetone is an organic compound with the formula (CH3)2CO. It is a colourless, volatile, flammable liquid, and is the simplest ketone. Acetone is a well-performed solvent for many plastics and some synthetic fibres. It is used for not only thinning polyester resin, cleaning tools used with it but also dissolving two-part epoxies and superglue before they become more hardened. It is the reason why decided to use acetone to dissolve the visco-elastic polymer that contains the loaded abrasive particles.

The process was described below: Firstly, put an amount of the media provided from Extrude Hone in a trough glass plate, the amount does not need to be very big as the concentration of grains per gram its very high. The acetone is disposed of in a glass

plate until it is clearly shown that there is enough quantity of liquid to dissolve the media.

To help the process of dissolution put the plate with the media in an ultrasonic mixer machine that was prefilled with water. This machine can help in the process of dissolution of the mixtures if we need to separate different components like in this case Silicon Carbide that we need to find and from the rest of the material presented in the media with a mix of oils and plastic (long-chain polymer). The equipment creates ultrasound waves able to stimulate the process of dissolution. In this occasion, the equipment used was an Engisonic machine as shown in Figure 6.2.

Figure 6.2 Dissolving the media with acetone in Ultrasonic cleaning machine

The observations doing while using the ultrasonic dispositive to separate and dissolve the particles from the media was a good result, after 10 minutes of using the ultrasounds the particles of the abrasive material finished being separate from the rest of the media. Then it could say that the process of dissolution in the experimental process was achieved with success.

Procedure 2 with White Spirit:

To separate the media apart from the use of the acetone was tried the use of another important dissolvent used in the chemistry industry that it is the White Spirit.

White Spirit is a petroleum distillate that is widely used as a paint thinner and mild solvent. For some industry purpose, the mineral spirits are used for cleaning and

degreasing machine tools and in conjunction with the cutting oil as a thread reaming and cutting lubricant [126].

Due to the great properties as a solvent of the White Spirit, it was used to dissolve another sample of our media to separate from the solid particles. The results achieved were similar to the ones with acetone due to the very good properties as a solver.

After successful separate the polymer part from the abrasive grains it was necessary to separate the mixture obtained to select only the grains that are necessary to work with, it was selected to do this task two filters from the brand Fisherbrand. It will be better to find a micro sieving mixer in the facilities to finish this work to get a better result.

The selection of these filters was based on the size of the particles between 5-20μm that this is the size that is required to work with.

The filters used are:

- Fisherbrand™ Grade 113 Cellulose Medium Filtering Qualitative Filter Paper, with a retention particle size of 5 to 8μm.
- Fisherbrand™ Grade 111 Cellulose Fast Qualitative Filter Paper, with a retention particle size of 12 to 15μm.

To get filtered, the samples were put into a watching plate after getting the separation from the filters using a Funnel and a graduated cylinder, and in every case, a filter paper was obtained with the sizes of the grid, the samples are shown in Figure 6.3. The liquid that it is obtained in the graduated cylinder will have the particles that are smaller than the retention particle size from the filters. The watching plate was situated in the fume cupboard to help and make quicker the evaporation of the filters and get ready the samples which are waiting for further procedures.

After obtaining the filters with all the samples, it is necessary to separate these grains with different particles sizes. The results of separation are shown in Figure 6.3, i.e.:

- Acetone 5 to 8μm
- White Spirit 12 to 15μm
- Heat-treated with acetone 12 to 15 μm

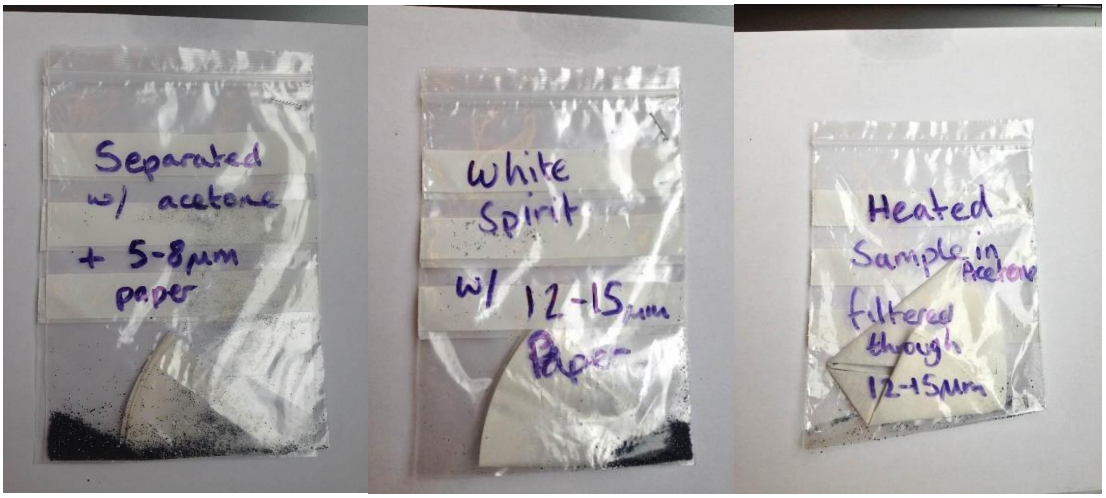

Figure 6.3 Specimen to use in our study of Acetone 5 to 8µm, White Spirit 12 to 15µm, Heat treated with acetone 12 to 15µm

T Microscope JEOL 6000 benchtop SEM microscope with EDS functionality is used in this research as Figure 6.4. This microscope belongs to the family of Scanning Electron Microscope (SEM), that can produce images of a sample by scanning along the surface with a focused beam of electrons. In this case, the SEM can achieve resolution better than 1 nanometre. Specimens can be observed in both high vacuum in conventional SEM and low vacuum or wet conditions in variable pressure with specialised instruments [127].

Figure 6.4 Microscope - JEOL 6000 benchtop SEM with EDS functionality

The samples were prepared to be analysed in the microscope putting a part of the specimen in a piece of tap conductive made by carbon and stick the specimen then

an inflated air source is applied to detach any loose particle that could contaminate the chamber or lent of the microscope. The configuration to use the microscope was different ones with high vacuum and low vacuum. The images represented in the microscope were not with enough good quality to detect the particles that were expected to find in the microscope as shown in Figure 6.5.

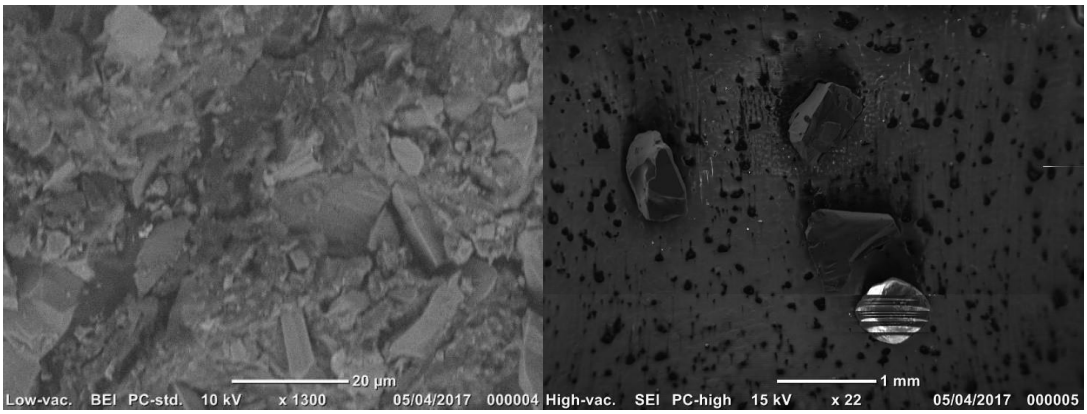

Figure 6.5 Images of the sample obtained under a microscope

The configuration to use the microscope was in the different images with low vacuum and high vacuum, the voltage that was applied 10 kV and 15 kV for the two images that we obtained. The one with less resolution which can observe particles around 1 mm is not necessary to observe. The magnification that is used to observe in the samples are 1,300x and 22x.

The EDS (Energy-Dispersive X-ray Spectroscopy) is a system that is integrated to the SEM microscope contains a crystal that absorbs the energy of incoming x-rays by ionisation, yielding free electrons in the crystal that become conductive and produce an electrical charge. The x-ray absorption thus converts the energy of individual x-rays into electrical voltages of proportional size; the electrical pulses correspond to the characteristic x-rays of the element, then with the pick that it is detected, it is possible to identify each element of the periodic table with good accuracy. With the help of the EDS system, the results are shown in Figure 6.6:

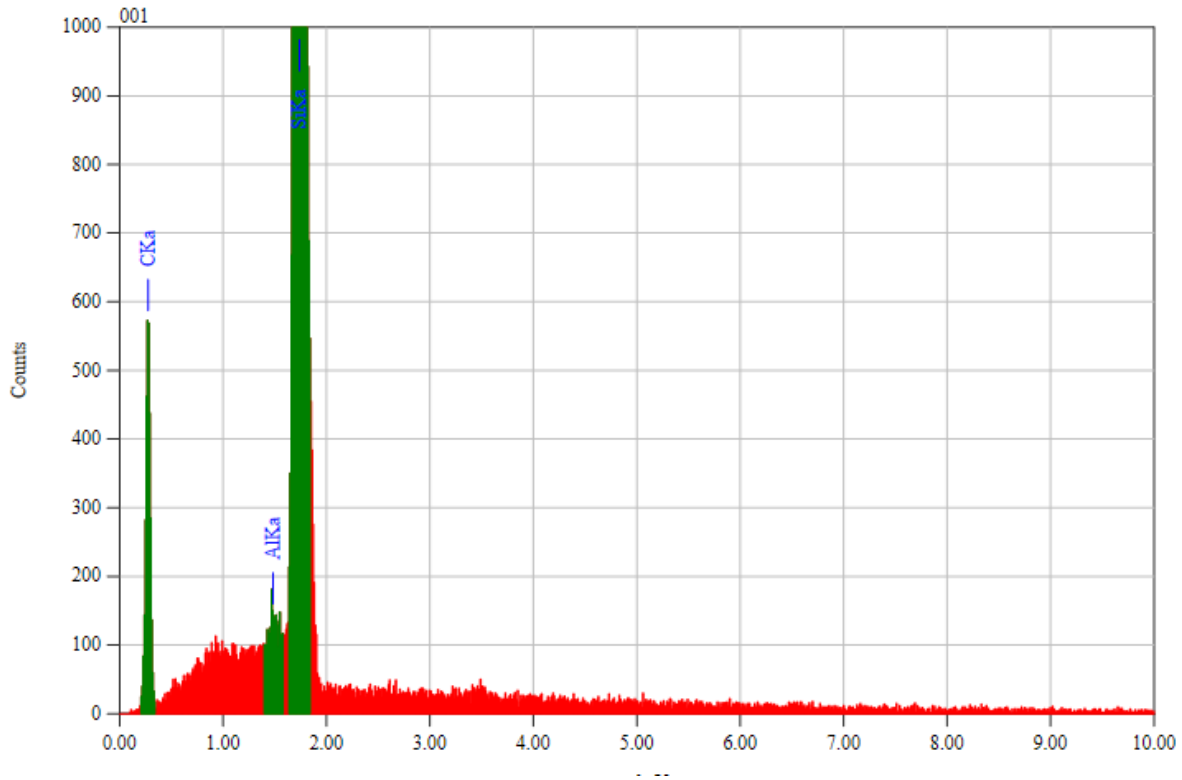

Figure 6.6 Spectrum of the specimen analysed with EDS

As it can be observed in Figure 6.6, the spectrum shows a high concentration of the Si and Component and a little bit fewer traces of Aluminium, Si and C were expected to find in the specimens because the abrasive particles in the media used were SiC.

The next and final machine to be used as the ‘Zeiss Supra 35VP FEG SEM’; however, the samples would need to be prepared correctly before being inserted into the machine. The samples were prepared in a separate room and adhered to carbon strips attached to a single sample stage on a rotational master stage. The samples were put through a plasma cleaner, as shown in Figure 6.7. The purpose of this exercise was to remove the volatile hydrocarbons which naturally vaporise from the sample which may damage the system with loose particles, decrease the image quality or contaminate the chamber for future use. It works by vaporising using oxygen and hydrogen RF (radio frequency) plasma, to bombard the sample and break down long-chain carbon into short-chain, so that all that is left is organic material.

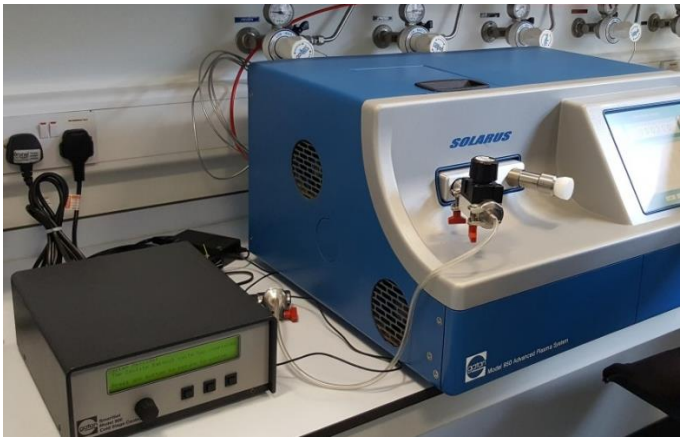

Figure 6.7 Gatan Model 950 Advanced Plasma System

Next step, it is possible to gather high-resolution images of the samples on the SEM (scanning electron microscopy). The machine uses a focused beam of high-energy from the electron gun/probe which scans horizontally across the surface of the sample in the x and y-axis to generate a variety of signals which are detected by the scan coils. In the x- scan, the coils generate a magnetic field in the y-axis, creating a force on an electron which travels in the z-axis which is subsequently detected in the x-axis. In the mode of y-scan, a procedure called '*raster -scanning'* is exercised, which essentially the electron probe moves in a saw-tooth manner to cover a rectangular area over the sample, the deflection of the beam across the sample is detected between points until the area has been fully scanned [128]. The two scans are then converted into pixels and displayed on a monitor as illustrated in Figure 6.8. It is noted that the display device depicted is a cathode-ray tube device, while those used in this exercise were digital LCD monitors.

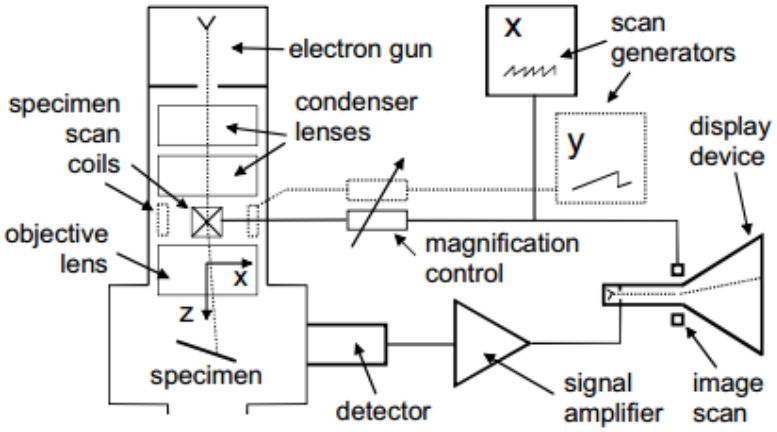

Figure 6.8 Diagram showing the components in an SEM [128]

After cleaning the samples were then attached to their separate stages via the use of adhesive carbon paper, such material would allow the samples to charge and doubling as a contrasting background. Then these stages would then be brought into a separate, air-conditioned room (23°C), placed into a rotational master stage, which was then placed into the chamber (Figure 6.9) of the Zeiss Supra (Figure 6.9). The method used for charging the samples relied on a variable pressure vacuum in the chamber; in some cases, the sample requires a conductive coating (typically gold) to be prepared before the study. However, the Supra was able to achieve resolution in low vacuum mode.

It was also found however that the heat-treated media sample still contained a presence of moisture. Thus the sample was not a solid specimen which the SEM requires to be able to conduct successfully. Otherwise, it will 'outgas' at high pressure. As a result, the grains had not been successfully separated. However, the sample was used in the next process for composition analysis.

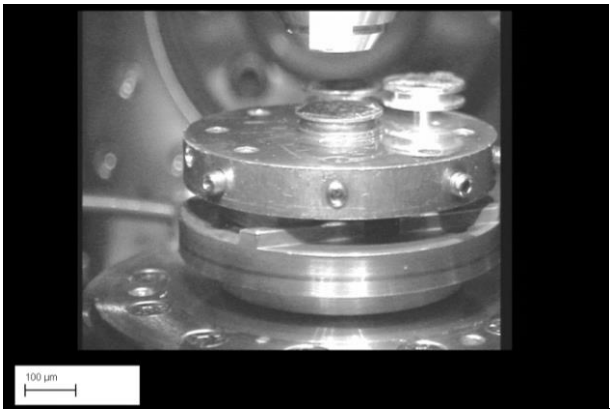

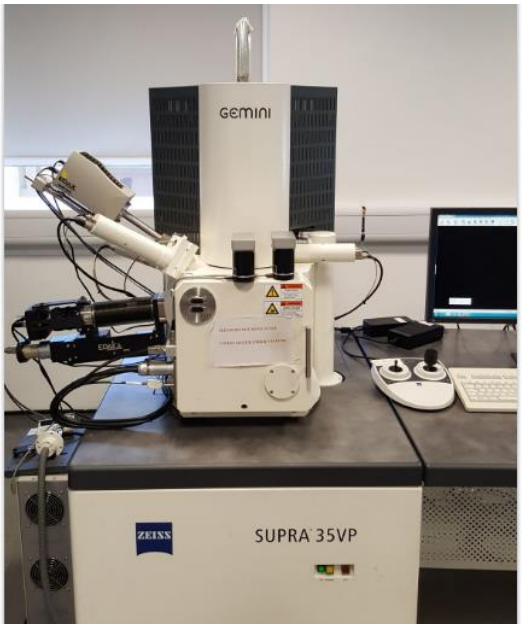

Figure 6.9 Two samples on the rotational stage inside the chamber and the Zeiss Supra 35VP FEG SEM

The process for measuring the grains once all the samples in the SEM had been visually captured and saved to a hard-disk, involved the use of 'Digimizer'. This as free to use software which allows for precise manual measurements from supported image formats. The procedure for the measurement of the grains involved using the scale

marked in the bottom left corner of each sample image, and setting the scale manually, from there the area of the grains could then be plotted.

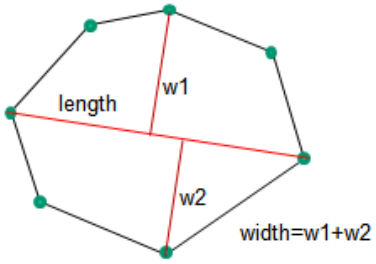

Figure 6.10 Geometry characteristics of a grain

To measure the grains, the area tool was used to trace around the perimeter of the grain in the image, which in turn would not only log the data but, using background formulae would be able to also log data regarding the circumference, maximum length across the grain as seen in Figure 6.10 and finally and most crucially, Digimizer also auto-calculated the roundness of each grain. In total, 2,323 grains were measured across 60 sample images as shown in Figure 6.11.

The data collected from each plot was then logged automatically into a table which could then all be gathered into one excel file, from here the calculations of the data could be executed.

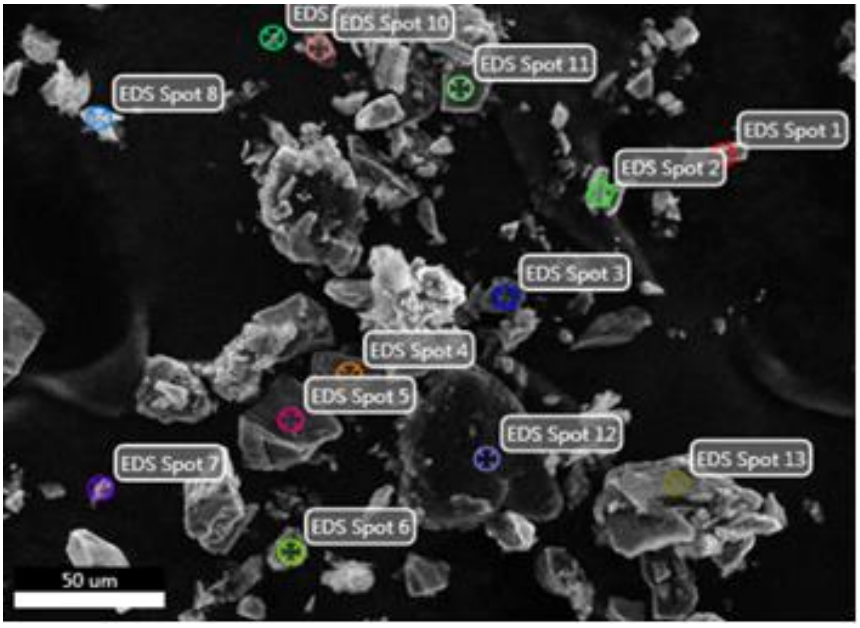

Figure 6.11 Heat-treated samples, 12-15 μm

Through the analysis from the EDX, it was found that the media consisted of majority Silicon and carbon, which is the most logical and expected result as the grains are made from silicon-carbide. However, throughout the samples and the various spots selected across the grains, there were insignificant traces of elements from across the periodic table, which would be put down to an error in the equipment and software. However, it should be noted as seen in Figure 6.13, that aluminium was significantly present in the grains. This would most likely be because the media had been used in machining aluminium in its service life at Extrude Hone. The other noticeable peak on the graph in Figure 6.12, is that the presence of carbon is significantly high. As each count, carbon is released into the chamber which is detected by the EDX system, as a result across all of the gathered data, there will be a high amount of carbon counted.

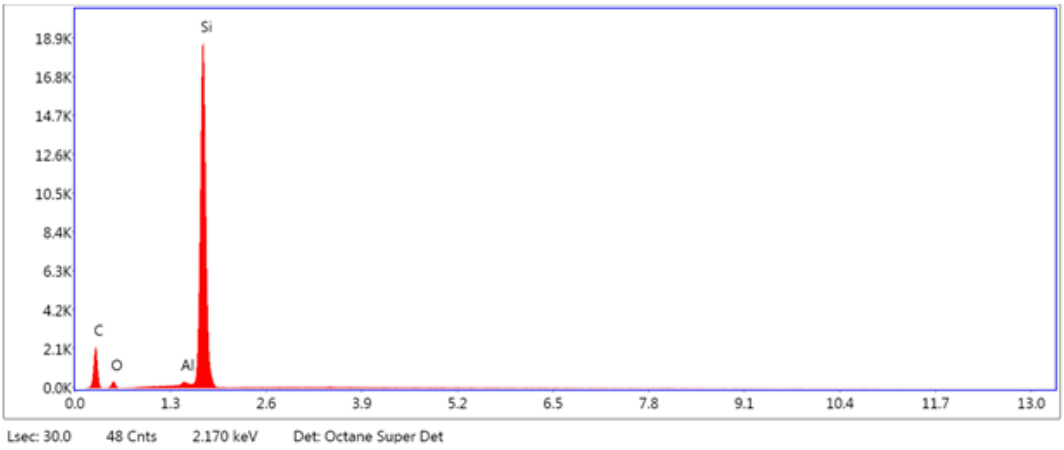

eZAF Smart Quant Results

Element	Weight %	Atomic %	Net Int.	Error %	Kratio	Z	R	A	F
C K	61.15	76.83	487.04	10.05	0.1090	1.0440	0.9747	0.1707	1.0000
O K	5.62	5.30	76.36	12.28	0.0070	0.9987	0.9947	0.1254	1.0000
AlK	0.51	0.28	80.80	7.07	0.0040	0.8878	1.0321	0.8508	1.0374
SiK	32.73	17.59	5555.37	1.88	0.2783	0.9072	1.0381	0.9346	1.0028

Figure 6.12 EDX Results

A total of 2,323 particles were measured creating a population of n= 2,323 of subjects sample where was measured all the parameters named above and calculated the Shape Factor (SF).

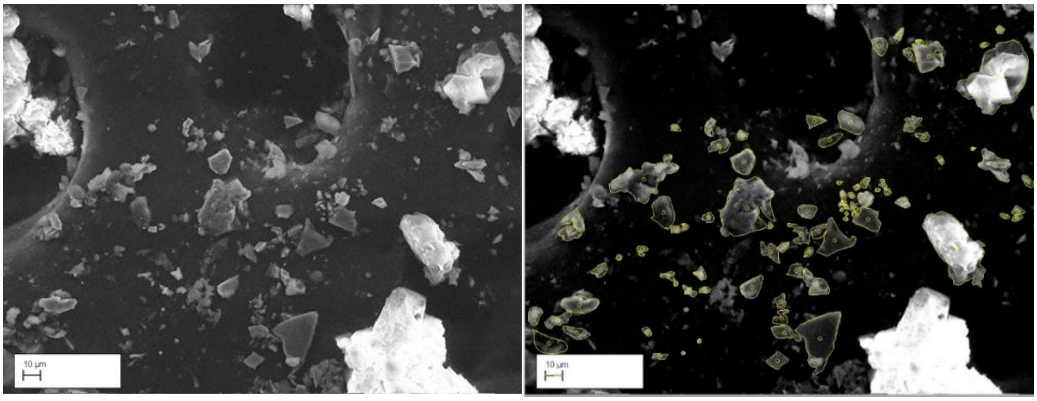

(a) (b)

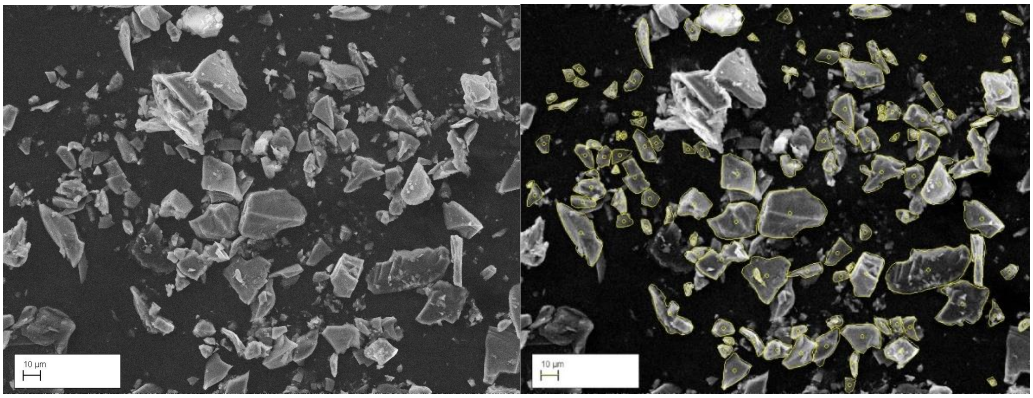

(c) (d)

Figure 6.13 (a) Heat-treated acetone sample 1; (b) Heat-treated acetone sample 1, with measurements in the grains; (c) SEM image from White spirit 12-15 µm sample 2; (d) SEM image from white spirit 12-15 µm sample 2, with measurements in the grains.

The software recommended to do this duty was SmartTiff a specialise software to visualise and measure SEM Images, but it was found that it did not have the told necessary to measure the parameter that we need. A research was done to find out another software able to measure this parameter and after trying the software ImageJ that is possible to use with many formats like all supported data types as TIFF (uncompressed) or as raw data. Open and save GIF, JPEG, BMP, PNG, PGM, FITS and ASCII. The final choose after different tries were to use the software Digimizer is a free easy-to-use and flexible image analysis software package that allows precise manual measurements as well as automatic object detection with measurements of object characteristics. The measure of the grains that were observed in the images collected in the SEM microscope gave us the base to measure the grains area

perimeter and other parameters if it is needed to use in order to calculate the Shape factor. Figure 6.13 shows a few of the pictures from the SEM microscope and the results after measuring the grain with the chosen software Digimizer.

To gather all the data was created an excel book to manage all together and calculate the parameters that we need to use in the study. The data in Table 6.1 were generated after the collection of all the data provided after the measurements. The mean of the roundness or shape factor is calculated in the excel file with a value of X= 0.71243735 and the Variance $\sigma^{2=}$ 0.01612654.

Table 6.1 Collection of data after measurements

	n	Variance	Mean	SD (standard deviation)
Area	2323	150004.66	167.21	387.30
Perimeter	2323	1337.17	42.34	36.57
Length	2323	189.31	15.97	13.76
Width	2323	77.32	10.15	8.79
Shape Factor	2323	0.017	0.71	0.127
W/L aspect ratio	2323	0.026	0.65	0.161

The last thing is necessary to figure out is the value of the Mean of the Shape Factor whose representative of the sample that was collected in the images from SEM to analyse this value among of other things. The circularity is equal to unity for circular shape and any deviation away from unity indicates departure from circularity, and accordingly, circularity increases as this parameter gets closer to unity, then a value of 0.712 as the mean of the Shape Factor give as a shape factor that it is not very good as its quite close to the value of 1, as studies show that the wear rate decreases with increasing particle SF.

The aspect ratio (W/L) can be used to describe the elongation of particles, as smaller values of aspect ratio indicate a greater elongation of the particles [129].

The standard deviation for these values is considered the most reliable value of reliability, it is affected by the individual values in the distribution, a low standard deviation indicates that the data points tend to be close to the mean (also called the expected value) of the set, while a high standard deviation indicates that the data points are spread out over a wider range of values.

The Shape Factor has a value of SD= 0.12 (Standard Deviation), that is a very close number to 0, the closer is the standard deviation to 0 the closer to the mean is, the further the data points are from the mean, the greater the standard deviation is. Then it could be determinate that the variation of the values for the shape factor is not very big due to the value of the standard deviation.

The aspect ratio standard deviation is 0.16 which is a small number with the meaning of that the variation in this parameter relating the width and the length of the grains is not big. For the perimeter, the value of the mean is 42.342 µm and the value of the SD is 36.57, then the similarity of the value and the high value of the SD point as to a great variation of the length of the perimeters in every grain, they variation is quite huge.

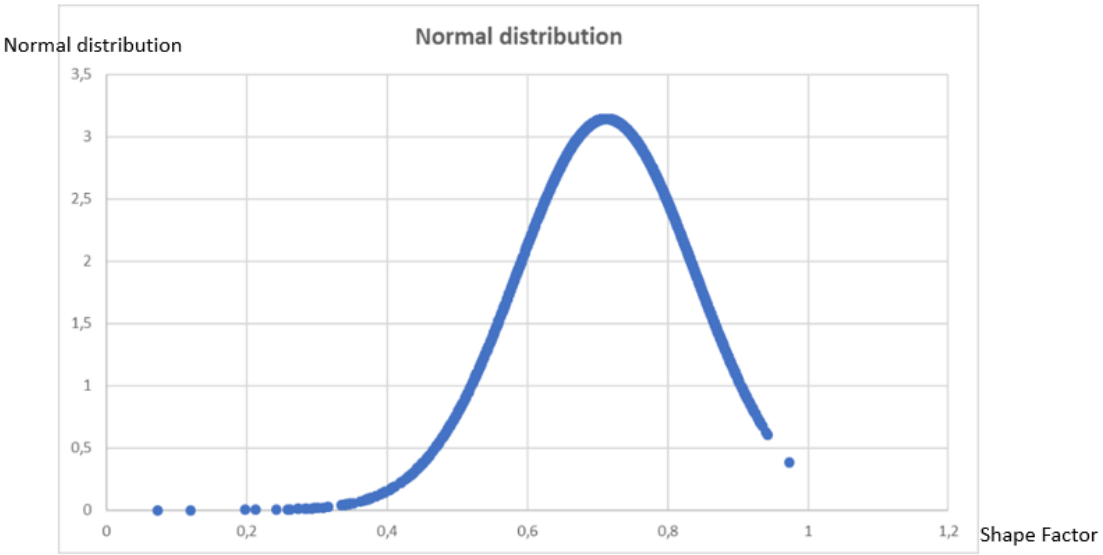

Figure 6.14 Normal distribution of the shape factor values

As it is represented in the graph created in Excel (Figure 6.14), the distribution of the values of Shape Factor follow a Normal distribution almost perfect with more values

situated to the left of the bell shape. The figure provides the impression that the values of the shape factor have a tendency of more shape factor values sitting less than the mean.

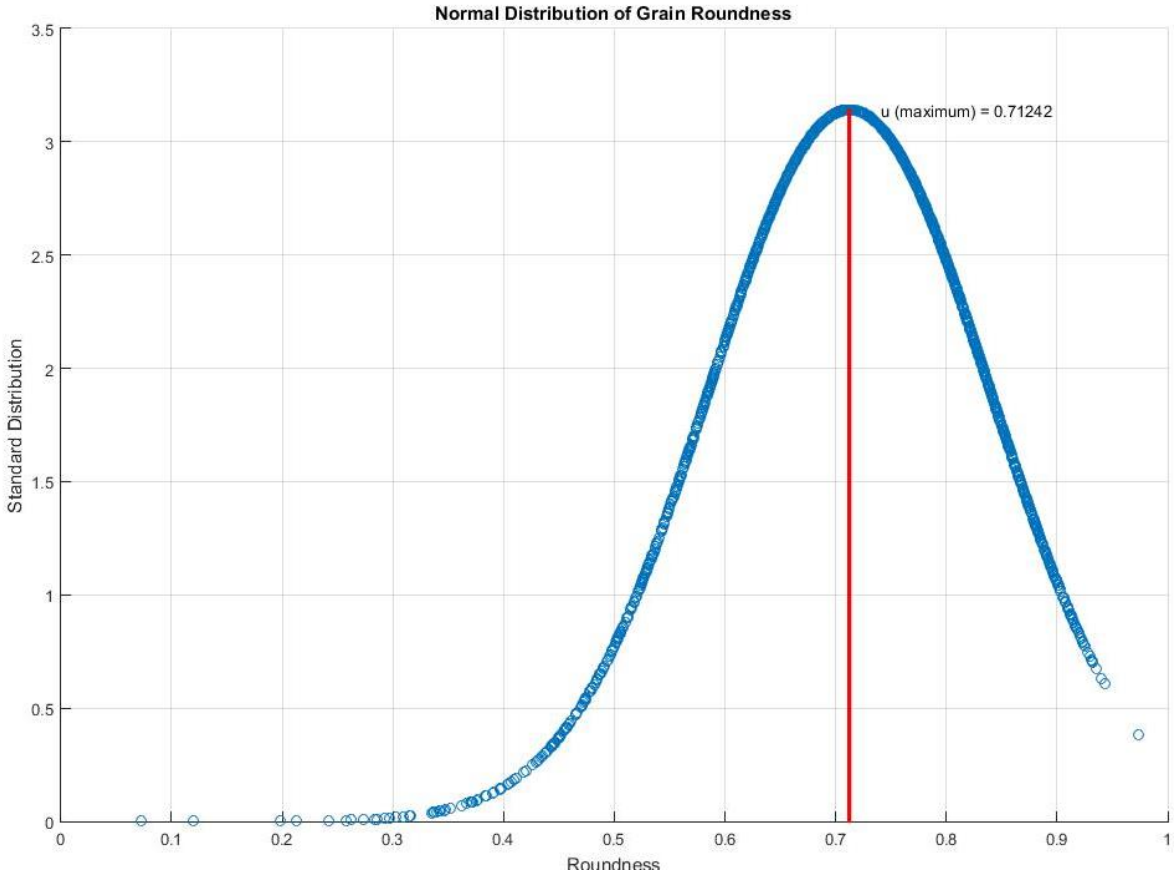

Figure 6.15 Normal distribution and mean, for the grit roundness

In Figure 6.15, a graph that was created in MATLAB. It represents the normal distribution for the grit roundness and the mean is situated in the centre of the bell shape representative of the normal distribution and coincident with the value of the mean.

Another parameter that could be considered to compare with the shape factor is the modified shape factor. Because of the spread in measured CF, the average results are corrected to:

$$SF_{modified} = \left(SF_{avg} SF_{max} SF_{min}\right)^{0.33} \tag{6.1}$$

6.3 Capillary rheometry for AFM media

It has been shown and discussed in chapter 2.7 that access to the media's rheological data is very much restricted and needed when studying the AFM process, the purpose of this part is to contribute to this underdeveloped area by proposing the design and experimental setup for a capillary rheometer which can be set up within a universal testing machine (UTM) to take advantage of its force and position controlling systems, this would allow for a researcher with access to reasonably standard equipment to develop:

- Viscosity vs shear rate curves for a variety of commercial AFM media, in the range of shear rates that are relevant to the process (1 to 10^3 [1/s]) by testing sets of capillaries with different lengths.
- Study the wall-slip behaviour of the media by testing different diameter capillaries and performing the appropriate correction.
- Develop an understanding of the transient and elastic properties of the media by measuring the transient response to loading and die swell diameter, respectively.
- Study the temperature dependence of viscosity.

The following procedures that describe the data collection and treatment can be found in researches from Dealy in 1982, Shenoy in 2013 and Morrison in 2014 [132,133,134]. These are fairly standard practices when conducting capillary rheometry of molten polymers, however, even when previous researchers have built such machines for AFM, some or all of these practices have not been followed. This author hopes that by compiling and describing them in the context of studying AFM media, the procedures may be used in the future to establish a well-established understanding of the media and process.

6.4 Capillary rheometer design for testing AFM media

Using the concepts laid out in the previous section, dimensioning the equipment and experiments to measure for AFM media requires approximate information of the

expected values of viscosity and the capabilities of the universal testing machine (UMT) that is to be used to extrude the media through the capillary.

The approximate media properties, as found in different sources are summarised in previous sections, with plots of fitted Power-Law models. It can be seen that there is no agreement between different sources even for media that is qualitatively described as “Medium Viscosity (MV)”. The fact that there are many different formulations and grit contents just aggravate the issue. There is also little evidence to justify the start of the curves’ Newtonian behaviour; it seems however that this part of the curve may be less important because the shear rates that the process produces are normally well over 1 [1/s].

In an attempt to test which model more accurately describes the flow, simulation of previous experiments were performed in COMSOL multiphysics using a purely viscous constitutive model with a shear rate dependent viscosity. The particular experiments selected were performed by Davies in 1993 for “Medium viscosity (MV)” and “Low Viscosity (LV)” media with 60 mesh grit and 66% grit content. The relevant experiment data is shown in table selected corresponds to a two cycle run of the media, the data from more cycles is hard to use as the media temperature was not constant and viscosity varied heavily through the run time [24].

Table 6.2 Flow data for 2 cycles, MV and LV, 60 mesh grit, 66% grit content [132]

Media	**Number of cycles**	**Volumetric Flow Rate x10^{-3} [m^3/s]**	**Piston Speed x10^{-3} [m/s]**	**Pressure drop [kPa]**	**Pressure drop [psi]**	**Die Diameter x10^{-3} [m]**
LV	2	0.1569	8.60	1480.01	214.66	15.0607
MV	2	0.0353	1.94	2189.17	317.51	15.1181

The simple geometry of the experiment allows the problem to be quickly solved in axisymmetric geometry, the die diameter and length are 15 mm. Results from the simulation are listed in Table 6.3. It can be found that the only available model accurately predicting the pressure drop in the chambers is the one published by Meguid in 1990 [136]. It corresponds to the media described as “Medium Viscosity”

[135], the error is 5.5% and could be attributed to a myriad of sources ranging from differences in the actual media tested by the two authors (grit size, grit concentration, modifiers, etc.) to errors in the simulation itself. This means that the result at this point can be attributed to coincidence. Hopefully further testing and simulation can further validate the material model published [136] not only for prediction of the pressure drop in the media cylinder but other flow results possibly coupled to abrasion models for process response prediction.

The results of experiments and simulation are listed in Table 6.3. For the media catalogued as “Low Viscosity” the model proposed by [54] provides better approximation, with a 22.7% error. By accepting the model by Meguid in 1990 as the most reasonable approximation of the media’s properties, the die and piston dimensions that produce the required shear conditions and practicable piston speed and force need to be determined.

Table 6.3 Comparison of Simulated results with Davies experiments using different material models [24]

Simulated Material Model	**Piston Speed x10^{-3} [m/s]**	**Experimental Pressure drop [kPa]**	**Simulated Pressure drop [kPa]**	**Error [%]**
Uhlmann in 2013	8.60	1480.01	281.88	81.0%
Wan in 2014	8.60	1480.01	1815.5	-22.7%
Meguid in 1990	8.60	1480.01	4376.7	-195.7%
Uhlmann in 2013	1.94	2189.17	161.54	92.6%
Wan in 2014	1.94	2189.17	590.65	73.0%
Meguid in 1990	1.94	2189.17	2069.1	5.5%

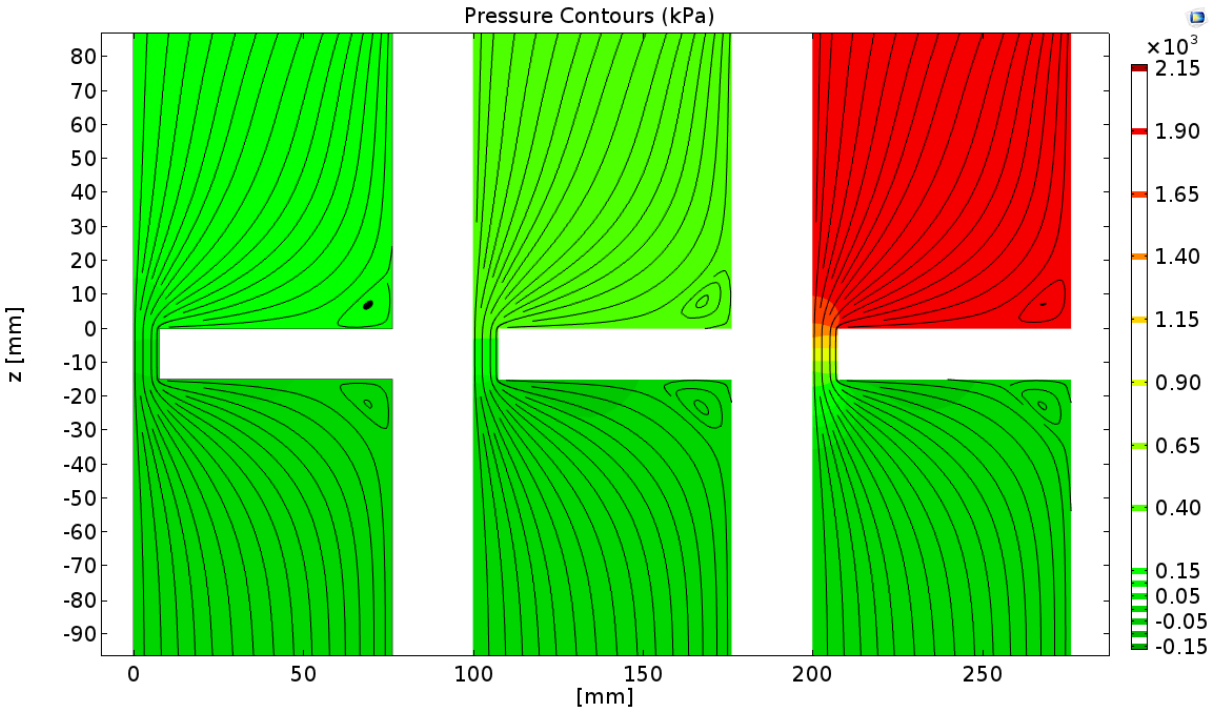

Figure 6.16 Simulation results for the flow of medium viscosity media in the experiment of Davies in 1993 using different material models. Material models from left to right: a) MTT10 by Uhlmann in 2013; b) LV by Wan in 2014; c) MV by Meguid in 1990 [137-139].

In the case of abrasive filled media by National Physical Laboratory in 2005, the measuring geometry is recommended to be at least 3-10 times larger than the particle size diameter, meaning that for testing a typical 36 grit size media that corresponds to a $503\ \mu m$ average particle size the capillary diameter should be around 5 mm. In order to test the loading conditions (piston speed and force) required to test such a setup a simulation model of the capillary rheometer was created, the results of it need to be checked against the capabilities of the UTM that is going to be used to control the piston force and speed [139].

As a reference, an Instron 5,697 universal testing machine (available at Brunel University Laboratory, Figure 6.17) has the relevant specifications as listed in Table 6.4:

Table 6.4 Specifications of Instron 5967 UTM

Instron 5967 UTM Specification	Value	Unit
Load capacity	3000	kgf
Minimum Speed	0.001	mm/min
Maximum Speed	1000	mm/min
Maximum load at full speed	3000	kgf
Vertical test space	1212	mm
Column spacing	418	mm

Figure 6.17 Instron dual-column UTM

The simulation model estimates the piston load and speed required to achieve the shear rates considered to be important to the process, results from a simulation of the smallest recommended die radius $(5\ mm)$ with length $20\ mm$, piston radius $12.7\ mm$ and $1\ s^{-1}$ shear rate are shown in Figure 6.18, the piston velocity that produces the shear rates required was determined through the analytical solution for power law fluids flowing through a circular die which may be found in sources. In this case $U0 = 2.019 \times 10^{-5}\left[\frac{m}{s}\right] = 1.2\ \left[\frac{mm}{min}\right]$.

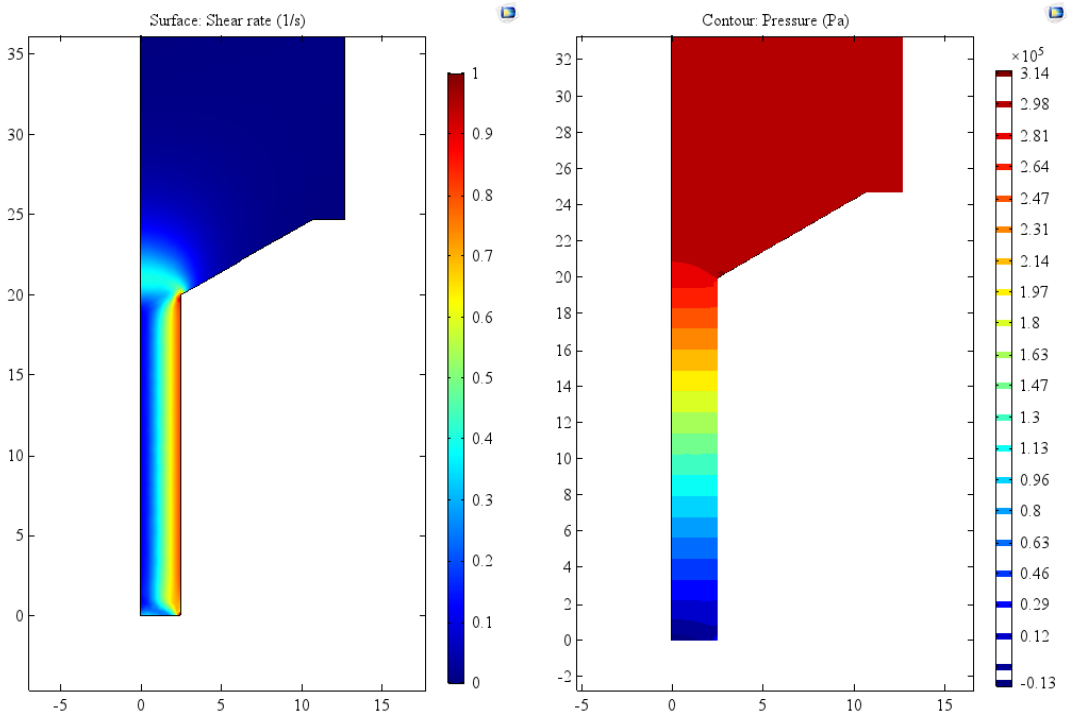

Figure 6.18 Simulation of capillary rheometer

A summary of the simulation results for other shear rates of interest to AFM is shown in Table 6.5. It can be seen from the table that the piston force and speed are within the capabilities of the Instron 5697 UTM so a machine with similar characteristics should prove adequate for this purpose. The basic dimensioning of the capillary rheometer is presented in Figure 6.19, the corrections detailed in the previous sections can be realized by changing die diameter lengths, sizes and modifying the speed or force of extrusion settings on the machine.

Table 6.5 Simulation results of capillary rheometer at shear rates of interest

Calculated shear rate [1/s]	Simulated shear rate [1/s]	Pressure Drop [Pa]	Piston force [kgf]	Piston speed [mm/min]
1	0.8	312360	16.6	1.2
10	10.5	1266000	67.2	12.1
100	104.7	4103100	217.8	121.1
600	627.8	10057000	534.0	726.6

The detailed design containing the coupling mechanisms, sealing, material selection and other considerations should be performed after a machine has been selected for the purpose. The procedure shown here could easily be modified to determine the target geometries for thinner or thicker media and variations between machine capabilities.

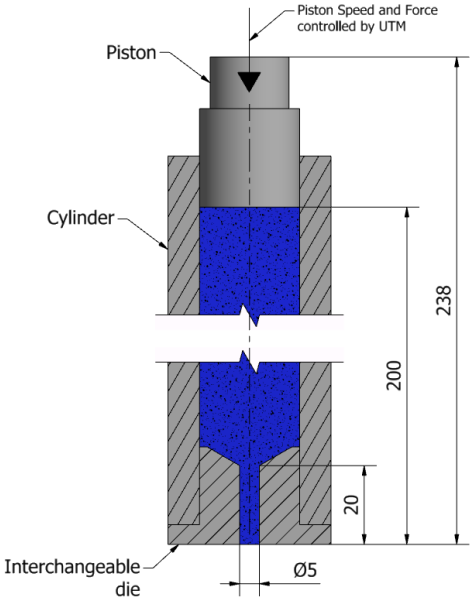

Figure 6.19 Basic dimensions of designed capillary rheometer for MV media and Instron 5697 UTM

With the help of this method, the viscosity of fluid media is tested by each experiment on different cases.

6.5 Discussion on the measurement results

With these work on getting the characteristic details of fluid media from Industrial company, the simulation can be worked better with more accurate prediction result. The result of this brand fluid media is used in ITP company currently with industrial cases introduced in next chapter. It shows great work on the prediction of material removal, profile accuracy of the edges and surface roughness. So the method is applicable for further research on the AFM process.

From the characterization of grains side, it is a useful piece of work as is a detailed description on how to practically perform such an analysis and how to process the collected data. If this same approach is applied to several samples a good tracking of grit properties change is sure to be achieved. The main goals of this measurement were to provide with a measurement on how the changes in the media could influence AFM processes and to offer a complete erosive wear mathematical model that could be used to simulate material removal rate and surface finish in a more accurate way. After collaborating this work with the simulation and models described above, it works in different industrial cases with a detailed description in Chapter 7.

From the viscosity of fluid media side, the procedure to determine the basic dimensions of a capillary rheometer suitable for measuring the viscosity of AFM media was presented in this chapter, an example was designed to be implemented into a universal testing machine to leverage its speed and force control mechanisms, and may prove useful for future researchers wishing to model the process. It is used to measure the viscosity with many different brands of fluid media in AFM for research and industrial purpose. For further work, the design process is not complete and should include an analysis of the load cell and encoder precision for the machine selected for the purpose and the detail design of components.

6.6 Summary

In this chapter, the measurement of the properties of fluid media in the AFM process is described with the method proposed and further industrial case studies with the industrial partner. The properties of the abrasive grains are essential in the modelling and simulation especially the grains shape factor. The details of fluid properties are used in the simulation to predict both well-designed experimental trials and two series of industrial case studies. More details about the cases and experiments will be further presented in next chapter.

Chapter 7 Experimental and industrial case studies

7.1 Introduction

In the previous chapters, theoretical studies were performed on material removal and surface generation in Abrasive Flow Machining by the proposed Multiscale Multi-physics modelling and simulation approach. The method of testing properties of Fluid media and grains inside is also introduced in Chapter 6. In this chapter, the details of Abrasive Flow Machining experiments based on coupons and aerofoil structures are described with the following purposes:

- Evaluation and validation of the multiscale multiphysics modelling approach on material removal and surface generation.
- In-depth study on the effects of material removal on different factors of process parameters.
- Optimization of the process parameters on industrial machining of real aerofoil structures to make the machining process better and more efficient.

7.2 Case study on steel coupons in Abrasive Flow Machining

7.2.1 Overview

An initial set of experiments was conducted during development of this dissertation as part of a NATEP Programme (National Aerospace Technology Exploitation Programme) funded project, with the goal to determine which factors are most influential on the process output (material removal and surface roughness) and provide data that can be used to develop simulation models.

The design of the experiment was developed with industrial partners in light of the NATEP project requirement. The experiment follows a four-factor full factorial design, with two levels (High and Low) on each factor in order to obtain the process

optimization and also provide the validation for simulations development. The agreed upon input factors are: Flow Rate, Volume, Media, Media Age.

7.2.2 Experimental setup details

7.2.2.1 Geometry and response measurement

Test piece geometry was designed to resemble IBR geometry as much as possible within complexity and budget limits, which is shown in Figure 7.1 and a photo of the non-processed test coupon in Figure 7.2.

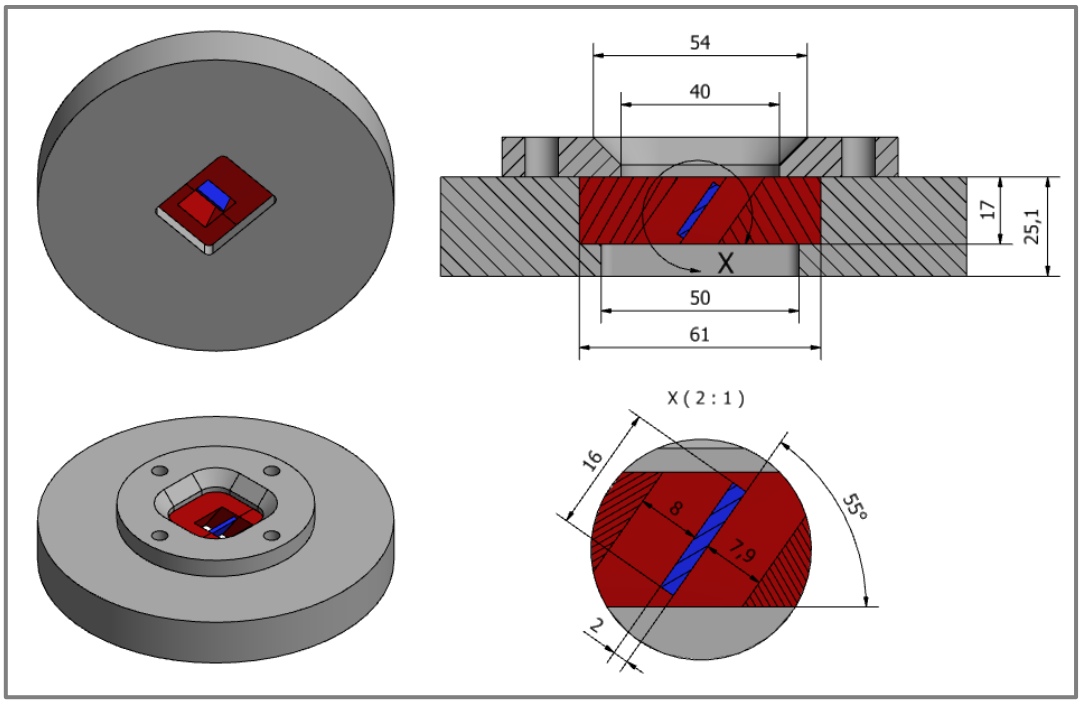

Figure 7.1 3D CAD model of AFM trial fixture, test coupon (blue), hardened steel coupon clamp (red)

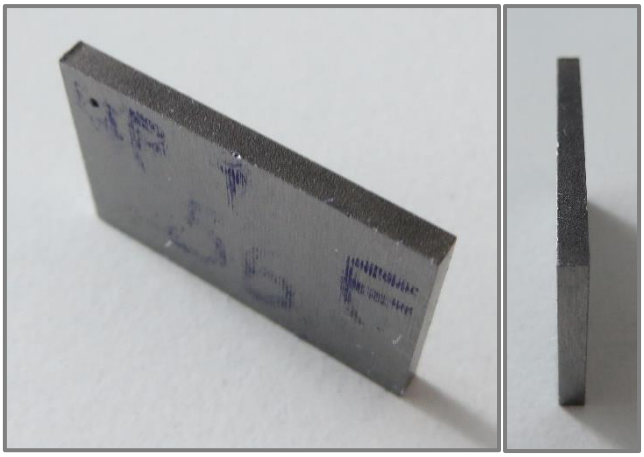

Figure 7.2 AFM trial test coupon

The test coupon was ground to a consistent thickness; the ends were cut with wire EDM thus a recast layer can be seen on both ends. Measurements of the coupon thickness and roughness were taken along nine evenly distributed points on the surface, and the coupon width was measured on three positions, the values are shown in the annexe. Measurements were performed with a Mitutoyo Digital Micrometer with a resolution of 0.001 mm and surface roughness obtained with a Taylor-Hobson Surftronic S-100 stylus roughness tester with a high-pass filter $\lambda_c = 0.8\,mm$, measuring length $l_n = 4\,mm$ and stylus tip radius $r_{tip} = 2\,\mu m$, the reported values all correspond to the average roughness (Ra) in μm.

The roughness measurements were performed along with two main directions shown in Figure 7.3, reference values for the tolerance that IBR manufacturers have to achieve are also given, it varies depending on the direction of the flow.

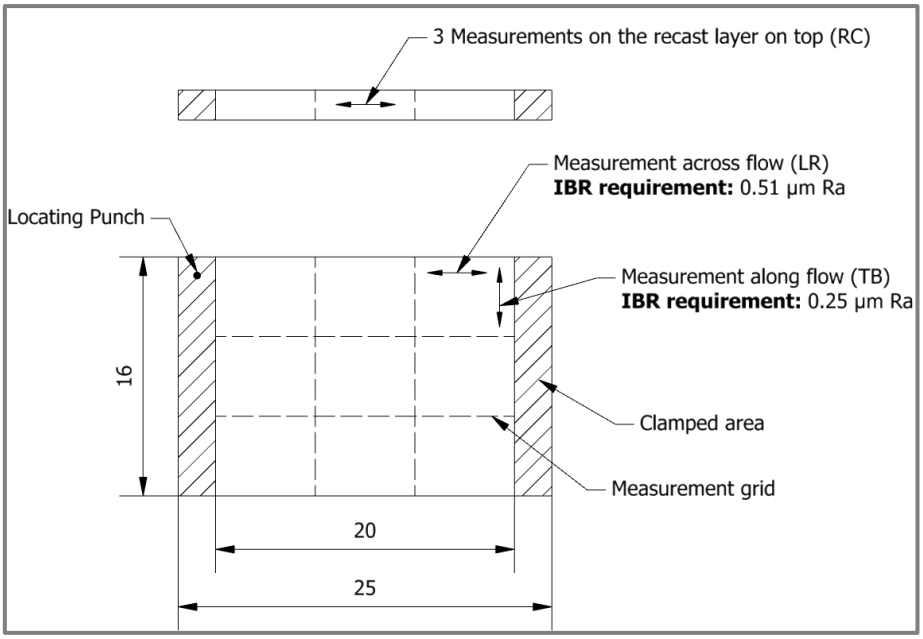

Figure 7.3 Surface roughness measurement locations and directions

The edge profile for the six first coupons tested was also moulded and captured with a TESA-VISIO 200 optical system, with the intent of comparison with the profile obtained by CFD based simulation.

7.2.2.2 The machine setup

It is useful to visualize the relationship between machine parameters with a simple linear model, in a model analogous to ohm's law. The flow rate through a part (electrical current in ohm's law) depends on the difference in pressure across the restriction (voltage in ohm's law). Imagining a constant representing the resistance to flow, which depends on media viscosity and part geometry (analogous to electrical resistance). This leads to:

$$\Delta P = Ep - Bp = \underbrace{R}_{f(\mu, geometry)} \cdot Q \qquad (7.1)$$

where *Ep* is the extrusion pressure, *Bp* is the back pressure, *Q* is flow rate and *R* is the flow resistance dependent on viscosity and geometry. This means that for a given

media viscosity and part geometry, a machine can only keep two parameters fixed, the third parameter will be a consequence.

The other parameter normally needed refers to the volume that is to be pushed through the part, it can be set independently of the parameters mentioned above and the way its specified varies depending on the machine used. It can be defined as volume, time or number of cycles. Although seemingly different, these are actually equivalent ways of measuring how much media has been worked through the part. The relationship between them is dependent on the flow rate selected and the piston size and stroke. Which can be represented as:

$$t = \frac{V}{Q} \tag{7.2}$$

$$n = \frac{V}{2 \cdot \pi \cdot r^2 \cdot l} \tag{7.3}$$

where *t* is the process time, *n* is the number of cycles, *Q* is flow rate, *r* is the cylinder radius and *l* is the cylinder stroke.

The extrude hone machine used in this experiment is equipped with what the manufacturer calls “AUTOFLOW” control which allows the user to set up the machine in one of three different modes. The machine counts volume only on upwards strokes so the total processed volume is twice the set value. The values for volume in this section will always be the total processed volume, the machine set up value will be shown in parenthesis for reference.

Pressure control mode with back pressure on:

> **Inputs required:** Extrusion Pressure (Ep), Back pressure (Bp), Volume (V)
>
> In this mode the machine will actively control the backpressure produced in the cylinder opposing the motion (keeping it constant), resulting in a higher flow rate if media viscosity reduces due to temperature build up, the machine stops the processing when it senses the cylinders have displaced the required volume.

Flow control mode with back pressure on:

Inputs required: Extrusion Pressure (Ep), Flow Rate (Q), Volume (V)

In this mode the machine will actively control the pressure in the cylinder opposing the motion, but the target in this case is keeping the flow rate constant (obtained by measuring the displacement rate of the cylinders), in this case if media viscosity reduces due to temperature build up, the backpressure rises (reducing the pressure drop across the restriction effectively compensating the viscosity drop to keep the flow rate constant), the machine stops the processing when it senses the cylinders have displaced the required volume.

Pressure control mode with back pressure off:

Inputs required: Extrusion Pressure (Ep), Volume (V)

In this mode the machine will not actively control the backpressure produced in the cylinder opposing the motion setting it zero, the machine stops the processing when it senses the cylinders have displaced the required volume.

7.2.2.3 Trial factors

The High-Low levels for the factors are:

Table 7.1 AFM trial levels

FACTOR	Unit	Low (-1)	High (+1)
Flow Rate (Q)	ml/s	16.4	32.8
Volume (V)	l	20 (10)	60 (30)
Media (M)	-	D100	649Z
Age (A)	-	Old	New

In this experiment, to determine the media with the lowest and highest viscosities in the absence of manufacturer-provided information, a simple flow test was devised with the media was extruded through a simple circular die which is shown in Figure 7.4. The machine was set up in flow control mode with backpressure enabled: Q=20 ml/s,

V=5000 ml (2500 ml), Ep=10 MPa. With different brands of fluid media used, the viscosity of each fluid media is determined following the way described above.

Both pressures and flow rate for each stroke were logged. Die length was 9.8 mm, its diameter was measured for each trial. The apparent viscosity shown in Figure 7.5 is thus obtained through the following equations:

$$shear\ stress = \tau = \frac{\Delta P \cdot R}{2L} \tag{7.4}$$

$$apparent\ shear\ rate = \dot{\gamma}_a = \frac{4Q}{\pi R^3} \tag{7.5}$$

$$apparent\ viscosity = \ \eta_a = \frac{\tau}{\dot{\gamma}_a} \tag{7.6}$$

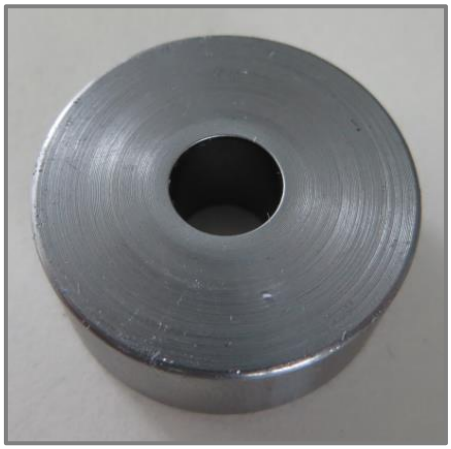

Figure 7.4 Flow rate test die

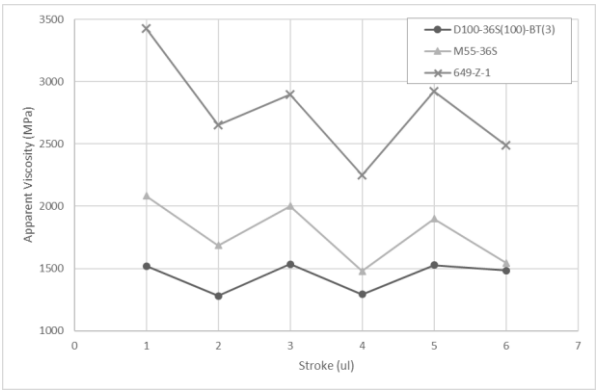

Figure 7.5 Relative apparent viscosities of the tested media

After all the equipment considerations, corrections and experimental procedure decision makings, the results serve only to establish the relative viscosity between the medias tested and should not be taken as rigorous measurements. The downward trend as the experiment progresses is explained due to the increasing temperature of the material due to viscous heating, the temperature change is less marked on thinner media which readily flows through the die.

In order to obtain media for the two different “Age” levels proposed, a new batch of media was subjected to an aging process, it was performed according to the project partner’s experience; a different machine was used to push the material through two 6 mm dies six times for 30 minutes at 3.5 MPa pushing pressure, backpressure was disabled.

In order to determine if the media aged appreciably, cut rate tests were performed on circular dies with an initial diameter of 6.985 mm, 10 mm length. Results are shown in Table 7.2.

Machine settings for the cut rate tests were: pressure control mode, with 10 MPa forward pressure, 5 MPa back pressure and 20,000 ml (10,000 ml) volume.

Table 7.2 Results from ageing cut-rate tests

MEDIA	Initial Diameter [mm]	Final diameter [mm]	Material Removal [mm]	% Change in Material Removal
649Z	6.985	7.696	0.711	46%
649Z Aged	6.985	7.366	0.381	
D100	6.985	7.061	0.076	33%
D100 Aged	6.985	7.036	0.051	

It can be found from the Table 7.2, the ageing procedure is managed to decrease the cut rate on the media by a considerable margin.

7.2.3 Results, analysis and discussion

The results obtained where analysed using main effects plots and an unequal variance, two sample t-test was conducted to evaluate if the difference of the means is statistically significant. Confidence level is 0.95 and the alternate hypothesis corresponds to a one-tailed test, the formal hypothesis statements are:

$$H_0: u_{-1} - u_{+1} = 0 \tag{7.7}$$

$$H_1: u_{-1} - u_{+1} < 0 \tag{7.8}$$

Were subscript -1 indicates the average for a low factor and +1 the average response for a high factor according to Table 7.1.

Making conclusions from differences that did not achieve statistical significance in this test was avoided, with a few exceptions where other data (from literature, other experiments or process experience) support the findings. The results were analysed with the help of Minitab software, the most important plots are presented in this section, the full treatment of the data may be found in the annex.

7.2.3.1 Material removal

With the exception of flow rate, the factors selected seem to have a marked influence on the MR Th of the system. It seems that, when all other factors are equal, flow rate does not appear to affect the material removed from the part (the difference in means is not statistically significant at the 0.95 confidence level), it is nevertheless an important factor to consider because the time that it takes to push through a certain volume (V) of media through a part is linearly dependent on the flow rate through its definition $t = V/Q$, it is then directly linked to the productivity of the process and one could conclude that it is in the interest of the AFM user to maintain as high a flow rate as possible within the limits set by machine capability and heat generation, if over work

(excessive material removal) occurs then the volume (V) pushed through the part can be decreased.

The trend that can be seen for Age (A) falls short of statistical significance, but if the results shown in Figure 7.6 are considered along with the trend shown in the main effects plot, media age does seem to have an effect on material removal, it is also widely known in industry that as media gets older, the cutting ability reduces mainly due to the rounding of the abrasive grit there is also a wealth of information on the literature and experience that confirms this phenomena, it may be simply that the ageing procedure used in this trial just wasn't long enough, further work may consider revising the ageing procedure used on this trial to check if a more pronounced effect can be produced, the shape of the response is also not well documented and neither is the effect of partially replenishing new media in the mix.

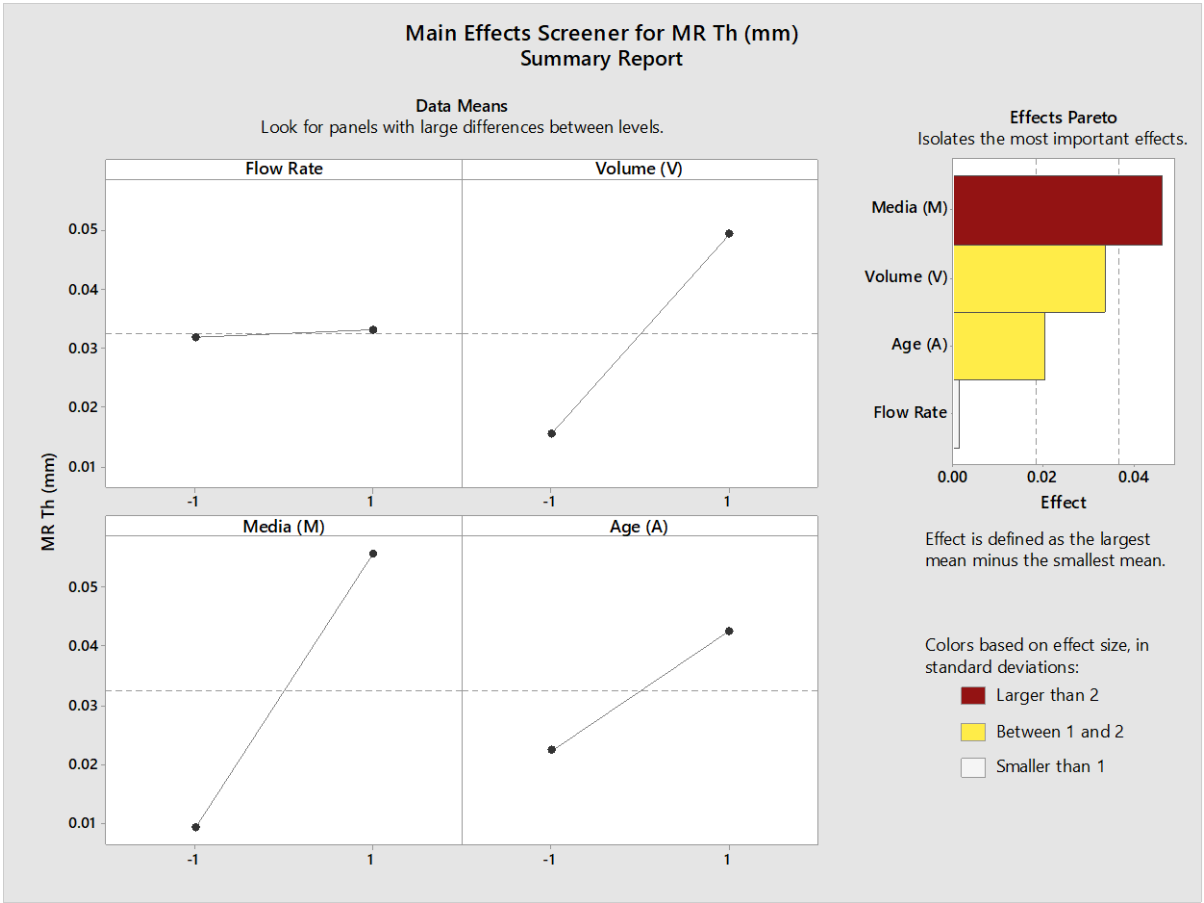

Figure 7.6 Material removal main effects plots from AFM trials

The effect of media viscosity (Media) is the strongest of all four tested, it is expected because more viscous media can strongly hold the abrasive particles against the workpiece, with an average response difference (effect) of 0.047 mm, changing media viscosity has an effect strong enough to be of importance to the processing of IBRs, from data obtained in meetings with the project partners, it is known that the tolerances required are in the order of 0.100 mm.

The second strongest effect is the amount of media extruded through the part (Volume), it is one of the most important parameters due to the fact that can be readily changed and continuously varied, because only two points where tested, it is not possible to determine the nature of the relationship between volume and material removal from the experimental data, however, there is evidence that it may be a linear relationship, this can be appreciated in Figure 7.6.

It can be seen from the plot that the material removed is consistently proportional with the volume of media that has been processed through the part after the first cycle, (shown at around 2e-3 m^3 on the graph), the material removal in the first cycle is higher and it is explained by the author to be due to the relatively easy removal of the peaks found in the initial surface. Also interesting is the fact that media that is being extruded with higher pressure removes material at a higher but still linear rate.

This graph suggests that pressure is another important factor influencing the material removal rate, in the case of the trials performed it has been kept constant, an extension of the trial to a 32 full factorial that includes 2 pressure levels is one possible avenue for follow up testing, another interesting proposition would be to try and replicate the linear relationship between seen in Figure 7.6, but for media viscosities, pressures and workpiece materials that are relevant to IBR processing.

7.2.3.2 Surface roughness

Roughness results are more difficult to interpret because the initial condition of the test coupons available was not classified, for this reason two different types of results were analysed: the final roughness (FR) and the percentage of surface roughness improvement (%SRI) with respect to the initial roughness (IR) according to:

$$\%SRI = \frac{IR - FR}{IR} \times 100 \quad (7.9)$$

The percentage is calculated for each of the data points in a coupon and then averaged.

The following short hand applies when referring to the different measurements in the following graphs and discussion, seeing Figure 7.3 for explanation on directions:

- **IR LR (µm):** average initial surface roughness measurement in the direction across the flow (left to right) (9 points)
- **FR LR (µm):** average final surface roughness measurement in the direction across the flow (left to right) (9 points)
- **IR TB (µm):** average initial surface roughness measurement in the direction along the flow (top to bottom) (9 points)
- **FR TB (µm):** average final surface roughness measurement in the direction along the flow (top to bottom) (9 points)
- **%SRI LR:** Percentage improvement in surface finish, calculated from the average initial and final surface roughness measurement in the direction across the flow (left to right) (9 points)
- **%SRI TB:** Percentage improvement in surface finish, calculated from the average initial and final surface roughness measurement in the direction along the flow (top to bottom) (9 points)

7.2.3.3 Surface roughness measured across the direction of flow (LR)

The main effects plots shown in Figure 7.7 and Figure 7.8 should exhibit opposing but similar gradients (by definition a lower FR will produce a higher %SRI). However, the plots show significant disagreement in Media, when looking at the FR there is a strong effect that is not present when evaluating the %SRI. Further investigation and discussion within the project team reveal that the initial surface roughness might have biased the results.

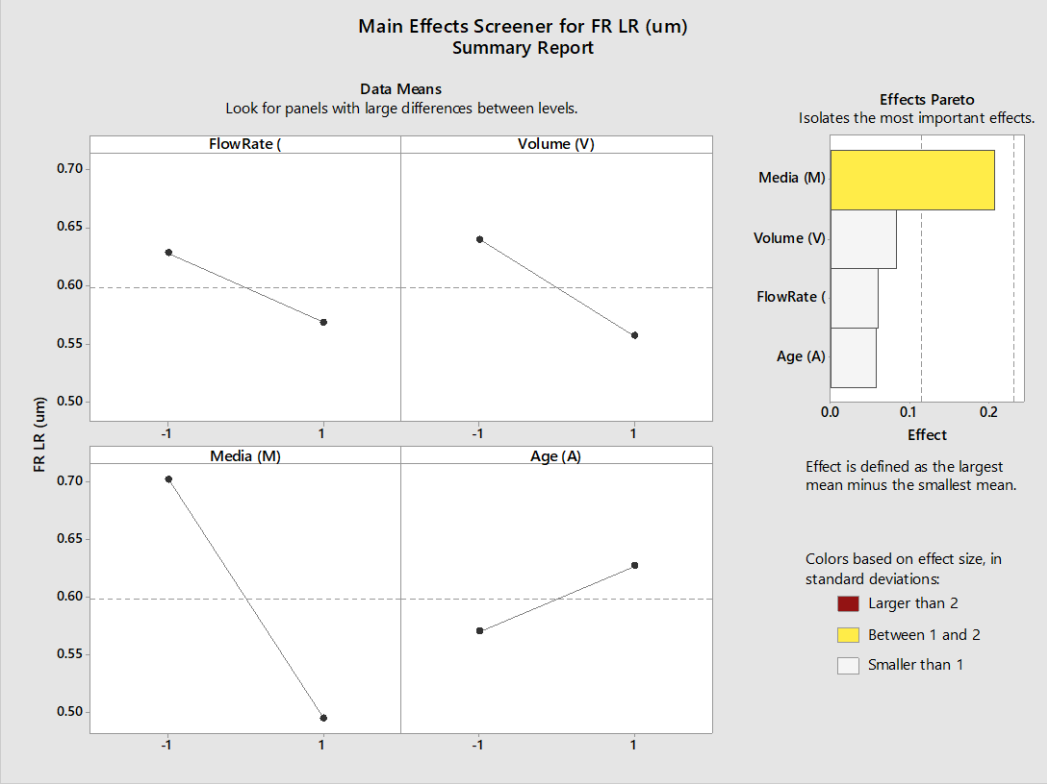

Figure 7.7 Main effects plot: final surface roughness across the direction of flow (LR)

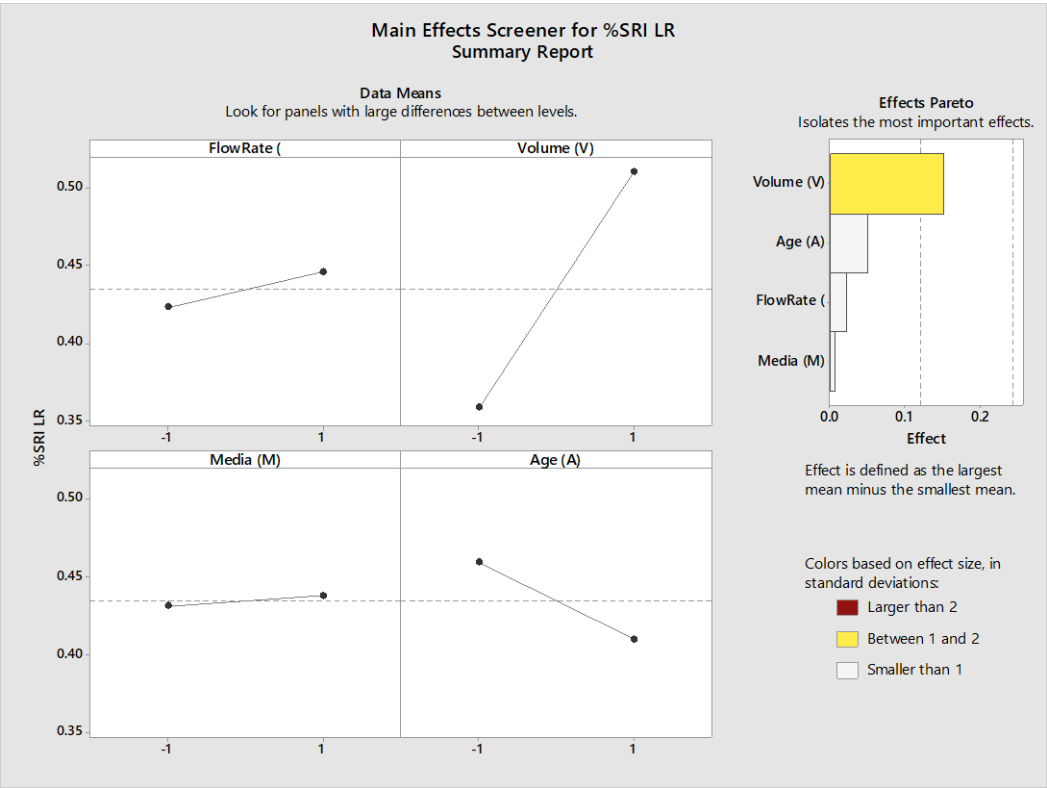

Figure 7.8 Main effects plot: surface roughness improvement across the direction of flow (LR)

To further evaluate this bias, Figure 7.9 was produced to show the variation in the initial surface roughness across the flow. This variation is significant and may affect the interpretation of the results. The only reasonable observations that can be made from this data is that AFM overall improved the surface finish measured across the flow.

As an example of this interference, the only processing conditions that were able to consistently reduce the roughness to a value below the reference tolerance was the 649Z media with a 60 L processing volume. However, the parts used for those conditions also registered some of the lowest starting roughness values. So it is not possible to separate the two effects.

The initial surface roughness on the main faces needs to be better controlled in future experiments to enable comparison between process parameters. The initial surface roughness should aim to coincide with that of a freshly milled IBR (around $0.75\ \mu m\ Ra$) according to the project partner's experience.

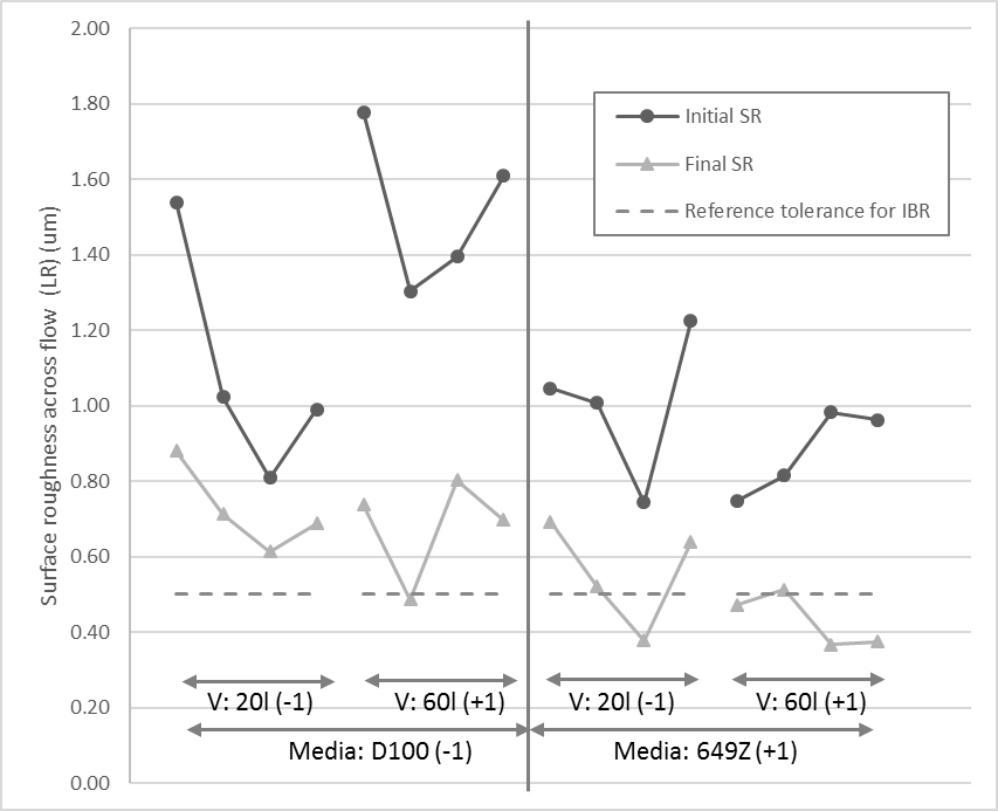

Figure 7.9 Initial coupon: surface roughness across the direction of flow (LR)

7.2.3.4 Surface roughness measured along the direction of flow (TB)

As a result of the manufacturing procedure used to make the coupons (grinding in one direction), the surface roughness along the flow lines (IR TB) was significantly lower than across the flow, averaging $0.36\ \mu m$ with the lowest value recorded as $0.21\ \mu m$ which is around 28% of the lowest value recorded in the other direction ($0.74\ \mu m$). This resulted in some samples getting rougher with the processing, it would seem that the limit roughness that can be achieved with the media tested was found, further improvement would require a reduction in grit size or viscosity, this relates with the behaviours shown in Figure 7.10, Figure 7.11 and Figure 7.12, where data from the William's publication in 1993 was plotted to show how roughness improvement plateaus after a few cycles [6].

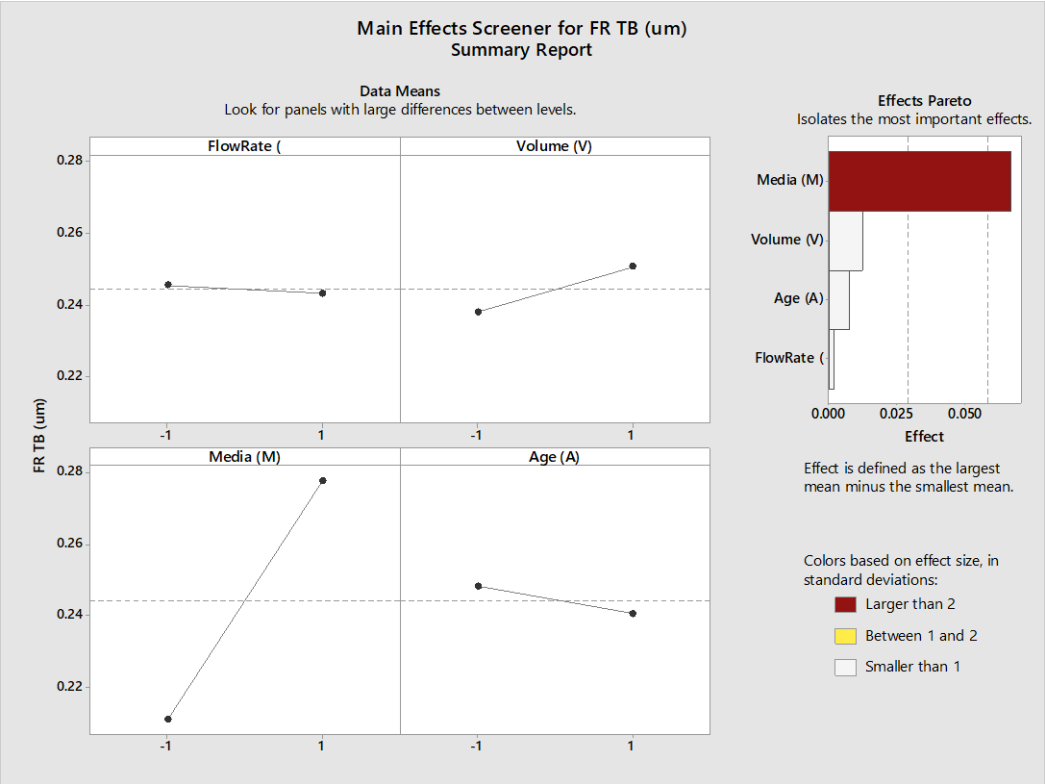

Figure 7.10 Main effects plot: final surface roughness along the direction of flow (TB)

The same limitation observed in the previous section applies for the interpretation of these results. The initial roughness is not constant enough to allow a good comparison of different process parameters. The strength and direction of the main effect with media is nevertheless interesting because it shows the thicker media consistently

produced a worse surface finish than the thinner media, even when the coupons assigned to those trials had some of the better starting surface finishes.

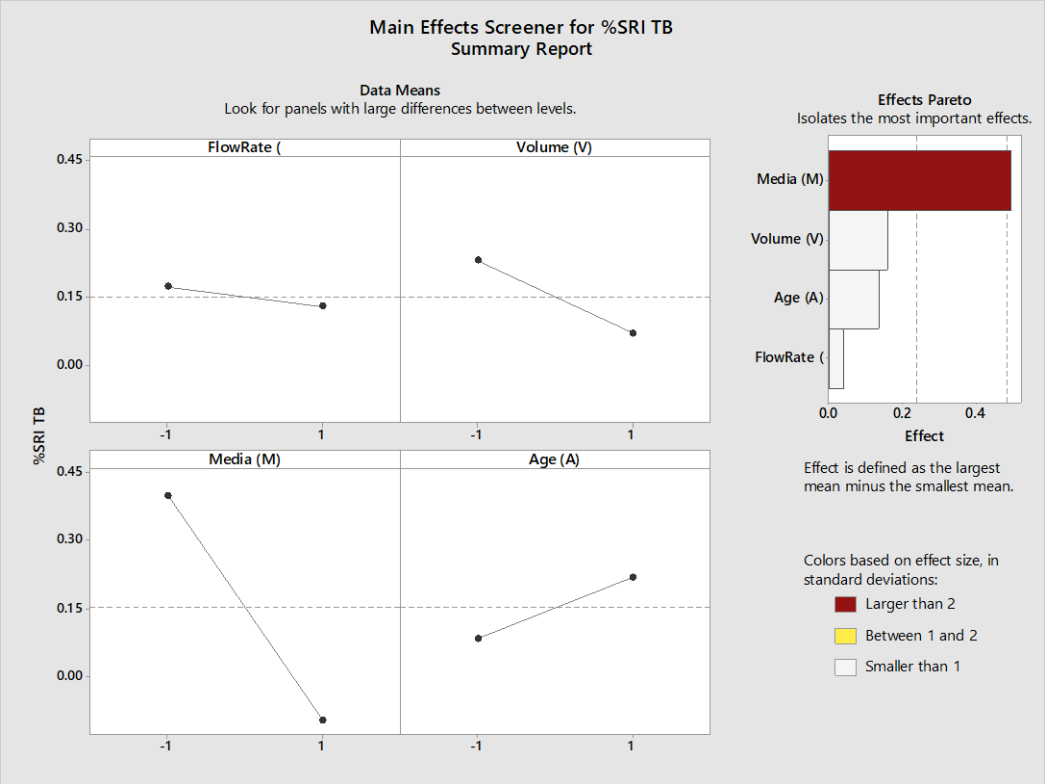

Figure 7.11 Main effects plot: surface roughness improvement along the direction of flow (TB)

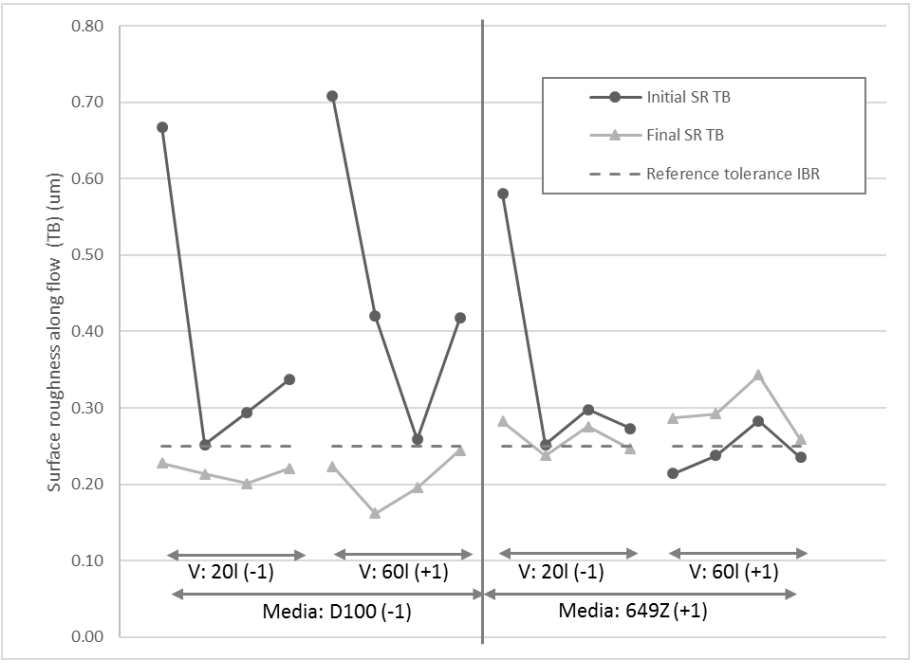

Figure 7.12 Initial coupon: surface roughness along the direction of flow (TB)

7.2.3.5 Surface roughness measured on the recast layer (RC)

The surface on top of the coupon correspond to a recast layer produced by the use of wire EDM to separate a single strip into the multiple test pieces. These measurements have a distinct advantage over the results in previous sections because the observed initial finish was very consistent, the agreement of the plots corresponding to final roughness and surface roughness improvement are a good indicator of the consistency of the initial roughness. The drawback is that the roughness produced by EDM is not representative of the initial condition of IBRs, the recast layer was measured at around $2.97\ \mu m$ which is almost 4 times what the project partners report as the roughness of a freshly milled IBR ($0.75\ \mu m$), this means that the conclusions drawn from these measurements might not apply to the process at lower starting roughness.

The main effects plots found in Figure 7.13, Figure 7.14 and Figure 7.15 reveal changes in Volume (V) and Media (M) as the most important effects that seem to directly influence the smoothing of the surface at these roughness level. The changes

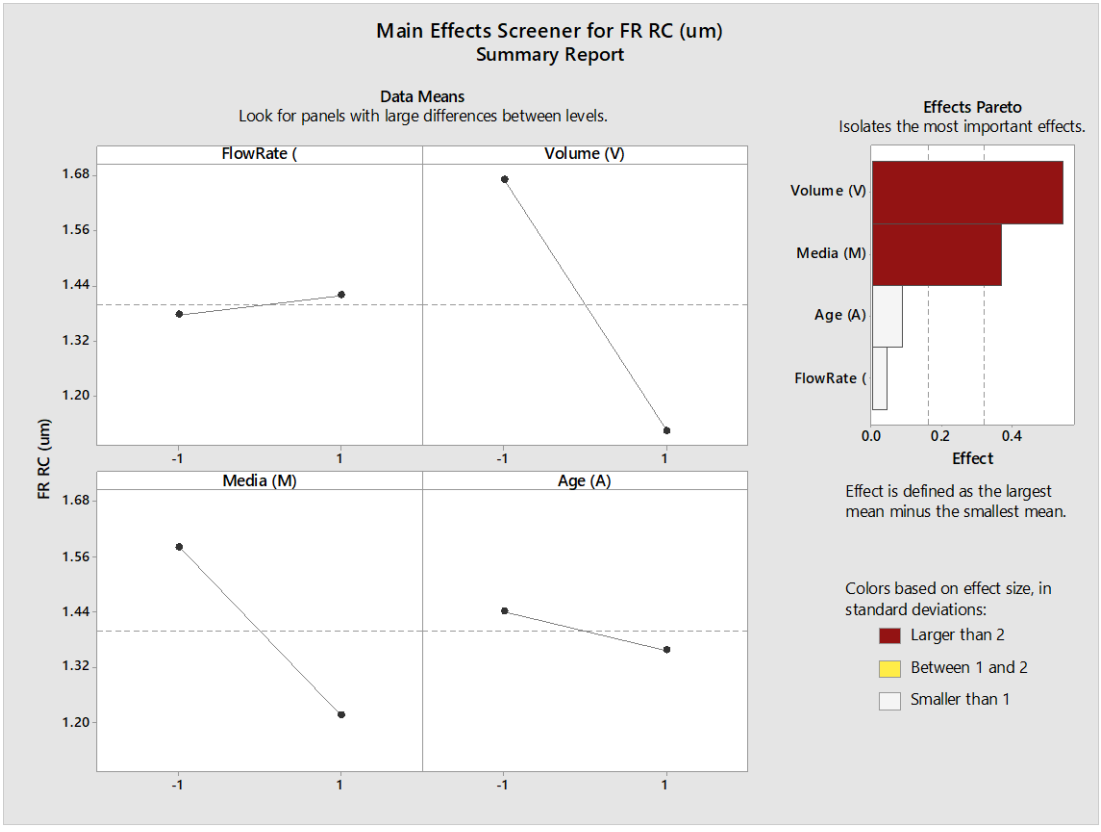

Figure 7.13 Main effects plot: final surface roughness in the recast layer (RC)

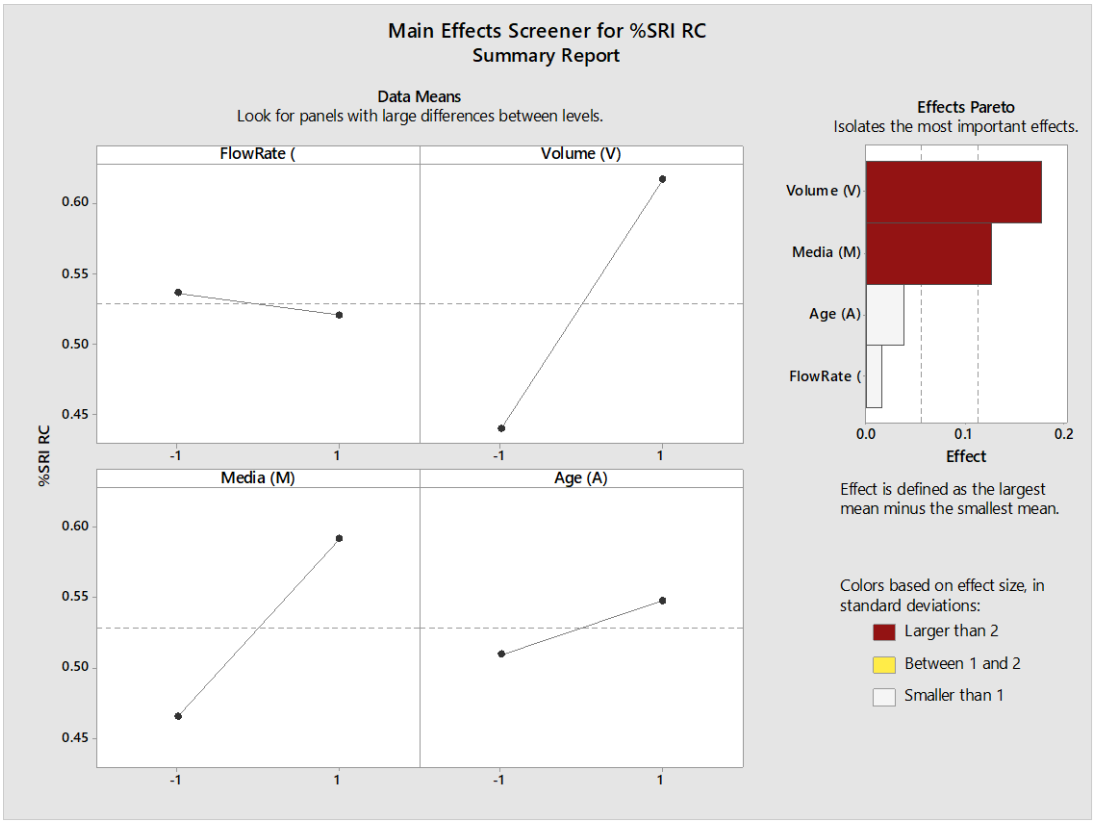

Figure 7.14 Main effects plot: surface roughness improvement in the recast layer (RC)

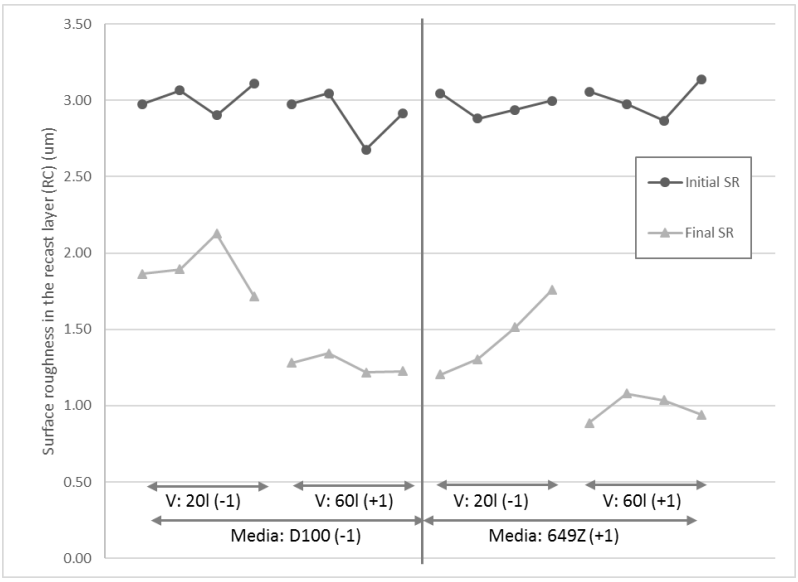

Figure 7.15 Initial coupon surface roughness in the recast layer (RC)

in Age (A) do not show a difference large enough to be of statistical significance but the ageing process could still be revised to find a new “Old” level which is likely to reveal that Age (A) is also a significant factor.

The surface roughness appears to be largely independent of Flow Rate (Q), in contrast with the Age (A) factor, one would be hard pressed to set an even higher level of flow rate in the without either exceeding the machine capacity or heating the media too much, so it is fairly safe to say flow rate does not influence the roughness response of the system. It is worth stressing the observation that the flow rate does change the time required to process a certain volume (V) of media, which is definitely important in a production environment.

7.2.4 Simulation results of material removal in AFM trials

The experiments described below in this section provide more data to test the simulation model against, the conditions for the coupon with the highest material removal were simulated first, the machine parameters where $Q = 16.4\left[\frac{ml}{s}\right]$, $D = 80\ [mm]$, $V = 60\ [l]$, $V1 = 2\ [l]$, in order to test if the abrasion coefficients obtained independently from these tests could be used to predict the process response, they were left unmodified for this simulation, the simulated shear rate field and the material removal results in thickness are shown in Figure 7.16.

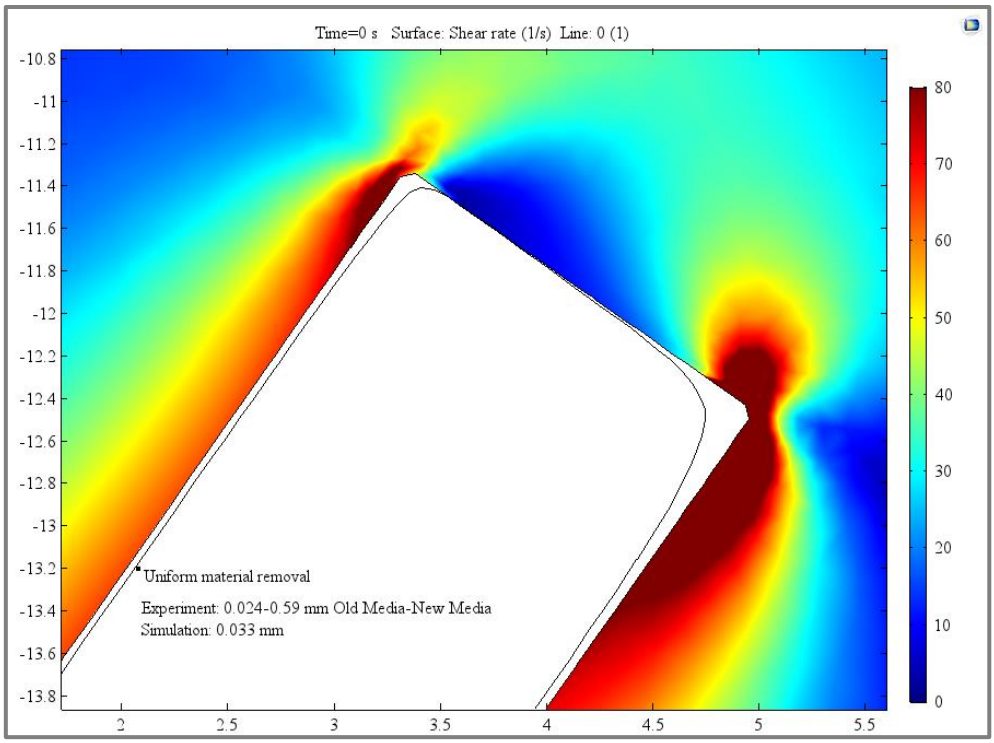

Figure 7.16 Simulation of the material removal in AFM trials

The profile was also reproduced with moulding paste and the resulting 2D profile was measured using the TESA-VISIO 200 optical system available in Brunel University Laboratory. The measured profile for Coupon 6 is shown in Figure 7.17 and the comparison with the simulated profile in Figure 7.18.

The simulated material removal estimated in this case lies in between the amount obtained by experimentation with old and new media, considering the abrasion coefficients where obtained from William's experiments and not from testing the actual media/material combination in our experiment. This is a reasonably close approximation.

Figure 7.17 Captured profile for Coupon 6

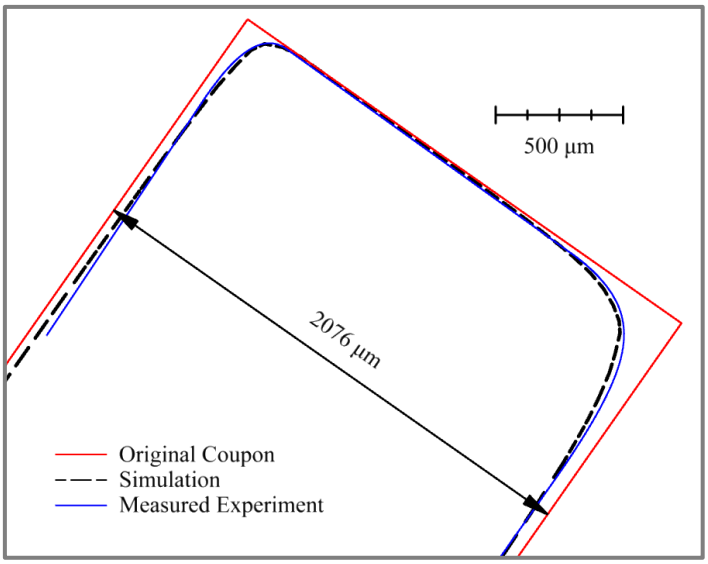

Figure 7.18 Comparison of the simulated and experimental Coupon 6 profile

The simulation was able to predict the resulting profile with reasonable accuracy, it is good enough that if such a prediction can be made before processing a single part, engineers could reduce the number of tests required when developing new parts with the process.

The main aspects that need to be worked on, before this can be considered as a tool for the AFM engineer, are:

- A library of viscosity curves to describe the different media available (in Chapter 6)
- The abrasion coefficients for media and workpiece material combinations of interest need to be determined, for this purpose, testing similar to the experiments by William's where the material removed from a circular die on each cycle is measured need to be performed.
- Experiments to find further validate and test the limits of the assumption made here that material removal is linearly related to shear rate also need to be conducted, this may be investigated by the use of different diameter dies.
- Pressure is considered in this model only via its connection to shear rate (i.e. higher extrusion pressure amounts to faster flowing media which results in a higher velocity gradient at the restriction), the magnitude of the backpressure's influence on material removal is not clear from the experiments performed, but the experience gained from the process indicates that it is well worth investigating.

7.3 Industrial case study on aerofoil structures in Abrasive Flow Machining

7.3.1 Simulation and manufacturing of T50 components

After the experiments on the steel coupons and the validation of the simulation with the results from the experiments. It is necessary to move forward to more complex aerofoil structures. First one is the T50 component. T50 component is a large ring made of titanium with 64 holes around which aims to guide the air flow between different blades. In this case Abrasive Flow Machining plays the role to machining and polishing the holes around to make the surface roughness of the holes better and improve the profile accuracy of the holes. The T50 component is shown in Figure 7.19

and the specification of the holes on T50 component is shown in Figure 7.20. The requirement of material removal on the hole is listed in Table 7.3.

Figure 7.19 T50 component

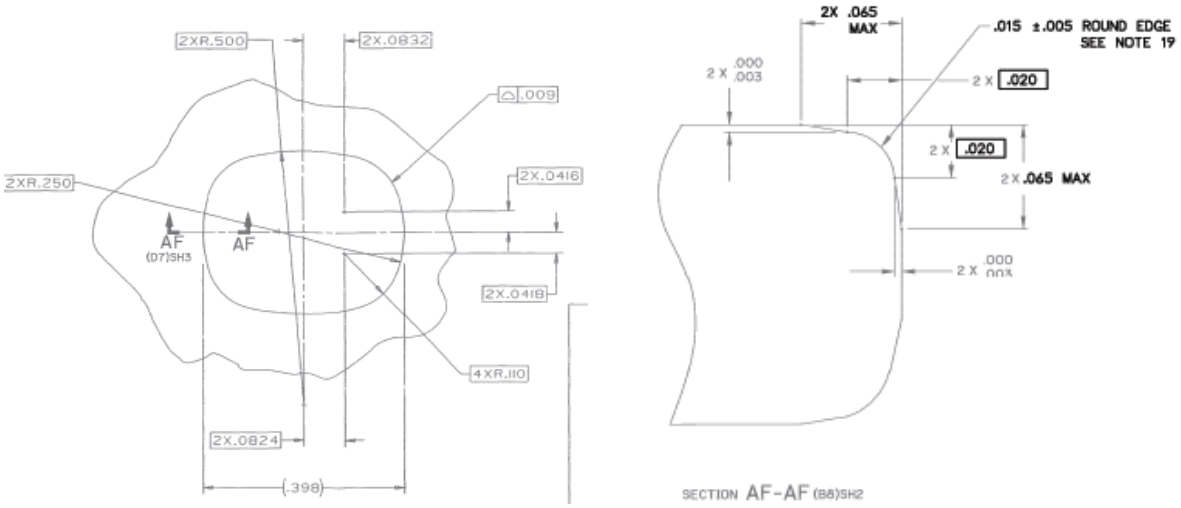

Figure 7.20 Specification of requirement on T50 component after AFM manufacturing

With the help of the simulations developed and validation from the AFM experiments on steel coupon, it is possible to import the 3D geometry of the fixture and T50 components to the simulations to predict and control the material removal rate and the process optimization (Figure 7.21). In Figure 7.21, the orange part is the T50 component while the other parts are fixures used to guide the fluid media flow through the critical holes at T50 component.

Table 7.3 Minimum stock removal requirements for holes manufacturing

<table>
<tr><td rowspan="2">Operation</td><td colspan="7">Pl1TF12 Class</td></tr>
<tr><td>A</td><td>B</td><td>C</td><td>D</td><td>E</td><td>F</td><td>G</td></tr>
<tr><td>Rough Machining ≥0.150 inch(3.81 mm) dia.</td><td>-</td><td colspan="5">Rough diameter must be a minimum of 0.006 inch (0.152mm) per side (0.012 inch/0.305 mm diameter) smaller than the minimum Finish Machining diameter</td><td>-</td></tr>
<tr><td>Rough Machining ≤0.150 inch(3.81 mm) dia</td><td>-</td><td colspan="5">Rough diameter must be a minimum of 0.002 inch (0.051mm) per side (0.004 inch/0.102 mm diameter) smaller than the minimum Finish Machining diameter</td><td>-</td></tr>
<tr><td>Finish Machining</td><td colspan="3">In accordance with the Engineering Drawing</td><td>Allow minimum 0.001 inch (0.025mm) per side for post-finish machining</td><td colspan="3">In accordance with the Engineering Drawing</td></tr>
<tr><td>Post- Finish</td><td>-</td><td>-</td><td>-</td><td>In accordance with the Engineering Drawing</td><td>-</td><td>-</td><td>-</td></tr>
</table>

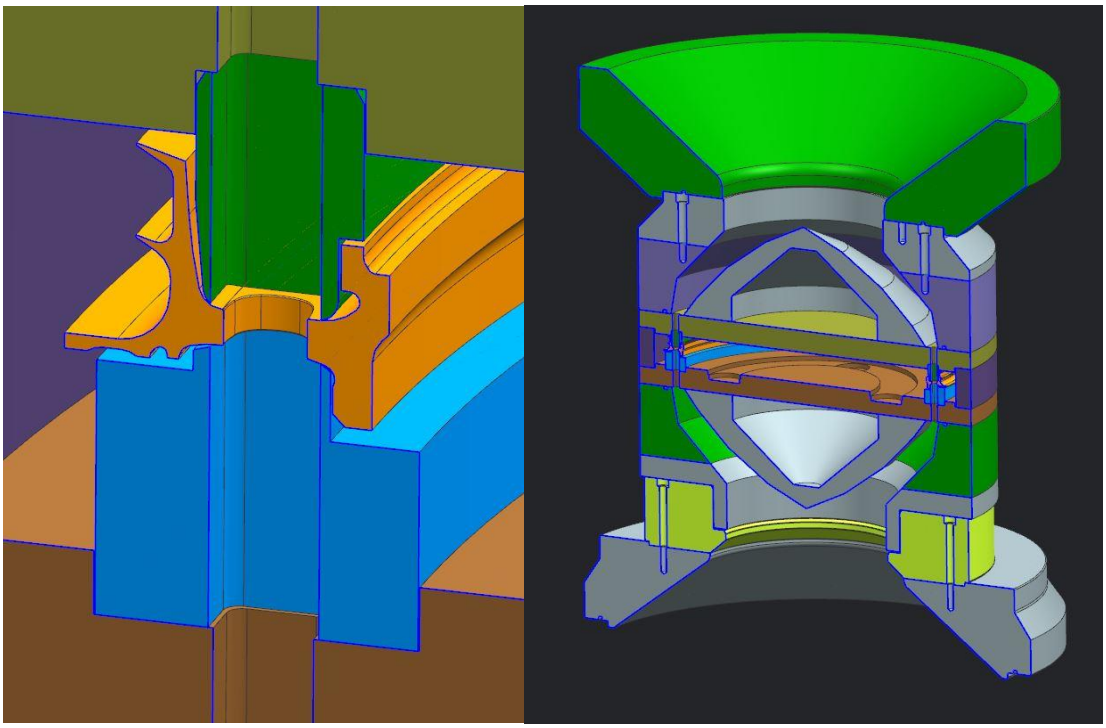

Figure 7.21 Design of the fixture for manufacturing T50 components in AFM process

In the first step of this case, the process parameters currently used by the company are imported into the simulation and the result of material removal is compared with industrial data. The process parameters are listed in Table 7.4. The results of simulation are shown in Figure 7.22, which are compared with the industrial results as listed in Figure 7.23. The results of comparation are listed in Table 7.5

Table 7.4 T50 - Process parameters

Programme Name	T50-555-1100-A04
Media Identity	EH Z649-Z1
Media Pressure	10 Bar
Media Volume	3,500 in^3
Process Cycles	12
Flow Rate	10 in^3/S
Media Temperature	28-35 C°
Process Time	N/A

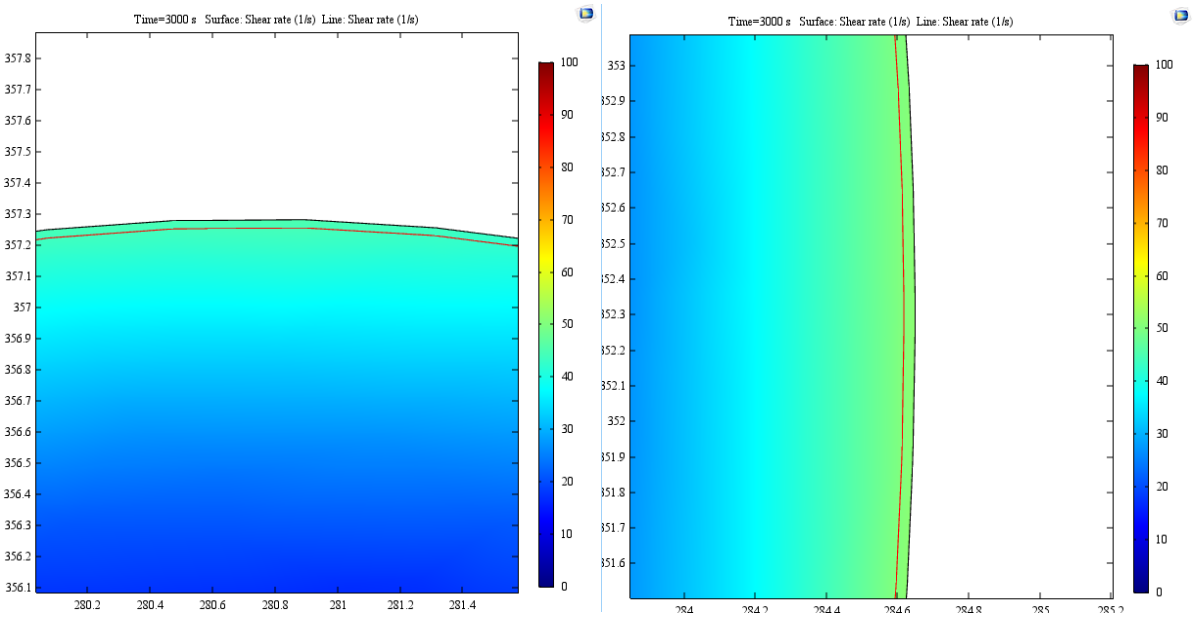

(a) (b)

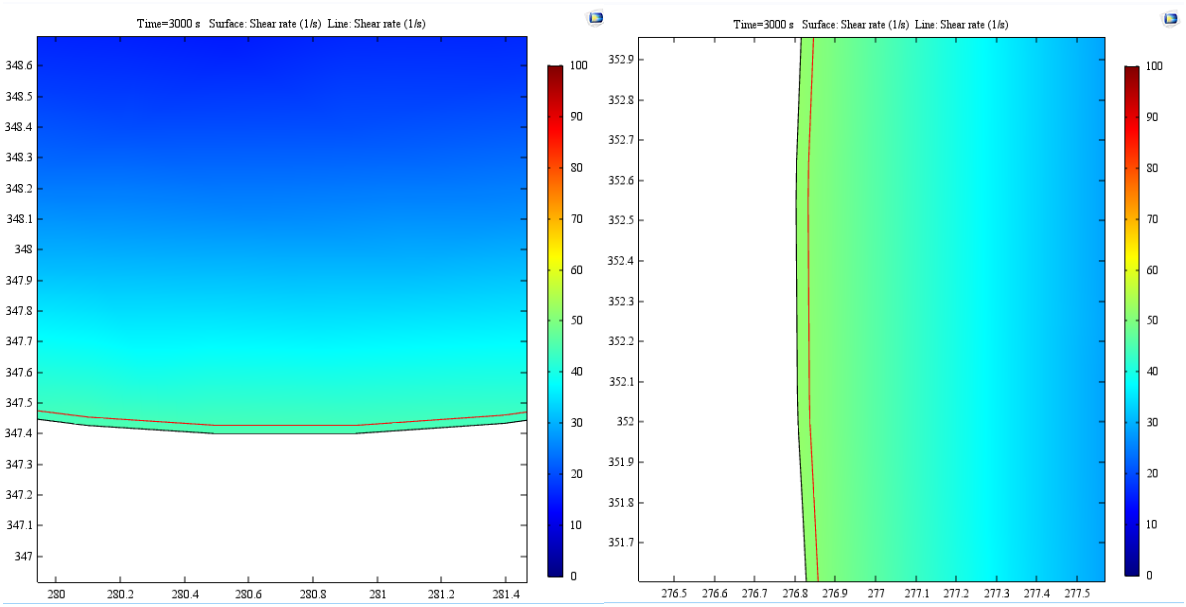

(c) (d)

Figure 7.22 Simulation results of material removal on process parameters

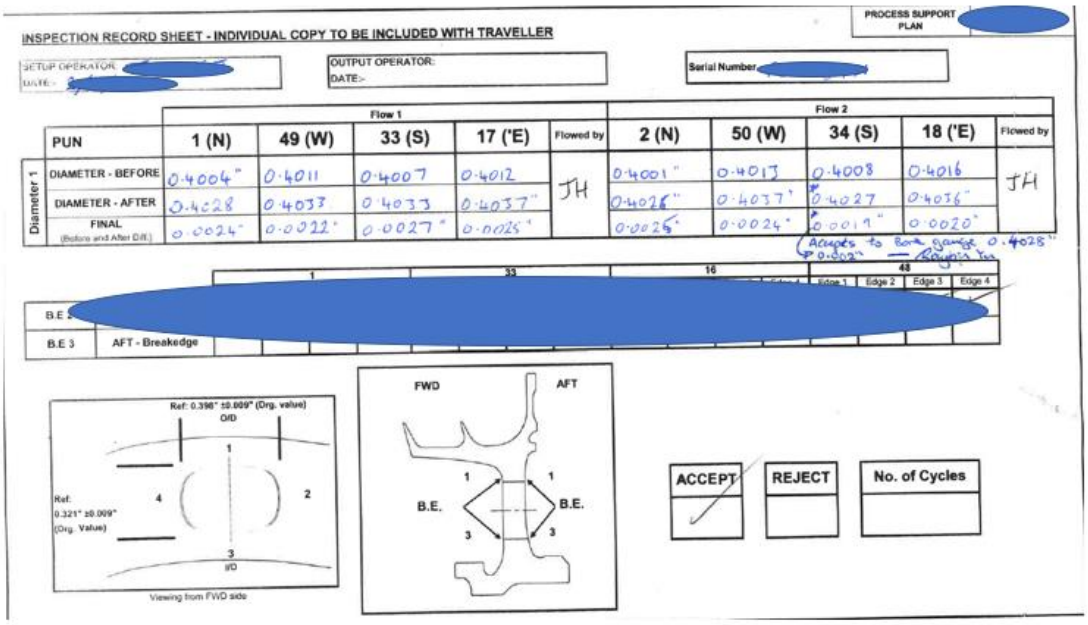

Figure 7.23 Partial industrial data log of material removal on T50 component

The results of material removal rate stay in high accuracy and can be used to predict real industrial cases. In the next step, the process parameter changed with the aim to shorten the manufacturing process so that the efficiency of manufacturing will be dramatically increased. It is obviously that increasing the pressure of fluid media will

increase the material removal rate and reduce the number of cycles of AFM process. However, it is necessary to figure out if it will be overdone and the profile accuracy of hole stays in the requirement.

Table 7.5 Comparation of simulation results and results on the shop floor industrial trials

Position	Predicted Depth	Error in Percentage
1(N)	0.0635	4.16%
2(W)	0.06096	2.08%
3(S)	0.04826	5%
4(E)	0.0508	4.16%

After several times of changing the parameters, all these results of simulation are compared to decide which one is the best to be used in manufacturing. The final process parameter are shown in Table 7.6. The material removal is shown in Figure 7.24. This setup decreases the process time from roughly 24 hours to 6 hours and also make the final work stay in the requirement of design.

Table 7.6 T50 - Process parameters after changes

Programme Name	T50-555-1100-A04
Media Identity	EH Z649-Z1
Media Pressure	30 Bar
Media Volume	3,500 in^3
Process Cycles	4
Flow Rate	30 in^3/S
Media Temperature	28-35 C°
Process Time	N/A

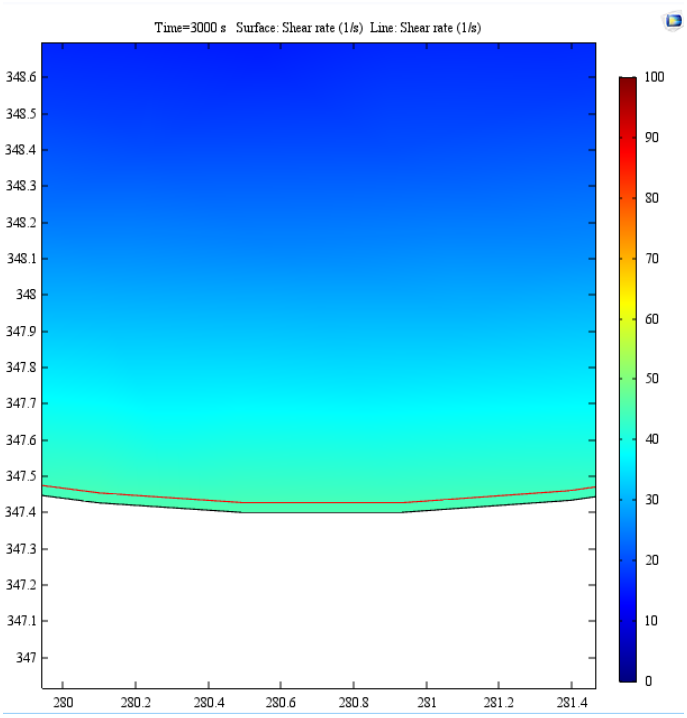

Figure 7.24 The material removal with new process parameters (Red line represents how much material being removed during the whole process while the colour bar representing the shear rate of fluid media during the machining process)

As a result of this case, the reliable of simulation is proved by the real industrial data. On the next step this simulation will be applied on some more complex geometry to prove the reliability of prediction and provide more help on the manufacturing of other types aerofoil structures.

7.3.2 Experimental manufacturing process on IBR segments and the simulation

After applying the simulation to T50 component and improve the manufacturing efficiency successfully, it is important to test the simulation on the manufacturing of the structures with more complex geometry. The next case is about the AFM manufacturing process of IBR. In the first step it is important to test the simulation with the geometry of blade on different manufacturing process parameters. As shown in Figure 7.25, the whole IBR Blisk is cut into 10 pieces to test under different process parameters. One of the segments is shown in Figure 7.26 and the specifications of the IBR segments are shown in Figure 7.27.

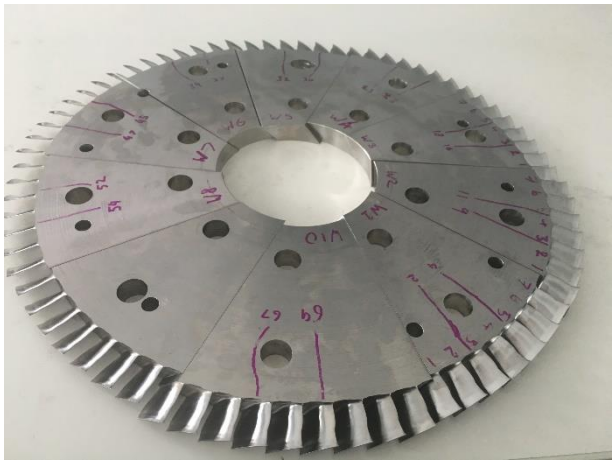

Figure 7.25 10 IBR segments cut from a whole piece of IBR component

Figure 7.26 One single IBR segment and the result of the blade surface after AFM machining

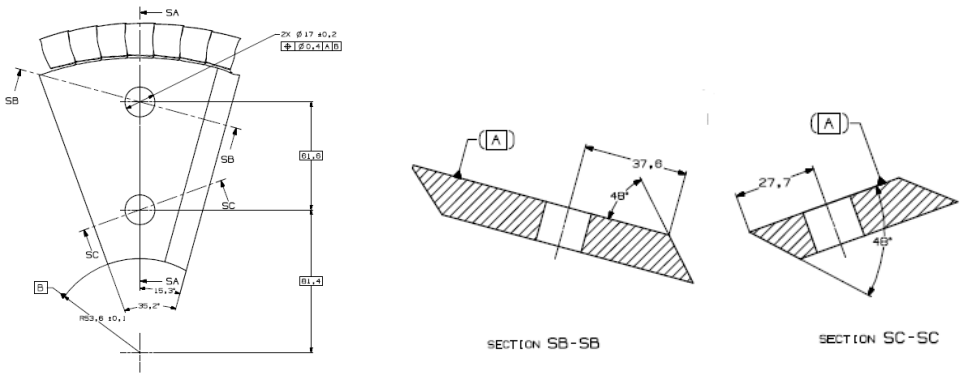

Figure 7.27 Specifications of the IBR segments

After cutting the IBR Blisk into pieces, the experiments are taken under different process parameters listed in Table 7.7. The design of these parameters aims to figure out under following description if the simulation can still predict the correct material removal and the profile of leading and trailing edge. On the other hand, this experiment also aims to figure out some more points not included in the experimental case of steel coupon. it is necessary to identify the role of back pressure in the process. The second and third parts are used to identify the simulation working on different back pressure with same flow rate. The second and fourth parts are used to identify the simulation working on different flow rate with the same back pressure. The fifth part is to find out if the surface roughness will be better with the final stage changed without changing the whole process. The sixth part is to simulate the real manufacturing process currently used.

Table 7.7 Process parameters of different IBR segments

Part Number	1	2	3	4	5		6
Total Volume (in^3)	500	2000	2000	2000	1500	500	5000
Media Pressure (Bar)	15	20	29	26	29	20	20
Flow Rate (in^3/s)	1	10	10	20	10	10	10
Back Pressure (Bar)	Default	Default	10	Default	10	Default	Default
Predicted back pressure (Bar)	13.07	0.95	10.15	0.37	10.15	0.95	0.95

The fixture is also very important as it has to limit the fluid only going through the gap of blades to monitor the machining environment as it is a whole IBR blade. The two blocks beside the segment own a similar geometry as the IBR blade. The fixture designed in this experiment is shown in Figure 7.28.

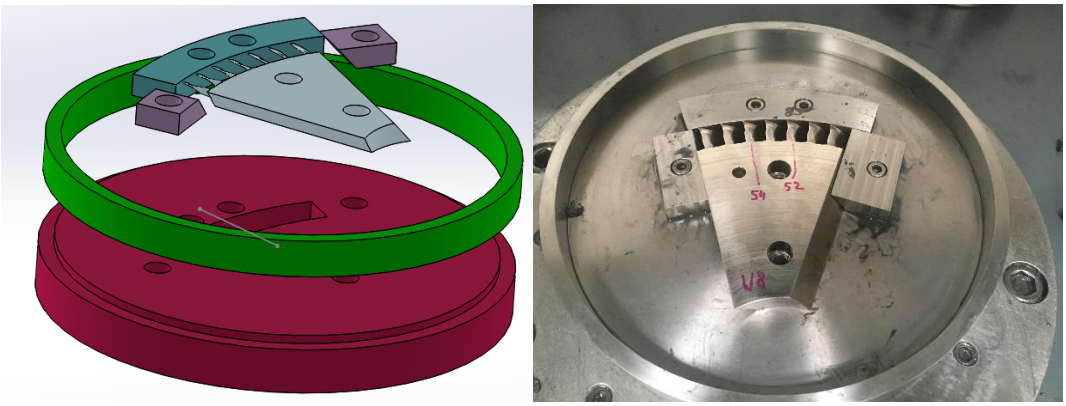

Figure 7.28 Fixture designed for the IBR segments AFM experiment

After the machining process with the process parameters described below, the blade shape is tested with CMM (Coordinate measuring machine). The inspection planes at which the parts were measured are at the following distances (as shown in Table 7.8)

Table 7.8 Inspection plane distance from component centreline

F-F	6.733		P-P	7.044
G-G	6.772		R-R	7.083
H-H	6.811		S-S	7.122
J-J	6.850		T-T	7.161
K-K	6.889		U-U	7.200
L-L	6.928		V-V	7.240
M-M	6.967		W-W	7.279
N-N	7.006		X-X	7.318

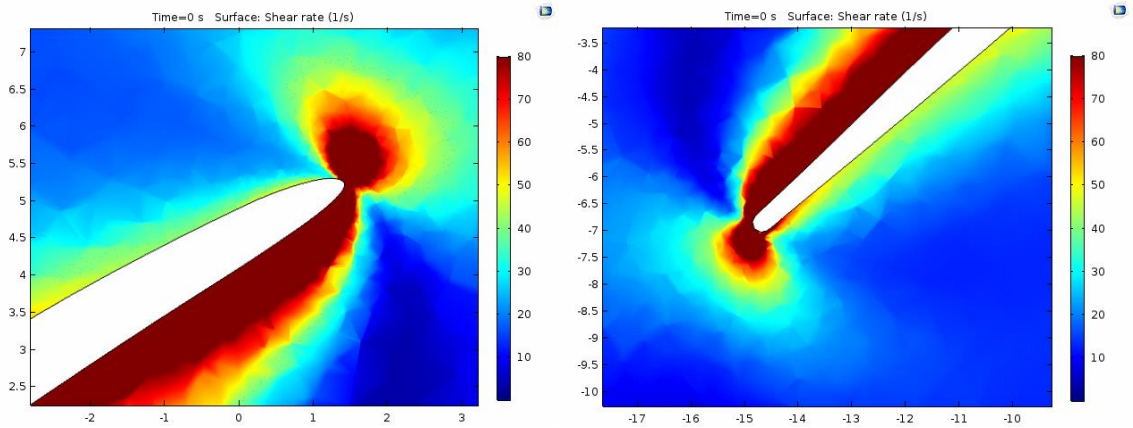

Figure 7.29 Simulation result around the leading edge profile and trailing edge profile (section view)

from the centreline of the component (dimensions are in inches). The inspection planes are parallel to the component centreline. For some reason the result of measurement can not be shown here, but the result of material removal matches with the result of experiments under different processing parameters. The simulation result of leading edge and trailing edge is shown in Figure 7.29.

7.3.3 IBR manufacturing

After the testing on IBR segments, it is essential to move forward to the validation of real industrial manufacturing data. The configuration of process parameters are suitable with the current manufacturing process.

7.3.3.1 The specifications of IBR manufacturing

In this case the IBR part is provided by ITP company which aims to find out the best process parameters for AFM process which provides better performance on both material removal rate and the surface roughness. The increase of material removal rate will lead to higher efficiency on the manufacturing of IBR parts and the better surface roughness will also decrease the noise of engine blades and improve the performance of blades in the engine.

The Blisks are machined as one complex part compared to an assembled fan blades, to reduce weight; improve fuel efficiency; and increase service life. The geometrical features include a thin blade around 0.1 mm to 0.6 mm, small arc radius of leading and trailing edges which is less than 0.1 mm. It is developed using CAD freeform surface to eliminate radial dimensioning. The design has a twist blade profiles and narrow channel of two adjacent blades only 4 mm in blade root and 15 mm in blade tip.

Design and manufacturing accuracies of the blade shape is very high. Aim is to keep the surface roughness R_a around 0.4 µm and minimising the surface contour errors to be less than 0.05 mm. Surface roughness is an important characteristics of the blade

as higher R_a could lead to boundary layer transition – airflow going from laminar to turbulent. As surface roughness increases from 0.5 µm to 800 µm, the performance loss coefficient increases by 56%. Hence, post process like abrasive flow machining can significantly enhances power transfer efficiency.

7.3.3.2 Simulation of material removal in IBR geometry

The rotors processed by AFM are normally made of Inconel 718 or Ti-6Al-4V alloys no information is currently available to calculate the abrasion constants for that material/media combination. This means that all of the results on this section serve as a qualitative indication of the abrasion, but no quantitative results can be obtained. Furthermore, the post AFM geometry is measured on a point-by-point basis with no actual digital profiles available to enable a comparison similar to what is shown in Figure 7.18, even if the profiles where routinely captured by the manufacturer, obtaining the information for academic research could prove very difficult due to confidentiality policy.

The simulation was run with machine parameters $Q = 564.67\left[\frac{ml}{s}\right]$, $D = 254\ [mm]$, $V = 508.2\ [l]$, $V1 = 2\ [l]$.

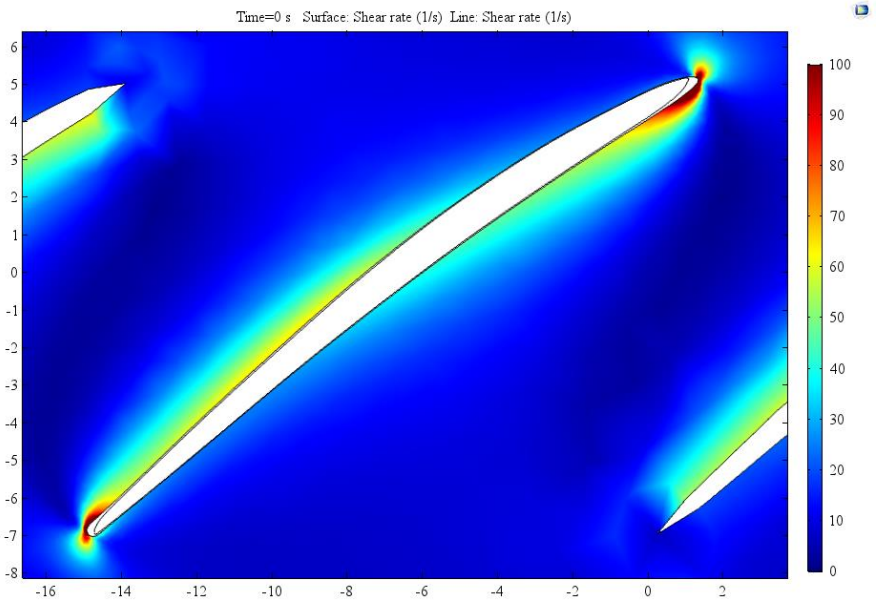

Figure 7.30 Simulated shear rate around the IBR profile (Section View)

It may be seen in Figure 7.30 that the predicted shear rate around the IBR profile suggests that material removal will not be uniform across along the profile, and the location of the points with higher abrasion corresponds to the most repeated AFM principle: abrasion occurs at the point where media enters the point of higher restriction, with almost no abrasion present in the leading side of the low-pressure face (top) and the trailing side of the high-pressure face (bottom).

The simulation suggests that the leading edge will change shape due to the non-uniform flow around it, the profile at 2 different simulation times is shown in Figure 7.31 and Figure 7.32 the lower part is subjected to higher abrasion due to the restriction created with the adjacent blade, the flow bending around the front of the profile causes a rather high chord length reduction when compared to the uniform material removal observed in the rest of the profile.

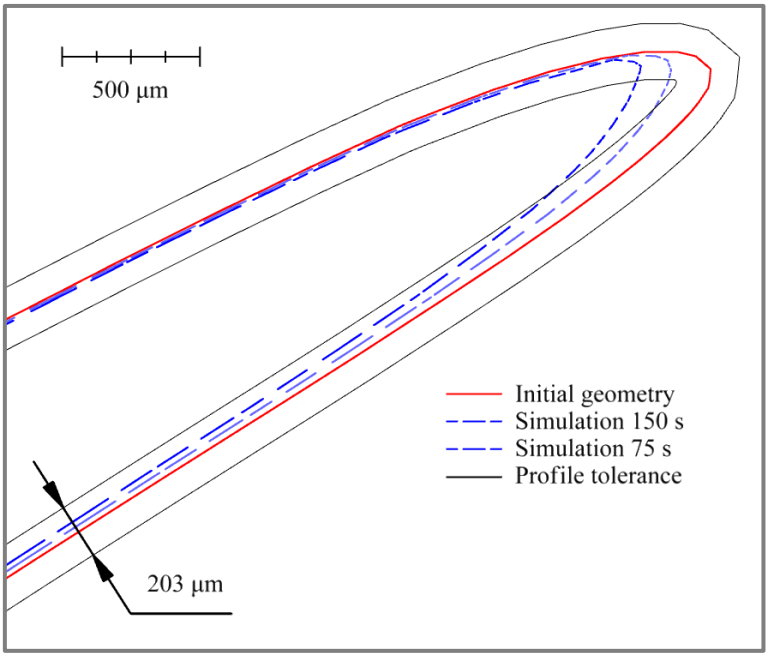

Figure 7.31 Simulated leading edge profile

The trailing edge simulation shows similar behavior, in this case the high abrasion area is swapped to the low pressure (top) side of the blade, again this coincides with the restriction created with the other adjacent blade, again the total chord length will be affected, the total reduction on the chord length is 0.34 mm at 150 s and 0.18 mm at 75 s, for reference the maximum IBR reduction aimed for the manufacturer is around

0.152 mm, so the simulation for 75 s should be fairly similar to what the end product looks like, the time taken to achieve this state will likely be much higher, due to the harder workpiece material.

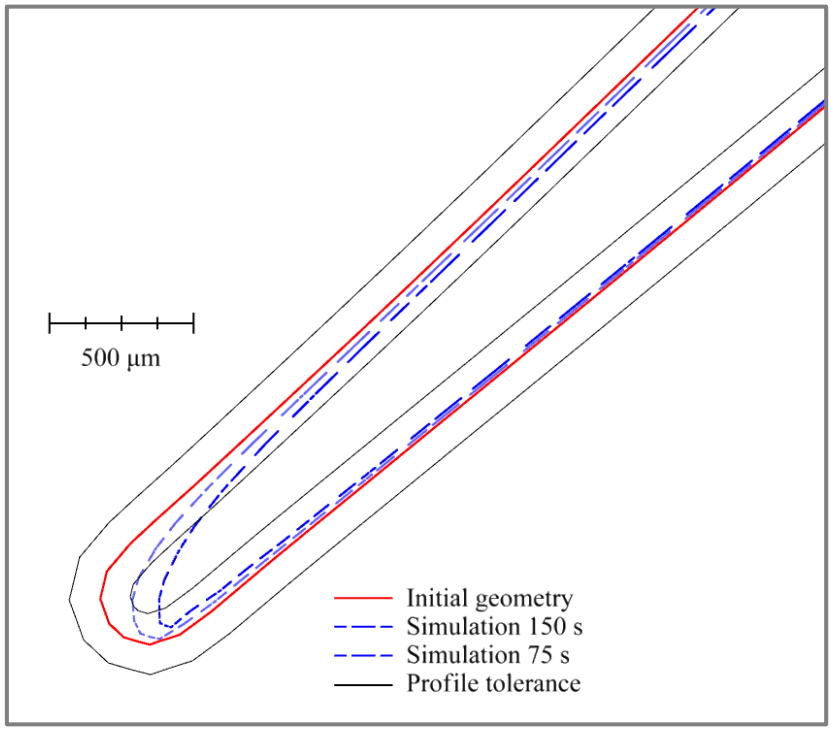

Figure 7.32 Simulated trailing edge profile

The simulations such as the one presented here can be used to:

- Determine the process parameters that are needed to process the part to a certain radius or shape.
- The simulation could potentially be run in reverse, starting with the desired final shape in order to obtain the geometry for rough milling the part. Ideally this could result in a reduction in fine milling stages.
- If the removal of certain features with a known depth such as machining grooves or scratches is required, the simulation could determine the process parameters most likely to erase them while keeping an eye for other unwanted removal.
- Tooling that directs and restricts the flow could be designed and simulated before the first article is processed.

An issue that is not readily apparent in previous plots can be appreciated in Figure 7.33. The mesh is not fine enough to calculate a smooth flow field around the leading edge, creating discontinuities that are not going to be present in real IBR. The number of elements that was used was limited by the hardware available, recommendations are proposed on the computational resources in Chapter 8.

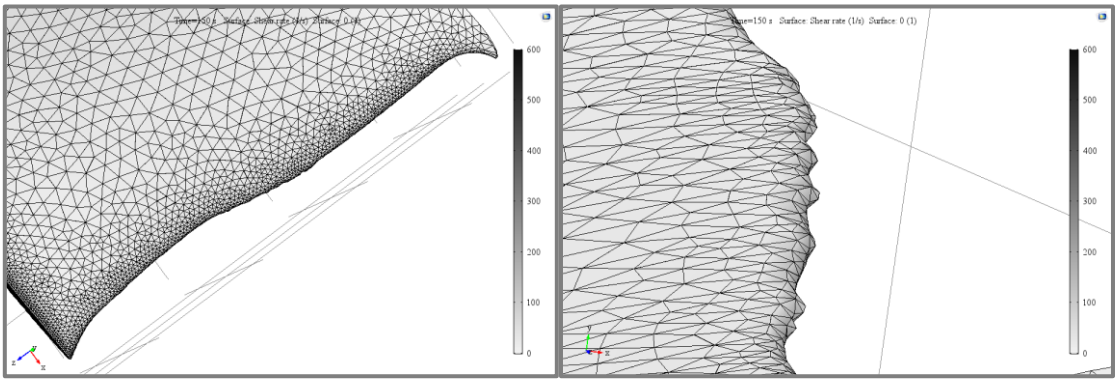

Figure 7.33 Discretization error at the leading and trailing edges

7.4 Conclusions

This chapter aims to validate the Multiscale Multi-physics modelling approach and simulation of Abrasive Flow Machining in previous chapters. AFM based trials on steel coupon and IBR segments have been carried out to achieve this aim. The industrial data from AFM process from ITP company is also used to validate the results of simulation. The following conclusions can be drawn:

(1) The simulation results agree quite well with the AFM trials results based on steel coupon with different process parameter and fluid media. The modelling and simulation proposed in the previous chapters can accurately predict the material removal and surface roughness to some extent.

(2) The simulation results fits well with the industrial data on T50 components and IBR component on material removal and profile accuracy. From different process parameter, the AFM process on T50 component was optimized significantly and help a lot with the manufacturing process of ITP company.

(3) The first version of simulation based virtual machining system on AFM has been handled to ITP company and be used to optimize the other components manufacturing on AFM process. It is basically working on new designed aerofoil components and help the company to decide machining process very conveniently.

From these conclusions, the Multiscale Multi-physics based modelling and simulation on AFM achieved the aims and objectives of this project.

Chapter 8 Conclusions and recommendations for future work

8.1 Assessment of the research

The objective of this research is to develop a multiscale multiphysics modelling and simulation approach for prediction of the material removal, surface generation, profile accuracy of leading edge and trailing edge of aerofoil structures in abrasive flow machining processes. With this aim and objective, this doctoral research has provided a thorough investigation on the approach and its implementation prospective by using COMSOL and MATLAB programming. The well-designed experimental trials and industrial case studies are set up to further evaluate and to validate the modelling and simulation. The conclusion sections at the end of each previous chapter highlight the modelling and simulation process, the results along with the underlying philosophy, the implementation and application perspectives of the approach.

The novelty and contributions to knowledge from this research lie in:

- The development of an innovative systematic approach for multiscale multi-physics based modelling and simulation of Abrasive Flow Machining process, which can provide a better scientific understanding of the relationships among the machining factors, properties of the particles in fluid media and material removal, and the surface generation.
- The prediction of material removal and profile accuracy of the AFM process from the multiscale multi-physics based modelling and simulation with the help of developing the Improved Preston equation and abrasion model.
- Investigation on the surface roughness and surface generation in Abrasive Flow Machining by using the Abrasive Process Modelling integrated with Hertz contact theory and Monte-Carlo Method.
- The method and basic experimental design to determine the viscosity functions using a capillary rheometer and the geometry properties of the solid abrasive particles in the fluid media, which provide the possibility to build the library of fluid media properties for developing the virtual AFM system.

- Development of the prototype virtual AFM system with the validation from well designed experiments and industrial manufacturing data on aerofoil structures. The virtual AFM system can be used to further optimise the AFM process for precision manufacturing of aerofoil structures.

8.2 Conclusions

The overall doctoral research aims to investigate the generation of high precision surfaces in relation to the affecting factors from the machine tool, tooling, workpiece material and operation conditions in precision manufacturing qualitatively and quantitatively. Precision turning process is modelled and simulated by MATLAB & Simulink. The modelling and simulation developed are thought to be suitable to simulate the precision surface generation, with a feature of efficiently modelling the nonlinear factors and the complex machining system. Molecular Dynamics simulation is used to model and simulate nanometric machining from the viewpoint of atomic structures and interactions. Precision machining trials and nanometric machining of silicon materials on an AFM are carried out to validate the model. The major results met with the research objectives can be summarised as follows:

- The multiscale multi-physics modelling and simulation is a critical methodology in the future. It can dramatically improve the feasibility and accuracy comparing to the model based on one single scale and physical field.
- The development tool – COMSOL and MATLAB can be used to model and simulate the multiscale multiphysics modelling and simulation. It offers significant advantages in terms of efficiency and comprehension compared other simulation tools.
- An improved Preston equation is introduced to solve the prediction of material removal of the AFM process. The development of the improved Preston equation provides a convenient means of predicting the material removal of Abrasive Flow Machining with different operating conditions.
- The development of the abrasion model provides an effective approach for predicting the surface roughness and profile accuracy of the component in the AFM process particularly by integrating with results from CFD simulation. With

theoretical and experimental considerations, flow rate and pressure distribution along the workpiece surface have been adopted as main factors in the model.

- The measurement of properties of fluid media in AFM process is described with both the method and a simple case from the industrial partner. The details of properties are essential in the modelling and simulation. The details of fluid properties are used in the simulation to predict both well-designed experimental trials and two series of industrial cases.
- The simulation results agree quite well with the AFM trials results based on steel coupon with different process parameter and fluid media. The modelling and simulation proposed in the previous chapters can accurately predict the material removal and surface roughness to some extent.
- The simulation results fits well with the industrial data on T50 components and IBR component on material removal and profile accuracy. From different process parameter, the AFM process on T50 component was optimized significantly and help a lot with the manufacturing process of ITP company.
- The first version of simulation based virtual machining system on AFM has been handled to ITP company and be used to optimize the other components manufacturing on AFM process. It is basically working on new designed aerofoil components and help the company to decide machining process very conveniently.

8.3 Recommendations for future work

As regarding the future work of this research, the following is suggested:

- Smoothed Particles Hydrodynamics is a possible method to optimise this multiscale multi-physics modelling and simulation. It is worthy to have a try on Smoothed Particles Hydrodynamics with the simulation of Abrasive Flow Machining.
- With the methods brought out in chapter 6 by measuring properties of fluid media and grains inside, it is hoped that such an approach may be used in the future to establish a “library” of media viscosities and geometry properties of

solid abrasive particles that can be used for the simulation-based virtual AFM system in the future.

- Currently the company is facing another challenge that how and when it is necessary to change the fluid media inside with the wear of grains which leads to the drop of machining efficiency and surface performance of the workpiece. It is possible to build a model in this simulation to optimize the procedure of changing the fluid media.
- ITP company brought a new challenge on controlling the temperature while AFM process. It is possible to involve the heat transfer model in this multiscale multi-physics based modelling and simulation to achieve this goal. With the control of temperature inside the virtual machining system, it will be more intelligent and automatically manufacturing the workpiece.

References

[1] Fletcher, A. J. and Fioravanti, A. "Polishing and honing processes: an investigation of the thermal properties of mixtures of polyborosiloxane and silicon carbide abrasive." *Proceedings of the Institution of Mechanical Engineers, Part C: Journal of Mechanical Engineering Science* 210.3 (1996): 255-265.

[2] Ikawa, N., et al. "Ultraprecision metal cutting—the past, the present and the future." *CIRP annals* 40.2 (1991): 587-594.

[3] Rhoades, Larry. "Abrasive flow machining: a case study." *Journal of Materials Processing Technology* 28.1-2 (1991): 107-116.

[4] Sehijpal, Singh, and H. S. Shan. "Development of magneto abrasive flow machining process." *International Journal of Machine Tools and Manufacture* 42 (2002): 953-959.

[5] Rhoades, Lawrence J. "Abrasive flow machining (AFM)." *Manufacturing Engineering* 101.5 (1988): 75-78.

[6] Perry, Kenneth E. "Abrasive flow machining method and tooling." U.S. Patent No. 4,005,549. 1 Feb. 1977.

[7] Perry, W. B. "Abrasive flow machining: principles and practices." *Nontraditional Machining* (1985): 121-127.

[8] Sankar, M. Ravi, V. K. Jain, and J. Ramkumar. "Abrasive flow machining (AFM): An overview." *Department of Mechanical Engineering, Indian Institute of Technology, Kanpur, India* (2011): 1-8.

[9] Rhoades, W. A. and Childs, R. L. TORT. Nuclear Science and Engineering, 107.4 (1991), 397-398.

[10] Bons, Jeffrey P. "A review of surface roughness effects in gas turbines." *Journal of Turbomachinery* 132.2 (2010): 021004.

[11] Meier, David L. "The theory and simulation of relativistic jet formation: towards a unified model for micro-and macroquasars." *New Astronomy Reviews* 47.6-7 (2003): 667-672.

[12] Eckardt, D. "Detailed flow investigations within a high-speed centrifugal compressor impeller." *Journal of Fluids Engineering* 98.3 (1976): 390-399.

[13] Bailey, C., et al. "Multiphysics modelling of the metals casting process." *Proceedings of the Royal Society of London. Series A: Mathematical, Physical and Engineering Sciences* 452.1946 (1996): 459-486.

[14] Zimmerman, William B. J. *Multiphysics modelling with finite element methods*. Vol. 18. World Scientific Publishing Company, 2006.

[15] Rhoades, Lawrence J. "Abrasive flow machining with an in situ viscous plastic medium." U.S. Patent No. 5,125,191. 30 Jun. 1992.

[16] Jain, V. K. "Magnetic field assisted abrasive based micro-/nano-finishing." *Journal of Materials Processing Technology* 209.20 (2009): 6022-6038.

[17] Rhoades, Lawrence J., et al. *Abrasive flow machining of cylinder heads and its positive effects on performance and cost characteristics*. No. 962502. SAE Technical Paper, 1996.

[18] Dubey, A. K. and Shan, H. S. "Micromachining by flow of abrasives." *17th AIMTDR, REC, Warangal, India* (1997): 269-275.

[19] Rhoades, Lawrence. "Abrasive flow machining with not-so-silly putty." *Met. Finish.* 85.7 (1987): 27-29.

[20] Garg, Vijay K. *Applied computational fluid dynamics*. CRC Press, 1998.

[21] Versteeg, Henk Kaarle, and Weeratunge Malalasekera. *An introduction to computational fluid dynamics: the finite volume method*. Pearson education, 2007.

[22] Bates, Paul D., Stuart N. Lane, and Robert I. Ferguson, eds. *Computational fluid dynamics: applications in environmental hydraulics*. John Wiley & Sons, 2005.

[23] Batchelor, Cx K. and Batchelor, G. K. *An introduction to fluid dynamics*. Cambridge University Press, 2000.

[24] Davies, Peter John. *The rheological and honing characteristics of polyborosiloxane/grit mixtures*. Diss. Sheffield Hallam University, 1993.

[25] Williams, R. E., Rajurkar, K. P. and Rhoades, L. J. "Performance characteristics of abrasive flow machining." *Non-Traditional Machining* , 1989.

[26] Williams, Robert Edward. *Investigation of the abrasive flow machining process and development of a monitoring strategy using acoustic emission*. Diss. University of Nebraska Lincoln, 1993.

[27] Buchely, M. F., et al. "The effect of microstructure on abrasive wear of hard facing alloys." *Wear* 259.1-6 (2005): 52-61.

[28] Jain, Rajendra Kumar and Vijay Kumar Jain. "Simulation of surface generated in abrasive flow machining process." *Robotics and Computer-Integrated Manufacturing* 15.5 (1999): 403-412.

[29] Jain, Rajendra K., Vijay K. Jain and Dixit, P. M. "Modeling of material removal and surface roughness in abrasive flow machining process." *International Journal of Machine Tools and Manufacture* 39.12 (1999): 1903-1923.

[30] Bungartz, Hans-Joachim, and Michael Schäfer, eds. *Fluid-structure interaction: modelling, simulation, optimisation*. Vol. 53. Springer Science & Business Media, 2006.

[31] Prasad, Sundar. "Numerical models in fluid structure interaction." *Canadian Journal of Civil Engineering* 33.3 (2006): 355-357.

[32] Dowell, Earl H., and Kenneth C. Hall. "Modeling of fluid-structure interaction." *Annual Review of Fluid Mechanics* 33.1 (2001): 445-490.

[33] Morand, Henri J-P. and Roger Ohayon. *Fluid structure interaction: Applied numerical methods*. Wiley, 1995.

[34] Weymouth, Gabriel David. *Physics and learning based computational models for breaking bow waves based on new boundary immersion approaches*. Diss. Massachusetts Institute of Technology, 2008.

[35] Weymouth, G., Dommermuth, D. G., Hendrickson, K. and Yue, D. K. P., *Advances in Cartesian-grid Methods for Computational Ship Hydrodynamics*, 26th Symposium on Naval Hydrodynamics, Rome, Italy, 17-22 September 2006.

[36] Mucha, Peter J., et al. "A model for velocity fluctuations in sedimentation." *Journal of Fluid Mechanics* 501 (2004): 71-104.

[37] Tornberg, Anna-Karin, and Michael J. Shelley. "Simulating the dynamics and interactions of flexible fibers in Stokes flows." *Journal of Computational Physics* 196.1 (2004): 8-40.

[38] Liu, Wing Kam, and Shaoqiang Tang. "Mathematical foundations of the immersed finite element method." *Computational Mechanics* 39.3 (2007): 211-222.

[39] Haase, Werner. "Unsteady aerodynamics including fluid/structure interaction." *Air & Space Europe* 3.3-4 (2001): 83-86.

[40] Kaligzin, G. and Iaccarino, G. "Toward immersed boundary simulation of high Reynolds number flows, Annual Research Briefs." *Center for Turbulence Research, Stanford University* (2003): 369-378.

[41] Fadlun, E. A., et al. "Combined immersed-boundary finite-difference methods for three-dimensional complex flow simulations." *Journal of Computational Physics* 161.1 (2000): 35-60.

[42] Hübner, Björn, Elmar Walhorn and Dieter Dinkler. "A monolithic approach to fluid–structure interaction using space–time finite elements." *Computer Methods in Applied Mechanics and Engineering* 193.23-26 (2004): 2087-2104.

[43] Grigoriadis, D. G. E., Stavros C. Kassinos, and Votyakov, E. V. "Immersed boundary method for the MHD flows of liquid metals." *Journal of Computational Physics* 228.3 (2009): 903-920.

[44] Degroote, Joris, et al. "Stability of a coupling technique for partitioned solvers in FSI applications." *Computers & Structures* 86.23-24 (2008): 2224-2234.

[45] Löhner, Rainald, et al. "Extending the range and applicability of the loose coupling approach for FSI simulations." *Fluid-Structure Interaction*. Springer, Berlin, Heidelberg, 2006. 82-100.

[46] de Boer, Aukje, Alexander H. van Zuijlen, and Hester Bijl. "Review of coupling methods for non-matching meshes." *Computer Methods in Applied Mechanics and Engineering* 196.8 (2007): 1515-1525.

[47] van Loon, Raoul, et al. "Comparison of various fluid–structure interaction methods for deformable bodies." *Computers & Structures* 85.11-14 (2007): 833-843.

[48] Campomanes, Marc Lorenzo, Charles Edward Becze, and Bastien Ste-Marie. "Method of machining airfoils by disc tools." U.S. Patent No. 7,303,461. 4 Dec. 2007.

[49] Phillips, James S., and Brian P. Arness. "Cooling duct turn geometry for bowed airfoil." U.S. Patent No. 5,716,192. 10 Feb. 1998.

[50] Beckman, Micah, and David Krzysztof Masiukiewicz. "Tool for abrasive flow machining of airfoil clusters." U.S. Patent No. 9,550,267. 24 Jan. 2017.

[51] Mittal, Rajat, and Gianluca Iaccarino. "Immersed boundary methods." *Annu. Rev. Fluid Mech.* 37 (2005): 239-261.

[52] Shyy, Wei, et al. "Computational fluid dynamics with moving boundaries." *AIAA Journal* 36.2 (1998): 303-304.

[53] Lefrançois, Emmanuel, and Jean-Paul Boufflet. "An introduction to fluid-structure interaction: application to the piston problem." *SIAM Review* 52.4 (2010): 747-767.

[54] Wan, S., et al. "Process modeling and CFD simulation of two-way abrasive flow machining." *The International Journal of Advanced Manufacturing Technology* 71.5-8 (2014): 1077-1086.

[55] Howard, Mitchell James. *Development of a machine-tooling-process integrated approach for abrasive flow machining (AFM) of difficult-to-machine materials with application to oil and gas exploration components*. Diss. Brunel University London, 2014.

[56] Schmitt, Joachim, and Stefan Diebels. "Simulation of the abrasive flow machining process." *ZAMM-Journal of Applied Mathematics and Mechanics/Zeitschrift für Angewandte Mathematik und Mechanik* 93.2-3 (2013): 147-153.

[57] Uhlmann, E., Doits, M. and Schmiedel, C. "Development of a material model for visco-elastic abrasive medium in abrasive flow machining." *Procedia CIRP* 8 (2013): 351-356.

[58] Uhlmann, Eckart, Christian Schmiedel and Wendler, J. "CFD simulation of the abrasive flow machining process." *Procedia CIRP* 31 (2015): 209-214.

[59] Fu, Youzhi, et al. "Blade surface uniformity of blisk finished by abrasive flow machining." *The International Journal of Advanced Manufacturing Technology* 84.5-8 (2016): 1725-1735.

[60] Brown, D. L., et al. *Applied Mathematics at the US Department of Energy: Past, Present and a View to the Future, United States Dept. of Energy, Washington*. DC, Technical report, 2008.

[61] Keyes, David E., et al. "Multiphysics simulations: Challenges and opportunities." *The International Journal of High Performance Computing Applications* 27.1 (2013): 4-83.

[62] Randrup, Jørgen and Peter Möller. "Brownian shape motion on five-dimensional potential-energy surfaces: nuclear fission-fragment mass distributions." *Physical Review Letters* 106.13 (2011): 132503.

[63] Siegel, A., et al. "Software design of SHARP." *Joint International Topical Meeting on Mathematics & Computation and Supercomputing in Nuclear Applications, Monterey, California*. 2007.

[64] Pointer, W. D. "Multi-physics reactor performance and safety simulations." *URL* http://www.ne.anl.gov/capabilities/sharp (2012) (accessed on 18 December 2019).

[65] Ashby, Steve, et al. "The opportunities and challenges of exascale computing." *Summary Report of the Advanced Scientific Computing Advisory Committee (ASCAC) Subcommittee* (2010): 1-77.

[66] Zwart, Simon Portegies, et al. "A multiphysics and multiscale software environment for modeling astrophysical systems." *New Astronomy* 14.4 (2009): 369-378.

[67] Benoit, Roland, et al. "Abrasive blade tip." U.S. Patent No. 5,603,603. 18 Feb. 1997.

[68] Fish, Jacob, ed. *Multiscale methods: bridging the scales in science and engineering*. Oxford University Press, 2010.

[69] Lucia, Angelo. "Multi-scale methods and complex processes: A survey and look ahead." *Computers & Chemical Engineering* 34.9 (2010): 1467-1475.

[70] Kumar, S. Santhosh and Somashekhar S. Hiremath. "A review on abrasive flow machining (AFM)." *Procedia Technology* 25 (2016): 1297-1304.

[71] Carter, R. Sykes, Robert L. Rhoades, and Charles H. Wood. "Lamp structure, having elliptical reflectors, for uniformly irradiating surfaces of optical fiber and method of use thereof." U.S. Patent No. 6,626,561. 30 Sep. 2003.

[72] Jain, V. K. and Adsul, S. G. "Experimental investigations into abrasive flow machining (AFM)." *International Journal of Machine Tools and Manufacture* 40.7 (2000): 1003-1021.

[73] L'vov, Victor S., et al. "Improved shell model of turbulence." *Physical Review E* 58.2 (1998): 1811.

[74] Machado, Margarida, et al. "Compliant contact force models in multibody dynamics: Evolution of the Hertz contact theory." *Mechanism and Machine Theory* 53 (2012): 99-121.

[75] Gorana, V. K., Jain, V. K. and Lal, G. K. "Forces prediction during material deformation in abrasive flow machining." *Wear* 260.1-2 (2006): 128-139.

[76] Singh, Sachin, et al. "Finishing force analysis and simulation of nanosurface roughness in abrasive flow finishing process using medium rheological properties." *The International Journal of Advanced Manufacturing Technology* 85.9-12 (2016): 2163-2178.

[77] Attinger, Sabine, Petros D. Koumoutsakos, and Summer Program in Multi-Scale. *Multiscale modelling and simulation*. New York: Springer, 2004.

[78] Weinan, E. *Principles of multiscale modeling*. Cambridge University Press, 2011.

[79] Tadmor, Ellad B., Michael Ortiz, and Rob Phillips. "Quasicontinuum analysis of defects in solids." *Philosophical Magazine A* 73.6 (1996): 1529-1563.

[80] Bird, G. A. "Recent advances and current challenges for DSMC." *Computers & Mathematics with Applications* 35.1-2 (1998): 1-14.

[81] Le Bris, Claude, and Tony Lelievre. "Multiscale modelling of complex fluids: a mathematical initiation." *Multiscale modelling and simulation in science*. Springer, Berlin, Heidelberg, 2009. 49-137.

[82] Le Bris, Claude, and Tony Lelièvre. "Micro-macro models for viscoelastic fluids: modelling, mathematics and numerics." *Science China Mathematics* 55.2 (2012): 353-384.

[83] Perry, Winfield B. and John Stackhouse. "Gas turbine applications of abrasive flow machining." *ASME 1989 International Gas Turbine and Aeroengine Congress and Exposition*. American Society of Mechanical Engineers Digital Collection, 1989.

[84] Howard, Mitchell and Cheng, Kai. "An industrially feasible approach to process optimisation of abrasive flow machining and its implementation perspectives." *Proceedings of the Institution of Mechanical Engineers, Part B: Journal of Engineering Manufacture* 227.11 (2013): 1748-1752.

[85] Cheng, Kai, et al. "Modelling and simulation of material removal rates and profile accuracy control in abrasive flow machining of the integrally bladed rotor blade and experimental perspectives." *Journal of Manufacturing Science and Engineering* 139.12 (2017): 121020.

[86] Uhlmann, Eckart, Christian Schmiedel and Wendler, J. "CFD simulation of the abrasive flow machining process." *Procedia CIRP* 31 (2015): 209-214.

[87] Schmitt, Joachim, and Stefan Diebels. "Simulation of the abrasive flow machining process." *ZAMM‐Journal of Applied Mathematics and Mechanics/Zeitschrift für Angewandte Mathematik und Mechanik* 93.2-3 (2013): 147-153.

[88] Cheng, Kai, et al. "Development of the improved Preston equation for abrasive flow machining of aerofoil structures and components." *Proceedings of the Institution of Mechanical Engineers, Part J: Journal of Engineering Tribology* 233.9 (2019): 1397-1404.

[89] Howard, Mitchell and Cheng, Kai. "An integrated systematic investigation of the process variables on surface generation in abrasive flow machining of titanium alloy 6Al4V." *Proceedings of the Institution of Mechanical Engineers, Part B: Journal of Engineering Manufacture* 228.11 (2014): 1419-1431.

[90] Cheng, K and Huo, Dehong. *Micro-cutting: Fundamentals and Applications*. John Wiley & Sons, 2013.

[91] Rosen, Jacob, et al. "Markov modelling of minimally invasive surgery based on tool/tissue interaction and force/torque signatures for evaluating surgical skills." *IEEE Transactions on Biomedical Engineering* 48.5 (2001): 579-591.

[92] Mi, J., et al. "Multiphysics modelling of the spray forming process." *Materials Science and Engineering: A* 477.1-2 (2008): 2-8.

[93] Shao, Yizhi, and Cheng, Kai. "Integrated modelling and analysis of micro-cutting mechanics with the precision surface generation in abrasive flow machining." *The International Journal of Advanced Manufacturing Technology* 105 (2019): 4571-4583.

[94] Trezona, R. I., Allsopp, D. N. and Hutchings, I. M. "Transitions between two-body and three-body abrasive wear: influence of test conditions in the microscale abrasive wear test." *Wear* 225 (1999): 205-214.

[95] Desale, Girish R., Bhupendra K. Gandhi and Jain, S. C. "Effect of erodent properties on erosion wear of ductile type materials." *Wear* 261.7-8 (2006): 914-921.

[96] Heinrich, Stefan, Johann Schnellbach and Hans Zimmermann. "Method of producing components subjected to flow, and components made by said method." U.S. Patent No. 6,991,434. 31 Jan. 2006.

[97] Kenda, Jani, Franci Pušavec, and Janez Kopac. "Modeling and Energy Efficiency of Abrasive Flow Machining on Tooling Industry Case Study." *Procedia CIRP* 13 (2014): 13-18.

[98] Sun, Xizhi and Cheng, Kai. "Multi-scale simulation of the nano-metric cutting process." *The International Journal of Advanced Manufacturing Technology* 47.9-12 (2010): 891-901.

[99] Fan, Jinghong. *Multiscale analysis of deformation and failure of materials*. Vol. 5. John Wiley & Sons, 2011.

[100] Liu, Wing Kam, Eduard G. Karpov, and Harold S. Park. *Nano mechanics and materials: theory, multiscale methods and applications*. John Wiley & Sons, 2006.

[101] Porter, Michael E. "International Air Transport Association Vision 2050." Harvard Business School, 2012.

[102] Turner, Barry. "International Air Transport Association (IATA)." *The Statesman's Yearbook*. Palgrave Macmillan, London, 2010. 45-46.

[103] Gillespie, LaRoux K. *Deburring and edge finishing handbook*. Society of Manufacturing Engineers, 1999.

[104] Jain, Rajendra K., Vijay K. Jain and Dixit, P. M. "Modelling of material removal and surface roughness in abrasive flow machining process." *International Journal of Machine Tools and Manufacture* 39.12 (1999): 1903-1923.

[105] Marinescu, Ioan D., et al. *Tribology of abrasive machining processes*. William Andrew, 2012.

[106] McGeough, Joseph A. *Micromachining of engineering materials*. CRC Press, 2001.

[107] Schmitt, Joachim, and Stefan Diebels. "Simulation of the abrasive flow machining process." *ZAMM-Journal of Applied Mathematics and Mechanics /Zeitschrift für Angewandte Mathematik und Mechanik* 93.2-3 (2013): 147-153.

[108] Uhlmann, Eckart and Roßkamp, Simon. "Modelling of Material Removal in Abrasive Flow Machining." *International Journal of Automation Technology* 12.6 (2018): 883-891.

[109] Uhlmann, Eckart, Schmiedel, Christian and Wendler, J. "CFD simulation of the abrasive flow machining process." *Procedia CIRP* 31 (2015): 209-214.

[110] Fu, Youzhi, et al. "Blade surface uniformity of blisk finished by abrasive flow machining." *The International Journal of Advanced Manufacturing Technology* 84.5-8 (2016): 1725-1735.

[111] Zhang, Xiaohong. *Chemical mechanical polishing and grinding of silicon wafers*. Diss. Kansas State University, 2007.

[112] Cherian, Jose and Issac, Jeoju M. "Effect of process parameters on wear performance in abrasive flow machining." *Applied Mechanics and Materials*. Vol. 766. Trans Tech Publications, 2015.

[113] Howard, Mitchell and Cheng, Kai. "An integrated systematic investigation of the process variables on surface generation in abrasive flow machining of titanium alloy

6Al4V." *Proceedings of the Institution of Mechanical Engineers, Part B: Journal of Engineering Manufacture* 228.11 (2014): 1419-1431.

[114] Stepanova, Maria, and Steven Dew, eds. *Nanofabrication: techniques and principles*. Springer Science & Business Media, 2011.

[115] Gorana, V. K., Jain, V. K. and Lal, G. K. "Forces prediction during material deformation in abrasive flow machining." *Wear* 260.1-2 (2006): 128-139.

[116] Barnes, Howard A. "A review of the rheology of filled viscoelastic systems." *Rheology Reviews* (2003): 1-36.

[117] Malkin, Stephen, and Changsheng Guo. *Grinding technology: theory and application of machining with abrasives*. Industrial Press Inc., 2008.

[118] Marinescu, Ioan D., et al. *Tribology of abrasive machining processes*. Elsevier, 2004.

[119] Fang, Liang, et al. "FEM computation of groove ridge and Monte Carlo simulation in two-body abrasive wear." *Wear* 258.1-4 (2005): 265-274.

[120] Mooney, Christopher Z. *Monte carlo simulation*. Vol. 116. Sage Publications, 1997.

[121] Bianchi, Lorenzo, et al. "Airfoil machine components polishing method." U.S. Patent Application No. 15/029,798.

[122] Clark, Daniel, and Andrew R. Walpole. "Electrochemical polishing of non-uniform features." U.S. Patent No. 10,493,549. 3 Dec. 2019.

[123] Heinrich, Stefan, Schnellbach, Johann and Zimmermann, Hans. "Method of producing components subjected to flow, and components made by said method." U.S. Patent No. 6,991,434. 31 Jan. 2006.

[124] Cheng, Kai, ed. *Machining Dynamics: Fundamentals, Applications and Practices*. Springer Science & Business Media, 2008.

[125] Desale, Girish R., Bhupendra K. Gandhi and Jain, S. C. "Development of correlations for predicting the slurry erosion of ductile materials." *Journal of Tribology* 133.3 (2011): 031603.

[126] Sallam, AM. *Studies on modelling angular soil particles using the discrete element method tampa*. Diss. Florida: University of South Florida, 2004.

[127] World Health Organization. "White Spirit (Stoddard Solvent) Health and Safety Guide-Health and Safety Guide 103." (1996).

[128] Head, Tilt. "Field SEM Released with Expanded Features." 2012.

[129] Egerton, Ray F. *Physical principles of electron microscopy*. New York: Springer, 2005.

[130] Al-Bukhaiti, M. A., et al. "Particle shape and size effects on slurry erosion of AISI 5117 steels." *Journal of Tribology* 138.2 (2016): 024503.

[131] Desale, Girish R., Bhupendra K. Gandhi, and S. C. Jain. "Effect of erodent properties on erosion wear of ductile type materials." *Wear* 261.7-8 (2006): 914-921.

[132] Dealy, John M. *Rheometers for molten plastics: a practical guide to testingand property measurement*. Society of Plastics Engineers., 1982.

[133] Shenoy, Aroon V. *Rheology of filled polymer systems*. Springer Science & Business Media, 2013.

[134] Morrison, Faith A. "Instructions for Time-Temperature Shifting of Rheological Data.", 2014.

[135] Morrison, Faith A. *Understanding rheology*. Topics in Chemical Engineering, 2001.

[136] Barnes, Howard A. "A review of the rheology of filled viscoelastic systems." *Rheology reviews* (2003): 1-36.

[137] Meguid, Michael M., et al. "Automated computerized rat eater meter: description and application." *Physiology & Behaviour* 48.5 (1990): 759-763.

[138] Hammond, D. W. and Meguid, S. A. "Fatigue fracture and residual stress relaxation in shot-peened components." *Surface Engineering*. Springer, Dordrecht, 1990. 386-392.

[139] Rides, Martin. "Rheological characterisation of filled materials: a review." (2005) *NPL Report DPEC-MPR 013*, Teddington, UK.

[140] Cheng, K., et al. "Modelling and simulation of the tool wear in nanometric cutting." Wear 255.7-12 (2003): 1427-1432.

Appendices

Appendix I

List of publications resulted from this research

1. Cheng, K., Shao, Y., Bodenhorst, R. & Jadva, M. (2017). Modeling and simulation of material removal rates and profile accuracy control in abrasive flow machining of the integrally bladed rotor blade and experimental perspectives. Journal of Manufacturing Science and Engineering, 139(12), 121020.

2. Shao, Y. & Cheng, K. (2019). Integrated modelling and analysis of micro-cutting mechanics with the precision surface generation in abrasive flow machining. The International Journal of Advanced Manufacturing Technology, 105, 2019, 4571-4583.

3. Cheng, K., Shao, Y., Jadva, M. & Bodenhorst, R. (2019). Development of the improved Preston equation for abrasive flow machining of aerofoil structures and components. Proceedings of the Institution of Mechanical Engineers, Part J: Journal of Engineering Tribology, 233(9), 1397-1404.

4. Shao, Y., Mayo, O.B. A. & Cheng, K. Development of multiscale multi-physics based modelling and simulations with the application to precision machining of aerofoil structures, Engineering Computations. (in press)

5. Shao, Y. & Cheng, K. (2018). Modelling and analysis of the micro-cutting mechanics and the associated precision surface generation in Abrasive Flow Machining, 6th International Conference on Nanomanufacturing, nanoMan2018, Brunel University London, UK, 4-6 July 2018.

6. Shao, Y., Mayo, O.B. A. & Cheng, K. Development of a multiscale multiphysics modelling and simulation approach with the application to precision machining of aerofoil components, International Conference on Computational Methods in Multi-scale, Multi-uncertainty and Multi-physics Problems, Porto, Portugal, 15-17 July 2019.

Appendix II

Specifications of the Extrude Hone Vector 200 and Extrude Hone AFM ECOFLOW

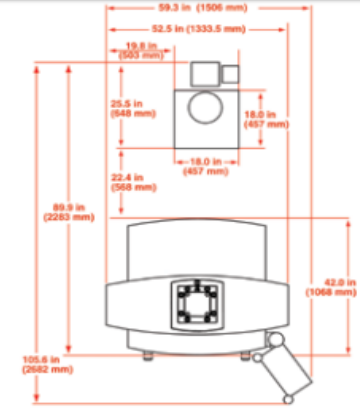

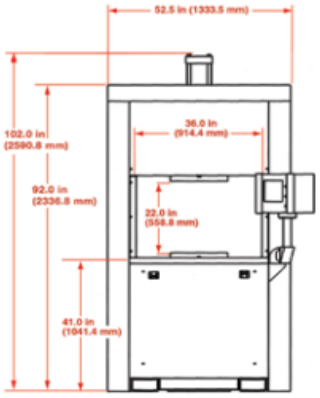

Machine Specifications

The standard EXTRUDE HONE VECTOR Abrasive Flow Machine consists of a machine with touch screen HMI and a hydraulic power unit.

Height fully open	102" (2590mm)
Height closed	92" (2335mm)
Width	52.5" (1335mm)
Depth	42" (1070mm)
Tabletop height	41" (1040mm)
Working distance between clamp columns	36" (915mm)
Estimated weight	4,300 lbs (1.955 kg)

Media Delivery

Media delivery is reciprocating between the top and bottom assemblies. Both assemblies consist of media cylinders, pistons, seals, and caps.

Hydraulic Specifications

Main components of the hydraulic system are a hydraulic power unit, two media hydraulic cylinders, and two clamp cylinders with an air/oil pump assist.

Standard Power Unit

Reservoir	20 gal (75,7 l)
Pump capacity @ 1,750 RPM	5 GPM (18,9 L/min)
Pressure	350–2500 psi (24,1–172,4 bar)

Clamp Cylinders
(clamping is powered hydraulically)

Bore diameter	5" (127mm)
Stroke	20" (508mm)
Maximum opening	22" (558,8mm)
Minimum opening	2" (50,8mm)

Electrical Specifications

The machine is controlled by a PLC.
The operator interface terminal is a touch screen. Standard functions include remote media pressure adjustment, automatic and manual mode, displacement counter, cycle counter, and cycle timer. The machine process parameters are preset via the operator interface terminal and can also be monitored on the terminal once the automatic cycle has been initiated.

Electrical

Voltage	230/460 VAC, 3 phase, 60 Hz 400 VAC, 3 phase, 50 Hz
Motor	7,5 kW
Peak amperage	15/7.5 amps
Standard PLC	Allen Bradley/Siemens

Controls

AUTOFLOW Controls are now standard with all EXTRUDE HONE VECTOR machines; 10" touch screen HMI.

Fluid Connection Specifications

Hydraulic	
Ports	NPT
Hose/tube	37° JIC
Water	
Ports	NPT
Hose/tube	NPT and/or Push Lok
Pneumatic	
Ports	NPT
Hose/tube	Push Lock

Accessories/Options

- Manually operated tooling slide cart.
- Light curtains.

System Configurations

	media cylinder diameter	hydraulic cylinder diameter	media stroke length	media capacity	hydraulic flow rate	media flow rate	media pressure min/max	expansion diameter max*
EXTRUDE HONE VECTOR 100	4" (100mm)	6" (150mm)	12.5" (320mm)	157 cu. in. (2,6 l)	5 GPM (18,9 L/min)	2.2 GPM (8,3 L/min)	500/4000 psi (34/276 bar)	N/A
EXTRUDE HONE VECTOR 150	6" (150mm)	6" (150mm)	12.5" (320mm)	353 cu. in. (5,8 l)	5 GPM (18,9 L/min)	5 GPM (19 L/min)	350/2400 psi (24/163 bar)	6.5" (165mm)
EXTRUDE HONE VECTOR 200	8" (200mm)	6" (150mm)	12.5" (320mm)	628 cu. in. (10,3 l)	5 GPM (18,9 L/min)	8.8 GPM (33,3 L/min)	200/1440 psi (13.6/98 bar)	8.7" (221mm)
EXTRUDE HONE VECTOR 250	10" (255mm)	6" (150mm)	12.5" (320mm)	981 cu. in. (16,1 l)	5 GPM (18,9 L/min)	14 GPM (53 L/min)	125/960 psi (8.5/65 bar)	10.9" (277mm)

*Maximum expansion diameter at maximum media pressure.
NOTE: Specifications and availability are subject to change without notice.

Kennametal Extrude Hone™ Limited

Kennametal Extrude Hone GmbH

Kennametal Extrude Hone GmbH
Berghauser Str. 62

EXTRUDE HONE®

TECHNICAL INFORMATION

AFM ECOFLOW

MACHINE SPECIFICATIONS

Dimensions:		
(W x D x H)	809 x 1367 x 2121mm (31.9 x 53.8 x 83.5")	
Weight	910 kg (2000 lbs)	
Table height	1050mm (41.3")	
Working area surface (W x D)	809 x 838mm (32 x 33")	
Maximum weight supported by the table	100 kg (220 lbs)	
Clamping System:		
Stroke	250mm (9.8")	
Max opening	250mm (9.8") without tooling plates	
Min opening	0mm (0") without tooling plates	
Media System:		
Media cylinder diameter	80mm (3.15")	100mm (3.8")
Media stroke length	250mm (9.8")	
Media capacity	1,3 L/1,7 kg (77 cu.in.)	2 L/2,6 kg (120 cu.in.)
Min media pressure	34 bar (500 psi)	24 bar (350 psi)
Max media pressure	207 bar (3000 psi)	140 bar (2000 psi)
Media flow rate	4.1 L/min (1.09 GPM)	6.5 L/min (1.71 GPM)
Hydraulic Unit:		
Maximum pressure	140 bar (2000 psi)	
Pump flow rate	6,5 L/min (1.71 GPM)/8 L/min (2.11 GPM)	
Tank capacity	50 l (11 gal)	

ELECTRICAL SPECIFICATIONS

The machine is PLC controlled with Siemens PLC.

Equipped with A 5.7" Siemens touchscreen.

Electrical (EU and Asia) 400 VAC, 3 Phase +N +PE, 50 Hz.

Electrical (North America) 230/460 VAC, 3 Phase, 60 Hz.

Control 24VDC.

Installed power/amperage peak 10 kVA/25A.

Status light: Red – Amber – Green

MACHINE FEATURES

Optimized aluminum extrusion frame construction maximizes strength while minimizing weight. ECOFLOW is easily moved with a standard pallet jack and is designed to fit through a normal mandoor.

AVAILABLE OPTIONS

Autoflow controls

Light curtain protection

Mitsubishi PLC and HMI

Cooling cup

NOTE: Specifications and availability are subject to change without notice.

www.extrudehone.com | help@extrudehone.com

Appendix III

Measurement results of grains in fluid media

Grid No.	Area	Perimeter	Length	Width	W/L	Shape Factor	Unit	Normal Distribution
1	8,480226	13,209342	5,126877	3,585071	0,699270	0,610738	µm	2,2796700
2	12,221503	13,990355	5,488358	3,502761	0,638217	0,784652	µm	2,6725093
3	211,372521	61,117273	19,010211	17,445875	0,917711	0,711100	µm	3,1413426
4	7,918310	12,254381	4,655450	3,593974	0,771993	0,662612	µm	2,9087860
5	16,558561	17,524034	6,148572	5,036910	0,819200	0,677586	µm	3,0254089
6	9,889770	14,387965	5,556894	2,476383	0,445642	0,600340	µm	2,1278366
7	15,739343	16,780874	6,904021	4,300219	0,622857	0,702372	µm	3,1316648
8	24,455321	21,148606	7,781061	5,380734	0,691517	0,687100	µm	3,0796033
9	7,669660	10,778630	3,790622	3,342575	0,881801	0,829581	µm	2,0528670
10	41,461993	25,249196	8,928378	7,101639	0,795401	0,817269	µm	2,2344043
11	9,004100	11,804988	4,484524	3,312296	0,738606	0,811931	µm	2,3112541
12	13,519629	16,135956	6,293001	4,168203	0,662355	0,652507	µm	2,8104593
13	15,352799	16,036184	6,055031	4,897452	0,808824	0,750232	µm	3,0054228
14	23,130293	25,173378	7,881124	6,731793	0,854167	0,458678	µm	0,4266424
15	83,584466	44,671977	15,052748	11,454774	0,760976	0,526338	µm	1,0734987
16	23,399876	19,632422	7,653794	5,656693	0,739070	0,762914	µm	2,9028952
17	21,081455	23,027663	7,520551	6,036515	0,802669	0,499587	µm	0,771066
18	14,552570	16,592313	6,718356	4,459599	0,663793	0,664256	µm	2,9233517
19	11,147891	15,037537	5,311327	3,494487	0,657931	0,619511	µm	2,4036081
20	10,447500	13,570182	4,851899	3,793303	0,781818	0,712937	µm	3,1414926
21	19,435852	18,146933	6,569008	5,502803	0,837692	0,741664	µm	3,0594107

22	159,436240	54,942202	21,010495	13,100771	0,623535	0,663720	µm	2,9186439
23	70,544943	33,614735	12,528584	9,211646	0,735250	0,784542	µm	2,6738197
24	93,385473	40,382271	14,662235	10,997340	0,750045	0,719627	µm	3,1364855
25	74,474915	35,614190	13,740244	9,430134	0,686315	0,737860	µm	3,0791933
26	41,420348	25,675395	10,526986	6,446300	0,612360	0,789568	µm	2,6123648
27	74,494370	39,945991	15,096339	7,845869	0,519720	0,586661	µm	1,9236349
28	129,455612	62,880095	28,291188	8,441970	0,298396	0,411438	µm	0,1893142
29	18,249078	18,163442	7,733409	3,637771	0,470397	0,695112	µm	3,1124139
30	42,120739	25,960570	8,946459	6,267306	0,700535	0,785376	µm	2,6638190
31	42,801675	25,141399	9,262716	7,586605	0,819048	0,850926	µm	1,7333615
32	50,681075	28,655284	10,183162	8,765543	0,860788	0,775615	µm	2,7758377
33	83,677275	40,141362	16,988232	8,307445	0,489012	0,652579	µm	2,8112113
34	47,529315	28,576337	11,451147	6,439146	0,562315	0,731406	µm	3,1066668
35	52,432052	30,880972	12,748711	6,467445	0,507302	0,690915	µm	3,0967227
36	45,194678	27,533505	10,409902	7,733604	0,742908	0,749159	µm	3,0128783
37	15,525335	18,817919	6,904021	4,734186	0,685714	0,550944	µm	1,3994794
38	23,502011	21,382317	8,719595	4,939914	0,566530	0,645960	µm	2,7392568
39	21,653757	17,932339	6,315329	5,594457	0,885854	0,846193	µm	1,8040167
40	32,451452	23,250905	8,788491	5,529887	0,629219	0,754335	µm	2,9751055
41	23,190726	24,396851	10,121840	5,289651	0,522598	0,489617	µm	0,6739189
42	19,416265	17,411789	6,308077	5,225302	0,828351	0,804801	µm	2,4113821
43	32,520325	26,290098	10,413427	5,295150	0,508493	0,591263	µm	1,9926231
44	18,420673	19,384967	7,432236	4,018294	0,540657	0,616006	µm	2,3546560
45	16,640725	17,789612	6,354318	5,132333	0,807692	0,660768	µm	2,8919537
46	30,533879	29,162335	12,304598	4,353307	0,353795	0,451177	µm	0,3784838
47	24,086555	21,774320	8,341921	5,129590	0,614917	0,638404	µm	2,6505547
48	14,955579	14,530712	5,113064	4,496489	0,879412	0,890101	µm	1,1806431

49	21,203089	22,923942	7,657054	5,101356	0,666230	0,507026	µm	0,8491645
50	25,797412	25,275497	10,169578	4,513932	0,443866	0,507442	µm	0,8536720

Appendix IV

Experimental setup and results of surface roughness and material removal of the steel coupon in AFM trials

Standard Run Order	Flow [L/S]	Visc.	Age	Tot. Vol. [L]	Aver. Roughness Left to Right	Aver. Roughness Top to Bot	Aver. Material removal [mm]	Aver. Material removal(2) [mm]
1	16.4	Low	New	10	0.88	0.23	0.01	0.016
2	32.8	Low	New	30	0.74	0.22	0.016	0.029
3	32.8	Low	New	10	0.71	0.21	0.003	0.020
4	16.4	Low	New	30	0.49	0.16	0.019	0.030
5	16.4	High	New	30	0.47	0.29	0.117	0.05
6	16.4	High	New	10	0.69	0.28	0.036	0.039
7	32.8	High	New	10	0.52	0.24	0.037	0.038
8	32.8	High	New	30	0.51	0.29	0.103	0.050
9	32.8	Low	Old	10	0.61	0.20	0.022	0.013
10	16.4	Low	Old	30	0.80	0.20	0.013	0.025
11	16.4	Low	Old	10	0.69	0.22	0.002	0.013
12	32.8	Low	Old	30	0.70	0.24	0.009	0.027
13	32.8	High	Old	10	0.38	0.28	0.027	0.033
14	16.4	High	Old	10	0.64	0.25	0.009	0.028
15	16.4	High	Old	30	0.37	0.34	0.047	0.053
16	32.8	High	Old	30	0.38	0.26	0.070	0.037

Appendix V

MATLAB codes for the surface generation and prediction of surface roughness

```
%% generate random grains %%

Num = 20;

i = 1;

index1 = 0;

r = 13.5;%the radius of grits

pos = zeros(6,20*Num);%µã×ø±êºÍÈý¸ö½ØÃæµÄ¼Ð½Ç

pos(:,:) = 100;

theta1 = zeros(1,20*Num);

theta2 = zeros(1,20*Num);

Cmin = 0.65829813;%average of measuring is 0.65829813

Cmax = 0.75829813;

thetaTemp = 0;

C = 1;

Cxy = 0;

Cxz = 0;

Cyz = 0;

k = 1;

compare = 13131313;

while( C > 0.9 )
```

```
i0 = i;
for i = i0:1:(i0+Num);
    theta1(1,i) = 2 * rand * pi;%Éú³ÉËæ»ú¼«×ø±ê
    theta2(1,i) = 2 * rand * pi;
    pos(1,i) = r * cos(theta2(1,i)) * sin(theta1(1,i));
    pos(2,i) = r * cos(theta2(1,i)) * cos(theta1(1,i));
    pos(3,i) = r * sin(theta2(1,i));
    pos(4,i) = atan(pos(2,i)/pos(1,i));%XY
    pos(5,i) = atan(pos(3,i)/pos(1,i));%XZ
    pos(6,i) = atan(pos(3,i)/pos(2,i));%YZ
    if pos(2,i) < 0
        pos(4,i) = pos(4,i) - pi;
    end
    if pos(1,i) < 0
        pos(5,i) = pos(5,i) - pi;
    end
    if pos(3,i) < 0
        pos(6,i) = pos(6,i) - pi;
    end
end
iTemp = i;



    pos4=pos(4,:);
```

```
[pos4,posz]=sort(pos4);
pos1xy=pos(1,posz);
pos2xy=pos(2,posz);
pos5=pos(5,:);
[pos5,posz]=sort(pos5);
pos1xz=pos(1,posz);
pos3xz=pos(3,posz);
pos6=pos(6,:);
[pos6,posz]=sort(pos6);
pos2yz=pos(2,posz);
pos3yz=pos(3,posz);
while k ~= 0
    k = 0;
    for index = 1:1:i-2

        if pos1xy(index) > pos1xy(index + 2)
            compare = (pos2xy(index+2) - pos2xy(index)) * ((pos1xy(index+1)-
pos1xy(index))) / (pos1xy(index+2)-pos1xy(index)) + pos2xy(index);
            if compare < pos2xy(index+1)
                pos1xy(index+1) = [];
                pos2xy(index+1) = [];
                index = index - 1;
                i = i - 1;
                k = k + 1;
            end
```

```
            else
                compare = (pos2xy(index+2) - pos2xy(index)) * ((pos1xy(index+1)-
pos1xy(index))) / (pos1xy(index+2)-pos1xy(index)) +pos2xy(index);
                if compare > pos2xy(index+1)
                    pos1xy(index+1) = [];
                    pos2xy(index+1) = [];
                    index = index - 1;
                    i = i - 1;
                    k = k + 1;
                end
            end
            index = index + 1;
        end
    end
    i = iTemp;
    while k ~= 0
        k = 0;
        for index = 1:1:i-2

            if pos1xz(index) > pos1xz(index + 2)
                compare = (pos3xz(index+2) - pos3xz(index)) * ((pos1xz(index+1)-
pos1xz(index))) / (pos1xz(index+2)-pos1xz(index)) + pos3xz(index);
                if compare < pos3xz(index+1)
                    pos1xz(index+1) = [];
                    pos3xz(index+1) = [];
```

```
                index = index - 1;
                i = i - 1;
                k = k + 1;
            end
        else
            compare = (pos3xz(index+2) - pos3xz(index)) * ((pos1xz(index+1)-pos1xz(index))) / (pos1xz(index+2)-pos1xz(index)) +pos3xz(index);
            if compare > pos3xz(index+1)
                pos1xz(index+1) = [];
                pos3xz(index+1) = [];
                index = index - 1;
                i = i - 1;
                k = k + 1;
            end
        end
        index = index + 1;
    end
end

i = iTemp;

while k ~= 0
    k = 0;
    for index = 1:1:i-2
```

```
            if pos2yz(index) > pos2yz(index + 2)
                compare = (pos3yz(index+2) - pos3yz(index)) * ((pos2yz(index+1)-
pos2yz(index))) / (pos2yz(index+2)-pos2yz(index)) + pos3yz(index);
                if compare < pos3yz(index+1)
                    pos2yz(index+1) = [];
                    pos3yz(index+1) = [];
                    index = index - 1;
                    i = i - 1;
                    k = k + 1;
                end
            else
                compare = (pos3yz(index+2) - pos3yz(index)) * ((pos2yz(index+1)-
pos2yz(index))) / (pos2yz(index+2)-pos2yz(index)) +pos3yz(index);
                if compare > pos3yz(index+1)
                    pos2yz(index+1) = [];
                    pos3yz(index+1) = [];
                    index = index - 1;
                    i = i - 1;
                    k = k + 1;
                end
            end
            index = index + 1;
        end
    end
    Lxy = Lxz = Lyz = Sxy = Sxz = Syz = 0;
```

```
for i1 = 1:1:(i0+Num-1)

    axy = sqrt((pos1xy(i1+1)-pos1xy(i1))^2+(pos2xy(i1+1)-pos2xy(i1))^2);
    bxy = sqrt(pos1xy(i1)^2+pos2xy(i1)^2);
    cxy = sqrt(pos1xy(i1+1)^2+pos2xy(i1+1)^2);
    p = (axy+bxy+cxy)/2;
    Sxy = Sxy + sqrt(p*(p-axy)*(p-bxy)*(p-cxy));
    Lxy = Lxy + axy;

    axz = sqrt((pos1xz(i1+1)-pos1xz(i1))^2+(pos3xz(i1+1)-pos3xz(i1))^2);
    bxz = sqrt(pos1xz(i1)^2+pos3xz(i1)^2);
    cxz = sqrt(pos1xz(i1+1)^2+pos3xz(i1+1)^2);
    p = (axz+bxz+cxz)/2;
    Sxz = Sxz + sqrt(p*(p-axz)*(p-bxz)*(p-cxz));
    Lxz = Lxz + axz;

    ayz = sqrt((pos3yz(i1+1)-pos3yz(i1))^2+(pos2yz(i1+1)-pos2yz(i1))^2);
    byz = sqrt(pos3yz(i1)^2+pos2yz(i1)^2);
    cyz = sqrt(pos3yz(i1+1)^2+pos2yz(i1+1)^2);
    p = (ayz+byz+cyz)/2;
    Syz = Syz + sqrt(p*(p-ayz)*(p-byz)*(p-cyz));
    Lyz = Lyz + ayz;
end
```

```
    Cxy = Lxy^2/(4*pi*Sxy);
    Cyz = Lyz^2/(4*pi*Syz);
    Cxz = Lxz^2/(4*pi*Sxz);
    C = (Cxy*Sxy+Cxz*Sxz+Cyz*Syz)/(Sxy+Sxz+Syz);
    C = 1/C;
end
%% generation of gaussian surface%%
 N = [200 200]; % size in pixels of image
 F = 8;        % frequency-filter width
 delta=2e-5;
 [X,Y] = ndgrid(1:N(1),1:N(2));
 i = min(X-1,N(1)-X+1);
 j = min(Y-1,N(2)-Y+1);
 H = delta*exp(-.5*(i.^2+j.^2)/F^2);
 Z = real(ifft2(H.*fft2(randn(N))));
 figure(1)
 meshz(X,Y,Z);
 title('Initial surface');
 set(gca,'fontsize',20)
 axis square
 xlabel ('X')
 ylabel('Y')
 zlabel('Surface Roughness')
```

```
[peakZ,ind] = findpeaks(Z(:));
 maxZ=peakZ(peakZ>0);
 minZ=peakZ(peakZ<0);
 peakX=X(ind);
 peakY=Y(ind);
[~,ind_maxZ] = ismember(maxZ,peakZ,'legacy');
 maxX=peakX(ind_maxZ);
 maxY=peakY(ind_maxZ);

 Z_datum1=Z(:,50);
 Z_datum2=Z(50,:);
 Z_sqrt1=Z_datum1.^2;
 Z_sqrt2=Z_datum2.^2;
 Z_mean1=sqrt(mean(Z_sqrt1));
 Z_mean2=sqrt(mean(Z_sqrt2));
 Z_dev1=abs(Z_datum1-Z_mean1);
 Z_dev2=abs(Z_datum2-Z_mean2);
 Ra_horizontal=1/N(1)*sum(Z_dev1);
 Ra_vetical=1/N(1)*sum(Z_dev2);
 Rq_horizontal=(1/N(1)*sum(Z_dev1.^2))^(1/2);
 Rq_vertical=(1/N(1)*sum(Z_dev2.^2))^(1/2);
 peak=[maxX,maxY,maxZ];
 ind_peak=(maxY-1)*N(1)+maxX;
```

```
%%data extraction (quater stroke)%%
load 'Pressurechange.txt'
X_c=Pressurechange(:,1);
P_c=Pressurechange(:,2);
p_c=polyfit(X_c,P_c,4);
x_c=linspace(15,13,200);
P2_c=p_c(1)*x_c.^4+p_c(2)*x_c.^3+p_c(3)*x_c.^2+p_c(4)*x_c+p_c(5);
P2_c=P2_c';
P_upper=repmat(P2_c,1,200);
P_aperture1=P_upper(ind_peak);



%%finishing simulation%%
 ind_P1_1=ind_peak-1;
 ind_P3_1=ind_peak+1;
 P1_1=[X(ind_P1_1),Y(ind_P1_1),Z(ind_P1_1)];
 P3_1=[X(ind_P3_1),Y(ind_P3_1),Z(ind_P3_1)];
  for i=1:size(peak)
   a_1(i,:) = norm(peak(i,:)-P1_1(i,:)); % The three sides' lengths
   b_1(i,:) = norm(P3_1(i,:)-peak(i,:));
   c_1(i,:) = norm(P1_1(i,:)-P3_1(i,:));
   s_1(i,:) = (a_1(i,:)+b_1(i,:)+c_1(i,:))/2;
   A_1(i,:) = sqrt(s_1(i,:)*(s_1(i,:)-a_1(i,:))*(s_1(i,:)-b_1(i,:))*(s_1(i,:)-c_1(i,:))); % Area
of triangle P1P2P3
   R1_1(i,:) = a_1(i)*b_1(i)*c_1(i)/(4*A_1(i,:)); % Radius of curvature at P2
```

```
  end


E1=90000; %MPa

E2=45000; %MPa Aluminium

niu1=0.35;

niu2=0.334;

Ecom=1/((1-niu1^2)/E1+(1-niu2^2)/E2); %[MPa]

R2=5e-6;

Ns=810;

n1=Ns/(8*sum(A_1))*10^(-6); %grain no.*microns



for i=1:size(peak)

R_1(i,:)=1/(1/R1_1(i,:)+1/R2);

r_1(i,:)=pi*P_aperture1(i,:)*R_1(i,:)/(2*Ecom);

delta_1(i,:)=pi*r_1(i,:)*P_aperture1(i,:)/(2*Ecom);%micron

end



maxZ_1=maxZ-delta_1*n1;

Z1=Z;

Z1(ind_peak(:))=maxZ_1(:);

[peakZ1,ind1] = findpeaks(Z1(:));

maxZ1=peakZ1(peakZ1>0);
```

```
minZ1=peakZ1(peakZ1<0);
peakX1=X(ind1);
peakY1=Y(ind1);
[~,ind_maxZ1] = ismember(maxZ1,peakZ1,'legacy');
maxX1=peakX1(ind_maxZ1);
maxY1=peakY1(ind_maxZ1);
peak1=[maxX1,maxY1,maxZ1];
ind_peak1=(maxY1-1)*N(1)+maxX1;
figure(2)
meshz(X,Y,Z1);
title('Indented Surface');
set(gca,'fontsize',20)
xlabel ('X')
ylabel('Y')
zlabel('Surface Roughness')
%%finishing simulation%%
 ind_P1_2=ind_peak1-1;
 ind_P3_2=ind_peak1+1;
 P1_2=[X(ind_P1_2),Y(ind_P1_2),Z1(ind_P1_2)];
 P3_2=[X(ind_P3_2),Y(ind_P3_2),Z1(ind_P3_2)];
  for i=1:size(peak1)
   a_2(i,:) = norm(peak1(i,:)-P1_2(i,:)); % The three sides' lengths
   b_2(i,:) = norm(P3_2(i,:)-peak1(i,:));
   c_2(i,:) = norm(P1_2(i,:)-P3_2(i,:));
```

```
   s_2(i,:) = (a_2(i,:)+b_2(i,:)+c_2(i,:))/2;

   A_2(i,:) = sqrt(s_2(i,:)*(s_2(i,:)-a_2(i,:))*(s_2(i,:)-b_2(i,:))*(s_2(i,:)-c_2(i,:))); % Area of triangle P1P2P3

   R1_2(i,:) = a_2(i)*b_2(i)*c_2(i)/(4*A_2(i,:)); % Radius of curvature at P2

  end

  P_aperture2=P_upper(ind_peak1);

for i=1:size(peak1)

R_2(i,:)=1/(1/R1_2(i,:)+1/R2);

r_2(i,:)=pi*P_aperture2(i,:)*R_2(i,:)/(2*Ecom);

delta_2(i,:)=pi*r_2(i,:)*P_aperture2(i,:)/(2*Ecom);%micron

end

n2=Ns/(8*sum(A_1))*10^(-6);

maxZ_2=maxZ1-delta_2*n2;

Z2=Z1;

Z2(ind_peak1(:))=maxZ_2(:);

[peakZ2,ind2] = findpeaks(Z2(:));

maxZ2=peakZ2(peakZ2>0);

minZ2=peakZ2(peakZ2<0);

peakX2=X(ind2);

peakY2=Y(ind2);

[~,ind_maxZ2] = ismember(maxZ2,peakZ2,'legacy');

maxX2=peakX2(ind_maxZ2);

maxY2=peakY2(ind_maxZ2);

peak2=[maxX2,maxY2,maxZ2];

ind_peak2=(maxY2-1)*N(1)+maxX2;
```

```
%%finishing simulation%%
 ind_P1_3=ind_peak2-1;
 ind_P3_3=ind_peak2+1;
 P1_3=[X(ind_P1_3),Y(ind_P1_3),Z2(ind_P1_3)];
 P3_3=[X(ind_P3_3),Y(ind_P3_3),Z2(ind_P3_3)];
  for i=1:size(peak2)
   a_3(i,:) = norm(peak2(i,:)-P1_3(i,:)); % The three sides' lengths
   b_3(i,:) = norm(P3_3(i,:)-peak2(i,:));
   c_3(i,:) = norm(P1_3(i,:)-P3_3(i,:));
   s_3(i,:) = (a_3(i,:)+b_3(i,:)+c_3(i,:))/2;
   A_3(i,:) = sqrt(s_3(i,:)*(s_3(i,:)-a_3(i,:))*(s_3(i,:)-b_3(i,:))*(s_3(i,:)-c_3(i,:))); % Area
of triangle P1P2P3
   R1_3(i,:) = a_3(i)*b_3(i)*c_3(i)/(4*A_3(i,:)); % Radius of curvature at P2
  end
P_aperture3=P_upper(ind_peak2);
for i=1:size(peak2)
R_3(i,:)=1/(1/R1_3(i,:)+1/R2);
r_3(i,:)=pi*P_aperture3(i,:)*R_3(i,:)/(2*Ecom);
delta_3(i,:)=pi*r_3(i,:)*P_aperture3(i,:)/(2*Ecom);%micron
end
n3=Ns/(8*sum(A_1))*10^(-6);
maxZ_3=maxZ2-delta_3*n3;
Z3=Z2;
Z3(ind_peak2(:))=maxZ_3(:);
[peakZ3,ind3] = findpeaks(Z3(:));
```

```
maxZ3=peakZ3(peakZ3>0);

minZ3=peakZ3(peakZ3<0);

peakX3=X(ind3);

peakY3=Y(ind3);

[~,ind_maxZ3] = ismember(maxZ3,peakZ3,'legacy');

maxX3=peakX3(ind_maxZ3);

maxY3=peakY3(ind_maxZ3);

peak3=[maxX3,maxY3,maxZ3];

ind_peak3=(maxY3-1)*N(1)+maxX3;


%%data extraction (quater stroke)%%

load 'Pressurechange.txt'

X_c=Pressurechange(:,1);

P_c=Pressurechange(:,2);

p_c=polyfit(X_c,P_c,4);

x_c=linspace(4,2,200);

P2_cl=p_c(1)*x_c.^4+p_c(2)*x_c.^3+p_c(3)*x_c.^2+p_c(4)*x_c+p_c(5);

P2_cl=P2_cl';

P_lower=repmat(P2_cl,1,200);

P_aperture9=P_lower(ind_peak8);


%%finishing simulation%%

 ind_P1_9=ind_peak8-1;

 ind_P3_9=ind_peak8+1;
```

```
 P1_9=[X(ind_P1_9),Y(ind_P1_9),Z8(ind_P1_9)];
 P3_9=[X(ind_P3_9),Y(ind_P3_9),Z8(ind_P3_9)];
  for i=1:size(peak8)
   a_9(i,:) = norm(peak8(i,:)-P1_9(i,:)); % The three sides' lengths
   b_9(i,:) = norm(P3_9(i,:)-peak8(i,:));
   c_9(i,:) = norm(P1_9(i,:)-P3_9(i,:));
   s_9(i,:) = (a_9(i,:)+b_9(i,:)+c_9(i,:))/2;
   A_9(i,:) = sqrt(s_9(i,:)*(s_9(i,:)-a_9(i,:))*(s_9(i,:)-b_9(i,:))*(s_9(i,:)-c_9(i,:))); % Area of triangle P1P2P3
   R1_9(i,:) = a_9(i)*b_9(i)*c_9(i)/(4*A_9(i,:)); % Radius of curvature at P2
  end
E1=90000; %MPa
E2=45000; %MPa Aluminium
niu1=0.35;
niu2=0.334;
Ecom=1/((1-niu1^2)/E1+(1-niu2^2)/E2); %[MPa]
R2=5e-6;
Ns1=810
for i=1:size(peak8)
R_9(i,:)=1/(1/R1_9(i,:)+1/R2);
r_9(i,:)=pi*P_aperture9(i,:)*R_9(i,:)/(2*Ecom);
delta_9(i,:)=pi*r_9(i,:)*P_aperture9(i,:)/(2*Ecom);%micron
end


n9=Ns1/(8*sum(A_1))*10^(-6);
```

```
maxZ_9=maxZ8-delta_9*n9;

Z9=Z8;

Z9(ind_peak8(:))=maxZ_9(:);

[peakZ9,ind9] = findpeaks(Z9(:));

maxZ9=peakZ9(peakZ9>0);

minZ9=peakZ9(peakZ9<0);

peakX9=X(ind9);

peakY9=Y(ind9);

[~,ind_maxZ9] = ismember(maxZ9,peakZ9,'legacy');

maxX9=peakX9(ind_maxZ9);

maxY9=peakY9(ind_maxZ9);

peak9=[maxX9,maxY9,maxZ9];

ind_peak9=(maxY9-1)*N(1)+maxX9;


%%finishing simulation%%

 ind_P1_10=ind_peak9-1;

 ind_P3_10=ind_peak9+1;

 P1_10=[X(ind_P1_10),Y(ind_P1_10),Z9(ind_P1_10)];

 P3_10=[X(ind_P3_10),Y(ind_P3_10),Z9(ind_P3_10)];

  for i=1:size(peak9)

   a_10(i,:) = norm(peak9(i,:)-P1_10(i,:)); % The three sides' lengths

   b_10(i,:) = norm(P3_10(i,:)-peak9(i,:));

   c_10(i,:) = norm(P1_10(i,:)-P3_10(i,:));

   s_10(i,:) = (a_10(i,:)+b_10(i,:)+c_10(i,:))/2;
```

```
  A_10(i,:) = sqrt(s_10(i,:)*(s_10(i,:)-a_10(i,:))*(s_10(i,:)-b_10(i,:))*(s_10(i,:)-c_10(i,:))); % Area of triangle P1P2P3
  R1_10(i,:) = a_10(i)*b_10(i)*c_10(i)/(4*A_10(i,:)); % Radius of curvature at P2
 end
P_aperture10=P_upper(ind_peak9);
for i=1:size(peak9)
R_10(i,:)=1/(1/R1_10(i,:)+1/R2);
r_10(i,:)=pi*P_aperture10(i,:)*R_10(i,:)/(2*Ecom);
delta_10(i,:)=pi*r_10(i,:)*P_aperture10(i,:)/(2*Ecom);%micron
end
n10=Ns1/(8*sum(A_1))*10^(-6);
maxZ_10=maxZ9-delta_10*n10;
Z10=Z9;
Z10(ind_peak9(:))=maxZ_10(:);
[peakZ10,ind10] = findpeaks(Z10(:));
maxZ10=peakZ10(peakZ10>0);
minZ10=peakZ10(peakZ10<0);
peakX10=X(ind10);
peakY10=Y(ind10);
[~,ind_maxZ10] = ismember(maxZ10,peakZ10,'legacy');
maxX10=peakX10(ind_maxZ10);
maxY10=peakY10(ind_maxZ10);
peak10=[maxX10,maxY10,maxZ10];
ind_peak10=(maxY10-1)*N(1)+maxX10;
```